Evaluation of Noise Mitigation Performance of the T-NMS 10000 During Offshore Monopile Installation

Numerical analysis of the influence of layered sandy soil configurations

CIEM0500: Master Thesis

Laurien Korteweg

Delft University of Technology

TU Delft

MARINE CONTRACTORS

Evaluation of Noise Mitigation Performance of the T-NMS 10000 During Offshore Monopile Installation

Numerical analysis of the influence of layered sandy soil configurations

by

Laurien Korteweg

to obtain the degree of

Master of Science

in Hydraulic & Offshore Engineering at the Delft University of Technology

Student number:	5083788	
Project duration:	November, 2025 – May, 2025	
Thesis committee:	Dr. ir. A. Tsouvalas,	TU Delft
	Dr. A. Tsetas,	TU Delft
	Dr. Y. Peng,	TU Delft
	MSc. K. A. Canny,	TU Delft
	MSc. G. J. Glasbergen,	Heerema Marine Contractors

Cover: Photograph of the deployment of the T-NMS 10000 during the installation of the monopile

TU Delft

MARINE CONTRACTORS

Preface

This graduation study, titled *"Evaluation of Noise Mitigation Performance of the T-NMS 10000 During Offshore Monopile Installation"*, was supported by Heerema Marine Contractors and the Delft University of Technology. This thesis fulfills the requirements for the Master of Science in Civil Engineering at the Delft University of Technology.

I believe that working on questions outside my comfort zone helps me grow and better understand the world around me. Since many aspects of underwater acoustics are still not fully understood, this research came with a range of technical challenges. Over the past months, there were moments I enjoyed the work, as well as moments where the process was difficult and frustrating. Looking back, this thesis has helped me develop not only my technical knowledge of underwater acoustics, but also my approach to research in general. Learning how to deal with uncertainty, limitations, and iterative problem solving has been an important part of this process. While this thesis does not aim to answer all remaining questions in underwater acoustics, I hope this work helps future students, researchers, and other interested readers gain a clearer understanding of the topic and offers useful insights into the noise mitigation performance of the T-NMS 10000.

I would like to take this opportunity to thank the people who supported me throughout this process. First, I would like to thank my company supervisor, Govert Jan Glasbergen. You encouraged me during challenging moments and provided valuable support along the way. Your observation that I often say I will do something 'eventjes' taught me that in the academic world, nothing is ever truly 'eventjes': behind every answer, many new questions arise.

Secondly, I would like to thank my committee at Delft University of Technology. To Yaxi Peng and Khairina Canny, our weekly meetings provided the insights and direction I needed throughout this project and your encouragement always came at the right moment when I needed it. I would also like to thank Athanasios Tsetas for your valuable suggestions regarding data processing and the structural aspects of the model. In addition, I thank the chair of my committee, Apostolos Tsouvalas. Your extensive knowledge of the subject challenged me throughout the process, and although it often took time to fully process your feedback, it consistently helped steer this research in the right direction.

Lastly, I want to thank my parents and roommates, who were always there when I needed to vent or seek advice. Finally, I thank my boyfriend, Ruben. Thank you for your encouragement and support. Whether you were familiar with the specific topic or not, you always challenged me to think twice about my approach, something I often needed. Thank you all.

I hope that you find this thesis useful and interesting. It has been my pleasure to contribute to this field.

Laurien Korteweg
Delft, May 2026

Summary

The installation of offshore monopiles (MPs) using hydraulic impact hammers generates high intensity impulsive underwater noise, which can pose risks to marine life and challenges compliance with underwater noise regulations. As offshore wind turbines continue to increase in size, the associated MPs become larger and require higher blow energies, further increasing underwater noise levels. To mitigate these effects, various noise mitigation systems have been developed. One of these systems is the T-NMS 10000 (NMS), a noise mitigation screen consisting of a double walled steel structure with an integrated air layer and a bubble injection system (see Figures 1 and 2).

Figure 1: Rendered image of the T-NMS 10000 installed around a MP during deployment (IQIP, 2023).

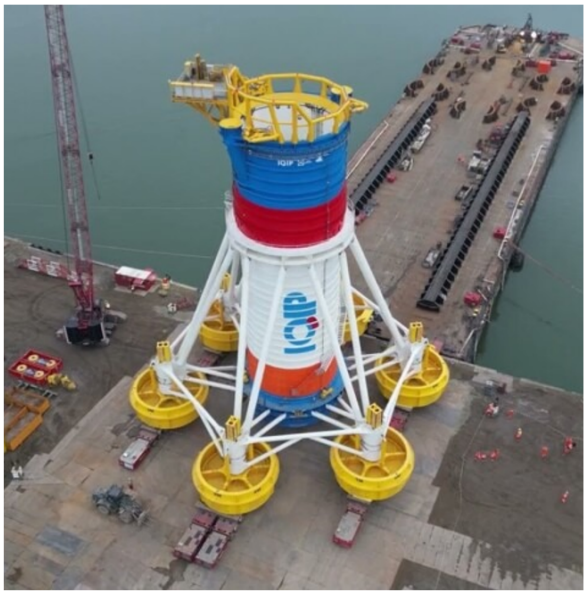

Figure 2: Photograph of the T-NMS-10000 during assembly at the fabrication yard (IQIP, 2024).

Despite its first deployment during the installation at a wind farm, the mechanisms governing the noise mitigation performance of the NMS have not yet been modeled, analyzed, or quantified in the published literature. As a result, the acoustic behavior of the system remains largely unknown. The deployment of the NMS at the wind farm therefore provided a unique opportunity to address this gap.

The main objective of this study was to investigate to what extent soil stratification and soil properties influence the noise mitigation performance of the NMS during offshore MP installation. To achieve this, an coupled numerical modeling approach was applied. The approach combines a finite element model to resolve near field interactions with a semi-analytical model for far field sound propagation. The resulting numerical framework was calibrated and validated using field measurements obtained during MP installation at the wind farm site.

The unmitigated model showed good agreement with the measured sound exposure levels (SEL), indicating that the dominant mechanisms governing underwater noise generation and propagation were captured. The NMS was represented in the numerical model using an air layer, reflecting its primary mitigation mechanism based on impedance mismatch. It was found that the actual NMS achieved approximately X% of the theoretically achievable noise reduction of a near field mitigation system at the wind farm, while the numerical NMS representation achieved only 46% mitigation. Although the modeled NMS performance does not fully match the observed behavior, the approach enables a comparison of NMS performance across different soil configurations.

The influence of soil conditions on NMS performance was investigated for four sandy soil configurations: uniform dense sand, uniform loose sand, and layered soils consisting of a loose upper layer overlying dense sand with varying thickness. For unmitigated cases, dense dominated soils result in a larger proportion of acoustic energy generated in the water column compared to loose dominated soils, thereby increasing the mitigation potential of the NMS. In layered configurations, reflections at soil interfaces promote repeated redirection of energy toward the seabed, increasing the likelihood of re-radiation into the water column. In particular, thinner loose top layers lead to more frequent interaction between seismic energy and the seabed, resulting in increased energy leakage back into the water column compared to thicker layers. Despite these differences in energy redistribution, soil properties and stratification only have a minor influence on unmitigated far field noise levels, with a maximum difference of 2.2 dB at 750 m across the investigated cases. Similarly, when the NMS representation is included, far field noise levels vary by only 1.6 dB between the different soil configurations.

In contrast, soil conditions have a strong influence on the noise mitigation potential. Dense dominated soils generate more waterborne energy near the pile, resulting in a higher absolute mitigation potential for near field noise mitigation systems such as the NMS. Loose dominated soils, however, show a higher relative mitigation performance, meaning that the NMS performs closer to its maximum achievable reduction under those conditions.

Due to the uncertainty in the numerical representation of the NMS, these results should be interpreted with caution. As the modeled NMS performance does not fully match the observed behavior, no conclusions are drawn in this study on which soil conditions are most favourable for NMS application.

Overall, the results indicate that soil properties and stratification primarily influence how acoustic energy is distributed between the water column and the seabed, and how the seismic energy is attenuated or can be re-radiated. While these findings provide guidance for identifying conditions in which noise mitigation may be more effective, more advanced NMS modeling approaches are required before firm conclusions can be drawn on soil dependent mitigation performance.

Contents

List of Figures

List of Tables

1 Introduction

In response to climate goals aimed at reducing greenhouse gas emissions, the global demand for renewable energy has increased in recent decades (Dinh and McKeogh, 2018; Yi Li et al., 2020). Offshore wind energy has emerged as a promising solution for clean energy generation, capitalizing on the strong and consistent winds that occur on ocean surfaces (Kaldellis and Kapsali, 2013).

Offshore wind turbines can be supported by several types of foundations (Wu et al., 2019; Tsouvalas, 2020), of which the monopile (MP) is most commonly used. This is mainly due to its adaptable design and relatively cost effective installation (Sánchez et al., 2019). In 2019, approximately 81% of all offshore wind turbines installed in European waters were supported by MP foundations (Soares-Ramos et al., 2020). MPs are typically installed using hydraulic impact hammers, which generate high intensity impulsive noise in both the water column and the seabed. This underwater noise can cause injury or behavioral disturbance to marine fauna, and therefore, strict regulatory noise thresholds are enforced (Southall et al., 2019; Thompson et al., 2020).

1.1. Problem Statement & Research Gap

Technological developments have led to increasingly larger offshore wind turbines, which require MPs with larger diameters and larger blow energies. As a result, underwater noise levels during installation have increased, leading to higher risks for marine life and making compliance with underwater noise regulations more challenging (see Figure 1.1).

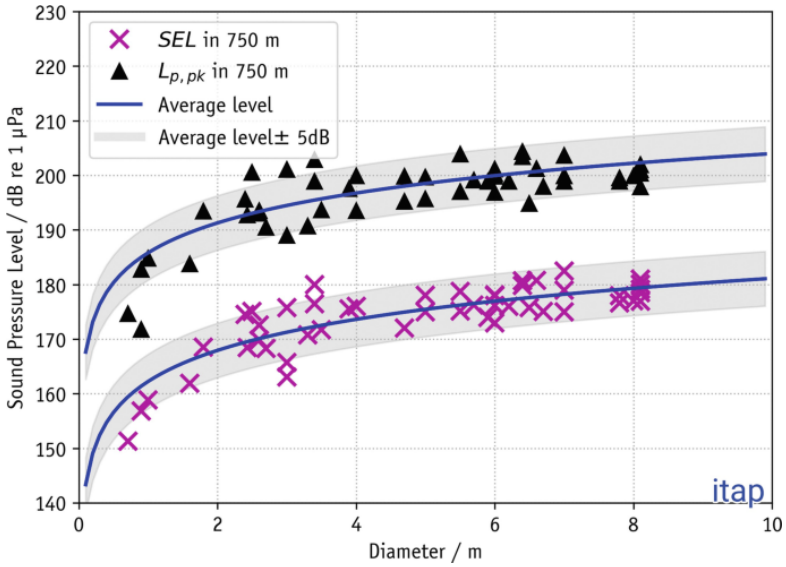

Figure 1.1: Measured zero-to-peak sound pressure levels ($L_{p,pk}$) and Sound Exposure Levels (SEL) during offshore impact pile driving as a function of pile diameter (Bellmann et al., 2020).

To meet these underwater noise regulations, the industry has developed various noise mitigation systems. A novel solution is the T-NMS 10000, a noise mitigation screen (NMS) developed by IQIP. This system consists of a double-walled steel structure with an integrated air layer and a bubble injection

system (see Figures 1.2 and 1.3) (Heerema Marine Contractors, 2024a).

Figure 1.2: Rendered image of the T-NMS 10000 installed around a MP during deployment (IQIP, 2023).

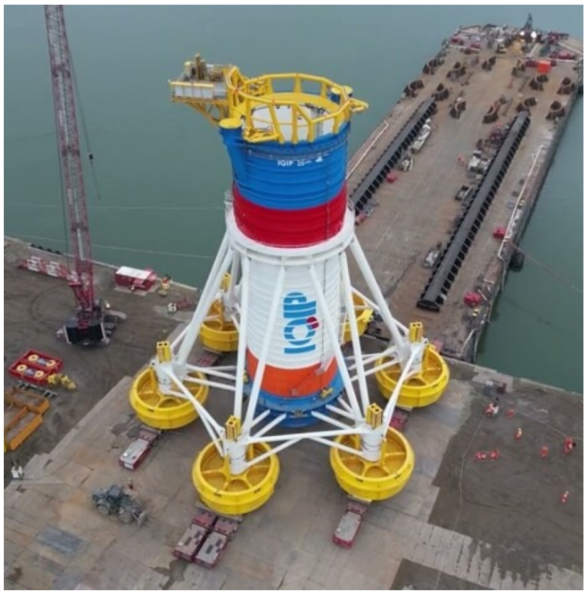

Figure 1.3: Photograph of the T-NMS-10000 during assembly at the fabrication yard (IQIP, 2024).

Currently, no scientific studies have established how the NMS can be modeled to mimic its mitigation behavior. Furthermore, analyses of its noise mitigation performance remain unpublished. The first deployment of the NMS at an offshore wind farm provides an opportunity to address this gap. The empirical data collected during this project enables the development and validation of a numerical representation for the NMS. In addition, the level of noise mitigation achieved during the project exceeded the expectations of the contractor, Heerema Marine Contractors (HMC). However, the physical mechanisms responsible for this high effectiveness are not yet fully understood. Therefore, validating the numerical model against field measurements is essential to both quantify the system's performance and improve understanding of its noise mitigation behavior.

While the NMS is designed to reduce noise propagating through the water column, its overall performance is limited by the so called "secondary noise path" (see Figure 1.4). Part of the energy generated during pile driving is generated into the seabed, propagates through the soil as seismic waves, and subsequently re-radiates back into the water column at larger distances. As a result, even when waterborne noise is reduced in the near field, this soil borne contribution can still lead to significant noise levels in the far field. The effect of this secondary noise path is believed to depend on soil conditions. Soil properties and stratification are thought to influence how much energy is transferred from the pile into the soil, how this energy propagates, and how efficiently it is re-radiated into the water column. Currently, there is a lack of scientific research quantifying how varying soil conditions affect the effectiveness of the NMS.

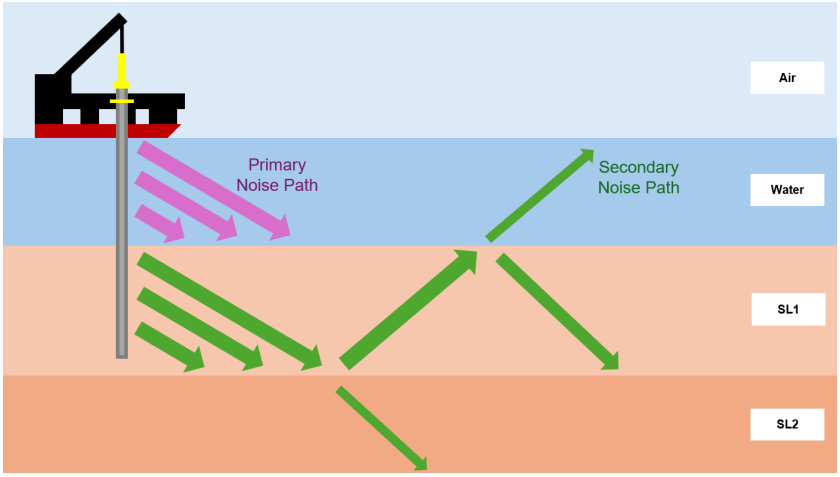

Figure 1.4: Illustration representing the primary (waterborne) and secondary (soil-borne) noise paths. The secondary path illustrates acoustic energy propagating through the seabed and re-radiating into the water column.

1.2. Research Questions

This study aims to model and analyze the noise mitigation effectiveness of the NMS during MP installations. To achieve this goal, the following research questions have been formulated:

Main Research Question:
To what extent do soil stratification and properties influence the noise mitigation performance of the T-NMS 10000 during offshore monopile installation?

Sub-Research Questions

1. What are the fundamental principles governing underwater acoustics, impulsive noise generation during pile driving, and the mechanisms of near-field noise mitigation?
2. What types of data have been collected during MP installation at the offshore wind farm, and how should these be used for numerical modeling?
3. How can the T-NMS 10000 be represented within a coupled numerical framework consisting of a near-field Finite Element Method model and a semi-analytical far-field propagation model?
4. Based on the validated model and field data from the wind farm project, what is the quantified noise mitigation effectiveness of the T-NMS 10000?
5. How do sandy soil properties and stratification, ranging from uniform dense and loose sand to layered systems with a loose top layer over dense sand, influence the noise mitigation performance of the T-NMS 10000?

1.3. Thesis Structure

The structure of this thesis is organized as follows.

Chapter 2 introduces the technical context of this study. It discusses relevant underwater noise metrics and presents the theoretical background of underwater noise generation, propagation, and mitigation. The chapter also introduces the NMS.

Chapter 3 describes the dataset obtained from the MP installation at the wind farm. It provides an overview of the project and its site conditions, details the selection of the relevant data, and presents information on hammer forces and hydrophone properties. The chapter concludes with a description of the model validation approach adopted in this study.

Chapter 4 outlines the adopted acoustic modeling approach. It describes the methodology, model geometry, and input parameters, and explains how unit-response results are converted to the response corresponding to the applied hammer force.

Chapter 5 analyzes the results of the model and evaluates its accuracy. Using the field data from the wind farm, the chapter presents the model results, performs a sensitivity analysis, and concludes with a discussion on the noise mitigation performance of the NMS.

Chapter 6 presents the analysis of the noise mitigation effectiveness of the NMS for different stratified sandy soil configurations. The chapter investigates noise generation and propagation mechanisms and concludes with the noise mitigation effectiveness of the NMS for the investigated sandy soils.

Chapter 7 discusses the interpretation of the key findings, the limitations of the study, and directions for future research.

Finally, Chapter 8 answers the research questions and presents the main conclusions and recommendations of this study.

Furthermore, Appendix H presents the case study performed to determine a numerical representation of the NMS, while Appendix K describes the additional case study underlying the assessment of the noise mitigation effectiveness of the NMS for different sandy soil configurations.

2
Technical Context

This chapter presents the technical context of this study. Section 2.1 describes the fundamental concepts of sound and details the acoustic metrics relevant to underwater noise. Section 2.2 describes the technical background of underwater noise during pile driving, focusing on noise generation and sound propagation. Lastly, Section 2.3 explains the working principle of the NMS system, presenting its relevant dimensions and providing a general overview of its structure.

2.1. Fundamentals of Underwater Acoustics

Sound in a medium, such as water, is generated by a disturbance that causes localized compressions and rarefactions (Bellmann et al., 2020). These pressure fluctuations propagate through the medium as a result of its compressibility, forming what is known as a pressure wave. Sound is defined as a rapid, often periodic, variation in pressure that is superimposed on the ambient pressure level, which in water corresponds to the hydrostatic pressure (Bellmann et al., 2020). This phenomenon involves the oscillatory motion of fluid particles around their equilibrium positions, described by the particle velocity (v), while sound velocity (c) refers to the speed at which the sound waves travel through a medium. In water, this propagation speed is typically assumed as $c = 1500\,m/s$, whereas particle velocity is significantly lower and reflects the local motion of individual particles (Bellmann et al., 2020).

The relationship between sound pressure (p) and particle velocity (v) is governed by the acoustic impedance (Z), a property that characterizes how a medium resists the transmission of sound waves. This relationship is expressed in Eq. 2.1 (Bellmann et al., 2020). When a sound wave encounters a boundary between two media with differing acoustic properties, an impedance mismatch occurs. As a result, part of the wave is reflected at the interface, while the other part is transmitted into the second medium (Jensen et al., 2011). A large difference in acoustic impedance between two media, such as water and air, is commonly referred to as an impedance gap. This gap implies that only a small portion of the sound is transmitted, while most of it is reflected.

$$Z = \frac{p}{v} = \rho c \tag{2.1}$$

2.1.1. The Decibel Scale

In a uniform acoustic medium, a medium with constant density (ρ) and sound speed (c), acoustic intensity I, which represents the energy flow per unit area, is proportional to the square of the acoustic pressure (p). This relationship is given by (Jensen et al., 2011):

$$I = \frac{p^2}{\rho c} = \frac{p^2}{Z} \quad [W/m^2] \tag{2.2}$$

In acoustics, sound is typically expressed in terms of sound level, measured in decibels (dB). The decibel is a dimensionless unit that represents a ratio of intensities (not pressure) expressed in terms of a logarithmic (base 10) scale (Jensen et al., 2011). The decibel is a dimensionless unit because it is a relative unit, not an absolute one. The use of a logarithmic scale serves two key purposes. Firstly, to accommodate the wide and dynamic range of sound encountered in everyday life. Secondly, to reflect that perceived loudness increases logarithmically rather than linearly with sound pressure (Kasteel, 2018). To compare two sound intensities, I_1 and I_2, the dB scale is used:

$$\Delta dB = 10 \log_{10}(\frac{I_1}{I_2}) \tag{2.3}$$

Since intensity is proportional to pressure squared, Eq. 2.2 can be substituted into Eq. 2.3, which results in Eq. 2.4. This relationship implies that a doubling of acoustic pressure corresponds to a 6 dB increase: $20\log_{10}(2) \approx 6\,dB$. It is important to note that what appears as a relatively small change on the logarithmic decibel scale often represents a significantly large change in non-logarithmic values.

$$\Delta dB = 10\log_{10}(\frac{p_1^2}{p_2^2}) = 20\log(\frac{p_1}{p_2}) \tag{2.4}$$

In underwater acoustics, decibel levels are absolute values defined by the ratio of the measured acoustic quantity to a specific reference level. The reference pressure (p_{ref}) for underwater sound is $1\,\mu Pa$ (Jensen et al., 2011). Consequently, all absolute pressure levels in this study are expressed in dB re $1\mu Pa$. While the shorthand 'dB' is used throughout this study for brevity, it refers to this $1\,\mu Pa$ reference.

2.1.2. Transmission Loss

When an acoustic signal propagates through the ocean, its strength decreases over distance. This is due to various phenomenon like geometrical spreading. In underwater acoustics, Transmission Loss (TL) is a metric used to quantify this decay in signal intensity over distance. It is defined in decibels as a ratio between the acoustic intensity at a specific point in the field $I(r,z)$, and the reference intensity measured at a distance of 1 m from the source I_0 (see Eq. 2.5) (Jensen et al., 2011). Because TL represents a ratio of two intensities, it is a dimensionless quantity expressed in decibels (dB). Unlike absolute sound levels (which are referenced to $1\,\mu Pa$), TL describes the relative loss of energy. Therefore, the unit is written as dB re $1m$. This indicates that the loss is calculated starting from 1 m reference point.

$$TL = -10\log_{10}\frac{I(r,z)}{I_0} = -20\log_{10}\frac{|p(r,z)|}{|p_0|} \qquad (dB \text{ re } 1m) \tag{2.5}$$

Transmission loss results from geometrical spreading and attenuation. While spreading loss accounts for the signal's natural expansion as it moves away from the source, attenuation accounts for different mechanisms. The most important attenuation mechanisms in ocean acoustics are volume attenuation, bottom reflection loss, and boundary and volume scattering loss, which are explained in detail by Jensen et al. (2011).

The geometry of the environment dictates how the acoustic energy spreads, i.e. geometrical spreading. Two fundamental models are considered here:

- **Spherical Spreading:**
  In an unbounded, homogeneous medium, a point source radiates power equally in all directions, forming an expanding sphere (see Figure 2.1). In a lossless environment, the intensity I is inversely proportional to the surface of the sphere, i.e. $I \propto 1/(4\pi R^2)$ (Jensen et al., 2011). Consequently, the transmission loss for spherical spreading is calculated as:

$$TL = 20\log r \tag{2.6}$$

- **Cylindrical Spreading:**
  In scenarios where the ocean acts as a waveguide, bounded by the sea surface and the seafloor (see Figure 2.1), the acoustic energy becomes trapped between these planes. At large distances, the wavefront expands as a cylinder of radius R and height D rather than a sphere. Since the intensity becomes inversely proportional to the surface area of this cylinder, i.e. $I \propto 1/(2\pi RD)$, the cylindrical spreading loss is defined as (Jensen et al., 2011):

$$TL = 10\log r \tag{2.7}$$

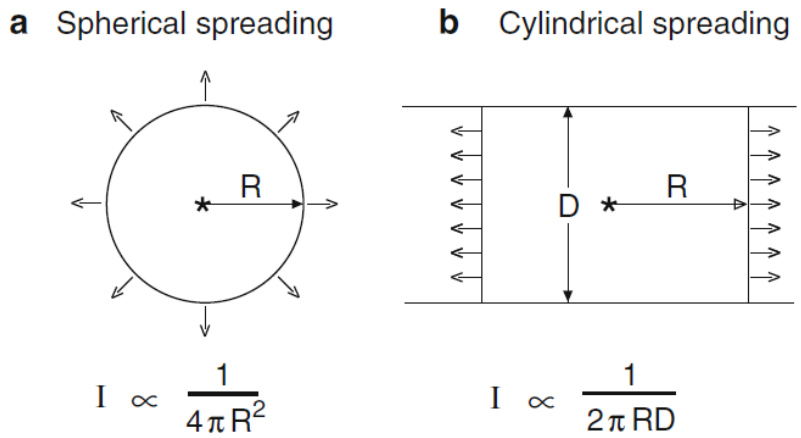

Figure 2.1: Illustration of geometrical spreading laws, showing spherical spreading (a) and cylindrical spreading (b) (Jensen et al., 2011)

2.1.3. Common Underwater Noise Metrics (SPL, SEL, L_{peak})

The most common metrics used to express underwater sound levels in decibels are:

1. **Sound Pressure Level (SPL):**
   The SPL quantifies the average sound pressure over a specified time interval. Acoustic pressure fluctuates around a mean value, the SPL allows for this variation by averaging over a certain time interval. The SPL is given by Eq. 2.8 (Bellmann et al., 2020), where T is the averaging time, $p(t)$ is the time-variant sound pressure, and $p_{ref} = 1\,\mu Pa$ for underwater noise levels.

$$SPL = 10\log_{10}\left(\frac{1}{T}\int_0^T \frac{p^2(t)}{p_{ref}^2}\,dt\right) \quad [dB \text{ re } 1\mu Pa^2] \tag{2.8}$$

2. **Sound Exposure Level (SEL):**
   For characterizing impulsive noise sources, such as pile-driving sounds, the Sound Pressure Level (SPL) alone is often insufficient (Bellmann et al., 2020). This is because SPL depends not only on the strength of individual blows but also on the chosen averaging time and the intervals between impulses. In contrast, the Sound Exposure Level (SEL) provides a more suitable metric by representing the total accumulated acoustic energy of a sound event, normalized to a reference duration. It can be seen as an 'average' continuous sound level over time, normalized to a duration os 1 second.

   The SEL is given by Eq. 2.9 (Bellmann et al., 2020), where $T_{ref} = 1\,s$, T_1 and T_2 is the starting and ending time respectively, of the averaging, $p(t)$ is the time-variant sound pressure, and $p_{ref} = 1\,\mu Pa$ for underwater noise levels.

$$SEL = 10\log_{10}\left(\frac{1}{T_{ref}}\int_{T_1}^{T2} \frac{p^2(t)}{p_{ref}^2}\,dt\right) \quad [dB \text{ re } 1\mu Pa^2 s] \tag{2.9}$$

3. **Zero-to-peak sound pressure level**
   This metric expresses the maximum sound pressure relative to the reference pressure. It is based on the peak value of the absolute pressure during a defined time interval. Unlike SPL and SEL, L_{peak} does not involve any form of averaging. The corresponding expression is given in Eq. 2.10 (Bellmann et al., 2020), where p_{peak} is the maximum positive or negative sound pressure, and $p_{ref} = 1\,\mu Pa$ for underwater noise levels.

$$L_{p,pk} = 10\log_{10}\left(\frac{p_{peak}^2}{p_{ref}^2}\right) \quad [dB \text{ re } 1\mu Pa] \tag{2.10}$$

A schematic representation of these sound levels is given in Figures 2.2-2.4.

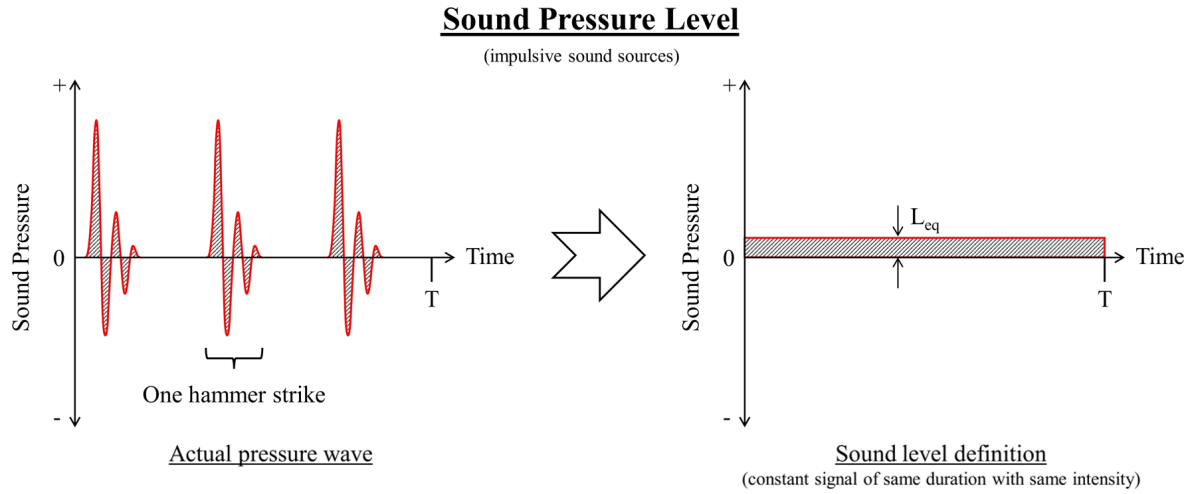

Figure 2.2: Schematic representation of SPL (Heerema Marine Contractors, n.d.).

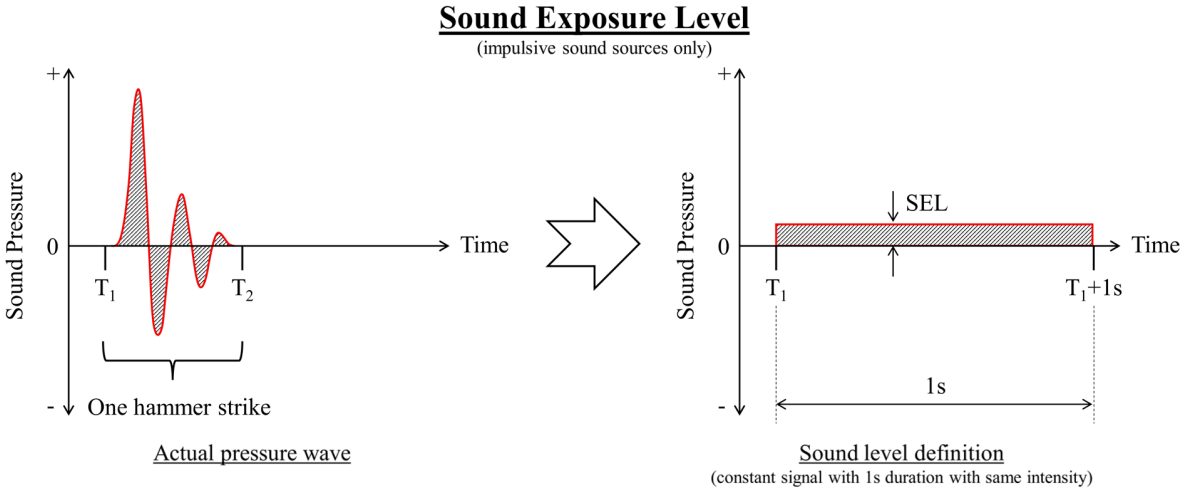

Figure 2.3: Schematic representation of SEL (Heerema Marine Contractors, n.d.).

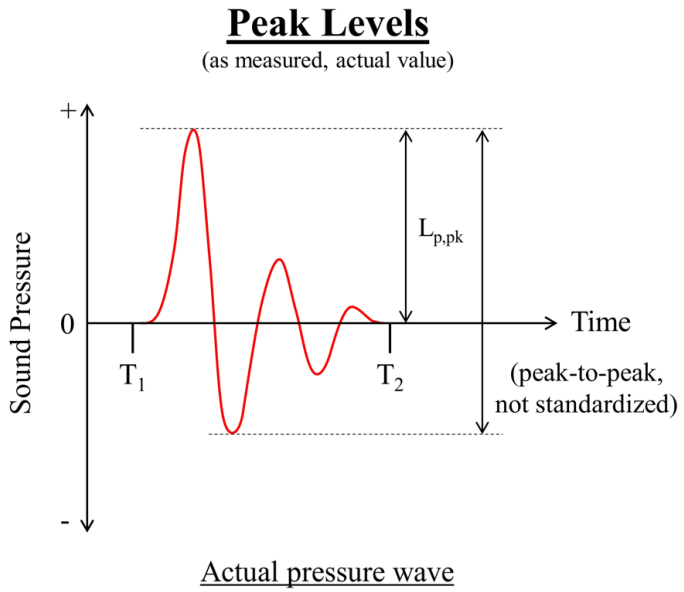

Figure 2.4: Schematic representation of L_{peak} (Heerema Marine Contractors, n.d.).

2.2. Noise Generation and Propagation During Offshore Impulsive Pile Driving

In this section, the technical background of underwater noise generation and propagation is outlined. Subsection 2.2.1 describes the different types of sound waves produced during offshore piling. Subsection 2.2.2 examines the pile-driving process in detail, from the hammer blow to the subsequent sound propagation in both water and soil. Because sound also transmits through the soil into the water column, both a primary and a secondary noise path exist; these are discussed in Subsection 2.2.3. Finally, Subsection 2.2.4 addresses the factors influencing underwater noise levels, including site-specific conditions and technical-constructive aspects.

2.2.1. Wave Types in the Pile-Soil-Water System

Sound waves can propagate in various forms depending on the medium through which they travel. This subsection outlines the types of sound waves relevant to underwater sound propagation: body waves and surface waves. These types of waves are explained below and graphically presented in Figure 2.5.

Body Waves

These waves travel through the interior of the medium and propagate relatively quickly.

- **Longitudinal Waves:** In longitudinal waves, the displacement of particles in the medium is parallel to the direction of wave propagation. This creates alternating regions of compression and rarefaction, corresponding to high and low sound pressure levels, respectively. Compressional waves, also known as P-waves, can propagate through gases, liquids, and solids (Jensen et al., 2011). In the context of this study, these waves are present in the pile, the surrounding water, and the sediment.
- **Transverse/Shear Waves:** In shear waves, particle motion occurs perpendicular to the direction of wave propagation. These waves require the medium to possess shear strength, which is absent in fluids and gases, which is why shear waves only propagate in solids. During impact piling, shear waves are generated by the downward movement of the pile, where friction between the pile wall and surrounding soil induces elastic deformation in the vertical direction. Shear waves are also known as S-waves (Jensen et al., 2011).

As mentioned above, P-waves propagate in the water, pile, and soil domains, whereas S-waves only propagate in the soil. Within the soil, both the P-wave and S-wave exist and are known as elastic

waves. These waves facilitate energy transmission through particle displacement, where particles ultimately return to their equilibrium positions (Kim et al., 2025). P-waves propagate via the volumetric compression and expansion of the soil. Consequently, their velocity depends on the medium's resistance to compression. However, S-waves propagate via shear deformation and therefore depend on the resistance to shear of the soil. The velocities for both P- and S-waves are defined in Eq. 2.11 (Kim et al., 2025). Notably, these speeds vary with depth as a function of the confining stress (Ku et al., 2017).

$$c_p = \sqrt{\frac{K}{\rho}}; \qquad c_s = \sqrt{\frac{G}{\rho}} \tag{2.11}$$

Typically, the bulk modulus K of soil is larger than its shear modulus G (Pan et al., 2019). As a result, compressional (P-) waves generally propagate faster than shear (S-) waves (see Eq. 2.11). This difference in stiffness also affects wave amplitudes. Pile-soil interaction induces both radial motion associated with P-waves and lateral motion associated with S-waves. Because soil deforms more readily under shear than under volumetric compression, S-waves often exhibit larger amplitudes in the near field.

In addition to differences in speed and amplitude, P- and S-waves also exhibit distinct attenuation behavior. Attenuation encompasses the combined effects of geometric spreading, material damping, and energy scattering (Castro et al., 1999). Both P- and S-waves follow the spherical spreading laws, explained earlier in Subsection 2.5. Scattering attenuation arises from medium heterogeneities, which redistribute wave energy through multiple reflections. Furthermore, intrinsic attenuation occurs due to the medium's inelasticity, converting a portion of the wave's energy into heat (Soham and Abhishek, 2016).

Surface/Interface Waves

Interface waves propagate along the boundary between two media. An example is the surface wave occurring at the air-water interface of the ocean. While they are slower than body waves, they often exhibit larger amplitudes because their energy remains trapped at the interface rather than spreading through a 3D volume. Unlike body waves, which undergo spherical spreading, interface waves propagate with cylindrical spreading, causing their amplitude to decay more slowly as they travel from the source (Meegan et al., 1999). Additionally, the energy of these waves is confined vertically, with particle motion decaying exponentially as the distance from the interface increases (Flores-Mendez et al., 2012).

- **Scholte Waves:** These waves propagate along the fluid–solid interface, specifically at the boundary between the water column and the seabed (Onen and Uz, 2015). They involve coupled longitudinal and transverse motion, resulting in an elliptical particle path. Scholte waves are non-dispersive if the solid medium is homogeneous and the interface is planer, meaning their phase velocity is independent of frequency and is primarily dictated by the shear stiffness of the solid medium (Mayer and Kovalev, 2003).
- **Stoneley Waves:** Stoneley waves are analogous to Scholte waves but occur at the interface between two solid media, such as different soil strata or the pile–soil contact (Onen and Uz, 2015). Like Scholte waves, they exhibit coupled motion in both media and remain localized at the boundary.

The combination of cylindrical spreading and localized energy confinement makes interface waves significant in the near-seabed environment. Despite their lower velocities, they have low attenuation and can therefore dominate the vibration profile near the interface, maintaining higher amplitudes over longer distances than P- or S-waves.

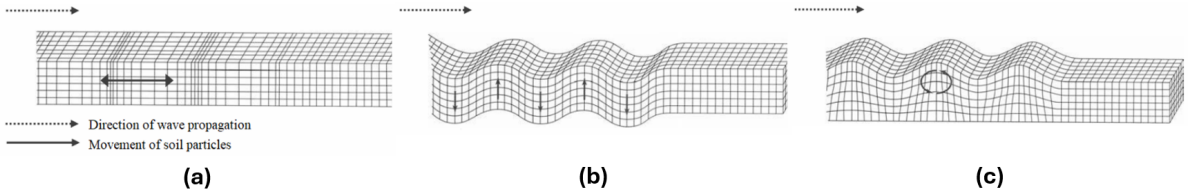

Figure 2.5: Type of sound waves: (a) Longitudinal body wave, (b) shear body wave, and (c) surface wave (de Jong, 2025).

2.2.2. Wave Generation Mechanisms During Piling

For impact piling, a hydraulic hammer is used to drive the MP into the seabed. During this process, an internal impact weight falls repeatedly onto the anvil, situated on the pile head. The anvil then transmits the blow to the pile, driving it into the soil. This impact initiates a downward propagating P-wave within the pile, which travels at a wave speed c_p. The wave speed c_p depends on the Young's modulus of the steel of the pile (E_s) and the density of the steel (ρ_s) and is described in Eq. 2.12 (Kuhn et al., 2014).

$$c_p = \sqrt{\frac{E_s}{\rho_s}} \tag{2.12}$$

Axial compression induced by the hammer impact causes a momentary radial expansion of the pile wall due to the Poisson effect. A material compressed in one direction (here, vertically) expands in the perpendicular direction (radially). This radial deformation behaves as a moving sound source that travels down the pile at speed c_p (Eq. 2.12) (Reinhall and Dahl, 2011; Kuhn et al., 2014).

As a result, the radial expansion of the pile generates pressure waves in the surrounding water. As the sound source moves downward along the pile axis, pressure waves are generated at different times along its path. The cumulative wave fronts from each point along the path of the moving source form a Mach cone centered around the pile axis (Reinhall and Dahl, 2011; Dahl and Reinhall, 2013; Zampolli et al., 2013; T. Lippert and Estorff, 2014).

A simplified illustration of the Mach cone is shown in Figure 2.6. It illustrates wave fronts expanding from two arbitrary positions of the moving sound source: one earlier (red) and one later (blue), separated by a distance L. The wave fronts from the earlier source have propagated farther than those from the later source. The superposition of wave fronts from all positions up to the latest forms the Mach cone (only one side of the pressure waves is shown in the figure).

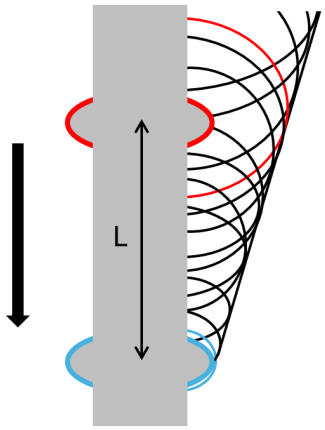

Figure 2.6: The radial expansion of the pile wall caused by the hammer strike (red line) propagates downward along the pile at speed c_p. After a time delay of L/c_p, the same deformation is shown at a lower position (blue line). The wave fronts emitted from the earlier (red) and later (blue) positions, along with those from all intermediate emissions (black lines), constructively combine to form a wave front inclined at an angle θ.

This Mach cone formation is a direct consequence of the difference between wave speeds in steel and

water. The longitudinal wave speed in steel is significantly higher than in water, with typical values of $c_p = 5050\,m/s$ and $c_w = 1500\,m/s$ (Dahl, Jong, and Popper, 2015). As a result, the wave fronts emitted from the radially expanding pile wall propagate into the water at an angle defined by:

$$\theta_w = \sin^{-1}(\frac{c_w}{c_p}) \approx 17.3°$$

When the radial expansion front of the pile reaches the sediment, it also releases a pressure wave into the sediment. This wave also propagates at an angle, denoted as θ_s, which depends on the wave speeds in the sediment relative to that in the steel, see Figure 2.7.

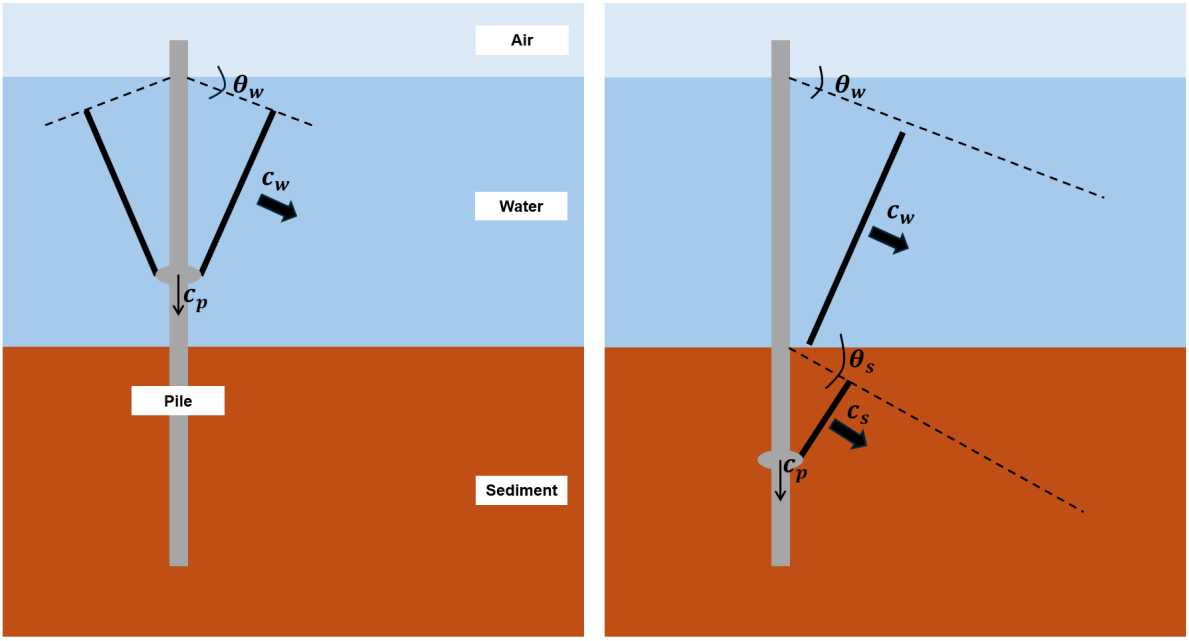

Figure 2.7: Illustration of downward propagating longitudinal wave in the pile, caused by the impact hammer. Additionally, the associated wave fronts and Mach cone formation in water and soil are shown.

As the compressional wave travels down the pile, it reaches the pile tip and reflects. The nature of the reflected wave, whether compressional or tensional, depends on the soil resistance and the impedance difference between the pile and the surrounding medium. In the early stages of driving, typically, the soil resistance and thus the soil impedance are very low, leading to reflection as a tension wave. This tension wave propagates back toward the pile head and causes a temporary axial elongation and radial contraction of the pile (Kuhn et al., 2014).

The extent to which wave components are reflected or transmitted at the pile tip depends on the impedance mismatch. A larger difference in impedance leads to increased reflection and a decrease in the amount of longitudinal wave energy transmitted into the soil (Reinhall and Dahl, 2011).

This sequence of wave propagation and reflection is illustrated in Figure 2.8, showing the progression from initial compression (frames 1–5) to reflected tension waves (frames 6–9).

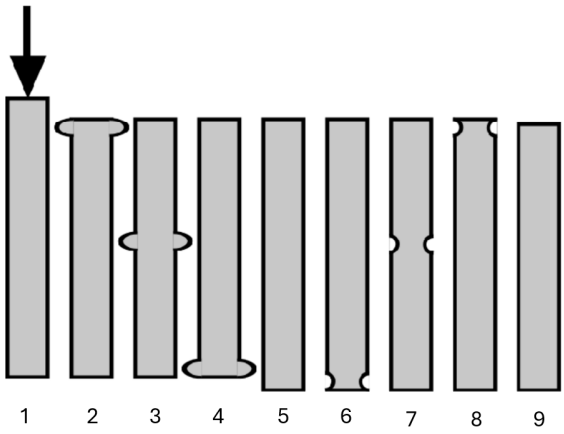

Figure 2.8: Illustration of wave propagation in a MP under low soil resistance conditions (Kuhn et al., 2014). Due to Poisson's effect, the downward propagating compressional wave induces radial expansion of the pile (stages 1–2). The wave continues towards the pile toe (stages 3–4), driving the pile into the soil (stage 5). Depending on the soil resistance, either a compression or tension wave is reflected at the pile toe. Under low soil resistance, a tension wave is reflected and propagates upward (stages 6–8), resulting in an associated radial contraction of the pile.

This upwards traveling longitudinal wave generates a compression wave field in the surrounding soil, producing an upward propagating Mach cone at an angle θ_s, see Figure 2.9. When the longitudinal wave reaches the pile-water interface again, the Mach cone re-emerges in the water, now propagating at an angle θ_w.

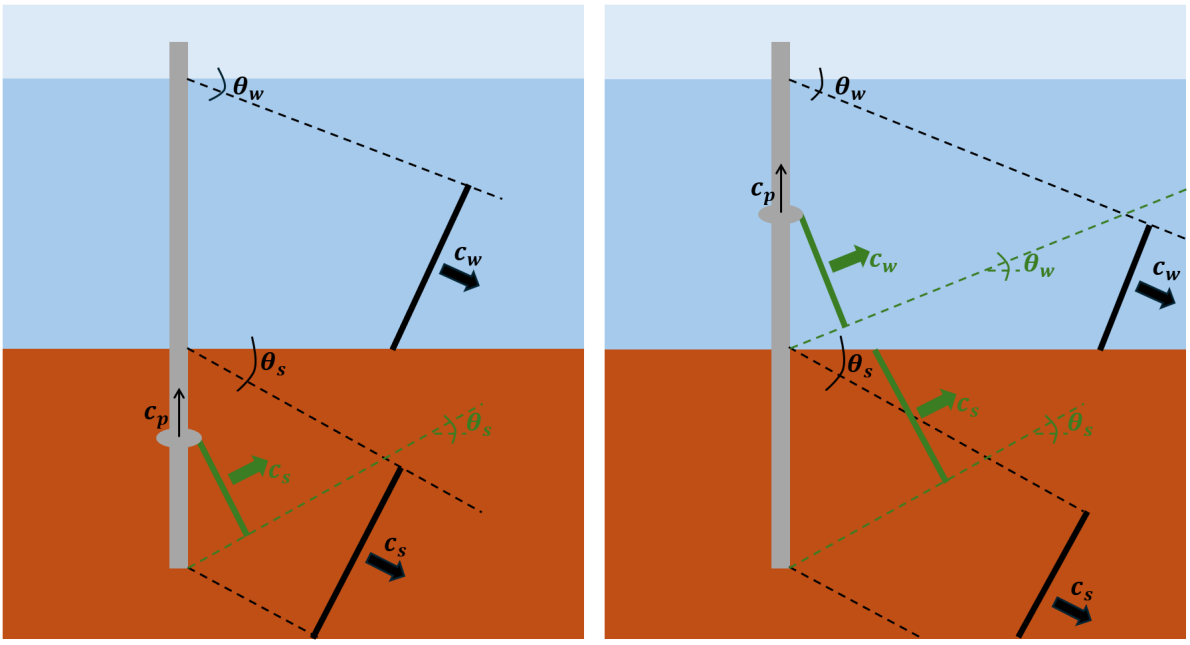

Figure 2.9: Illustration of upward propagating longitudinal wave in the pile, caused by the reflection of the downward propagating longitudinal wave caused by the impact hammer. Additionally, the associated wave fronts and Mach cone formation in water and soil are shown in dark green, while the propagating wave fronts of the initially downward propagating wave in the pile are presented in black.

As discussed in Subsection 2.2.1, offshore impact piling excites both compressional (P-) and shear (S-) waves in the soil. These waves arise because the dynamic interaction between the pile wall and the surrounding sediment imposes both normal and shear stresses at the pile-soil interface, thereby generating vertical and radial deformation within the sediment. Numerical simulations by Tsouvalas (2015) show that shear waves dominate the soil response, whereas compressional waves are present

but of much lower amplitude, with shear motion being the primary carrier of energy into the soil.

The same study demonstrated that the vast majority of the hammer's input energy is absorbed by the soil domain. More than 90% of the energy put into the pile propagates into the soil as shear waves, compressional waves, and Scholte waves. Only a very small fraction (<1%) is radiated directly into the water column as acoustic pressure waves from the pile surface. The rest of the energy goes to internal pile damping, reflections, etc. The energy that enters the soil subsequently partitions among different wave types: shear waves dominate the soil response, compressional waves contribute a smaller portion, and a limited but important share of the soil energy generates Scholte waves at the water-seabed interface. These Scholte waves account for roughly a few percent of the total hammer energy and act as a secondary underwater noise source because they couple efficiently back into the water column at low frequencies.

Together, these findings highlight that accurate underwater noise prediction requires realistic modeling of the soil.

To conclude, Figure 2.10 provides a simplified illustration of the different types of sound waves generated during piling activities. In this figure: (a) represents the hammer impact on the pile; (b) shows the resulting pressure wave propagating through the surrounding water, caused by the radial expansion of the pile at an angle (e.g., forming a Mach cone); (c) depicts the surface wave at the water–soil interface, which in this case is a Scholte wave. Between soil layers, this would correspond to a Stoneley wave. Finally, (d) illustrates the body waves generated within the soil due to the vertical motion of the pile and the soil friction, as well as the radial expansion/contraction of the pile.

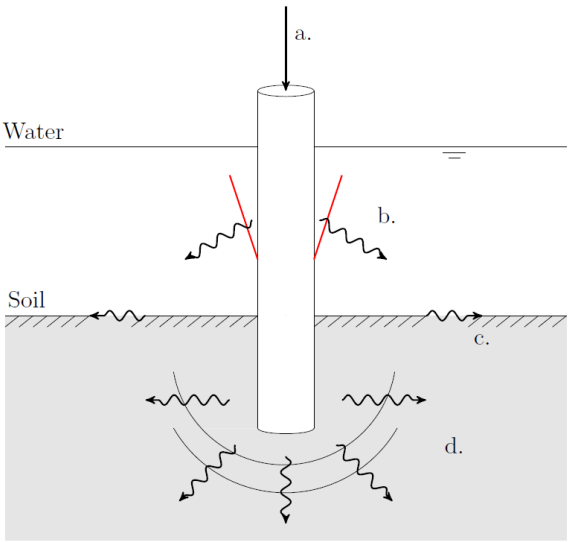

Figure 2.10: Types of sound waves due to offshore piling activities: a) represents the hammer impact on the pile; (b) shows the resulting pressure wave propagating through the surrounding water, caused by the radial expansion of the pile at an angle (e.g., forming a Mach cone); (c) depicts the surface wave at the water–soil interface, which in this case is a Scholte wave. Between soil layers, this would correspond to a Stoneley wave. Finally, (d) illustrates the body waves generated within the soil due to the vertical motion of the pile and soil friction, as well as the radial expansion/contraction o fthe pile (Glasbergen, 2020).

2.2.3. Primary and Secondary Noise Path

In the case of impact pile driving, the downward propagating compressional wave in the pile is faster than the speed of sound in the surrounding water. This creates a "Mach cone" effect, where the generated pressure waves propagate at a specific angle, known as the Mach angle (mentioned in Subsection 2.2.2). Consequently, when these waves encounter the seabed, they hit the interface at an oblique angle rather than at normal incidence.

When a wave front encounters a change in medium, such as the water–soil interface or the boundary between two soil layers, part of the wave is reflected, while the remainder is transmitted into the new medium. The angles of these waves are governed by Snell's Law, as presented in Eq. 2.13 (Jensen

et al., 2011). Note that in this formulation, θ represents the grazing angle (the angle measured from the interface).

$$\frac{\cos\theta_1}{c_1} = \frac{\cos\theta_2}{c_2} \tag{2.13}$$

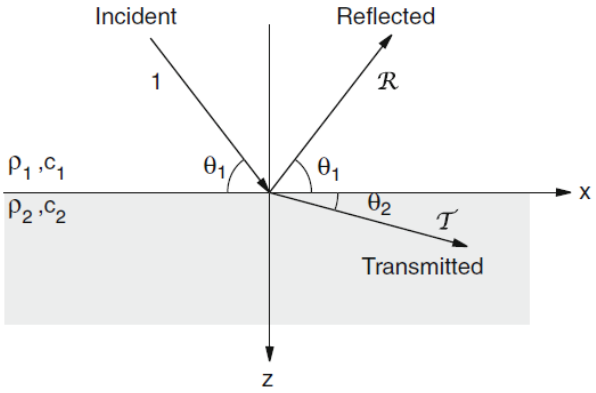

Figure 2.11: An incident sound wave undergoes partial reflection and transmission upon reaching the interface between two distinct media (Jensen et al., 2011).

Because the waves hit at an angle, the standard acoustic impedance ($Z = \rho c$) used for 1D normal incidence must be replaced by the vertical impedance (Z_i). This accounts for the fact that only the vertical component of the particle velocity is used to satisfy boundary conditions at the horizontal seabed:

$$Z_i = \frac{\rho_i c_i}{\sin\theta_i} \tag{2.14}$$

Furthermore, since the seabed is a solid medium that supports shear waves, an incident pressure wave in the water will generate both a transmitted compressional wave (P-wave) and a transmitted shear wave (S-wave) in the soil. To calculate the reflection (R) and transmission (T) coefficients, the total effective impedance (Z_{tot}) is defined for the soil that incorporates both wave types (Jensen et al., 2011):

$$Z_{tot} = Z_p \cos^2(2\theta_s) + Z_s \sin^2(2\theta_s) \tag{2.15}$$

where Z_p and Z_s are the vertical impedances for the P- and S-waves in the soil, respectively, and θ_s is the grazing angle of the transmitted shear wave.

The pressure reflection and transmission coefficients are then determined by the mismatch between the water impedance (Z_w) and the total soil impedance (Z_{tot}):

$$R = \frac{Z_{tot} - Z_w}{Z_{tot} + Z_w}, \quad T = \frac{2Z_{tot}}{Z_{tot} + Z_w} \tag{2.16}$$

A larger impedance mismatch between the two media results in a higher reflection coefficient (R) and a lower transmission coefficient (T). Consequently, cases of extreme mismatch, the majority of the energy is reflected, and the transmitted energy is significantly weakened.

Layered Seabed Noise Path

In layered seabed structures, traveling sound waves encounter multiple soil–soil interfaces. Each interface reflects and transmits part of the wave energy, resulting in complex propagation patterns. Some of this energy eventually radiates back into the water column at a distance from the source. Figure 2.12 illustrates this process, showing wave paths such as $T_{12}R_{23}T_{21}$ and $T_{12}R_{23}^2R_{21}T_{21}$, which represent sound energy leaking back into the water (Jensen et al., 2011).

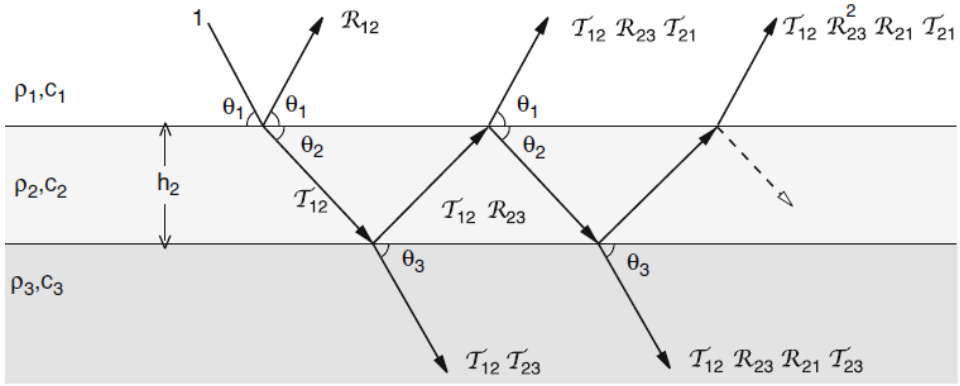

Figure 2.12: Illustration of wave transmission and reflection across a layered soil structure, showing sound energy returning to the water column. The arrows in the figure represent sound waves (Jensen et al., 2011).

Tsouvalas (2015) emphasized the importance of the geoacoustic model in predicting underwater noise, particularly due to elastic waves traveling through or along the boundaries of the medium. The shear rigidity of the soil strongly influences the penetration depth of Scholte waves into the water column near the seabed (Tsouvalas, 2015). Greater penetration depth of the Scholte waves correlates with higher noise levels near the seabed. While soil layering affects sound propagation, the depth and properties of the top soil layer predominantly govern the resulting noise levels (Tsouvalas, 2015).

Due to the acoustic impedance mismatch between seawater and sediment, most of the sound energy from the soil tends to be transmitted back into the water column. So because of this, there are two noise paths contributing to the underwater noise levels:

- **Primary noise path:** originating directly from the initial pile impact in the water column.
- **Secondary noise path:** generated by sound energy transmitted into the soil and subsequently re-radiated into the water column.

This known, the noise path identified in 2.9 should be modified. Figure 2.13 presents an updated version, the sound wave propagates upward through the sediment and enters the water column, where its angle of propagation transitions from θ_s to θ_{ws}. This results in two distinct wave fronts: one radiating at angle θ_w, and another at angle θ_{ws}.

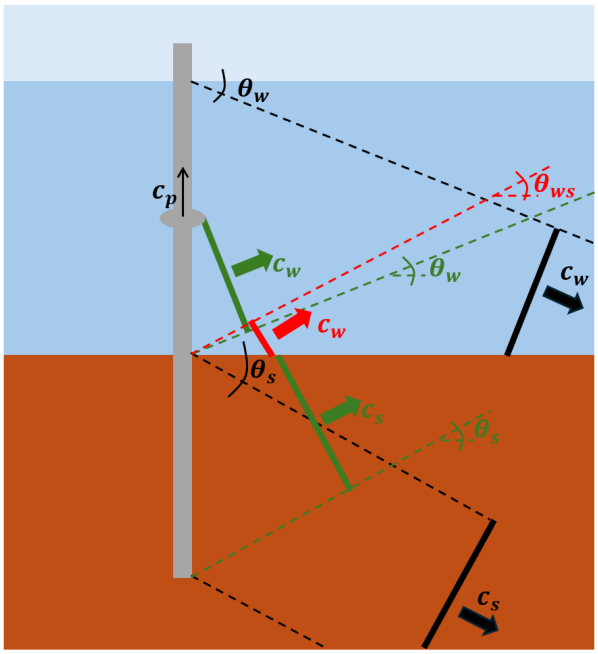

Figure 2.13: Illustration of Mach cone formation in both water and soil, illustrating the primary and secondary underwater noise paths.

2.2.4. Environmental and Operational Factors Influencing Underwater Noise

This section outlines the key parameters that affect underwater noise levels during MP installation. These factors can be categorized into site-specific and technical-constructive influences.

Site-Specific Influencing Factors

Site-specific characteristics play a crucial role in how underwater noise propagates through the environment. Parameters such as water depth, soil composition, seabed topography, bathymetry, and ocean currents all influence the transmission and attenuation of sound (Bellmann et al., 2020). These factors determine the acoustic pathways and the extent to which noise travels from the source. The primary site-specific influencing factors relevant to this study are:

- **Soil Coupling:**
  When the impact hammer strikes the pile, a portion of the energy is transferred into the surrounding soil. This energy travels through the subsurface and can reflect back up due to deeper soil layers. Some of these reflected waves leak back into the water column, contributing to the secondary underwater noise path as described in Subsection 2.2.3. While its contribution to far-field noise levels is generally minor compared to direct noise radiated from the pile (primary noise path), it can significantly affect the performance of near-field noise mitigation systems by creating alternative transmission paths through the soil (Bellmann et al., 2020). The influence of soil coupling is highly dependent on the soil's mechanical properties and stratification.
- **Water Depth:**
  Water depth influences pile-driving noise in two main ways: by affecting how much noise enters the water and by shaping how it propagates (Bellmann et al., 2020). In shallow water, a cut-off frequency restricts the transmission of low-frequency noise. This means that very low-frequency sounds cannot easily enter or travel through the water, with shallower depths leading to higher cut-off values. For sandy soils at around 25 m depth, this cut-off frequency is typically below 50 Hz, so frequencies near or below this threshold couple poorly into the water and attenuate more strongly with distance (Bellmann et al., 2020).

  In the German EEZ, where offshore wind farms are generally built in depths of 20–40 m, the cut-off frequency lies below the unmitigated pile-driving noise spectrum (63–250 Hz) (Bellmann et al., 2020). Measurements confirm that within this depth range, water depth has little influence

on overall noise levels from impulsive piling (Bellmann et al., 2020).

- **Soil Resistance:**
  Soil resistance has a direct impact on the blow energy required to drive a pile into the seabed (Bellmann et al., 2020). Higher resistance necessitates greater blow energy, which typically leads to increased underwater noise emissions. Although site-specific conditions, such as soil composition and layering, can vary significantly, the overall correlation between blow energy and noise levels remains evident.
- **Bathymetry, current and sound velocity:**
  According to Bellmann et al. (2020), the influence of bathymetry, current, and sound velocity on underwater sound propagation is generally limited in shallow waters with sandy seabeds, such as those found in the German EEZ where this study is focused. While bathymetry can significantly affect sound transmission over long distances, at shorter ranges, typically up to a few kilometers, the sea surface can be approximated as flat. As noted by Schecklman et al. (2015), average water depth is the dominant factor influencing long-range sound propagation, whereas local bathymetric variations tend to produce only localized acoustic effects.

Technical-Constructive Influencing Factors

Technical-constructive parameters govern the generation of underwater noise at the source. These include the design of the foundation and pile, the type of impact hammer used, the blow energy applied, the pile-driving procedure, and the final embedding depth. Additionally, offshore logistics, such as the configuration and operation of construction vessels, can influence the characteristics of impulsive noise emissions (Bellmann et al., 2020). The main technical-constructive influencing factors for this study are:

- **Pile diameter:**
  This study examines MP foundations. According to Bellmann et al. (2020), pile diameter is a critical factor influencing noise emissions during MP installation. Figure 1.1 shows that larger pile diameters result in higher SEL and $L_{p,pk}$. To overcome the increased soil resistance of larger MPs, greater hammer size and blow energy are required, which leads to these elevated noise levels.
- **Impact hammer**
  The performance of an impulse impact hammer is defined by three key parameters: (i) the drop mass, (ii) the acceleration applied (which determines the power output), and (iii) the design of the anvil (which transfers the force into the pile head). The hydraulic control system, typically operated through power packs, is essential for lifting and accelerating the drop mass. The acting force is the product of mass and acceleration, while the anvil plays a crucial role in transmitting the blow energy into the pile. To ensure efficient energy transfer, the anvil must be specifically adapted to the diameter of the pile and the design of the pile head (Bellmann et al., 2020).

2.3. Design and Noise Mitigation Mechanisms NMS-T-10000

To mitigate the underwater noise levels during MP installation at the wind farm, a system known as the T-NMS 10000 (NMS) was employed (see Figure 2.14). T-NMS 10000 stands for Noise Mitigation Screen and act as a pile driving Template for MPs with a maximum diameter of 10.0 m. Its primary functions are mitigating noise generated by impact piling, and ensuring accurate positioning of the MP. The NMS can be deployed from either a floating vessel or a jack-up vessel (Heerema Marine Contractors, 2023).

Figure 2.14: Deployment of the NMS from the semi-submersible heavy-lift vessel Thialf during MP installation (Heerema Marine Contractors, 2024b)

2.3.1. Structural Components

The NMS design builds on earlier noise mitigation screen concepts developed by IQIP, such as the NMS 8000. According to Bellmann et al. (2020), earlier noise mitigation screens (applicable up to water depths of approximately 40 m) showed standalone noise mitigation performance in the range of 13 to 17 dB. Building on these designs, IQIP introduced the NMS-T-10000, featuring a larger diameter screen and a support structure to ensure stability during offshore installation.

The complete system consists of two main structural assemblies, shown in Figure 2.15: the NMS 10000 unit (the noise mitigation screen), and the Template (the supporting frame on which the NMS-10000 is connected). In short, the system is set up as follows:

- Inner screen with guides and bumbers to guide the MP
- Annulus filled with water during deployment and filled with air during pile driving
- Outer screen with rubber interfaces connecting the inner screen
- Template structure with tabular members
- Mudmats with movable skirts and a hydraulic leveling system

Both components are described in more detail in this subsection.

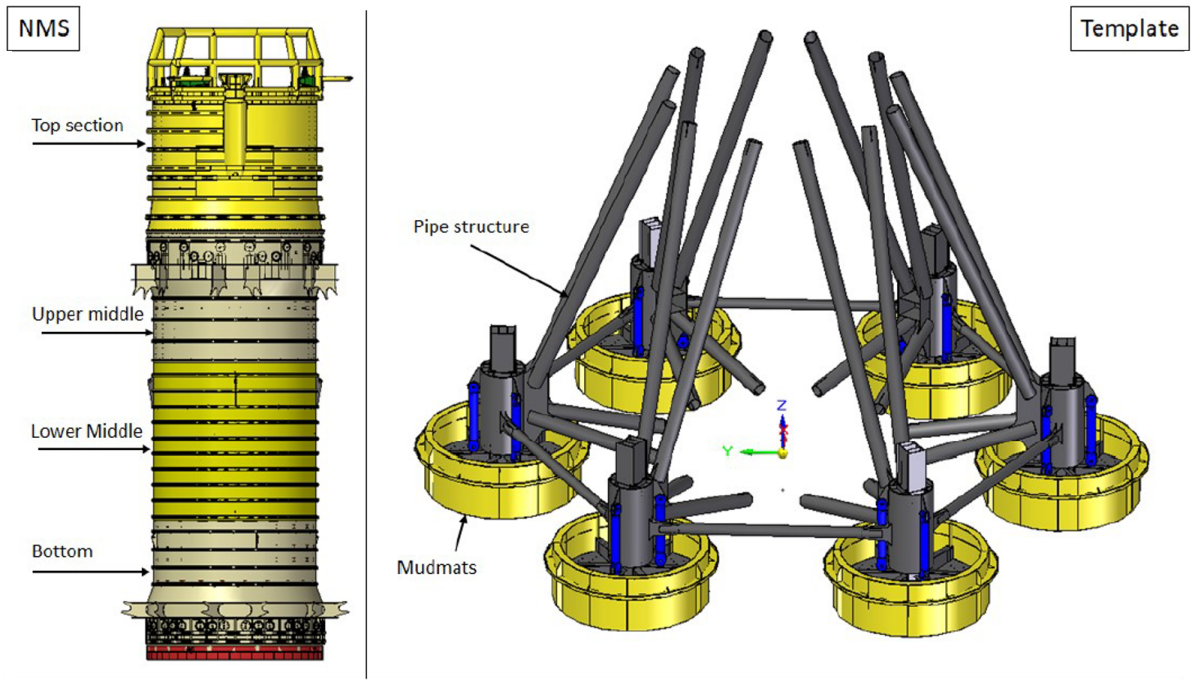

Figure 2.15: Main components of the NMS. Left: the NMS 10000 unit, which serves as the noise mitigation element. Right: the positioning template, used to ensure accurate alignment of the MP during installation.

NMS 10000

The NMS 10000 forms the noise mitigation system. It is deployed around the MP, making it a near-field noise mitigation system. The system consists of a double walled steel screen with an enclosed air layer between the inner and outer screens. It also includes two bubble injection systems that are capable of generating varying bubble sizes.

The inner screen is supported by the seabed and supported by the outer screen. The inner and outer screens do not make direct steel to steel contact, instead, they are connected only at specific locations via rubber support blocks. The inner screen incorporates stiffeners to increase rigidity, whereas the outer screen does not contain such stiffeners. Structurally, the NMS 10000 is divided into four sections: the top, middle upper, lower middle, and bottom section as shown in Figure 2.15.

Both the upper middle and bottom sections contain centralizers, which ensure the correct alignment of the MP within the system. The supporting rubber blocks are located in the upper middle section. After MP installation is complete, the NMS 10000 can be retrieved by lifting it.

Illustrations of the individual sections are provided in Appendix A.

Figure 2.16 provides an overview of the NMS 10000 unit, while Table 2.1 presents the corresponding descriptions and functions of its elements.

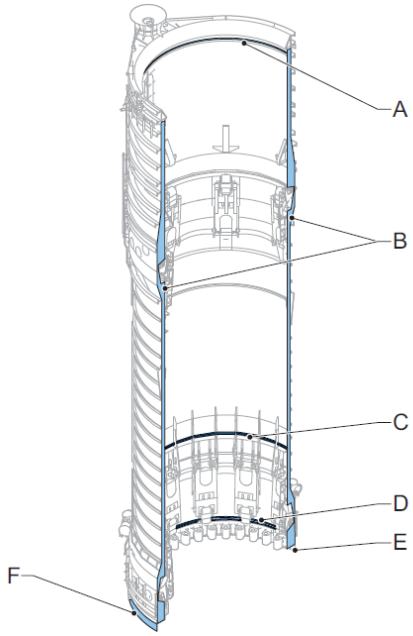

Figure 2.16: Illustration of the NMS 10000, showing the main components and their locations within the structure. Corresponding component descriptions are provided in Table 2.1.

Letter	Item	Function
A	Omega seal	Mechanical isolation Seals annulus air-tight
B	Annulus	Fills with air during piling
C	Air bubble hose	Forms inner bubble screen
D	Bottom bubble pipe	Forms inner bubble screen
E	Outflow	Prevents overpressure Enables smooth air filling
F	NMS skirt	Penetrates seabed Provides internal sealing

Table 2.1: Overview of the NMS 10000 system components shown in Figure 2.16

Template

The outer screen of the NMS 10000 is mounted on a structural framework referred to as the Template. This Template functions as the primary support and stabilization system during MP installation. It forms the interface between the noise mitigation system and the seabed, ensuring that the NMS 10000 is properly positioned and vertically aligned throughout the installation process.

Structurally, the Template consists of a rigid steel frame equipped with mudmats and moveable skirts at its base. These components play a crucial role in stabilizing the system.

- Mudmats act as broad, load-spreading foundation plates that increase the effective bearing area of the Template. By distributing the loads imposed over a larger seabed footprint, the mudmats reduce the risk of excessive settlement or tilting.
- Skirts attached along the perimeter of the mudmats penetrate into the seabed to a specific depth. Their primary function is to provide additional lateral and rotational restraint.

Together, the mudmats and skirts ensure that the Template maintains sufficient stiffness and stability while resting on the seabed. To accommodate variations in seabed topography, the Template is also equipped with an integrated leveling system. This system allows to compensate for seabed inclination.

Figure 2.17: Photograph taken during fabrication of the NMS. The image shows one of the mudmats together with the upper part of its skirt.

2.3.2. Noise Mitigation Mechanisms

The NMS-10000 is designed as a double wall cylindrical shell structure with an air gap between the inner and outer shells. The mitigation of underwater noise is achieved through an acoustic impedance mismatch between the different media, i.e. steel, air, and water. When piling induced vibrations propagate through the MP and into the surrounding water, the double wall system forces the wave to cross multiple interfaces with a difference in acoustic impedance. At each interface (water-steel, steel-air, air-steel, steel-water), a fraction of the acoustic energy is reflected, thereby reducing the radiated energy in the water column at the other side of the NMS. The air layer plays a dominant role because air has an acoustic impedance several orders of magnitude lower than that of steel. At these boundaries, the difference in impedance causes a significant portion of the energy to be reflected back toward the source rather than being transmitted into the far-field.

Additionally, the NMS is equipped with two bubble injection systems located on the inside of the inner screen (facing the MP) at two different elevations, as shown in Figure 2.16. The air bubbles form an additional barrier around the MP. The noise mitigation mechanism of these bubbles arises from the impedance mismatch introduced by the presence of air bubbles in the water. This mismatch causes partial reflection of incoming sound waves back towards the MP (Peng, Tsouvalas, Stampoultzoglou, et al., 2021). Gottsche, Juhl, and Steinhagen (2013) further note that bubbles may oscillate when the wave field passes, which absorbs acoustic energy due to bubble vibration. However, this absorption mechanism is only effective at high frequencies, which lie outside the dominant frequency range associated with impact piling of large diameter MPs (Brandt, 2022).

2.3.3. Main Dimensions

The NMS was developed by IQIP, which holds the associated intellectual property rights. As a result, not all material properties and geometric dimensions are available. However, HMC has access to partial technical drawings of the system, which form the basis for the geometric representation used in this study.

To provide an overview of the principal dimensions, Figure 2.18 and Table 2.2 summarize several key

geometric characteristics of the NMS. In addition, Figure 2.19 presents a top view technical drawing of the Template, showing the layout of the mudmats, the steel frame, and selected dimensions and angles relevant to the overall structural configuration.

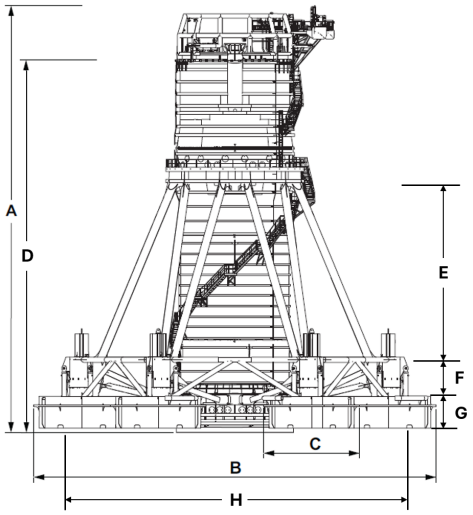

Figure 2.18: 2D front view of the NMS indicating key geometric dimensions. Corresponding values are listed in Table 2.2.

Letter	Item	Specification [mm]
A	Total height	49009
B	Total width	46190
C	Mudmat skirt diameter	10990
D	Total height of screens	43205
E	Height of upper frame	25240
F	Height of lower frame	4181
G	Height of mudmat skirt	3694
H	Diameter of lower frame	35200

Table 2.2: Key dimensions of the NMS as indicated in Figure 2.18.

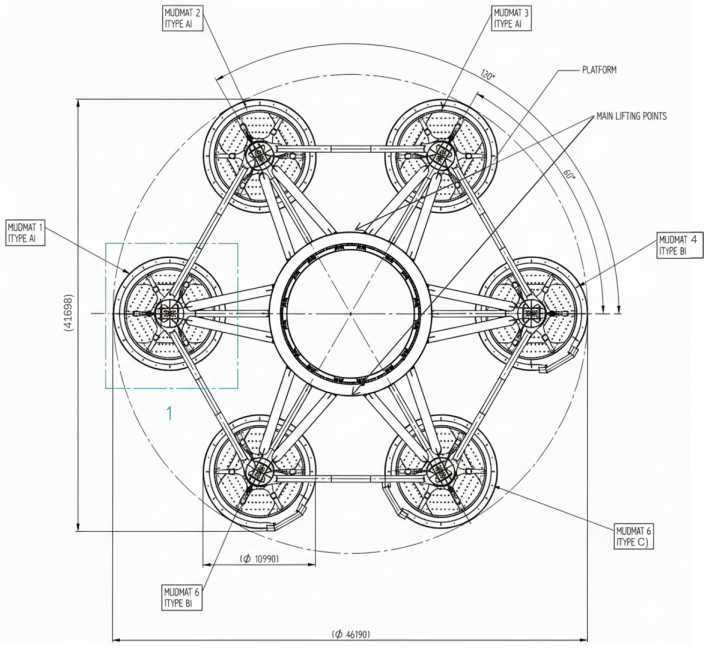

Figure 2.19: Top view of the NMS, showing the NMS 10000 located at the center, surrounded by the supporting frame and mudmats. Due to the scale of the figure, not all labels are readible; all mudmats are equally spaced.

3
Project Data, Site Conditions, and Datasets

In this study, the numerical representation of the NMS is validated against data measured during the wind farm project, an offshore wind farm located in the German North Sea. Additional background information on the project is provided in Section 3.1. Section 3.2 describes the selection of the relevant datasets used in this work, while Section 3.3 outlines the site conditions at the corresponding locations. The force applied to the MP is presented in Section 3.4, and the measured noise data and associated metrics are explained in Section 3.5.

3.1. Wind Farm Project Overview

The wind farm is located in German waters. The turbine sites are situated in water depths ranging between 38.1 m and 40.5 m.

For the wind turbines, MPs are used as the foundation type. Their main dimensions are summarized in Table 3.1. The pile geometry is tapered: the diameter at the pile head differs from that at the pile base. From the pile head down to -25.05 m LAT, the diameter increases linearly from the top diameter value to the bottom diameter value, see Figure 3.2.

Pile Characteristic	Pile Dimension	Unit
Bottom Diameter	9.2	m
Top Diameter	7.0	m
Wall Thickness	100	mm
Length	min 65 / max 73	m

Figure 3.1: MP dimensions for the wind farm project. The bottom and top diameters, as well as the wall thickness, are constant for all MPs. The total pile length varies depending on the installation location.

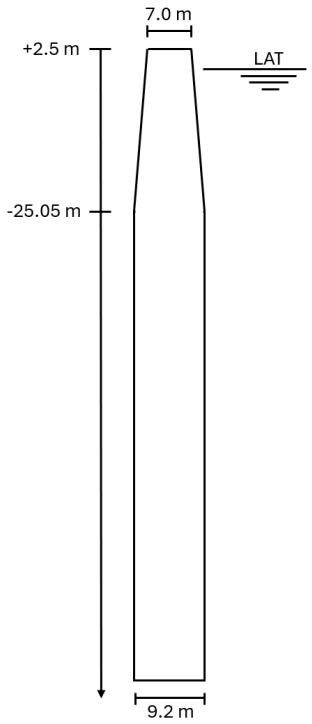

Figure 3.2: Illustration of MP dimensions. While the overall pile length varies between MPs, the tapered section is identical for all. The top diameter, bottom diameter, and wall thickness remain constant across each MP.

The NMS was used for the first time to mitigate the underwater noise. In addition, the PULSE hammer damper from IQIP and a Double Big Bubble Curtain (DBBC) from Hydrotechnik Offshore were deployed. These two noise mitigation systems are explained below:

- **PULSE Hammer Damper:**
  The PULSE system has been deployed in several projects and demonstrated effective as a noise reduction system (itap GmbH, 2024). Based on experience from previous applications, multiple improvements and design modifications have been implemented.

  The PULSE system is installed between the hammer ram and the anvil, which transfers impact energy to the MP flange. It consists of two steel plungers with a fluid-filled chamber between them, see Figure 3.3. This water acts as a cushion, extending the duration of each hammer blow and creating a softer impact that reduces noise. By adjusting the fluid volume, the system can vary the impact stiffness, thereby minimizing vibrations transmitted through both water and soil (IHC IQIP, 2020b).

  The damping properties of the PULSE unit are controlled by the fill level, which can range from 7% to 100% (approximately 50 mm to 700 mm). Tests conducted during the Arcadis Ost offshore construction project indicate that at PULSE Max (700 mm fill level), a noise reduction of 4–6 dB can be achieved. At PULSE Med (300 mm), the expected reduction is 3–4 dB (itap GmbH, 2024). During pile driving of the MPs, the PULSE unit was typically operated with three fill levels, 700 mm, 300 mm, and 150 mm, where the fill level was gradually reduced as installation progressed.

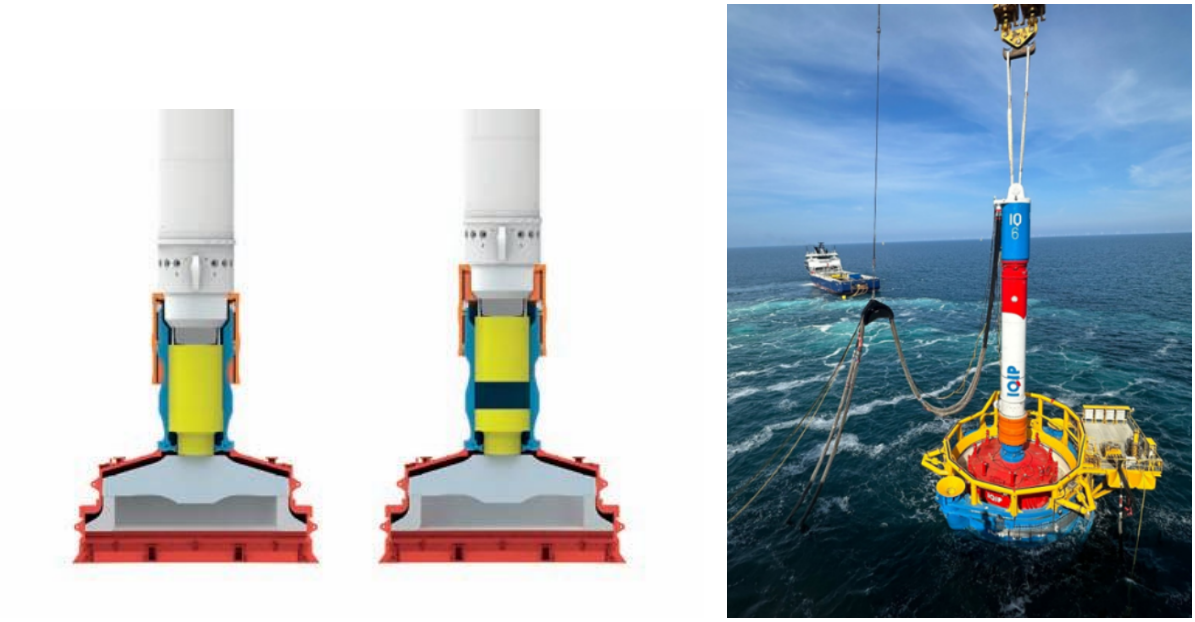

Figure 3.3: Illustrations of the PULSE system (left) (IHC IQIP, 2020a) and the PULSE damper on top of the MP with the NMS in place.

- **Bubble Curtains:**
  A bubble curtain is created by injecting compressed air through perforated hoses laid on the seabed at a defined radial distance around the MP. The rising bubbles form a continuous barrier that attenuates underwater noise by scattering and disrupting sound propagation (Gottsche, Juhl, and Steinhagen, 2013). Figure 3.4 shows an aerial view of a deployed DBBC together with the installation and support vessel. For increased effectiveness, two layers of bubble curtains can be deployed instead of one.

  The DBBC is currently the only far field noise mitigation system and is among the most practical and widely used solutions, with more than 1,200 applications to date (itap GmbH, 2024). Field experience demonstrates that in areas with very low currents, such as the Baltic Sea, sound reductions of up to 18 dB have been achieved at water depths of 40 m (maximum measured reduction) (Bellmann et al., 2020).

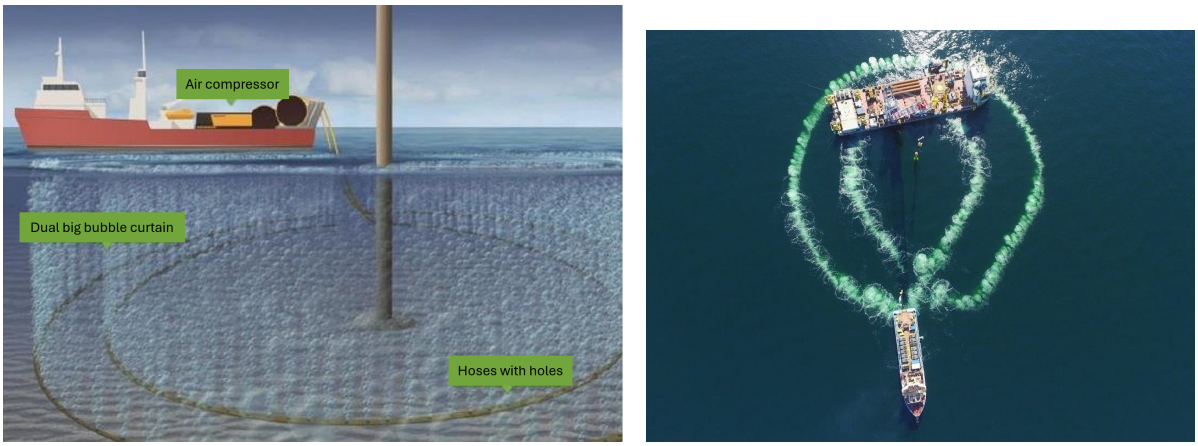

Figure 3.4: Illustration of the DBBC (left) (Defingou et al., 2019) and its offshore application (right) (grow, n.d.). In the right figure, the two rings visible on the water surface indicate the bubbles rising to the sea surface.

3.2. Selection of Relevant Data

The noise mitigation configuration at the wind farm included a PULSE hammer damper, the NMS, and a DBBC. A hydrophone was positioned 750 m from the pile and 2 m above the seabed, which is in compliance with the German regulations (see Appendix B). However, eight MP installations deviated from this setup for test and reference purposes.

The first four installed foundations, A (#1), B (#2), C (#3), and D (#4), were each monitored using five measurement positions: four at 750 m and one at 1500 m. These measurements served as test cases to verify the directional independence of all noise mitigation systems. For four additional installations, E (#9), F (#12), G (#15), and H (#18), six measurement positions were used (four at 750 m and two at 1500 m). These measurements aimed to determine the effectiveness of individual noise mitigation systems as well as their combined performance. This is defined as insertion loss. It is the reduction is SEL due to the application of a noise mitigation system. An overview of these test and reference MP installations is given in Table 3.1.

MP Name	Number	Noise Mitigation Configuration	Purpose
A	1	DBBC + NMS + PULSE (700 mm)	Directionality assessment
B	2	DBBC + NMS + PULSE (700 mm)	Directionality assessment
C	3	DBBC + NMS + PULSE (700 mm)	Directionality assessment
D	4	DBBC + NMS + PULSE (700 mm)	Directionality assessment
E	9	No DBBC; NMS + PULSE (700 mm, 300 mm), then PULSE only (700 mm, 300 mm, 150 mm) after NMS removal at 23 m* embedment depth	Insertion loss evaluation
F	12	NMS + DBBC + PULSE (700 mm, 300 mm, 150 mm)	Insertion loss evaluation
G	15	NMS + DBBC + PULSE (700 mm, 300 mm, 150 mm)	Insertion loss evaluation
H	18	No DBBC; NMS + PULSE (700 mm, 300 mm, 150 mm)	Insertion loss evaluation

Table 3.1: Overview of the special MPs and their associated noise mitigation configurations. Piles 1–4 were monitored using five measurement locations (four at 750 m and one at 1,500 m), whereas Piles 9, 12, 15, and 18 were monitored using six locations (four at 750 m and two at 1,500 m).
*The NMS was removed at an embedment depth of 23 m, to avoid any risk of pile inclination.

In this study, pile E is selected as the pile for further analysis. This choice is driven by the objective of assessing the performance of the NMS. For this pile, no DBBC was applied during installation, which avoids the influence of additional mitigation systems. In addition, the NMS was only deployed up to an embedment depth of 23 m and removed afterwards. This means that, within the same pile and under the same site conditions, both a situation with NMS and without NMS are available. This makes it possible to isolate the effect of the NMS more clearly. For this reason, focusing on E is sufficient to meet the objectives of this study. Further details are provided in Section 4.1.

Measurements during pile driving were conducted at six locations for pile E. Their placement was designed to ensure reliable real-time signal transmission to the installation vessel. Each hydrophone had to maintain contact with the bubble curtain vessel, which relayed signals to antennas on the installation vessel with an unobstructed line of sight. In addition, hydrophone deployment required consideration of seabed conditions, such as trenches, unexploded explosions, and exclusion zones, to ensure safe anchoring and compliance with operational constraints.

3.3. Site Conditions Wind Farm Project

The client commissioned Fugro Consult GmbH and GEMS Geotechnical Engineering and Marine Services Ltd. as the primary geotechnical contractors to carry out a soil investigation in the wind farm field.

The investigations were conducted in 2010 and again in 2021 to characterize the soil conditions and geotechnical properties of the site.

The soil investigation comprised one cone penetration test with pore pressure measurement at each MP location, reaching depths beyond the target pile penetration, as well as fourteen boreholes with soil sampling distributed across the field.

3.3.1. Site Conditions at Location E

For the selected MP location, E, the variation of cone resistance (q_c) and sleeve friction (f_s) per depth is shown in Figure 3.5. This processed CPT data serves as the basis for defining the soil layering that will be used in the model.

Processing of the raw CPT measurements was necessary to remove artificial values introduced by the testing procedure. A CPT is performed by pushing a cone equipped with sensors into the seabed in a series of steps. After each push, the equipment must be paused so that an additional rod segment can be attached to continue the penetration. During these short pauses, the downward force on the cone and sleeve is temporarily released. As a result, the recorded resistance often drops to 0 MPa at the start or end of each segment, even though this does not reflect the actual soil behavior.

These drops in resistance do not reflect the actual physical properties of the soil. To ensure a realistic profile, these dropped values were removed from the dataset. The resulting gaps were filled using linear interpolation between valid data points immediately preceding and following the removed values.

After processing, the smoothed resistance profiles allow for the identification of soil layers. For modeling purposes, two dominant layers were distinguished for E, and the interfaces between these layers are indicated in Figure 3.5. At E, the soil consists of a softer top layer overlying a stiffer layer. The upper layer at E is determined to have a thickness of 11 m.

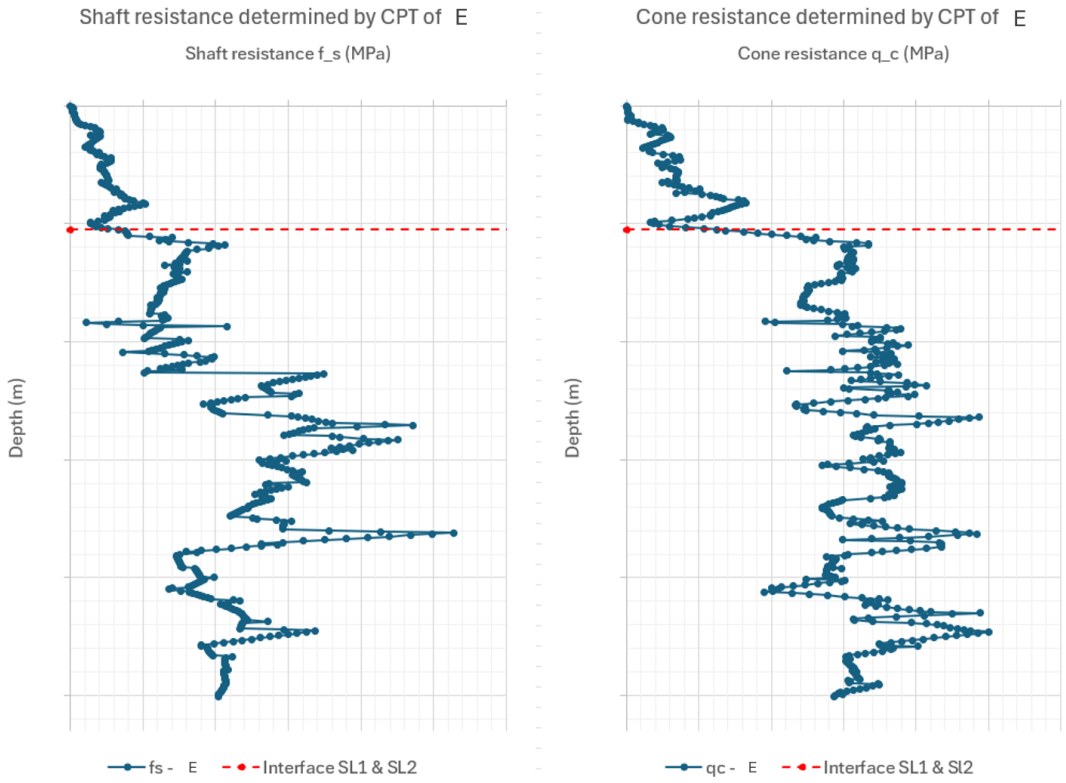

Figure 3.5: Processed shaft resistance (left) and cone resistance (right) for MP location E. From these graphs, two soil layers are identified for modeling purposes. The interface between these layers is indicated in both graphs.

Table 3.2 summarizes the depth intervals for the E location.

Location	Layer	Depth relative to LAT [m]	Layer Thickness [m]
E	Layer 1	[-39.58; -50.58]	11.0
	Layer 2	[-50.58; -90.00]	39.42

Table 3.2: Soil layering for location E. Depths are given relative to LAT.

3.3.2. Surrounding Site Conditions

In addition to the site specific conditions at MP location E, the surrounding CPT profiles must also be examined to ensure that the soil stratification does not vary significantly in the nearby area. This check is important because part of the underwater noise generated during impact piling travels through the soil and re-enters the water column (see Section 2.2.3). If nearby CPTs exhibit significantly different soil stiffness or layering, these lateral variations influences the measured noise levels at the hydrophone locations.

Based on the MP locations of the wind farm, the surrounding CPT locations relevant for pile E were identified. It is determined that the CPTs at I, J, and K are of particular interest. These locations were selected because the hydrophones were positioned in their direction, meaning that the corresponding soil conditions are expected to influence the measured underwater noise levels.

For the surrounding of interest CPTs of E the raw CPT data should be processed to remove zero-values caused by the CPT testing procedure (i.e., stopping and restarting cone penetration). After outlier removal and interpolation, the processed data were used to define the soil profile for each CPT. From the processed CPT curves, the final soil layering was determined. The resulting stratification and corresponding CPT parameters are summarized in Table 3.3.

Location	Layer	Depth relative to LAT [m]	Layer Thickness [m]
E	Layer 1	[-39.58; -50.08]	10.50
	Layer 2	[-50.08; -90.00]	39.92
I	Layer 1	[-39.44; -44.94]	5.5
	Layer 2	[-44.94; -90.00]	45.06
J	Layer 1	[-39.56; -44.06]	4.50
	Layer 2	[-44.06; -90.00]	42.77
K	Layer 1	[-39.58; -46.08]	6.50
	Layer 2	[-46.08; -90.00]	43.92

Table 3.3: Soil layering for relevant surrounding CPT locations of E, these are I, J, and K. Depths are given relative to LAT.

As shown in Table 3.3, the surrounding CPTs exhibit variations in the thickness of the top soil layer. These differences are considered minor and are therefore assumed not to have a significant influence on the measured noise levels at the hydrophone locations. Consequently, the assumption of a horizontally stratified soil profile is considered appropriate for modeling purposes at the E location.

3.4. Forcing Data

The IQ-6 hydraulic hammer from IQIP with a nominal maximum power of 5,500 kJ was used for the pile driving process of the MPs. For each individual blow, both the applied blow energy and the corresponding penetration depth are known. The penetration depth is recorded in increments of 0.25 m, meaning that, for example, blows 2500 and 2250 fall within the depth interval of 24.50–24.75 m. Figure 3.6 presents the blow energy data for pile E. The figure shows the average blow energy per 0.25 m of penetration depth. It can be observed that the first recorded blow energies occur after an initial

penetration has already taken place. This initial depth corresponds to the self-weight penetration of the pile.

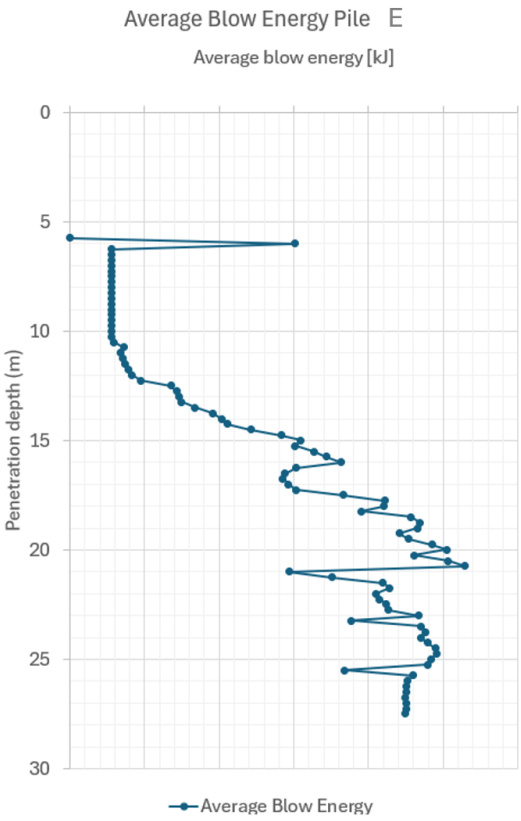

Figure 3.6: Average blow energy recorded during the installation of pile E. The self-weight penetration depth is 5.75 m for E.

The PULSE hammer damper was employed to reduce the noise generated during installation. As explained in Subsection 3.1, the damper extends the force application time and lowers the peak load on the pile, thereby reducing noise emissions. Figure 3.7 presents the force diagram for different PULSE liquid heights. These data were generated using DYNPAC, an in-house computational model for drivability analysis developed by Heerema Engineering Solutions.

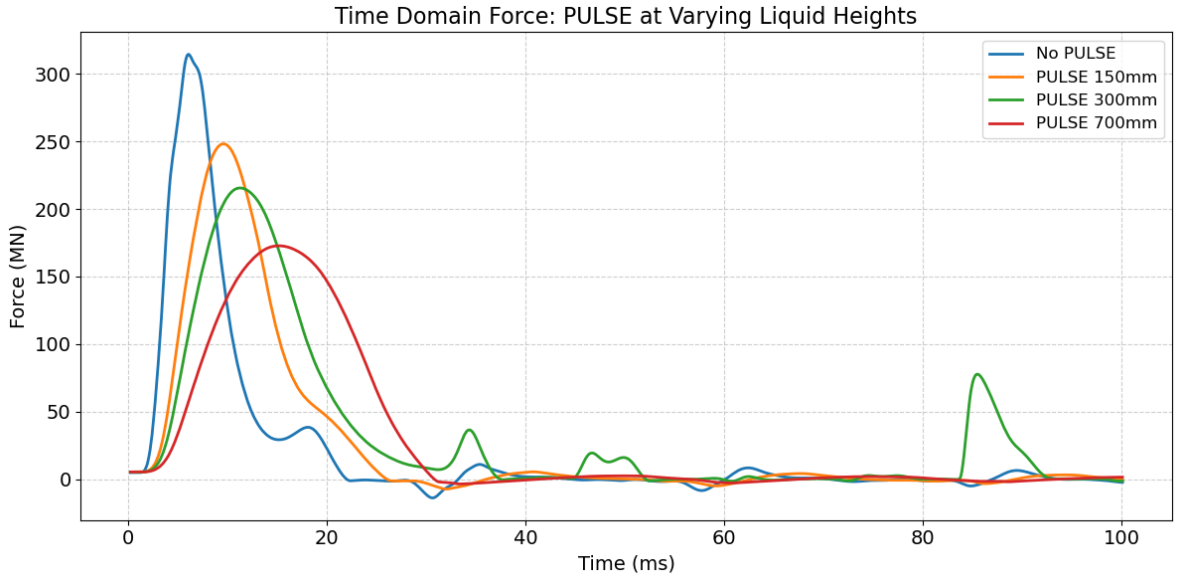

Figure 3.7: Force–time diagram of hammer impact for different PULSE fluid heights. The results show that increasing the fluid height in the PULSE system extends the impact duration while reducing its peak force.

The forces presented in Figure 3.7 show clear differences between the various PULSE configurations. In particular, the force signal corresponding to the 300 mm liquid height exhibits a distinct secondary peak appearing shortly after 80 ms, a feature that is not present in the other PULSE settings (see Figure 3.7). As this feature deviates from the general force signal characteristics observed in Figure 3.7, the 300 mm force signal was replaced by a smoothed exponential representation. This smoothed force is defined by Eq. 3.1 (expressed in units of MN) and shown in Figure 3.8, together with the original measured 300 mm force as well as the original 700 mm force. For this study only PULSE liquid heights 300 mm (i.e. the smoothed exponential) and liquid height 700 mm are relevant since these are used for modeling. This is further explained in Section 4.2.

$$F(t) = 993 \sin(106(t - 0.005)) \cdot e^{-170(t-0.005)}, \qquad t \geq 0.005 \tag{3.1}$$

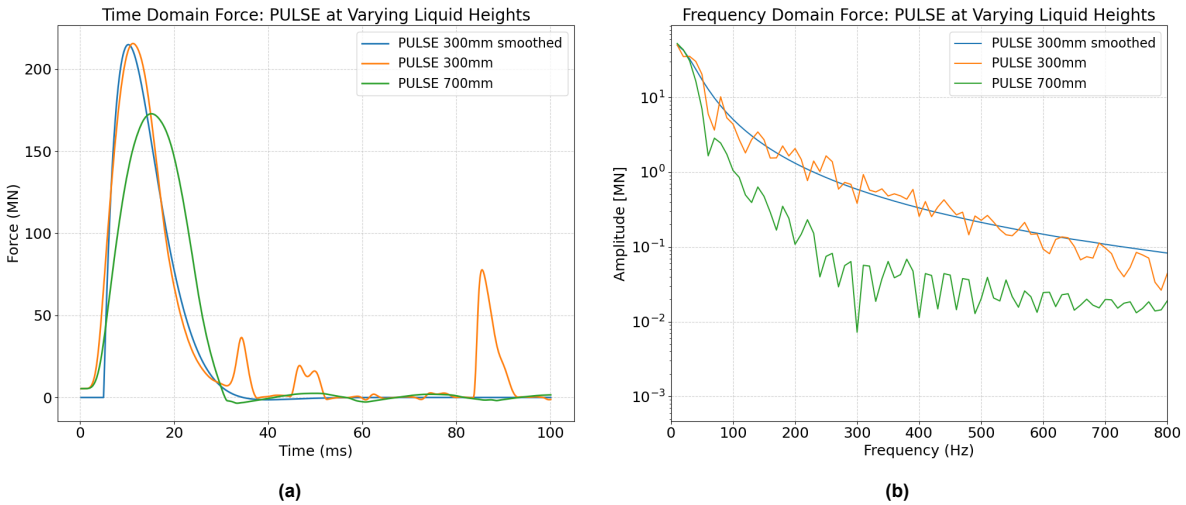

Figure 3.8: Time domain force signals for PULSE 300 mm and PULSE 700 mm, together with the smoothed exponential function (left). The corresponding frequency domain representations of all three signals are shown in the right plot.

A sensitivity analysis on the force is performed and this showed that using the smoothed force curve

instead of the original measured force does not influence the predicted SEL. Although the peak levels exhibit small differences, these do not affect the conclusions of this study. For this reason, the smoothed 300 mm curve is adopted as the force input for all cases in which the 300 mm PULSE liquid height was used.

Unlike the 300 mm case, the 700 mm force does not exhibit a strong late time pulse that would motivate smoothing. The PULSE 700 mm liquid height can therefore be applied without modification.

A frequency analysis of the forcing functions is performed using the Fast Fourier Transform (FFT). Figure 3.8 shows the force represented as a single-sided frequency spectrum. The FFT of a real-valued time signal produces a two-sided spectrum, where the negative frequency components are a mirror image of the positive ones. For practical purposes, these negative frequencies are discarded when creating a single-sided spectrum. However, removing the negative side effectively halves the energy representation. To compensate for this, the amplitude of the remaining positive frequencies is multiplied by two.

Additionally, Figure 3.7 shows the force-time diagram corresponding to the maximum hammer blow energy of 5500 kJ. In practice, this maximum energy is rarely applied during MP installation. For lower blow energies, the corresponding force–time diagram could, in principle, be approximated by scaling the maximum force curve by the ratio of applied to maximum blow energy:

$$F_{actual}(t) = \frac{E_{blow,actual}}{E_{blow,max}} \cdot F_{max}(t)$$

This approach provides a first order estimate of the force at the hammer-pile interface based on the hammer's delivered energy. However, it is important to emphasize that this relationship describes only the energy generated by the hammer, not the energy actually transferred into the pile. During impact, several mechanisms reduce the transmitted energy. Part of the hammer energy is dissipated through deformation of the cushion and anvil, which results in energy losses as heat. In addition, misalignment between the hammer, pile, and sleeve can introduce lateral motions, further reducing the effective energy transfer. Consequently, the energy transmitted into the pile is always lower than the nominal hammer blow energy (Flynn and McCabe, 2016). Because these losses vary from blow to blow, the true transferred energy cannot be reliably inferred from the blow log.

Although the scaling approach described above was initially considered, it was not applied in the present study. This decision was made because the underlying assumption of a linear relationship between blow energy and force-time response does not adequately capture the complex, non-linear interaction between the hammer system, pile, and soil. Applying such a scaling could therefore introduce additional uncertainty into the model results. Instead, the analysis was performed using the force-time diagram corresponding to the maximum blow energy.

3.5. Overview of Measured Underwater Noise Data

In this section, an overview is provided of the noise measurement and data-processing procedure (Subsection 3.5.1), followed by a description of the measurement dataset supplied for this study (Subsection 3.5.2).

3.5.1. Hydrophone Specifications

Underwater noise was measured using bottom-mounted hydrophones deployed for monitoring. All hydrophones were positioned at a height of approximately 2 m above the seabed. This placement follows the requirements of BSH (2011b) and ISO (2017b) for in-situ underwater sound measurements (see Appendix B).

Two types of measurement systems were used. At distances of 750 m and 1500 m from each MP, itap WiFi-Online systems enabled real-time noise monitoring during installation. These systems provide a usable frequency response of 10 Hz–22 kHz and operate with a 44.1 kHz / 24-bit sampling configuration. In addition, a permanent far-field monitoring station (S08) located approximately 12 km northeast of the wind farm recorded background noise and far field propagating piling noise. This station, used autonomous SoundTrap ST600 recorders, also placed 2 m above the seabed, with an extended bandwidth of 10 Hz–24 kHz and a 48 kHz sampling rate.

Each hydrophone system underwent a calibration process to ensure reliable and comparable results. Prior to and immediately after offshore deployment, the full measurement chain, comprising the hydrophone, preamplifier, digitizer, and storage electronics, was calibrated in a DAkkS-certified pressure chamber using known reference levels of 154 dB and 171 dB re 1 μPa at 250 Hz. A GRAS 46AG reference microphone served as the traceable calibration standard. In accordance with ISO (2017a) requirements, the total allowable sensitivity deviation across the measurement chain was maintained within $\pm 1\,dB$.

During piling, low-frequency seismic pre-blows (frequencies <10 Hz), e.g. the P-waves in the soil, often arrived at the hydrophones before the main waterborne pulse due to faster propagation through the sediment. These pre-blows were sometimes detected as separate impulse. However, for the considered pile E, these pre blows were only minimal times observed and are therefore not considered during the validation process.

Overall, the hydrophone setup and calibration procedures ensured high-quality acoustic measurements that accurately reflect the underwater noise levels experienced during MP installation at the wind farm itap GmbH (2024).

3.5.2. Measured Noise Data

As outlined in Section 3.2, six hydrophones were deployed during the installation of pile E, which means that six datasets are relevant for the study of pile E. Each dataset contains the parameters described in Appendix C. The datasets include three key acoustic metrics: Equivalent Continuous Sound Level (L_{eq}), Peak Sound Pressure Level ($L_{p,pk}$), and Sound Exposure Level (SEL):

- $\mathbf{SEL}$: represents the total sound energy over a pulse (see Section 2.1.3).
- $\mathbf{L_{peak}}$: denotes the maximum SPL during a pulse (see Section 2.1.3).
- $\mathbf{L_{eq}}$: is a time-averaged SPL over a defined period. During the measurements, the averaging time was set to 5 s, meaning L_{eq} reflects the average SPL over 5-second intervals.

To capture the frequency-dependent nature of underwater sound, noise levels are also provided in third-octave bands from 12.5 Hz to 16 kHz, following BSH guidelines (BSH, 2011a). These standardized bands are spaced logarithmically, meaning each band is separated by a constant ratio rather than a fixed number of Hz.

The metrics L_{eq} and SEL are available in four distinct data representations, whereas $L_{p,pk}$ is provided in only two of these formats. The four data types are defined as follows:

- **Spectral Statistics:**
  Spectral statistics provide a frequency-domain summary of the entire dataset of one specific MP installation. For each third-octave band, percentiles (L_{01}, L_{05}, L_{50}, L_{90}), maximum, and minimum levels are calculated across all the blows.
- **Spectro-Temporal Values:**
  Spectro-temporal values represent the most detailed form of the data, capturing both time and frequency dimensions. Each blow is recorded with its full third-octave spectrum, resulting in a matrix where rows correspond to individual measured blows and columns to frequency bands.
- **Temporal Statistics:**
  Temporal statistics summarize the broadband noise levels across all blows. Similar to spectral statistics, these include percentiles and extreme values but without frequency resolution.
- **Temporal Values:**
  Temporal values are the broadband sound levels for each individual blow.

An overview of the data is given in Table 3.4

Noise Metric	Data Type	Description	Data Shape	Content
L_{eq}	Spectral statistics	Aggregated values (percentiles, max, min) for each third-octave band across all blows	[32]	L_{01}, L_{05}, L_{50}, L_{90}, Max, Min
	Spectro-temporal values	Full-resolution data for each blow across all third-octave bands (time-frequency matrix)	[X, 32]	raw values
	Temporal statistics	Aggregated broadband values (percentiles, max, min) across all blows	[1]	L_{01}, L_{05}, L_{50}, L_{90}, Max, Min
	Temporal values	Raw broadband sound level for each individual blow	[X]	raw values
SEL	Spectral statistics	Aggregated values (percentiles, max, min) for each third-octave band across all blows.	[32]	L_{01}, L_{05}, L_{50}, L_{90}, Max, Min
	Spectro-temporal values	Full-resolution data for each blow across all third-octave bands (time-frequency matrix)	[Y, 32]	raw values
	Temporal statistics	Aggregated broadband values (percentiles, max, min) across all blows	[1]	L_{01}, L_{05}, L_{50}, L_{90}, Max, Min
	Temporal values	Raw broadband sound level for each individual blow	[Y]	raw values
$L_{p,pk}$	Temporal statistics	Aggregated broadband values (percentiles, max, min) across all blows	[1]	L_{01}, L_{05}, L_{50}, L_{90}, Max, Min
	Temporal values	Raw broadband sound level for each individual blow	[Y]	raw values

Table 3.4: Overview of noise-related data obtained during MP installation for the the wind farm project. Here, X represents the number of time steps for the complete installation (calculated as total duration divided by the 5 s averaging interval) for L_{eq}, while Y indicates the number of measured blows for SEL and $L_{p,pk}$. The value 32 corresponds to the number of center frequencies in the one third octave band. Percentile values L_{01}, L_{05}, L_{50}, and L_{90} represent the 99th, 95th, 50th, and 10th percentiles, respectively. “Max” and “Min” denote the maximum and minimum observed values.

4

Numerical Modeling Framework and Methodology

Appendix E presents an overview of the underwater predictions models developed. In current literature, the semi-analytical approach developed by Peng et al. (2021) is frequently used to model the underwater noise produced by offshore pile driving. This framework consists of a Sound Generation Module (SGM) to accurately model the interactions between the pile, fluid, and seabed, and a Sound Propagation Module (SPM) based on the Boundary Integral Method (BIM) to propagate the acoustic field into the far-field.

While this semi-analytical model is efficient, this study adopts a numerical approach using FEM in COMSOL Multiphysics for the near-field modeling. The motivation for selecting FEM is its capability to accurately resolve the wave field in the coupled fluid-structure-soil system near the pile. FEM also allows for modeling geometrical details that cannot be represented in the semi-analytical model. For example, a tapered MP can be modeled in FEM but not in the semi-analytical approach, which would already introduce additional uncertainty in the predictions. Additionally, FEM allows for the implementation of non-reflecting boundaries. These boundaries represent an infinite ocean domain more accurately than the rigid boundary assumption used in the semi-analytical approach by Peng et al. (2021), as they prevent reflections from bouncing back into the study area.

However, the use of FEM introduces certain limitations. Most notably, the computational cost is significantly higher than that of the model proposed by Peng et al. (2021). Because the domain must be discretized into a very fine mesh to maintain accuracy the FEM approach requires more computer memory and longer processing times.

4.1. Model Scenarios

As explained in Section 3.2, the data from MP E is identified as relevant for this study. Pile E was installed using both PULSE and the NMS up to an embedment depth of 23 m, and using PULSE alone beyond 23 m. Because both mitigation configurations (i.e., with NMS and without NMS) occur at this pile, E provides an opportunity to assess the effectiveness of the NMS, which is an objective of this research.

The first modeling case considers E at an embedment depth of 24.75 m. At this depth, only the PULSE hammer damper was deployed. This configuration is therefore used to validate the model input parameters and geometry without the NMS. As the model results show agreement with the measured underwater noise levels at 750 m, this configuration is considered validated.

Next, the E situation at an embedment depth of 20.50 m is modeled. At this depth, both the NMS and the PULSE hammer damper were used during installation. The input parameters and geometry have already been validated in the first model, meaning that the only new component introduced in this scenario is the NMS. Consequently, this model is used to validate the NMS implementation.

After these two validated configurations, the effectiveness of the NMS can be assessed. To do this, the results of the model with 20.50 m embedment depth at location E using the NMS can then be compared with a corresponding model assuming a “Perfect System” and the unmitigated case. This Perfect System is defined as a system where no acoustic energy is transmitted through the perfect system, into the water column in the near field, i.e., all remaining energy measured at 750 m propagates

exclusively through the soil. The noise mitigation effectiveness can then be quantified by using the SEL at 750 m for the unmitigated, Perfect System, and NMS case.

This approach using a Perfect System is chosen because the maximum possible effectiveness of the NMS occurs when no acoustic energy is transmitted through the system. The Perfect System therefore represents the theoretical upper limit of noise mitigation. Expressing the NMS noise mitigation performance as a quantity considering unmitigated, Perfect System, and NMS achieved SEL at 750 m, provides a comparable effectiveness metric. It enables an evaluation metric of how the NMS performs under specific conditions. In this study, the effectiveness of the NMS under different soil conditions is examined in more detail in Chapter 6.

The chosen embedment depths of 20.50 m and 24.75 m are based on the blow log presented in Figure 3.6. These depths correspond to the points at which the highest blow energies were applied. Since higher blow energies are known to generate higher underwater noise levels (see Section 2.2), selecting these embedment depths ensures that the NMS is evaluated under the 'worst-case' acoustic scenario.

The modeling approach is summarized in Table 4.1.

Model	Pile	Configuration	Embedment Pile [m]	Purpose
Model 1	E	PULSE (SEF)	24.75	Validate input parameters and geometry
Model 2	E	NMS + PULSE (700 mm)	20.50	Validate NMS implementation
Model 3	E	NMS + PULSE (700 mm) Perfect System + PULSE (700 mm)	20.50	Determine NMS effectiveness

Table 4.1: Overview of the phased modeling approach used to evaluate NMS effectiveness at wind farm. SEF denotes the smoothed exponential function defined in Section 3.4.

4.2. Coupled Modeling Approach: Theoretical Framework

A coupled modeling approach is adopted in which sound generation and sound propagation are treated in two interconnected modules, following the semi-analytical framework of Peng et al. (2021). The aim of the modeling approach is a computationally efficient strategy while aiming for an accurate prediction. The model consists of the following two modules:

1. **Sound Generation Module (SGM):** models the near-field pile–water–soil interaction using FEM and computes the generated wave field.
2. **Sound Propagation Module (SPM):** propagates the generated wave field to large distances using the SILENCE model.

The two modules are linked through a boundary integral formulation, in which wave field quantities obtained from the SGM on a cylindrical boundary surrounding the pile serve as input for the SPM.

4.2.1. Sound Generation Module: COMSOL Multiphysics

The SGM is used to model how underwater sound is generated close to the MP during impact piling. In this near-field region, the motion of the pile interacts with the surrounding water and the layered seabed, leading to the generation of acoustic waves in the water and elastic waves in the soil. To capture this coupled pile–water–soil interaction, the near field is simulated using FEM implemented in COMSOL Multiphysics and solved in the frequency domain.

It is modeled in a cylindrical coordinate system (r, θ, z) using a 2D axisymmetric formulation. This assumption implies that the loading and the geometry are symmetric about the central vertical axis, reducing the problem to the radial (r) and axial (z) coordinates.

The computational domain is subdivided into four main regions (Figure 4.1):

- **The pile:** A linear elastic thin shell of length L, top radius r_1 and bottom radius r_2, and thickness t, representing the response of the pile.
- **Water column:** an inviscid, compressible fluid domain extending from the free surface at z_0 to the seabed at z_2, in which acoustic pressure waves propagate.
- **Soil Layer 1:** A linear elastic medium extending from z_2 to z_3.
- **Soil Layer 2:** A linear elastic medium extending from z_3 to z_{bot}.

The MP is centered within the domain and excited at the pile head by a hammer force, representing the impact loading during installation.

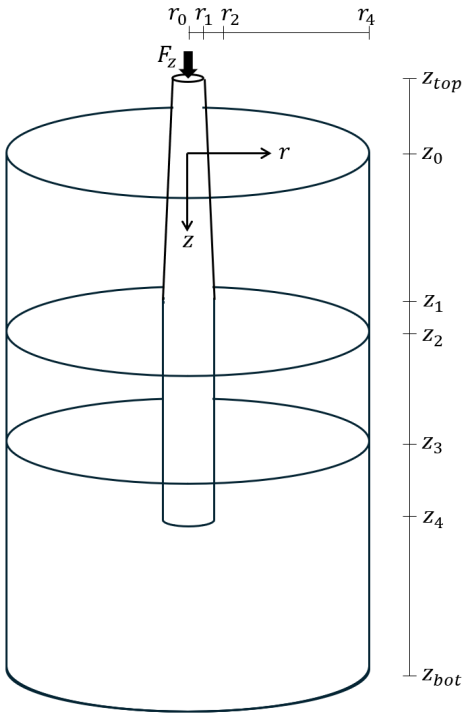

Figure 4.1: Schematic representation of the SGM geometry. The computational domain consists of three layers: the water column ($z_0 \leq z \leq z_2$) and two underlying soil layers ($z_2 \leq z \leq z_3$ and $z_3 \leq z \leq z_{bot}$). The MP is defined by its length L, top radius r_1, and bottom radius r_2, is positioned centrally within the domain. The excitation is modeled as unit force F_z, applied to the pile head. At z_2, the linearly increasing radius of the MP stops and from that point goes straight down. The location z_4 represents the location of the pile tip.

Governing Equations of Motions

The dynamic behavior of the coupled pile-soil-water system is governed by a set of three equations of motion (Peng et al., 2021). These equations describe the vibration of the pile shell, the acoustic wave propagation in the water column, and the elastic wave propagation in the soil. The three equations of motions are presented below. The equations are coupled through interface conditions, ensuring continuity between the domains. For a more detailed explanation of the equations of motions, the boundary and interface conditions, and how these are implemented and solved by COMSOL Multiphysics, see Appendix F.

Pile

The pile is modeled as a shell in COMSOL Multiphysics. The governing equation is derived by integrating the 3D continuum mechanics equations over the shell thickness h. This results in a 2D representation where the dynamic balance of the mid-surface is given by:

$$\rho_p h \frac{\partial^2 \mathbf{u}}{\partial t^2} - \nabla \cdot \boldsymbol{\sigma}_p = \mathbf{f}_{ext}(t) \tag{4.1}$$

where $\mathbf{u}$ is the displacement vector of the mid-surface, σ_p represents the internal stress resultants, $\mathbf{f}_{ext}$ is the sum of external surface tractions, h is the shell thickness, and ρ_p is the density of the shell.

To transition to the frequency domain, the Fourier transform is used:

$$\tilde{G}(\omega) = \int_{-\infty}^{\infty} g(t)e^{-i\omega t}\,dt \qquad \text{and} \qquad g(t) = \frac{1}{2\pi}\int_{-\infty}^{\infty} \tilde{G}(\omega)e^{i\omega t}\,d\omega \tag{4.2}$$

where $g(t)$ denotes the examined quantity. This transformation replaces the operator $\partial^2/\partial t^2$ with $-\omega^2$. Substituting this into Eq. 4.1 yields:

$$-\omega^2 \rho_p h \tilde{\mathbf{u}} - \nabla \cdot \tilde{\boldsymbol{\sigma}}_p = \tilde{\mathbf{f}}_{ext} \tag{4.3}$$

The external coupling force $\tilde{\mathbf{f}}_{ext}$ accounts for the interaction with the hammer and the environment. It represents the total surface traction exerted on the shell by its environment:

$$\tilde{\mathbf{f}}_{ext} = \tilde{\mathbf{f}}_{impact} + (\tilde{\boldsymbol{\sigma}}_s \cdot \mathbf{n})_{soil} - (\tilde{p} \cdot \mathbf{n})_{fluid} \tag{4.4}$$

The terms are defined as follows:

- $\tilde{\mathbf{f}}_{impact}$: This is the hammer force which is applied at the top of the pile.
- $(\tilde{\boldsymbol{\sigma}}_s \cdot \mathbf{n})_{soil}$: This term represents the force vector exerted by the soil domain onto the pile wall. In continuum mechanics, the product of the soil's stress tensor $\tilde{\boldsymbol{\sigma}}_s$ and the unit normal vector $\mathbf{n}$ (which points from the soil toward the pile) defines the traction vector. It accounts for both the friction along the pile skin and the lateral soil resistance.
- $-(\tilde{p}\cdot\mathbf{n})_{fluid}$: Since water cannot support shear, its influence is purely normal. The term $\tilde{p}\cdot\mathbf{n}$ represents the acoustic pressure acting perpendicularly to the pile surface. The negative sign indicates that a positive pressure in the fluid acts as a compressive load against the radial expansion of the pile.

By including these terms, the shell equation is "coupled" to the rest of the model. The vibration of the shell is restricted by the soil and water, while simultaneously, the shell's movement acts as the source that generates waves in those domains.

Fluid Domain
The water is modeled as an inviscid, compressible fluid. In the time domain, the acoustic pressure $p_f(r, z, t)$ satisfies the scalar wave equation:

$$\nabla^2 p_f(r, z, t) - \frac{1}{c_f^2}\frac{\partial^2 p_f(r, z, t)}{\partial t^2} = 0. \tag{4.5}$$

where c_f is the speed of sound in water. The scalar-wave equation assumes small-amplitude fluctuations which results in ignoring non-linear effects. By applying the Fourier Transform (Eq. 4.2), Eq. 4.5 moves into the frequency domain. The second-order time derivative $\partial^2/\partial t^2$ is replaced by $-\omega^2$, resulting in the Helmholtz equation:

$$\nabla^2 \tilde{p}_f(r, z, \omega) + \frac{\omega^2}{c_f^2}\tilde{p}_f(r, z, \omega) = 0 \tag{4.6}$$

Defining the acoustic wavenumber as $k = \omega/c_f$, the equation is simplified to:

$$\nabla^2 \tilde{p}_f + k^2 \tilde{p}_f = 0 \tag{4.7}$$

Soil Domain
The soil consists of horizontal, linear elastic isotropic layers. The motion in each layer j is governed by the Navier-Cauchy equations:

$$\mu_j \nabla^2 \mathbf{u}_j + (\lambda_j + \mu_j)\nabla(\nabla \cdot \mathbf{u}_j) - \rho_j \frac{\partial^2 \mathbf{u}_j}{\partial t^2} = \mathbf{0} \tag{4.8}$$

where μ_j and λ_j are the Lamé constants. Transforming to the frequency domain yields:

$$\mu_j \nabla^2 \tilde{\mathbf{u}}_j + (\lambda_j + \mu_j)\nabla(\nabla \cdot \tilde{\mathbf{u}}_j) + \rho_j \omega^2 \tilde{\mathbf{u}}_j = \mathbf{0} \tag{4.9}$$

Finite Element Method Procedure

COMSOL Multiphysics solves the governing equations using the finite element method:

1. The strong-form governing equations presented above are converted into their weak-form. This introduces the natural boundary terms, reduces the order of the differential equations, and prepares the problem for discretization.
2. The continuous domain is then discretized into a finite number of elements.
3. Within each element, the unknown fields are approximated using shape functions, transforming the PDEs into a set of algebraic equations for the nodal degrees of freedom.
4. The element-level matrices are assembled into the global system:

$$\mathbf{K}\,\tilde{\mathbf{u}} - \omega^2 \mathbf{M}\,\tilde{\mathbf{u}} = \tilde{\mathbf{f}}(\omega)$$

   where $\mathbf{M}$ is the global mass matrix, $\mathbf{K}$ the global stiffness matrix, and $\tilde{\mathbf{u}}$ the vector of nodal unknowns across the structural, soil, and acoustic domains.
5. Finally, the resulting sparse linear system is solved using the direct solver MUMPS.

The resulting near-field solution captures the complex interaction between the pile, water, and sediment. At a specific distance from the MP, the boundary data of the cylindrical boundary is extracted. In the water column the pressure and particle velocity is extracted, while for the soil domain, the displacements and stresses are extracted.

A more detailed explanation of the FEM procedure can be found in Appendix F.

4.2.2. Sound Propagation Module: SILENCE

The environment at the the wind farm site consists of a water column overlying two sediment layers. Such a configuration forms an acousto-elastic waveguide, meaning that sound does not simply radiate outward in all directions (Jensen et al., 2011). Instead, the acoustic field is shaped by interactions with the water surface, the seabed, and the interfaces between the sediment layers. As a result, sound energy may:

- reflect repeatedly between the sea surface and seabed
- leak into adjacent layers
- convert between pressure waves (in the water column) and shear waves (in the seabed)
- travel along the seabed as interface waves (e.g., Scholte waves)
- propagate with different speeds and attenuation characteristics depending on frequency

Consequently, the acoustic field comprises a combination of water borne compressional waves, shear and compressional waves in the seabed, evanescent waves, and interface waves such as Scholte waves.

Due to these complex propagation paths, far-field sound propagation in a layered environment cannot be described using geometric spreading laws. Instead, a frequency dependent modal decomposition approach is used. This approach is adopted in the SPM through SILENCE. This approach is based on work from Peng et al. (2021), the approach consists of a root finding algorithm, Green's function and the Boundary Integral Method. In the following subsections the approach is explained. However, for a more in depth explanation see Appendix G.

Root Finder

In the SPM, the first step is to determine which wave types the layered water-soil environment can support at a given frequency. These wave types are called modes, and each is characterized by a complex horizontal wavenumber $k_m(\omega)$. The SILENCE model computes these modal wavenumbers through a root-finding algorithm.

The root finding algorithm starts by the observation that the acoustic field in the water and the elastic field in the soil can be represented by cylindrical wave potentials. When these potentials are substituted into

the boundary and interface conditions at the free surface, water-soil interface, and soil-soil interfaces, they produce a homogeneous linear system:

$$D(k_r, \omega)a = 0 \tag{4.10}$$

where a contains the unknown amplitudes of the vertical wave components and $D(k_r, \omega)$ is a matrix determined by the environmental properties. For a non-trivial solution to exist, the system must be singular, which requires:

$$det(D(k_r, \omega)) = 0 \tag{4.11}$$

Eq. 4.11 is the dispersion relation of the acousto-elastic waveguide. Its solutions, the roots in the complex k_r plane, are the modal wavenumbers $k_m(\omega)$. Each root corresponds to a physically possible wave type, such as a water-borne mode, a shear sediment mode, a leaky mode, or a Scholte interface mode. The real part of k_m determines the horizontal phase speed, while the imaginary part determines radial attenuation.

The SILENCE model employs the root finding algorithm to identify all roots at each frequency. A more detailed explanation of this procedure can be found in Appendix G.1.

Green's Function

Once the modal wavenumbers of the environment are known, the next step in the SPM is to determine how the layered water-soil system responds to elementary sources. This response is described by the Green's functions of the waveguide. A Green's function represents the acoustic field generated by a unit source at a specific location in the medium and therefore fully characterized how pressure, particle velocity, and stresses propagate through the coupled fluid-solid system. In other words, a Green's function expresses the full acoustic and elastic field generated throughout the domain by a small disturbance at a point.

Because the governing equations are linear, the Green's function allows the wave field generated by an arbitrary source distribution to be obtained by superposition of point-source responses. In the SPM, this means that once the near-field quantities are extracted from the SGM at the cylindrical interface $r = r_4$, the Green's functions determine how each boundary point radiates sound into the far field. For a layered water-soil environment, they include effects such as cylindrical spreading, reflections, transmission into the seabed, P-S mode conversion, and interface wave behavior.

To compute these Green's functions, SILENCE adopts the formulation of Peng et al. (2021), which is based on Hankel transforms and complex wavenumber integration. The Hankel transform separates the radial and vertical dependencies of the wave equation, such that each radial wavenumber k_r produces an independent one-dimensional vertical problem. Solving the transformed equations for each k_r, subject to the boundary and interface conditions of the layered system, yields the Hankel-domain Green's function $\hat{U}(k_r, z, \omega)$. The physical Green's function in real space is then obtained through an inverse Hankel transform.

A feature of this formulation is that the integrand contains poles, branch points, and branch cuts in the complex k_r-plane. To correctly evaluate the inverse transform, the integration contour must be deformed around these singularities. This produces a Green's function consisting of three distinct contributions: (i) discrete modal components (such as water borne modes, Scholte interface waves, and leaky modes), (ii) evanescent components that decay rapidly with radial distance, and (iii) continuous spectrum contributions corresponding to downward propagating P- and S-waves in the sediment.

Together, these contributions form the complete response of the layered water-soil system. The resulting Green's function specifies how pressure at a source point (r_s, z_s) produces pressure, velocity, displacement, and stress at any receiver location (r, z). A more detailed explanation is provided in Appendix G.2.

Boundary Element Method

Once the Green's functions of the layered water-soil environment are known, the final step in the SPM is to propagate the near-field solution from the SGM into the far field. This is accomplished using the Boundary Integral Method (BIM).

Within the SGM, the wave field is generated and wave development mechanisms take place. Beyond the SGM boundary, however, the environment becomes a horizontally stratified water column over an elastic halfspace, where propagation is governed by linear wave equations. In this region, the Green's functions fully describe how a unit disturbance radiates through the medium.

The BIM is based on the idea that the cylindrical interface at $r = r_4$ can be viewed as being covered by an equivalent distribution of acoustic sources. From the SGM, the necessary boundary data on this surface is extracted: pressure and particle velocity in the water, and stresses and displacements in the soil. The Green's functions then determine how each boundary element radiates into the far field. The total acoustic field at a receiver is obtained by superimposing the contributions from all boundary elements.

When implemented numerically, the continuous boundary surface is discretized into boundary elements. This numerical implementation is known as the Boundary Element Method (BEM). Because only the boundary needs to be discretized, rather than the full three-dimensional domain, this approach is computationally efficient.

A more detailed explanation of this method is provided in Appendix G.3.

4.2.3. Frequency Domain Analysis

The numerical simulation of the acoustic structure interaction is conducted in the frequency domain using a spectral decomposition approach. In this method, the system is excited by a unit harmonic force across a frequency spectrum to determine its response, which are subsequently scaled by the actual force spectrum of the hammer strike. This approach is preferred over a time domain (transient) simulation for several reasons:

- At high frequencies, the MP exhibits high-order vibrational modes. In the frequency domain, the interaction between the steel vibration and the surrounding water is governed by the Helmholtz equation. This reduces the physics to a set of steady-state algebraic equations where the coupling is handled simultaneously. In the time domain, a transient solver must constantly exchange data between the MP and water nodes at every discrete time step to maintain stability. To capture high frequency waves accurately, the time step must be extremely small. This leads to massive computational costs.
- Additionally, this method is able to separate the source (hammer) from the path (environment). The actual acoustic response (P) is obtained by multiplying the unit-force response (H) by the spectral density of a specific hammer strike (F): $P(f) = H(f) \cdot F(f)$ (see Subsection 4.2.4). If the hammer strike characteristics change, such as variations in PULSE liquid heights, the new pressure can be calculated in a post-processing script (e.g. Python). In a time domain model, any change to the input force would require a re-run of the entire FEM simulation, which is computational expensive.

4.2.4. From Unit Response to Forcing Response

The underwater noise generated during MP installation is not modeled using the full, time varying hammer force. Instead, the excitation in the model is represented by a unit force. This subsection explains how this unit force is applied in the SGM and how the resulting wave field is subsequently scaled to obtain the response corresponding to the real hammer loading.

The model is formulated in the frequency domain, where the governing equations of linear acoustics, linear elasticity, and linear shell theory are solved. All the domains exhibit linearity, meaning that the structural and acoustic responses scale proportionally with the applied load. Because of this property, the solution for any real pile driving force can be obtained by scaling the solution computed for a unit force.

Solving the SGM and SPM once for a unit load allows the model to be reused for any hammer blow without rerunning the simulations. This reduces computational effort when multiple forcing scenarios must be evaluated. In addition, the unit force response reveals the intrinsic behavior of the system, making it easier to identify which frequencies are efficiently transmitted through the pile-soil-water system.

In the SGM, the model is solved using a vertical loading of $F_z = 1\,MN$. This produces a unit load

response at the cylindrical boundary: $p_{1,SGM}(\omega)$, $u_{1,SGM}(\omega)$, and $\sigma_{1,SGM}(\omega)$.

These unit responses are then used as boundary input for the SPM. From the hammer specifications and the measured blow energy, the force–time signal is constructed, and its frequency spectrum $F(\omega)$ is obtained. The physical pressure field at the receiver locations is then determined by scaling the SPM unit force response:

$$p_{force}(\omega) = F(\omega) \cdot p_{1,SPM}(\omega)$$

from which the different noise metrics are computed.

4.3. Numerical Model Setup

As described in Section 4.1, two modeling scenarios are considered in this study to validate the components of the model setup against measured data, i.e. Model 1 and Model 2. All scenarios share the same modeling framework, consisting of a near-field SGM and a far-field SPM. The differences between Model 1 and Model 2 are limited to variations in geometry and including the NMS, while the numerical methods remain unchanged.

Section 4.3.1 presents the configuration of the SGM, including the global model geometry and the required input variables. Finally, Section 4.3.2 provides an overview of the SPM, describing its geometric representation and input parameters.

4.3.1. Sound Generation Module - COMSOL Multiphysics setup

In this subsection, the geometry of the numerical model is presented. The main description focuses on the configuration without the NMS. A paragraph at the end of this subsection explains how the NMS is incorporated into the model.

Model geometry

The MPs installed at the wind farm have a tapered geometry, with larger diameters at the base and smaller diameters near the top (see Figure 3.2). Figure 4.2 represents the model geometry with the specific lengths and distances shown. The numerical values of the geometric parameters used for the two modeled scenarios are summarized in Table 4.2.

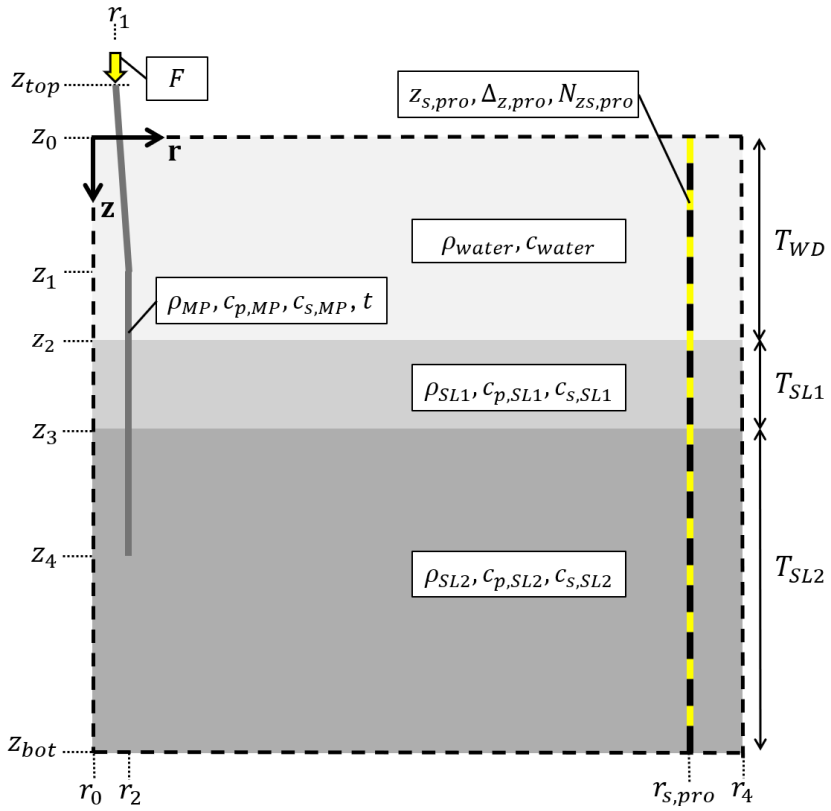

Figure 4.2: Illustration of the geometry of the SGM in COMSOL Multiphysics. Besides the presented coordinates and distances also input variables are presented for each domain, these will be further discussed in Section 4.4.

Parameter	Unit	Model 1	Model 2
z_{top}	m	5.25	11.50
z_0	m	0	0
z_1	m	22.3	16.05
z_2	m	39.58	39.58
z_3	m	50.58	50.58
z_4	m	64.33	60.08
z_{bot}	m	$z_4 + 10$	$z_4 + 10$
r_0	m	0	0
r_1	m	3.5	3.5
r_2	m	4.6	4.6
$r_{s,pro}$	m	50	50
r_3	m	55	55
T_{WD}	m	39.58	39.58
T_{SL1}	m	11	11
T_{SL2}	m	23.75	19.5
r_l	m	–	5.93
r_r	m	–	6.19

Table 4.2: Geometry parameters of the SGM corresponding to the setup shown in Figure 4.2 for Model 1, and Figure 4.4 for Model 2. The parameters r_l and r_r represents the location of the representation of the NMS as depicted in Figure 4.4. All the input variables depicted in the figure are described in Section 4.4.

Modeled Situation in COMSOL Multiphysics

As discussed in Subsection 4.2.2, the SGM is implemented as a 2D-axisymmetric model in COMSOL Multiphysics, formulated in the (r, z) coordinate system.

Within the SGM, three types of physical domains are defined:

- **Pressure Acoustic, Frequency Domain:** Applied to the water domain ($r_0 \leq r \leq r_4$, $z_0 \leq z \leq z_2$). This interface solves the Helmholtz equation for the acoustic pressure (p) in the fluid medium.
- **Solid Mechanics:** Applied to the two soil layers ($r_0 \leq r \leq r_4$, $z_2 \leq z \leq z_{bot}$). This interface solves the linear elastic wave equation governing compressional and shear wave propagation in the seabed.
- **Shell:** The MP is modeled using a Shell feature, which represents the pile as a structural shell defined along a single line corresponding to the pile centerline in the axisymmetric model.

Boundary and interface conditions are applied between the different domains. These conditions are summarized below, and their locations are indicated schematically in Figure 4.3.

- **Axisymmetry:** An axisymmetry condition is applied along the central axis ($r = r_0$) for both the Pressure Acoustics and Solid Mechanics domains. This condition enforces symmetry of the solution about the z-axis.
- **Pressure Acoustics Boundaries:** In addition to the axisymmetry condition, the following boundary conditions are defined in the fluid domain:
  - Cylindrical Wave Radiation: Applied at the outer radial boundary ($r = r_4$) of the water domain. This non-reflecting boundary condition allows outgoing acoustic waves to leave the computational domain without reflection, thereby representing an unbounded fluid medium.
  - Pressure Release Boundary: Applied at the water–air interface, where the acoustic pressure is set to zero ($p = 0$). This boundary condition models the free water surface as a pressure-release boundary.

- **Solid Mechanics Boundaries:** In the soil domain, a low-reflecting boundary condition is applied at the bottom and outer radial boundaries. This condition simulates an elastically infinite domain by absorbing outgoing compressional and shear waves.
- **Shell Boundaries:** Free boundary conditions are applied at the top and bottom ends of the MP shell. These boundaries allow the pile ends to move and rotate freely.

In addition to the boundary conditions, interface (multiphysics) couplings are defined to ensure continuity between the domains. The following couplings are applied in COMSOL Multiphysics:

- **Water-Soil Coupling:** An Acoustic–Structure Boundary is applied at the interface between the water and soil domains. This coupling enforces dynamic continuity across the fluid–solid interface. This means that pressure in the water acts as a load on the soil, while normal acceleration of the soil surface induces waves in the water column.
- **MP-Fluid Coupling:** An Acoustic–Structure Boundary is applied along the shell boundaries adjacent to the water domain. This coupling transfers structural vibrations of the MP into the surrounding fluid as acoustic waves, while fluid pressure loads are simultaneously applied to the shell.
- **MP-Soil Coupling:** A Solid–Thin Structure Connection is applied along the interfaces between the MP shell and the soil domains. This coupling ensures kinematic continuity at the pile–soil interface by enforcing shared displacements between the shell and the surrounding solid elements.

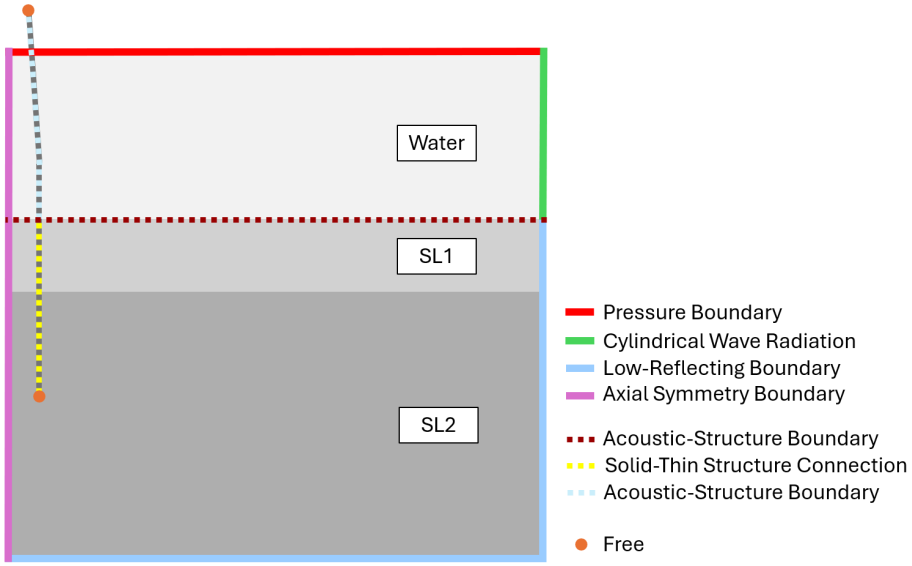

Figure 4.3: Illustration of the boundary and interface conditions assigned in the SGM. Solid lines indicate boundary conditions, while dashed lines denote interface (multiphysics) couplings. Free boundaries are marked by circular symbols.

Implementation of the NMS in the SPM

In the second model, the NMS is implemented and the pile embedment depth changes. The NMS is located around the pile, and the calibration process is detailed in Appendix H. In this study, the NMS is simplified to only an air layer located in the water column. The NMS is illustrated in Figure 4.4. Since the air layer is also part of the Pressure Acoustics Domain, the same boundary and interface conditions apply to Model 2.

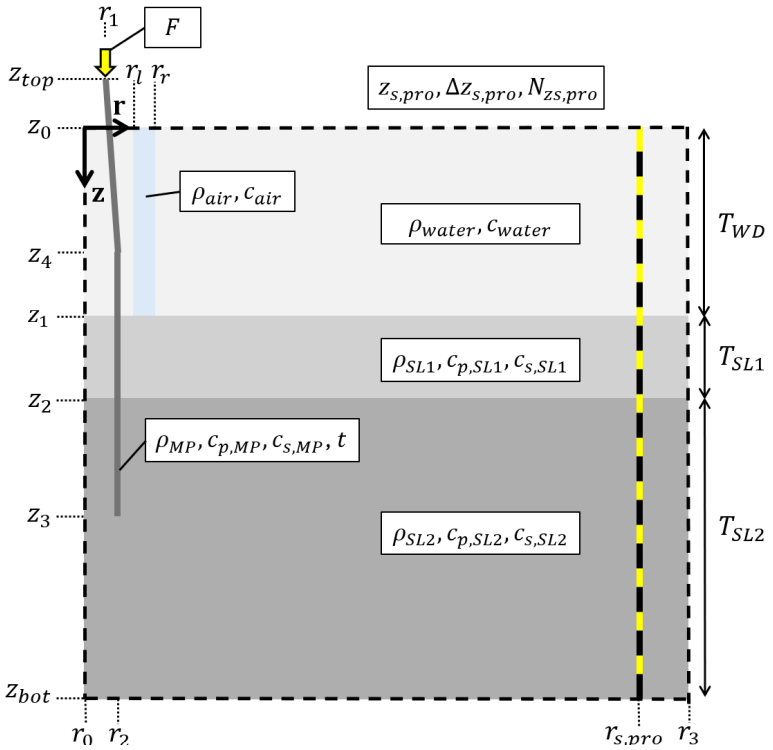

Figure 4.4: Illustration of the SGM geometry implemented in COMSOL. The model is based on Model 1, with the inclusion of the NMS in Model 2 represented as an air layer. The geometric parameters for Model 2 are provided in Table 4.2. The rationale for representing the NMS as an air layer, along with the associated assumptions, uncertainties, and limitations, is discussed in Appendix H.

4.3.2. Sound Propagation Module - SILENCE setup

In the SPM, the wave field data extracted from the SGM are propagated into the far field using a combination of modal decomposition, Green's functions, and BEM. The modeled environment consists of a water column overlying two soil layers, with the deepest soil layer represented as a half-space. The radial and vertical coordinate system is defined consistently with that used in the SGM.

In the SGM, specific field quantities are extracted on a cylindrical boundary located at $r = r_{s,pro}$. In the SPM, this boundary data is interpreted as an equivalent distribution of sources located at the same radial position. From these sources, the wave field is propagated through the system using the SILENCE model.

As a result, the wave field can be evaluated at arbitrary receiver locations, both in the water column and within the seabed, at any radial distance from the MP and at any depth along the z-axis. Because the SPM relies on Green's functions that satisfy radiation conditions, no additional boundary or interface conditions are required. Figure 4.5 provides a schematic overview of the SPM geometry and model setup. Since the NMS is not located in the SPM domain, no NMS is modeled in the SPM.

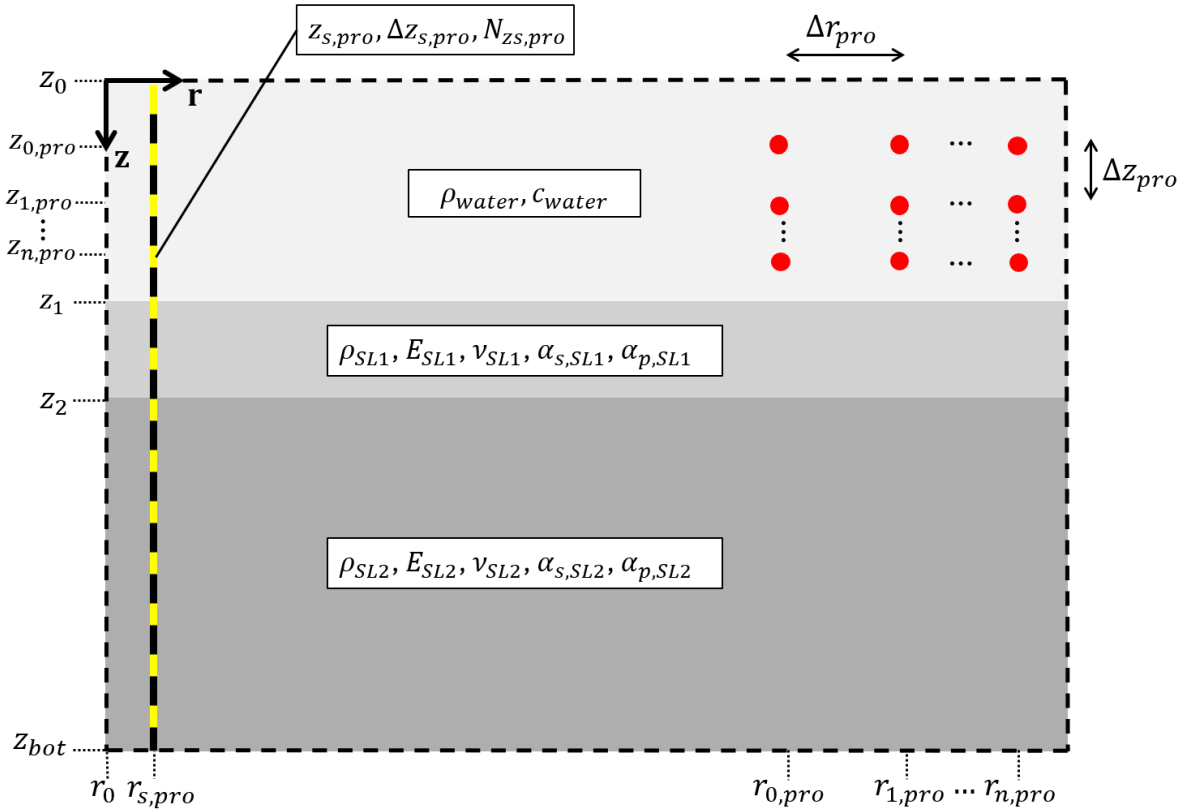

Figure 4.5: Illustration of the geometry of the SPM in SILENCE. Besides the presented coordinates and distances also input variables are presented for each domain, these will be further discussed in Section 4.4. Additionally, receiver locations are indicated by red circular symbols; although only shown in the water column here, receivers can also be placed within the seabed.

Parameter	Unit	Model 1	Model 2
z_0	m	0	0
z_1	m	39.58	39.58
z_2	m	50.58	50.58
z_{bot}	m	74.33	70.08
r_0	m	0	0
$r_{s,pro}$	m	50	50

Table 4.3: Geometry parameters of the SPM corresponding to the setup shown in Figure 4.5. The input variables illustrated in the figure are described in Section 4.4. The geometry parameters related to the receiver locations (indicated by the red symbols in the figure) are also included in this section.

4.4. Model Input Variables

The setup and geometry of the models are presented in Section 4.3. This section continues by defining all input variables for the different modeling scenarios. Subsection 4.4.1 introduces the input parameters for the SGM, including the additional parameters required when the NMS is modeled. Finally, Subsection 4.4.2 provides the input variables used in the SPM.

4.4.1. Sound Generation Module

The SGM is solved for frequency range 0.5 Hz to 600 Hz with frequency step of 0.5 Hz. The main input variables required for the SGM are shown in Figures 4.2 and 4.4. These parameters are summarized in

Table 4.4. A detailed explanation of the physical meaning, underlying logic, and additional parameters, such as time- and frequency domain settings, mesh resolution, and the data extraction procedure at $r_{s,pro}$, is provided in Appendix I.

Parameter	Unit	Model 1	Model 2	Description
F_z	N	1	1	Vertical unit load applied to the MP
ρ_{MP}	kg/m^3	7850	7850	Density of the MP steel
$c_{p,MP}$	m/s	5848	5848	Compressional wave speed in the MP
$c_{s,MP}$	m/s	3233	3233	Shear wave speed in the MP
t	m	0.1	0.1	Wall thickness of the MP
ρ_{water}	kg/m^3	1025	1025	Density of seawater
c_{water}	m/s	1500	1500	Speed of sound in seawater
ρ_{air}	kg/m^3	–	1.225	Density of the air layer which represents the NMS
c_{air}	m/s	–	350	Speed of the air layer that represents the NMS
ρ_{SL1}	kg/m^3	2292	2292	Density of top soil layer
$c_{p,SL1}$	m/s	2136 + 36.2i	2136 + 36.2i	Compressional wave speed of top soil layer
$c_{s,SL1}$	m/s	255.9 + 12.4i	255.9 + 12.4i	Shear wave speed of top soil layer
ρ_{SL2}	kg/m^3	2520	2520	Density of bottom soil layer
$c_{p,SL2}$	m/s	2195 + 34.6i	2195 + 34.6i	Compressional wave speed of bottom soil layer
$c_{s,SL2}$	m/s	404.8 + 19.9i	404.8 + 19.9i	Shear wave speed of bottom soil layer
$r_{s,pro}$	m	30	30	Data extraction radius
$\Delta_{z,pro}$	m	0.5	0.5	Vertical spacing of extraction points
$N_{zs,pro}$	$--$	79 + 69	79 + 61	Number of extraction points

Table 4.4: Overview of the input variables of the SGM used for all modeling scenarios. A detailed explanation of the parameter logic, as well as additional SGM input variables, is provided in Appendix I.

4.4.2. Sound Propagation Module

The primary input variables required for the SPM are shown in Figure 4.2. These parameters, together with the geometry of the receivers, are summarized in Table 4.5. A detailed explanation of their meaning, underlying logic, and additional SPM specific parameters, such as time- and frequency-domain settings, is provided in Appendix I.

Parameter	Unit	Model 1	Model 2	Description
ρ_{water}	kg/m^3	1025	1025	Density of seawater
c_{water}	m/s	1500	1500	Speed of sound in seawater
ρ_{SL1}	kg/m^3	2292	2292	Density of top soil layer
E_{SL1}	MPa	450.0	450.0	Young's modulus of top soil layer
ν_{SL1}	$--$	0.493	0.493	Poisson ratio of top soil layer
$\alpha_{p,SL1}$	dB/λ	0.93	0.93	Compressional wave attenuation coefficient of top soil layer
$\alpha_{s,SL1}$	dB/λ	2.64	2.64	Shear wave attenuation coefficient of top soil layer
ρ_{SL2}	kg/m^3	2520	2520	Density of bottom soil layer
E_{SL2}	MPa	1224	1224	Young's modulus of top soil layer
ν_{SL2}	$--$	0.482	0.482	Poisson ratio of top soil layer
$\alpha_{p,SL2}$	dB/λ	0.86	0.86	Compressional wave attenuation coefficient of top soil layer
$\alpha_{s,SL2}$	dB/λ	2.69	2.69	Shear wave attenuation coefficient of top soil layer
$r_{0,pro}$	m	750	750	First receiver radius in the r-grid
Δr_{pro}	m	arbitrary	arbitrary	Radial spacing between receivers
$N_{r_{r,pro}}$	$--$	1	1	Number of receivers in the r-grid
$z_{0,pro}$	m	$T_{WD}-2$	$T_{WD}-2$	First receivers depth in the z-grid
Δz_{pro}	m	arbitrary	arbitrary	Vertical receiver spacing
$N_{z_{r,pro}}$	$--$	1	1	Number of receivers in the z-grid

Table 4.5: Overview of the input variables of the SPM used for all modelling scenarios. A detailed explanation of the parameter logic, as well as additional SPM input variables, is provided in Appendix I.

4.5. Modeling Assumptions

The SGM and SPM rely on several assumptions which are outlined in this section. The assumptions are distributed in geometric and environmental assumptions and physical assumptions.

Geometric and Environmental Assumptions

- Axisymmetric domain: The model is assumed axisymmetric. This allows the problem to be formulated in 2D cylindrical coordinates (r, z) reducing computational cost.
- Horizontally stratified water-soil system: The seabed is represented as a sequence of horizontal layers with material properties that vary only with depth, not with radial position. This assumption makes it possible to apply modal decomposition and the Hankel transform in the SPM.
- Unbounded water and soil domains: In the SGM, the computational domain is truncated with cylindrical radiation conditions (fluid) and non-reflecting boundaries (soil). In the SPM, radiation is handled through Green's functions.

Physical Assumptions

- The model assumes linear acoustic behavior in the water column, where pressure perturbations are considered small relative to the ambient hydrostatic pressure. This allows the propagation of sound to be governed by the linear Helmholtz equation. However, it is acknowledged that in the immediate near-field of the pile, this linear assumption is an approximation. During a hammer strike, extremely high pressure amplitudes can occur, leading to non-linear effects such as bubble formation near the pile. These bubbles can dissipate energy and increase attenuation, effects that are not captured by a linear model. Despite these limitations, a linear approach was chosen

for this study, as non-linear models would require significantly higher computational resources and are outside the scope of the present work.

- Each soil layer is modeled as a linear, isotropic, and homogeneous elastic material, characterized by constant Lamé parameters λ and μ. Effects such as plastic deformation and material anisotropy are not included.
- The influence of currents, turbulence, depth dependent sound speed profiles, temperature variations, and salinity changes is neglected. The water column is treated as a homogeneous fluid.

5
Model Results & Validation

In this chapter, the model results are compared with real-world measurements obtained during the MP installation of pile E at the wind farm. In addition to evaluating noise levels, the model must also be assessed for its sensitivity to parameter variations and mesh refinement before it can be validated. The chapter is structured as follows: first, the simulated results are compared with the measured underwater noise data. Next, a sensitivity analysis is conducted, corresponding to Sections 5.1 and 5.2, respectively. Finally, Section 5.3 presents the assessed noise mitigation performance of the NMS at the wind farm, based on the results discussed in this chapter.

5.1. Comparison Model Results & Measured Data

This section presents an overview of the obtained model results and compares them with the real-world measurements. Subsection 5.1.1 presents the results of Model 1 and Subsection 5.1.2 presents the results of Model 2.

5.1.1. Model 1

The objective of Model 1 was to validate the representation of the environment in the model. In this modeling case, the embedment depth of the pile is 24.75 m and no NMS was included. The force that was used is the smoothed exponential function described in Section 3.4. The model results are compared with the measured data, and an overview of the results is provided in Table 5.1. The pressure responses in both the frequency domain and the time domain, as obtained from SILENCE, are shown in Figure 5.1. Additionally, the one third octave band spectra of the model results and the measured data is presented in Figure 5.2.

Model 1

Noise Metric	Model Result [dB]	Measured Data [dB]	Difference [dB]
SEL at 750 m	177.9	Y	Z
L_{peak} at 750 m	197.6	Y	Z
SEL at 1500 m	172.5	Y	Z
L_{peak} at 1500 m	188.3	Y	Z

Table 5.1: Summary of broadband model results for SEL and L_{peak} compared with the measured noise levels during driving of pile E corresponding to Model 1.

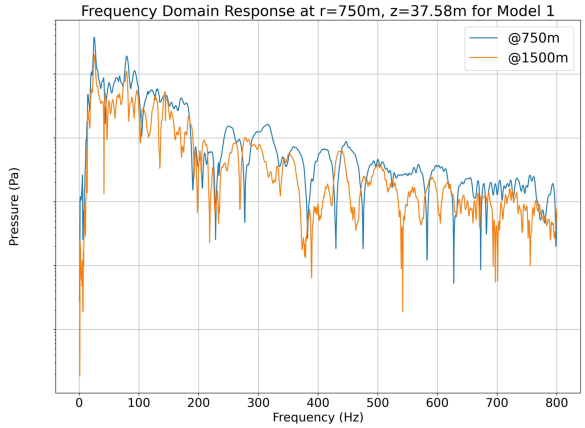

(a) Model 1 results of pressure in frequency domain at 750 m and 1500 m from the pile.

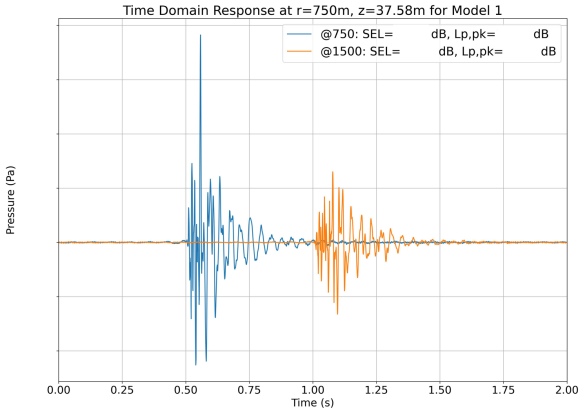

(b) Model 1 results of pressure in time domain at 750 m and 1500 m from the pile.

Figure 5.1: Model 1 results in both the frequency (left) and time domain (right).

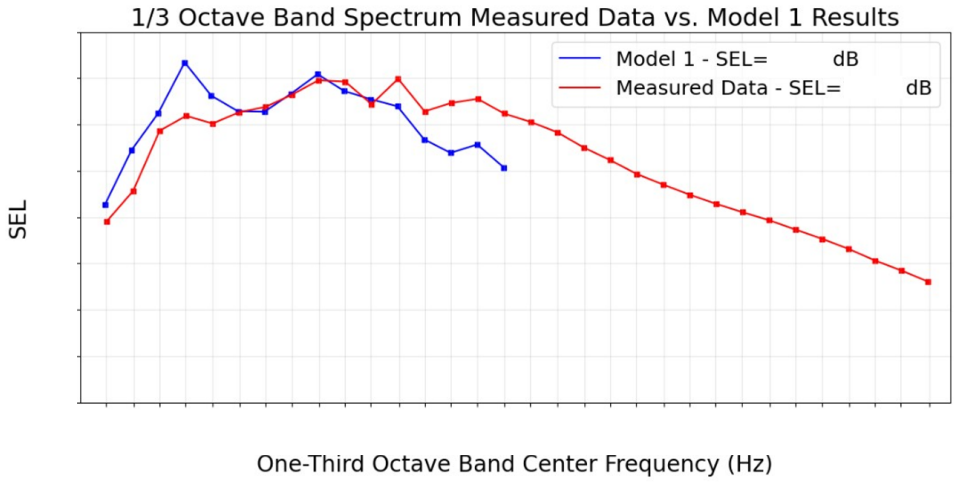

Figure 5.2: Comparison of the measured one third octave spectra of Model 1 results and the measured data at 750 m from the piling location and 2 m above seabed.

Discussion of Model 1 Results

From the comparison between the modeled results and the measured data in Table 5.1, it can be seen that the modeled noise levels are close to the measured noise levels. The discrepancy in SEL at 750 m is X dB. Following the validation approach defined in Appendix D this discrepancy is small enough to potentially validate the model after a sensitivity study which will be performed in Section 5.2. First, the frequency and time domain responses are examined in more detail below, as well as the one third octave band spectra.

Pressure Response in the Frequency Domain

Figure 5.1a shows the modeled pressure spectra measured 2 m above the seabed at distances of 750 m and 1500 m from the pile. Both spectra display a decrease in amplitude with increasing frequency. This trend is characteristic of impact pile driving, whose energy is concentrated at low frequencies and decays toward higher frequencies, reflecting the frequency content of the impact force.

Superimposed on this broadband trend are a series of narrow peaks and troughs. The peaks correspond to structural resonances of the MP and the surrounding environment (i.e. modes). Conversely, the narrow dips suggests anti-resonances of the system. This is typical for underwater wave fields and, therefore, represents an expected outcome of the modeling results (Jensen et al., 2011).

The comparison between the two distances shows that the overall spectral shape is preserved, indicating that the same resonance mechanisms govern the sound field at both ranges. However, the amplitude decreases with distance due to geometric spreading which result in lower pressure amplitudes for the 1500 m spectrum compared to 750 m spectrum.

Pressure Response in the Time Domain
The modeled pressure response in the time domain exhibits behavior consistent with expectations for underwater impulse pile driving. As shown in Figure 5.1b, the wave field arrives at approximately 0.5 s at 750 m and at approximately 1 s at 1500 m. These arrival times correspond to the propagation at the speed of sound in water:

$$\frac{r_{0,pro}}{c_{\text{water}}} = \frac{750}{1500} = 0.5\,s, \qquad \frac{r_{1,pro}}{c_{\text{water}}} = \frac{1500}{1500} = 1\,s.$$

confirming that the initial pressure peak represents the water borne waves arrival.

As expected, the amplitude at 1500 m is lower than at 750 m due to geometric spreading and propagation losses. In addition, the pressure waveform at both distances shows a behavior consistent with impulsive underwater sources: a strong initial peak followed by a gradually decaying tail. Literature describes this behavior as typical for shallow water acoustic waveguides, where the initial peak is dominated by the fastest and least attenuated paths (direct path and lowest order modes), while the subsequent oscillatory tail is the signature of slower, more attenuated arrivals such as higher order modes, seabed reflected energy, and scattered/converted waves (Jensen et al., 2011; S. Lippert et al., 2016). This behavior is clearly visible in the modeled pressure result. The early arrival contains the largest pressure amplitude, after which the waveform becomes more oscillatory and gradually decays in magnitude.

One Third Octave Band Spectra
The one third octave band spectra of both the measured data and the model results are presented in Figure 5.2 for a receiver distance of 750 m. Overall, the model reproduces the general spectral shape observed in the measurements, indicating that the main noise generation and propagation mechanisms are captured. In particular, an agreement in the mid-frequency range can be observed, where both the modeled and measured spectra show similar levels and trends.

At lower and higher frequencies, some differences can be observed. The model slightly overestimates the SEL at low frequencies, while it underestimates the levels at higher frequencies. These deviations could be related to the simplified representation of the site conditions at the wind farm location. In the model, the soil is represented by two horizontal, homogeneous layers with constant properties and attenuation. In reality, the soil layering and conditions are more complex, exhibiting gradual layering, lateral variability, and changing attenuation, which are not fully captured by this simplified approach.

In addition, the model assumes a perfect coupling between the pile and the surrounding soil, which is unlikely to occur under real offshore conditions. Imperfect pile-soil coupling can introduce additional damping mechanisms, resulting in lower measured levels than predicted by the model. This may explain the observed overestimation of low frequency SEL. At higher frequencies, the underestimation by the model is likely related to discrepancies between the assumed attenuation coefficients and real-world conditions. In the model, attenuation is defined as frequency dependent in terms of decibel loss per wavelength (dB/λ), leading to increasing attenuation with frequency. If the actual sediment attenuation is weaker than assumed, the model will attenuate high frequency components more strongly than observed in the measurements.

5.1.2. Model 2

The objective of Model 2 was to validate the representation of the NMS in a way such that the noise mitigation behavior is mimicked. In this modeling case, the embedment depth of the pile is 20.50 m and the PULSE 700 mm force function was used (see Section 3.4). The model results are compared with the measured data, and an overview of the results is provided in Table 5.2. The pressure responses in both the frequency domain and the time domain, as obtained from SILENCE, are shown in Figure 5.3, while the one third octave band spectra for the model results and the measured data is presented in Figure 5.4.

Model 2			
Noise Metric	**Model Result**	**Measured Data**	**Difference**
SEL at 750 m	169.2	Y	Z
L_{peak} at 750 m	180.6	Y	Z
SEL at 1500 m	163.6	Y	Z
L_{peak} at 1500 m	174.6	Y	Z

Table 5.2: Summary of broadband model results for SEL and L_{peak} compared with the measured noise levels during driving of pile E. The results shown correspond to Model 2.

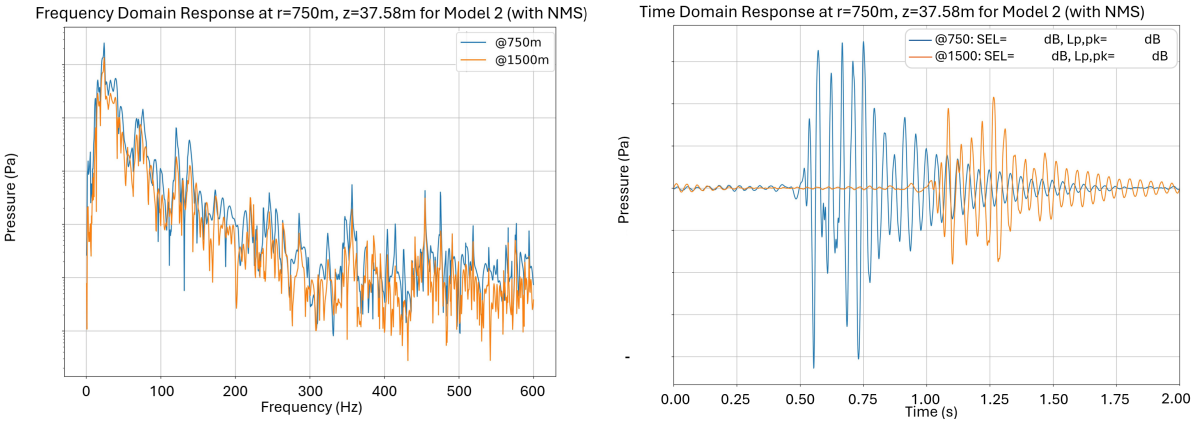

(a) Model 2 results of pressure in frequency domain at 750 m and 1500 m from the pile.

(b) Model 2 results of pressure in time domain at 750 m and 1500 m from the pile.

Figure 5.3: Model 2 results in both the frequency (left) and time domain (right).

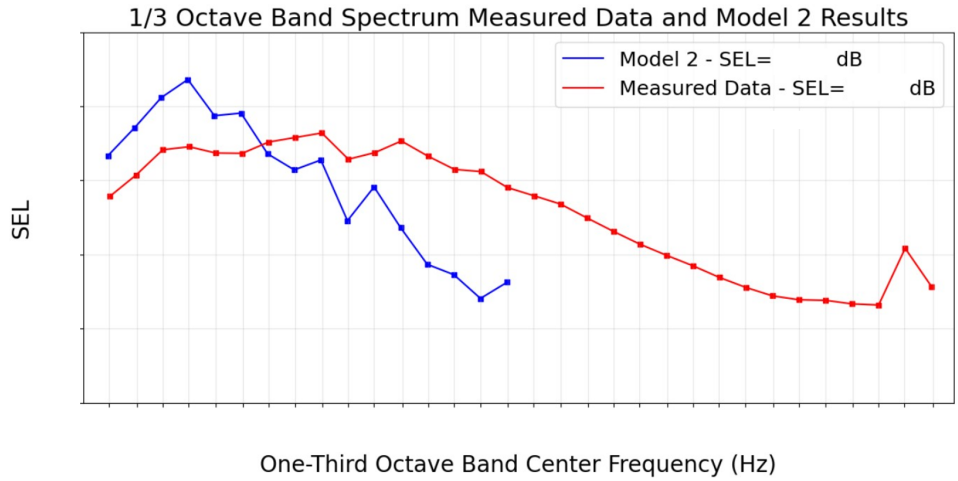

Figure 5.4: Comparison of the measured one third octave spectra of Model 2 results and the measured data at 750 m from the piling location and 2 m above seabed.

Discussion Model 2 Results

A comparison between the modeled results and the measured data in Table 5.1 reveals that the modeled noise levels, specifically the SEL, deviate significantly from the measured values. The discrepancy in the SEL at 750 m is X dB. Following the validation criteria defined in Appendix D, this discrepancy is too large to validate the model.

It is hypothesized that the primary cause for this deviation is the overestimation of low frequency content in Model 1. This is further explained in this section. Since the modeled NMS cannot mitigate these lower frequencies, their over representation contributes to a larger broadband SEL, making it difficult to align the modeled results with the measured data. The frequency and time domain responses, and the one third octave band spectrum are examined in greater detail in the following sections.

Pressure Response in the Frequency Domain
The frequency response of Model 2 exhibits a significantly more ' noisy' appearance compared to the smoother response of Model 1. In Model 1, the waves propagate 'freely' through the water column, resulting in a spectrum defined by vertical modes. In Model 2, the introduction of the air layer creates a resonant cavity between the pile and the NMS. In this region, energy is trapped and standing waves occur. This trapped energy creates a high density of local resonant modes, which causes the far-field frequency spectrum to appear with stronger spectral fluctuations compared to Model 1.

Additionally, it is observed that the magnitude of the lower frequency content in Model 2 remains similar to that of Model 1. However, the higher frequency content is much more mitigated. This demonstrates that the air layer behaves as a frequency-dependent mitigation system. Because the air layer is relatively thin compared to the wavelengths of the low frequencies, these low frequencies can propagate through the barrier without being reflected. These low frequency waves excite the air layer rather than reflect. Conversely, for the higher frequencies, the air layer acts as a impedance barrier and almost all energy is reflected in the water column.

Pressure Response in Time Domain
In the time-domain response, Model 1 is characterized by a high-amplitude pressure spike reaching approximately X Pa. In contrast, this sharp peak is absent in Model 2, where the maximum pressure is reduced to roughly X Pa. This is explained by the fact that sharp impulsive peaks are composed of high-frequency energy (see Appendix J.2). Since the air layer mitigates these higher frequencies, as observed in the spectral analysis, the initial pressure peak is suppressed.

By comparing the time-domain responses of Model 1 and Model 2, the latter initially appears to exhibit a more dispersed behavior. However, closer inspection reveals that this perceived dispersion is largely a result of the different scales on the y-axis. The later arrivals of the wavefield maintain a similar magnitude in both models, which suggests that no additional dispersion has taken place.

Lastly, the waveform shifts from the jagged appearance of Model 1 to a smoother, quasi-sinusoidal shape in Model 2. Because the air layer is 'acoustically transparent' to low-frequency waves, only the long wavelength components propagate through the NMS into the far field. The appearance of the time domain response in Model 2 is therefore a result of these low frequency components being more present compared to the attenuated high-frequency content.

One Third Octave Band Spectra
The one third octave spectra of both the measured data and the results of Model 2 are presented in Figure 5.4 for the receiver distances of 750 m. Compared to Model 1, larger deviations between the modeled and measured spectra are observed across the frequency range. In particular, the low frequency SEL is more strongly overestimated, while the high frequency SEL is more strongly underestimated. This indicates that the frequency dependent mitigation effects introduced by the air layer as explained in Appendix H, amplify the discrepancies already present in the unmitigated case.

At low frequencies, the air layer is less effective at reflecting incident waves because the acoustic wavelengths are large compared to the air layer thickness. As a result, low frequency energy can excite the air layer and propagate through it instead of being fully reflected. This frequency dependent mitigation effect could be overestimated in the numerical model, as the air layer represents a simplified approximation of the real NMS and primarily captures the dominant mitigation mechanism associated with impedance mismatch rather than the full real world behavior. If in reality the NMS mitigates some of the low frequency content and the numerical representation only minimal low frequency content this results in this more stronger overestimation in the lower frequencies compared to Model 1.

Since Model 1 already overestimates low frequency energy due to the simplified soil representation and idealized pile-soil coupling, the inclusion of a simplified, frequency dependent NMS representation

further amplifies this effect. Consequently, low frequency energy is insufficiently attenuated in the model, leading to an increased overestimation of low frequency SEL compared to the measured data.

At higher frequencies, the air layer mitigates sound more effectively because the wavelengths are small relative to the air layer thickness, leading to almost full reflection of energy in the water column within the model. Consequently, a large portion of the high frequency energy is trapped inside the cavity between the MP and the air layer and is subsequently partly transmitted into the soil, as discussed in Appendix H. However, this modeled frequency dependent mitigation behavior could be idealized and these reflections are therefore modeled stronger than in reality. In addition, the numerical model is linear and does not account for nonlinear effects within the cavity between the pile and the air layer. In reality, such nonlinear interactions may redistribute part of the acoustic energy rather than directing it entirely into the soil. In the model, a larger fraction of high frequency energy could be injected into the soil, where frequency dependent attenuation is applied. Since higher frequencies are more strongly attenuated in the soil (attenuation has unit dB/λ), this leads to increased attenuation of these components compared to real world conditions.

Furthermore, Model 1 already showed an underestimation of high frequency levels. Combined with the idealized reflection behavior of the air layer and the absence of nonlinear effects, these assumptions result in a pronounced underestimation of high frequency SEL in Model 2 compared to the measured data.

5.2. Sensitivity Study

In this section, the sensitivity of Model 1 and Model 2 to several modeling parameters is evaluated. Each model is re-run with refined parameters that increase numerical accuracy but also computational cost. The outputs of these Sensitivity Analysis Models (SAMs) are then compared to the Original Model (OM). If no significant differences are observed, the OM assumptions can be considered valid. The parameters tested in the sensitivity study are:

- Mesh size (Subsection J.1)
- Maximum frequency range (Subsection J.2)
- SGM truncation domain (Subsection J.3)
- Extraction radius (Subsection J.4)

A detailed description of each test is provided in Appendix J. Below, a summary of the results is presented.

Model 1: Pile E 24.75m Embedment Depth - No NMS

For Model 1, four SAM cases were evaluated:

- Mesh size: maximum element size reduced by 20% in all domains.
- Frequency range: upper limit extended from 600 Hz to 800 Hz.
- SGM truncation domain: outer boundary extended from 55 m to 70 m.
- Extraction radius: extraction moved from 50 m to 60 m (with domain radius extended to 70 m).

The results are summarized in Table 5.3. None of the SAM variations produced notable deviations relative to the OM. This confirms that the original mesh resolution, frequency range, truncation domain, and extraction radius are sufficiently accurate and do not introduce numerical errors into the predicted far field noise levels. Based on the sensitivity study and the results summarized in Table 5.1, Model 1 is considered validated. This validation confirms that the model configuration and selected parameters are accurate, justifying their application in Model 2. Consequently, the effects of the NMS can be isolated within Model 2 since the underlying environmental, pile, and force parameters were validated in Model 1. This means that any deviations from reality can be attributed to the NMS in Model 2.

Model Configuration	SEL at 750m $\mathbf{m}$ [$\mathbf{dB}$]	L_{peak} at 750 $\mathbf{m}$ [$\mathbf{dB}$]
Measured Data	Y	Z
Original Model (OM)	177.9	197.6
SAM: Mesh Size	177.9	197.6
SAM: Frequency Range	177.8	197.7
SAM: Truncation Domain	177.8	197.6
SAM: Extraction Radius	177.8	197.7

Table 5.3: Comparison of the Sensitivity Analysis Models (SAMs) with the Original Model (OM) and the measured data. The results show no significant differences between the OM and SAM, confirming that the modeling assumptions applied in the OM are sufficient to achieve accurate model results.

Model 2: Pile E 20.50m Embedment Depth - With NMS
For Model 2, four SAM cases were evaluated:

- Mesh size: maximum element size reduced by 20% in all domains.
- Frequency range: upper limit extended from 600 Hz to 800 Hz.
- SGM truncation domain: outer boundary extended from 55 m to 70 m.
- Extraction radius: extraction moved from 50 m to 60 m (with domain radius extended to 70 m).

The results are summarized in Table 5.4. None of the SAM variations produced notable deviations relative to the OM. This confirms that the original mesh resolution, frequency range, truncation domain, and extraction radius are sufficiently accurate and do not introduce numerical errors into the predicted far field noise levels. However, the sensitivity study and the results summarized in Table 5.2 show that the measured data deviates significantly from the model predictions. As a result, the proposed numerical representation of the NMS cannot be validated. Nevertheless, this study continues to use an air layer as a numerical representation of the NMS. The justification for this choice is discussed in Appendix H.

Model Configuration	SEL at 750m $\mathbf{m}$ [$\mathbf{dB}$]	L_{peak} at 750 $\mathbf{m}$ [$\mathbf{dB}$]
Measured Data	Y	Z
Original Model (OM)	169.2	180.6
SAM: Mesh Size	169.3	180.6
SAM: Frequency Range	169.2	180.6
SAM: Truncation Domain	169.5	180.7
SAM: Extraction Radius	170.3	181.6

Table 5.4: Comparison of the Sensitivity Analysis Model (SAM) with the Original Model (OM) and the measured data. The results show no significant differences between the OM and SAM, confirming that the modeling assumptions applied in the OM are sufficient to achieve accurate model results.

5.3. NMS Noise Mitigation Performance at the wind farm

The NMS is modeled in a simplified way by using an air layer. Although this approach cannot be validated directly against measured data, it is justified in Appendix H. While a direct validation is not possible, the results can still be used qualitatively. Since a real NMS reflects nearly all water borne noise, an air layer represents this behavior as well.

The effectiveness of the NMS is quantified by comparing the modeled SEL at distance 750 m from the pile and 2 m above the seabed for three scenarios:

- The unmitigated case, representing the SEL without any form of mitigation.

- A case with the NMS implemented, representing the actual performance of the NMS
- A perfect System case, representing the maximum theoretically achievable noise reduction.

The Perfect System is implemented as an absorbing boundary located at the position of the NMS. Physically, this represents an idealized 'wall' that absorbs all acoustic energy in the water column without transmitting or reflecting any energy. This represents the theoretical upper limit of noise mitigation that any near-field system could achieve.

The performance of the NMS is quantified using a metric referred to as the Mitigation Performance (η). This parameter expresses the fraction of the maximum theoretically achievable noise reduction that is realized by the NMS.

Let:

- L_0 denote the unmitigated SEL level at 750 m from the pile and 2 m above the seabed, obtained from the unmitigated model.
- L_{nms} denote the SEL obtained with the NMS implemented at the same receiver location.
- L_{ps} denote the theoretical lower bound in SEL corresponding to the Perfect System at the same receiver location.

All levels are expressed in dB. The Mitigation Performance η is then defined as presented in Eq. 5.1. This equation expresses the ratio between the noise reduction actually achieved by the NMS and the noise reduction that is theoretically achievable. It is defined as the insertion loss between the unmitigated and NMS cases, divided by the insertion loss between the unmitigated case and the Perfect System case. Insertion loss refers to the reduction in sound level, expressed in decibels, between the unmitigated reference condition and a mitigated condition.

$$\eta = \frac{IL_{nms}}{IL_{ps}} = \frac{L_0 - L_{nms}}{L_0 - L_{ps}} \tag{5.1}$$

The resulting quantity is dimensionless and takes values between 0 and 1:

- $\eta = 0$ corresponds to no mitigation, i.e. system performance equal to the unmitigated case
- $\eta = 1$ corresponds to perfect mitigation, i.e. system performance equal to the Perfect System case
- intermediate values indicate the fraction of the maximum achievable noise reduction attained by the NMS

The results for the the wind farm site are presented in Table 5.5.

	L_0 [dB]	L_{nms} [dB]	L_{ps} [dB]	IL_{nms} [dB]	IL_{ps} [dB]	η
Measured Result	178.6	X	159.4	Y	19.2	0.Z
Model Result	178.6	169.3	159.4	9.3	19.2	0.48

Table 5.5: Effectiveness of the NMS at the wind farm site based on measured data and model results. The unmitigated and Perfect System SEL values are derived using the validated Model with the pile embedment depth adjusted to 20.50 m, while the modeled NMS result is obtained using the numerical representation of the NMS, i.e. Model 2 results. Additionally, the measured NMS result is derived from the measurements during installation of the wind farm.

From Table 5.5, it can be observed that the effectiveness achieved by the NMS based on the measured data corresponds to approximately X% of the mitigation achieved by the Perfect System. In contrast, the numerical representation of the NMS yields a noticeably lower η, indicating that the model underestimates the noise mitigation performance of the NMS under the assumed conditions.

It should be noted that the effectiveness values presented in this section should be interpreted as approximate indicators rather than exact quantitative measures. The unmitigated and Perfect System noise levels are derived from Model 1, which, although validated, exhibits a small discrepancy with

respect to the measured data. Consequently, the Mitigation Performance values (η) inherit this model uncertainty.

Furthermore, in the evaluation of the NMS effectiveness at the wind farm site, measured NMS results are combined with modeled results. This introduces an additional source of uncertainty. As a result, the calculated effectiveness values may marginally exceed unity or fall below zero in edge cases, although such deviations should be interpreted as artifacts of model uncertainty rather than physically meaningful outcomes.

For this reason, the reported effectiveness values should be understood as estimates within a small uncertainty band and are primarily intended for comparative assessment rather than absolute quantification.

6

Analysis of NMS Effectiveness in Different Soil Conditions

The noise mitigation performance of the NMS is thought to be governed by the soil. The system is designed to mitigate noise within the water column, however, it does not address the energy that is generated in the soil and re-radiates in the water column in the far field. This phenomenon is known as soil coupling (Bellmann et al., 2020). The noise field can be divided into two main components (see Figure 6.1):

- The Primary Noise Path: Noise traveling directly through the water
- Secondary Noise Path: Noise traveling through the seabed and re-radiating into the water column.

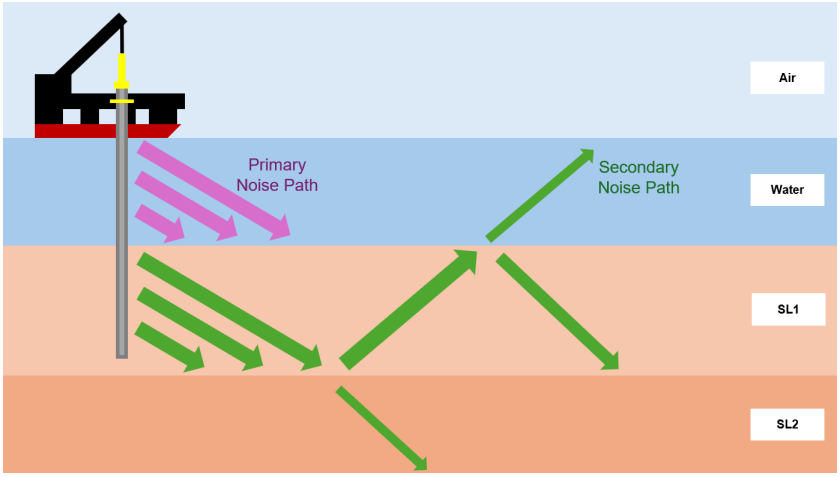

Figure 6.1: Illustration representing the primary (waterborne) and secondary (soil-borne) noise paths. The secondary path illustrates acoustic energy propagating through the soil and re-radiating into the water column.

In an unmitigated scenario, the dominant path is the primary noise path. However, when a near-field noise mitigation system is deployed, it significantly reduces the primary noise path. As this primary path decreases, the secondary noise path can become dominant. The maximum achievable noise reduction can be estimated using a Perfect System (see Section 5.3), which is defined as a fully absorbing boundary at the location of the NMS. In this case, all energy measured in the water column beyond the NMS originates from the secondary noise path, i.e. energy that is re-radiated into the water column from the soil. As shown in Section 5.3, the NMS does not behave as a perfect system and also it is thought that the amount of noise generated during pile driving differs per site. Therefore, it is expected that the noise mitigation performance of the NMS depends on the soil conditions. In some soils, the NMS may achieve a larger absolute reduction in sound levels, which can support the use of the NMS under those specific conditions.

This chapter investigates how different soil configurations affect the noise mitigation performance of the NMS. Section 6.1 defines the soil configurations and model input parameters that will be analyzed in this chapter. Subsequently, Section 6.2 presents the conclusions that are drawn in the Soil Case

Study which can be found in Appendix K. Lastly, Section 6.3 provides the noise mitigation performance of the NMS in the investigated soil conditions.

6.1. Definition of Soil Configurations and Input Parameters

This section defines the various soil stratification and presents the other model input parameters. First, Subsection 6.1.1 presents the four distinct soil models utilized to determine the noise mitigation effectiveness of the NMS in the different soils. While Subsection 6.1.2 presents the other input variables used for the models.

6.1.1. Definition of Different Soil Configurations

This study investigates the influence of soil type (loose vs. dense sand) and soil layering (uniform, thin top layer, thick top layer) on the performance of the NMS. In all configurations, the seabed is represented either as a single uniform layer or as a two layer system consisting of a top layer and an underlying layer. More complex, multi layered stratification are not considered in this analysis. Additionally, this study focuses exclusively on sandy soil stratifications

In principle, this approach results in six possible soil configuration types. However, configurations in which a dense top soil layer overlies a loose underlying layer are considered less relevant for typical offshore environments and therefore of lower priority for this investigation. In addition, the overall modeling effort must remain feasible within the time constraints of this thesis. For these reasons, only the four most representative and relevant configurations are analyzed:

- Uniform dense sand (Soil Case A in Figure 6.2)
- Uniform loose sand (Soil Case B in Figure 6.2)
- Thin loose top layer over a dense underlying layer (Soil Case C in Figure 6.2)
- Thick loose top layer over a dense underlying layer (Soil Case D in Figure 6.2)

The thicknesses of the layers are determined based on CPT data from the OWF Empire Wind site and are summarized in Figure 6.2. The soil properties for these stratifications were calculated using the empirical relations defined by Hamilton (1980). These equations utilize cone resistance and shaft friction as inputs. Based on Byrne et al. (2018) and a discussion with a foundation engineer from HMC, the input values presented in Table 6.1 were assumed as properties of sandy soils typically encountered in the North Sea. The resulting loose and dense sand properties are detailed in Tables 6.2.

Consistent soil parameters are used for all loose and dense sand layers to ensure that the influence of soil layering and soil type (i.e. loose or dense sand) can be isolated from the influence of varying soil stiffness. Using a fixed $q_c = 25\,MPa$ and $f_s = 1\%$ for all loose sand layers, and $q_c = 50\,MPa$ and $f_s = 3\%$ for all dense sand layers, ensures that differences between the model outcomes can be attributed solely to the configuration and thickness of the layers rather than to variations in material properties.

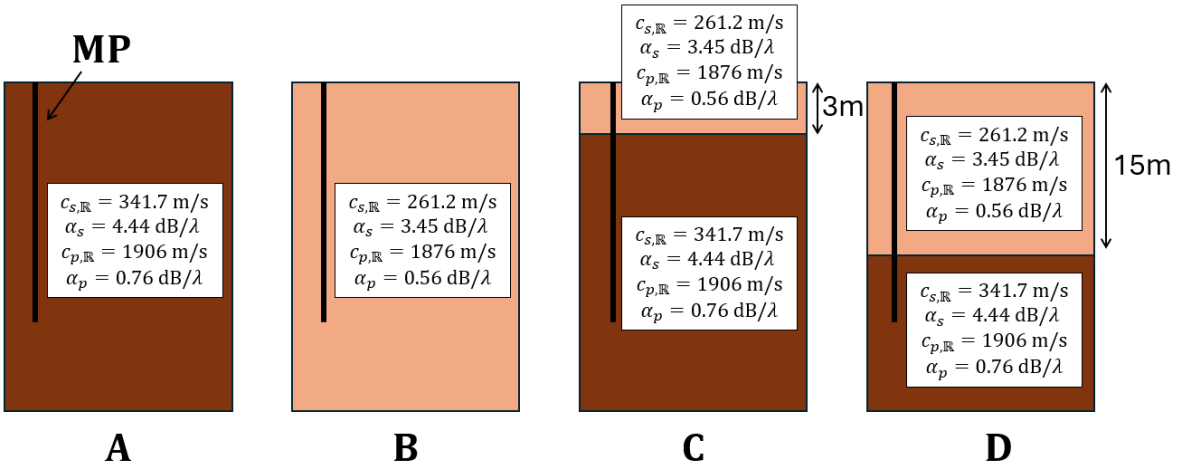

Figure 6.2: Illustration of the four soil stratifications utilized to evaluate the noise mitigation effectiveness of the NMS. Case A represents a uniform dense sand profile, while Case B represents a uniform loose sand profile. Cases C and D represent layered stratifications consisting of a loose top layer (with thicknesses of 3 m and 15m, respectively) overlying a dense sand substrate.

Parameter	Unit	A	B	C		D	
				SL1	SL2	SL1	SL2
q_c	MPa	50	25	25	50	25	50
f_s	MPa	0.3	0.1	0.1	0.3	0.1	0.3
Soil type	–	Dense	Loose	Loose	Dense	Loose	Dense
ρ	kg/m^3	1945	1846	1846	1945	1846	1945
Layer thickness	m	35	35	3	32	15	20
λ	GPa	6.61	6.24	6.24	6.61	6.24	6.61
μ	MPa	227	126	126	227	126	227
E	MPa	674	375	375	674	375	674
ν	–	0.48	0.49	0.49	0.48	0.49	0.48

Table 6.1: Overview of the soil parameters used in the modeling of the four soil configurations (A–D), as presented in Figure 6.2. Additional material properties defining the loose and dense sand types are provided in Table 6.2.

Parameter	Unit	Dense Sand	Loose Sand
$c_{s,\mathbb{R}}$	m/s	341.7	261.2
$c_{p,\mathbb{R}}$	m/s	1906	1876
α_s	dB/λ	4.44	3.45
α_p	dB/λ	0.76	0.56
c_s	m/s	344.0 + 28.0i	261.2 + 16.6i
c_p	m/s	1907 + 26.6i	1876 + 19.3i

Table 6.2: Material properties assigned to loose and dense sand used in the soil configuration models.

Soil attenuation is specified in terms of decibel loss per wavelength, with values of 3.45 dB/λ and 4.44 dB/λ assigned to shear waves, and 0.56 dB/λ and 0.76 dB/λ assigned to pressure waves, for loose and dense sand respectively. This definition implies a constant attenuation per wavelength rather than per unit distance. Since the wavelength depends on frequency according $\lambda(f) = \frac{c}{f}$, this

results in a frequency dependent attenuation behavior. At low frequencies, where wavelengths are long, the specified attenuation is distributed over a larger distance, whereas at higher frequencies, with shorter wavelengths, the same attenuation is concentrated over a shorter distance. As a result, higher frequencies experience a larger attenuation per unit distance than lower frequencies.

To quantify this behavior, the attenuation specified in dB/λ was converted to attenuation per meter (dB/m). This was done by dividing the wavelength at each frequency by the assigned decibel loss per wavelength. This conversion was performed using the shear and pressure wave velocities for loose and dense sand (Table 6.2). The resulting frequency dependent attenuation per unit distance is shown in Figure 6.3. The figure illustrates that attenuation increases with frequency and that the differences between loose and dense sand become more pronounced at higher frequencies, while low frequency components are only weakly attenuated.

As an example, at 100 Hz, pressure waves in dense sand exhibit a higher attenuation per meter than in loose sand, with values of approximately 0.04 dB/m and 0.03 dB/m, respectively. In contrast, shear waves are attenuated much more strongly than pressure waves at the same frequency. For shear waves, the attenuation at 100 Hz is approximately 1.30 dB/m in dense sand and 1.32 dB/m in loose sand.

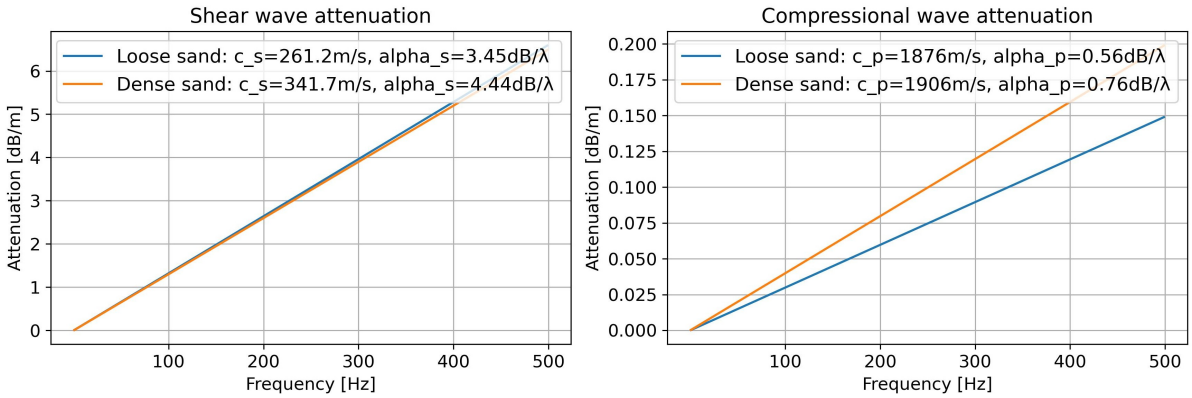

Figure 6.3: Frequency dependent attenuation per distance for shear and pressure waves in loose and dense sand, derived from the specified attenuation values expressed in decibel loss per wavelength.

6.1.2. Model Input Parameters

In addition to the soil properties, several other input parameters must be defined for the analysis of the effectiveness of the NMS in different soil conditions. These include the geometric model setup, MP properties, water properties, frequency and time parameters, and the meshing and extraction parameters. All of these inputs are kept consistent with those used in Model 1. A detailed description and justification of these parameters is provided in Appendix I. Furthermore, the smoothed exponential force function introduced in Section 3.4 is applied in all simulations.

6.2. Conclusion Soil Case Study

The case study presented in Appendix K investigated the influence of soil properties and stratification on underwater noise generation, propagation, and mitigation performance of the simplified representation of the NMS.

The unmitigated cases provide insight into the distribution of energy generated in the water column and the soil. This distribution determines how much energy is accessible to the NMS and the Perfect System, which are only able to mitigate waterborne energy and not seismic energy.

The Perfect System was used as a reference to quantify the amount of energy present in the water column in the vicinity of the pile. The difference between the unmitigated and Perfect System results provides a measure of the maximum achievable mitigation.

The effectiveness of the NMS is therefore governed by how the soil profile controls the partitioning of energy between waterborne and soil borne paths near the pile. However, the NMS introduces additional

mechanisms that influence the noise path. In this study, the presence of the NMS resulted in frequency dependent mitigation behavior. This behavior is attributed to the relatively thin air layer compared to the wavelengths at low frequencies, allowing low frequency energy to be transmitted through the NMS, while higher frequency components are predominantly reflected due to the large impedance mismatch between water and air.

As a result, reflected energy may become trapped within the cavity formed by the pile and the air layer. It should be noted that, in reality, non-linear effects may occur within this cavity due to the significant high pressure levels. However, these effects are not captured in the present linear modeling approach. Consequently, results obtained for scenarios including the NMS should be interpreted with caution. The trapped energy tends to follow the path of least resistance and is partly transmitted into the soil, where pressure waves in the water are converted into compressional, shear, and interface waves in the soil. It is also observed that the total energy at $r = 50\,m$ is significantly lower compared to the unmitigated case. This suggests that the reflected energy may contribute to increased damping of the pile vibrations, thereby altering the pile response. As a result, the source is modified, leading to a reduction in the total radiated energy when the NMS is included.

The effectiveness of the NMS depends not only on the initial partitioning of energy between soil and water, but also on how efficiently soil energy propagate to the far field and re-radiate into the water column at larger distances.

It was found that uniform dense and uniform loose sand primarily influence the total amount of generated energy and its initial distribution between the soil and the water column. Layered soil profiles also have an influence on both the magnitude of the generated energy and its distribution between the soil and water column. In addition, layered soils influence how energy propagates toward the far field and how much energy can re-radiate back into the water column. In particular, layered configurations were observed to promote repeated interactions between energy in the upper soil layers and the water column. This increases the amount of energy that leaks back into the water column.

In the following subsections, these mechanisms are discussed in more detail. First, the influence of uniform dense and loose sand profiles is concluded, followed by the findings of layered soil configurations with thin and thick loose upper layers, and a comparison with the uniform soil cases.

6.2.1. Dense versus Loose Dominated Soils

For uniform dense sand, strong coupling between the pile and the surrounding soil leads to large reaction forces acting on the pile. The high mechanical impedance of dense sand, i.e. its strong resistance to dynamic motion, results in a high radiation resistance, meaning that vibrational energy of the pile is efficiently converted into propagating waves. As a result, a significant fraction of the hammer energy is transferred into propagating waves, rather than being dissipated locally. Since pile vibrations is the source for both soil borne and waterborne sound radiation, the vibrational energy of the pile leads to strong radiation into both the surrounding soil and the water column. Consequently, a large amount of energy is present in the water column near the pile, which increases the noise mitigation potential of the Perfect System.

In contrast, for uniform loose sand, the lower stiffness and mechanical impedance reduce the radiation resistance. In this case, a larger portion of the hammer energy is dissipated through soil deformation and internal friction, rather than being converted into propagating waves. The pile is less constrained, it behaves as a weaker radiator, and the total radiated energy is therefore lower than in the case of uniform dense sand.

For uniform dense sand, the NMS achieves a moderate noise reduction, approximately half of the theoretical mitigation potential indicated by the Perfect System. This indicates that a considerable fraction of the energy still reaches the far field, either through the soil transmission and re-radiating back into the water column or due to incomplete blocking of waterborne radiation. In particular, low frequency components can propagate through the air layer because their wavelengths are large relative to the thickness of the air layer.

It was found that the near field intensity magnitude decreases when the NMS was applied for both the uniform cases. This suggests that the energy reflected by the air layer dampens the vibrations of the

pile, resulting in a reduction of the source strength. Nevertheless, due to modeling assumptions and limitations, especially in the near field region where non-linear effects may occur, these results should be interpreted with caution.

While uniform dense sand generates more energy compared to loose sand, it was found that, in the far field, dense sand results in lower SEL than loose sand. This can be explained by the higher attenuation coefficients assigned to the dense sand. As a result, seismic energy is attenuated more strongly in dense sand than in loose sand. Over larger distances, this increased attenuation leads to a reduction in the energy available for re-radiation into the water column. Consequently, less energy propagates back into the water column, resulting in lower SEL in the far field compared to the loose sand case.

6.2.2. Role of Stratification and Top Layer Thickness

In this case study, it was found that for layered soils a slightly larger fraction of the generated intensity is present in the water column at a distance of $r = 50\,m$ compared to the uniform soil cases. It should be noted that this increase in the water column fraction is small and not very pronounced. In absolute terms, the total intensity magnitude levels were lower for the layered soils than for the uniform soil cases. This could be related to changes in the pile-soil interaction. The presence of layers with different stiffnesses alters the way the pile is clamped by the surrounding soil, which could reduce the efficiency with which the pile vibrates and radiates energy. As a consequence, less total energy is generated and available for transmission into both the soil and the water column.

For the unmitigated configuration, it was observed that although layered soils generate less total energy than the uniform soils, the far field SEL values are the highest. This behavior can be explained by the impedance mismatch between the loose upper layer and the underlying dense sand. Reflections at the loose-dense interface reduce the amount of energy transmitted into the deeper soil. Instead, energy is repeatedly redirected within the upper soil layer, propagating back and forth between the loose-dense interface and the seabed. These repeated interactions with the seabed promote coupling with the water column, allowing part of the energy to leak back into the water column and thereby increasing the water column energy.

The thickness of the loose upper layer influences how frequently these interactions occur. For a thin loose top layer, interactions between the energy trapped in the upper layer and the seabed occur more frequently, providing more opportunities for energy to radiate back into the water column. For a thicker loose top layer, the amount of energy in the top layer is larger than for the thin top layer, but it undergoes fewer seabed interactions and therefore has fewer opportunities to leak into the water column and contribute to far field noise levels. However, it should be noted that the difference in unmitigated far field SEL between the thin and thick loose top layer cases was only 0.9 dB. This indicates that, for the unmitigated configuration, the thickness of the loose upper layer does not have a significant influence on the far field SEL. However it is observed that layered soils results in larger SEL in the far field compared to uniform soils.

In addition, the near field intensity magnitude was found to be higher for the thin loose top layer than for the thick loose top layer. This can be attributed to the fact that, in the case of a thin loose layer, the pile response is still strongly influenced by the underlying dense sand and therefore has a dense dominated response, while the thick loose top layer provides a loose dominated response. As discussed earlier, dense sand has larger radiation efficiency compared to loose sand which explains why the thin loose top soil layer has a larger intensity magnitude in the near field than the thick loose top layer case.

With respect to mitigation, it was found that the thin loose top layer case shows a mitigation potential similar to that of uniform dense sand, while the thick loose top layer case shows a mitigation potential comparable to that of uniform loose sand. This suggests that the average soil properties have a dominant influence on the achievable mitigation potential.

Finally, it was observed that loose dominated soils tend to perform more closely to the Perfect System than dense dominated soils. This behavior may be related to the way energy that is redirected from the cavity into the soil propagates within the soil. It is possible that, in loose soils, this energy propagates in wave types that are less effective at re-radiating back into the water column, or that remain confined within the soil for longer distances. However, this behavior was not explicitly studied, and therefore no firm conclusions can be drawn regarding the underlying mechanisms.

6.2.3. Main Findings of the Soil Case Study

Based on the results of the soil case study, the main findings of the soil case study can be summarized as follows:

- The unmitigated cases show that soil properties control how much energy is generated and how it is partitioned between the water column and the soil near the pile. This determines how much energy is accessible for mitigation.
- The Perfect System provides an upper bound for mitigation by removing all waterborne energy near the pile. Dense dominated soils show a higher mitigation potential for the Perfect System, because a larger amount of the generated energy is present in the water column in these cases and therefore available for mitigation.
- The NMS deviates from the Perfect System because part of the reflected waterborne energy is redirected into the soil. As a result, the effectiveness of the NMS depends not only on the initial waterborne energy, but also on how redirected energy propagates through the soil and re-radiates into the water column at larger distances. Additionally, the reflected energy propagates back to the pile which can change the vibration pattern of the pile and therefore changes the source.
- The mitigation performance of the NMS is frequency dependent. Low frequency components are less effectively mitigated due to their large wavelengths relative to the air layer thickness, while higher frequency components are more strongly reflected by the air layer.
- The soil type in contact with the water column governs the frequency content observed at 750 m in the water column. It was found that all cases with a loose top layer (Soil Cases B, C, and D) exhibit similar unmitigated one third octave band spectra.
- While dense soil generates more energy, it was found that, in the far field, uniform dense soil results in the lowest SEL levels compared to the other investigated soil configurations. This can be explained by the higher attenuation coefficients assigned to the dense soil, which reduce the amount of energy available for re□radiation into the water column.
- Uniform dense sand results in strong pile-soil coupling and high radiation resistance, leading to high near field energy levels and a large theoretical mitigation potential. However, the NMS achieves only approximately half of this potential, indicating that the injected energy into the soil can relatively easy re-radiate back into the water column.
- Uniform loose sand generates less waterborne energy, which limits the mitigation potential of the Perfect System. When the NMS is applied, redirected energy injected into the soil is less effectively re-radiated into the water column, causing the NMS to perform more closely to the Perfect System.
- Layered soil profiles generate less total energy than uniform soils but result in the highest unmitigated far field SEL. This behavior is attributed to impedance contrasts that promote repeated redirection of energy within the upper soil layer and frequent coupling with the seabed.
- The thickness of the loose upper layer determines whether the response is dense or loose dominated. A thin loose top layer behaves similarly to uniform dense sand, whereas a thick loose top layer behaves similarly to uniform loose sand in terms of radiation and mitigation performance.
- A thin upper soil layer leads to more frequent reflections of energy within the top layer. This increases the number of interactions between seismic energy and the seabed, creating more opportunities for energy to leak back into the water column.

6.3. Noise Mitigation Performance of NMS in Different Soil Configurations

To assess the effectiveness of the NMS under varying soil conditions, the Mitigation Performance η is calculated for each soil case. This metric, introduced earlier in Section 5.3, is used to quantify the effectiveness of the NMS. While the Mitigation Performance η provides a measure of how efficiently the NMS performs relative to the theoretically achievable noise reduction for a given soil condition, it does not reflect the absolute magnitude of noise reduction. In soil conditions where the difference between the unmitigated and Perfect System noise levels is small, high values of η may coincide with limited

absolute noise reduction. Therefore, the normalized mitigation effectiveness is interpreted together with absolute noise reduction metrics when assessing the suitability of the NMS across different soil conditions.

Table 6.3 provides an overview of the mitigation performance η, together with the absolute noise reduction achieved by the NMS and the Perfect System for each soil case. It can be seen that the simplified NMS representation performs relatively worse compared to the Perfect System for dense dominated soils, whereas for loose dominated soils the mitigation performance η is relatively higher.

Soil Case	L_0 [dB]	L_{nms} [dB]	L_{ps} [dB]	IL_{nms} [dB]	IL_{ps} [dB]	η
A	176.2	166.1	155.7	10.1	20.5	0.49
B	177.5	165.3	163.3	12.2	14.2	0.86
C	178.5	166.8	158.8	11.7	19.7	0.59
D	177.6	166.0	162.8	11.6	14.8	0.78

Table 6.3: Overview of the mitigation performance η and the absolute noise reduction achieved by the NMS and the Perfect System for the considered soil configurations. Values of η close to one indicate a high NMS effectiveness relative to the theoretical mitigation potential. The mitigation performance η, defined in Section 5.3, is given by the ratio IL_{nms} to IL_{ps}, where IL_{nms} and IL_{ps} represents the insertion loss when applying the NMS and the Perfect System, respectively.

Based on the results presented in Table 6.3, a ranking could in principle be established to indicate under which soil conditions the simplified NMS representation, which only captures the large impedance mismatch between water and air and not the real world behavior, performs most closely to the Perfect System. Such a ranking would be based on the effectiveness parameter η. However, it is important to emphasize that the simplified NMS representation does not adequately capture the physical behavior of the NMS. As a result, significant uncertainties are associated with a ranking derived from the numerical representation of the NMS. For this reason, no ranking of soil conditions based on η is presented in this study. Instead, the results are interpreted qualitatively.

This decision is supported by the large difference observed between the performance of the numerical NMS representation and the real NMS applied at the wind farm site. While the real NMS achieved an effectiveness of $\eta = 0.Z$, the numerical representation achieved only $\eta = 0.48$. This discrepancy indicates that the simplified NMS model substantially underestimates the performance of the real NMS at the wind farm and that conclusions regarding effectiveness across soil conditions would not be robust.

Although a quantitative ranking of NMS effectiveness is therefore not justified, the mitigation potential can still be used to identify soil conditions in which near field mitigation systems are expected to be most promising. Based on the Perfect System results, dense dominated soils offer the highest mitigation potential, as they generate relatively large amounts of energy, a significant fraction of which is present in the water column and therefore accessible for mitigation. This observation can be used as guidance to identify favorable soil conditions for near field noise mitigation. However, more advanced numerical modeling is required before firm conclusions can be drawn on the effectiveness of the NMS in different soil conditions.

7
Discussion

This study aimed to investigate the influence of soil stratification and soil properties on the noise mitigation performance of the NMS during offshore MP installation. This was achieved through the development and validation of a coupled numerical modeling approach supported by field measurements from a wind farm. In this chapter, the uncertainties in the results are discussed, the limitations of this study are addressed, and directions for future research are given. This is discussed in Sections 7.1, 7.2, and 7.3, respectively.

7.1. Uncertainties of the Results

During this study, several methodological and modeling choices were made that influence both the results and their interpretation. These choices, along with uncertainties of the results, are discussed in this section.

7.1.1. General Model Uncertainty

In this study, a linear modeling approach was assumed, which allows for the superposition of the sound waves and for scaling the unit response with the applied impact force. However, impact pile driving generates high amplitude pressure and stress waves for which nonlinear effects can be expected. Examples include bubble formation in the water column (cavitation), non-linear pile-soil coupling, and nonlinear damping in the soil. In reality, these nonlinear mechanisms lead to additional energy dissipation, which is not captured in the linear model. This is especially relevant when the NMS representation is applied. The air layer reflects a large portion of the energy, causing energy to become trapped within the cavity between the MP and the air layer. As a result, higher pressure amplitudes occur within this region, which further enhances nonlinear effects. Since these processes are not included in the linear modeling approach, the model does not accurately capture the wave behavior and energy dissipation under these conditions.

7.1.2. Model Validation

Model 1 showed good agreement with the measured SEL, indicating that the unmitigated model captures the main mechanisms of noise generation and propagation during impact pile driving. However, an overestimation of low frequency energy was observed in the one third octave band spectra. This discrepancy could be attributed to several simplifications in the model, such as assuming vertically layered waveguides, assuming perfect pile-soil coupling, and using the force signal from the hammer rather than the force actually transmitted to the pile. In reality, these factors could lead to stronger attenuation of low frequency components than is represented in the model.

In this study, model validation was performed using broadband SEL rather than requiring agreement across the one third octave band spectra. This approach was chosen because it is common practice in the validation of acoustic models (Peng et al., 2021). Since SEL is widely used as a validation metric, the observed spectral mismatch was considered acceptable.

This choice does, however, have implications for the interpretation of the NMS results. The numerical representation of the NMS showed frequency dependent mitigation behavior, where low frequency waves have wavelengths that are large compared to the thickness of the air layer used to represent the NMS. As a result, these waves can excite the air layer rather than being reflected. Because the unmitigated model already overestimates low frequency energy and since the lower frequencies are not effectively mitigated, a larger amount of energy is able to pass through the air layer in the NMS

simulations than seen in reality. This leads to an overestimation of the mitigated SEL levels and, consequently, an underestimation of the actual effectiveness of the NMS.

Therefore, it could be useful to calibrate the frequency spectrum of the unmitigated model against the measured data. This is important, as the current overestimation of the lower frequencies influences the predicted noise mitigation performance of the NMS. One way to achieve this is by adjusting the applied force signal so that the hammer impact contains less low frequency energy. In addition, the representation of the soil profile can be improved. Increasing the thickness of the top soil layer reduces the interaction between seismic energy and the water column, which results in less energy being re-radiated into the water column. Since attenuation in the soil affects higher frequencies more strongly than lower frequencies, it is expected that relatively more low frequency energy is re-radiated from the seabed. This contributes to the overestimation of low frequency energy in the model. The underestimation of higher frequencies could be addressed by adjusting the attenuation properties of the soil. By decreasing the attenuation coefficients, higher frequencies experience less damping, which may improve their representation in the model results. The model could also be further refined by reducing some of the simplifying assumptions. For example, additional damping could be introduced at the pile–soil interface to better represent imperfect coupling. Furthermore, gradual soil layering could be implemented instead of idealized homogeneous layers. However, such calibrations should always be carried out with care, ensuring that all adjusted parameters remain physically realistic.

In addition, the interpretation of the results should take into account the calibration process used to determine the soil properties for the unmitigated case (Model 1). In this study, several empirical relations from different literature sources were evaluated to identify soil properties that provided sufficient agreement between the modeled and measured SEL at 750 m. As none of these relations provided a sufficiently accurate match, an additional uncertainty factor of 15% was applied to the density, as well as to the shear and pressure wave velocities. Using this calibration approach, the unmitigated model could be validated against the measurements. Although this approach was justified in this study by the uncertainty that exist in soil characterization, it introduces ambiguity in the interpretation of the results. Different calibration choices or alternative empirical relations could also have resulted in sufficient agreement with the measured data, but with different underlying soil properties and therefore different results. As a result, the calibrated soil parameters may not accurately represent the actual site conditions at the wind farm, and the observed agreement could partly be the result of compensating other model assumptions or simplifications. The dependence of the predicted NMS noise mitigation performance at the wind farm on the assumed soil properties should therefore be considered when interpreting the findings of this study.

7.1.3. NMS Case Study

In the NMS case study performed, the focus was on near field results, with SEL evaluated at $r = 50\,m$. While this choice reduced computational time and effort compared to a far field analysis, it limits the interpretation of the results. Energy injected into the soil can propagate through different wave types, such as body waves and interface waves (e.g. Scholte waves), which have different attenuation rates and radiation patterns. Scholte waves, for example, are known to propagate along the seabed–water interface over large distances, potentially leading to elevated underwater noise levels in the far field even when near field levels look relatively small. By restricting the analysis to the near field, this case study does not fully capture how energy from the cavity injected into the soil may contribute to sound levels at larger distances. As a result, certain NMS representations that appear favorable at 50 m may show different NMS noise mitigation performance in the far field. An analysis over a larger distance would be required to fully assess the redistribution of energy and its influence at far field locations.

Additionally, the observation that the modeled shells act as a secondary sound source suggests that not all physical processes are captured by the simplified NMS representations in the case study. Considering the high NMS mitigation effectiveness observed in field measurements, it is unlikely that the shell act as secondary radiator in reality. Instead, it is more plausible that mechanisms such as structural damping or fluid–structure interactions limit shell excitation in reality. These findings highlight that representing the NMS numerically remains challenging and that not all noise mitigation mechanisms associated with the NMS are understood. As a result, a simplified representation was adopted in this study, in which the NMS is modeled as an air layer.

Despite this, the choice to represent the NMS by an air layer is not considered incorrect. In the real NMS, the air layer is the dominant noise mitigation mechanism, as it introduces a strong impedance mismatch that blocks a large portion of the waterborne energy. The simplified representation therefore captures the primary mitigation behavior of the NMS and allows for a comparison between different soil configurations which was the main objective of this study. However, the results of this case study should be interpreted with caution, as they do not represent the complete behavior of the NMS.

7.1.4. Soil Case Study

In the soil case study, the differences in the unmitigated SEL between the four soil configurations were small, with a maximum difference of 2.2 dB. The one third octave band spectra showed that the frequency response of three of the soil cases were almost identical, while only one case exhibited deviations at higher frequencies. This outcome was unexpected, as variations in soil properties were anticipated to result in clearer differences in the spectral response. The limited influence of soil type therefore indicates that the modeled response is only weakly affected by deeper soil properties for the conditions considered. Instead, the results suggest that the top soil layer plays a dominant role in the unmitigated case, determining the spectral response.

Additionally, in the soil case study, the NMS appears to provide stronger noise mitigation than the Perfect System at 200 Hz for Soil Case A. One possible explanation is that reflected energy interacts with the pile, thereby altering the pile response and the resulting radiated noise. The observed dip at 200 Hz is not present in either the Unmitigated or Perfect System cases, suggesting that reflections introduced by the NMS may play a role. However, it is considered likely that this locally stronger mitigation, where the NMS representation predicts lower levels than the Perfect System, is a numerical artifact rather than a physically realistic effect. It is therefore not interpreted as an actual improvement in noise mitigation performance. That said, this assumption cannot be fully confirmed based on the current results, and further research is required to better understand this behavior.

During the soil case study, soil properties were assigned to loose and dense sand layers based on empirical relations defined by Hamilton (1980). These relations use cone resistance and shaft friction as input parameters. In this study, values for cone resistance and shaft friction were assumed, after which the empirical relations were applied to derive the acoustic soil properties. This approach resulted in a higher attenuation coefficient for dense sand compared to loose sand. However, this is not consistent with typical values find in the field, where loose sand generally exhibits higher attenuation than dense sand. As a result, the soil configurations used in this study represent a specific case where dense sand is assigned a higher attenuation than loose sand. The presented results should therefore be interpreted with caution and should not be directly generalized to all loose-dense sand configurations. Instead, the conclusions are only strictly valid for the specific soil conditions as defined in this study.

7.2. Limitations

Several assumptions and simplifications were made in this study, which influence the obtained results and their interpretation. While these choices were necessary to keep the problem computationally manageable within the available timeframe and to enable comparison between cases, they limit the applicability of the findings. The main limitations of the modeling approach, as well as those specific to the soil and NMS case studies, are discussed in Subsection 7.2.1, 7.2.2, and 7.2.3, respectively.

7.2.1. General Model Limitations

A limitation of this study is the assumption of linear behavior. In reality, impact pile driving generates high amplitude pressure and stress waves, for which nonlinear effects can occur in both the water column and the soil, such as cavitation, non-linear pile-soil coupling, and non-linear soil damping. This affects the predicted results and the results should therefore be interpreted with this limitation in mind.

The soil is represented by stratified layers with homogeneous material properties. This simplified representation does not fully reflect real seabed conditions, where lateral heterogeneity, gradual property transitions, and more complex stratifications may occur.

Furthermore, no attenuation is included in the fluid domain. Consequently, frequency dependent absorption of energy in water is neglected, which may lead to an overestimation of SEL at larger distances

or an overestimation of higher frequencies. In addition, hydrodynamic and oceanographic effects such as currents, surface waves, and water column stratification are not considered.

The model further assumes axisymmetry. This assumption excludes asymmetric effects such as non uniform seabed conditions or inclined piling, which may influence both the pile response and noise radiation.

Finally, the results strongly depend on the assumed soil parameters for the wind farm site. In this study, these parameters were derived from CPT data and using empirical relations, after which they were calibrated to obtain agreement between the unmitigated model and the measured data. Although this approach improves the match with measurements, it introduces uncertainty, as different combinations of model parameters could lead to a similar level of agreement. For example, discrepancies between the model and measurements could also be compensated by adjusting the applied force signal rather than the soil properties. As a result, it cannot be guaranteed that the calibrated soil parameters accurately represent the actual site conditions. The model may therefore show good agreement with the measured data while not fully capturing the physical behavior. Although validation has been performed, additional validation using additional datasets or alternative calibration strategies would be required to increase confidence in the results. The findings of this study should therefore be interpreted with caution.

7.2.2. NMS Case Study Limitations

In the NMS case study, only a single pile penetration depth and one set of pile parameters were considered. Changes in embedment depth or pile properties can influence pile-soil interaction and could therefore lead to different results. The conclusions drawn in this study may therefore not directly apply to other pile configurations or embedment depths.

Due to the axisymmetric modeling approach, the NMS is represented in a simplified way. As a result, non axisymmetric components such as the structural frame of the NMS are not included in the model. In reality, these components are expected to affect both sound propagation and noise mitigation performance.

The NMS case study was conducted for the wind farm site conditions, which are characterized by dense sand. Other soil types, such as clays or mixed sediments, may exhibit different NMS behavior. The applicability of the results to such conditions is therefore uncertain and has not been investigated within the scope of this study.

7.2.3. Soil Case Study Limitations

In the soil case study, the analysis was limited to four soil configurations. While this allows for comparisons, it restricts the ability to draw conclusions to the wide range of soil conditions encountered in offshore environments.

In addition, the soil case study considered only a single excitation force. The resulting conclusions are therefore specific to this loading condition and may not be directly applicable to other force magnitudes or force spectra. Different excitation characteristics could lead to different frequency responses.

Similar to the NMS case study, only one pile penetration depth and one set of pile parameters were evaluated. The observations made in the case study of the soils, may vary with changes in embedment depth and pile properties, which is not investigated within the scope of this work.

7.3. Future Research

Based on the limitations of the present study and the observed results, several directions for future research are recommended.

First, an improved numerical representation of the NMS is needed to draw more robust conclusions about the NMS noise mitigation performance. The results of this study indicate that interactions between the pile, fluid, soil, and NMS play an important role in the response of the system. It is therefore recommended to consider a nonlinear modeling approach that can better capture these effects. In addition, further investigation of the shell behavior seen in the NMS case study is recommended, as the shells appear to act as a secondary sound source. A better understanding of this behavior could help

determine whether it is a real characteristic of the NMS or a phenomenon that can be reduced through improvements in the model representation.

Second, future studies should consider a wider range of soil profiles, including cohesive soils such as clay and more complex stratifications. This would allow assessment of the applicability of the conclusions and improve understanding of soil dependent noise mitigation performance of the NMS. It is recommended to focus on extreme soil conditions, thereby defining a representative range within which potential offshore sites may fall. Such an approach could support prediction of NMS performance for new project locations.

Third, the influence of pile penetration depth, pile geometry and parameters, and excitation force should be further investigated. Variations in these parameters may affect pile-soil-fluid interaction, radiation efficiency, and noise mitigation effectiveness of the NMS.

Additionally, extending the model to include non-axisymmetric effects would enable a more realistic geometrical representation of the NMS, including its frame. This could provide insight into asymmetric sound propagation and mitigation behavior that cannot be captured within the current axisymmetric model.

Finally, further validation against empirical data is recommended to strengthen confidence in the model predictions and to ensure that the observed agreement in model results and measured data is not the result of coincidence or inaccuracies from calibration.

8

Conclusions & Recommendations

The installation of offshore MPs using hydraulic impact hammers generates high intensity impulsive underwater noise, which can pose risks to marine life and challenges compliance with underwater noise regulations. To reduce these effects, the NMS was for the first time deployed during MP installation at a wind farm. Despite its successful deployment, the mechanisms governing its noise mitigation performance had not yet been modeled, analyzed, or quantified.

The primary aim of this study was to investigate to what extent soil stratification and soil properties influence the noise mitigation performance of the NMS during offshore MP installation. This was achieved through the development, validation, and application of a coupled numerical modeling approach, supported by field data obtained during the installation of the wind farm.

Underwater noise generated during impact pile driving was shown to propagate through both the water column and the seabed. While the NMS mitigates the waterborne noise path by introducing a large impedance mismatch, its overall effectiveness is limited by a secondary noise path through the soil, where energy bypasses the NMS and is re-radiated into the water column behind the NMS.

The dataset collected at the wind farm, consisting of measured noise levels, hammer data, and geotechnical information, enabled the setup, calibration, and validation of the numerical model. The use of a test and reference pile where both mitigated and unmitigated conditions occurred under identical environmental settings was valuable. The developed model is based on this specific MP situation where the effect of the NMS could be isolated.

The unmitigated model showed good agreement with measured data, with differences in SEL of 1.6 dB at a distance of 750 m. Although the model overestimated lower frequencies in the one third octave band spectra, validation based on broadband SEL values was considered sufficient for this study. The NMS was represented by an air layer with a thickness 0.23 m extending over the full water column. This representation reflects the primary mitigation mechanism of the NMS, i.e. the impedance mismatch introduced by the air layer which reflects most of the propagating energy in the water column. Using this representation, the Mitigation Performance (η) of the numerical representation of the NMS, defined as the insertion loss when using the NMS divided by the insertion loss when using the Perfect System, was found to be 0.48, compared to η of 0.Z observed in reality. This indicates that the real NMS performs relatively well in practice and mitigates X% of the potential noise. However, the simplified numerical representation of the NMS used in this study underestimates the NMS performance under the specific conditions at the wind farm and therefore when interperting the results should be done with caution and keeping in mind that in only represents the main mitigation aspect of the NMS and not the real world behavior.

The NMS case study showed that part of the waterborne energy blocked by the NMS is trapped inside the cavity between the pile and the air layer and is partially redirected into the soil. This redirected energy can bypass the NMS and re-radiate into the water column behind the system, thereby reducing the mitigation performance. To investigate how this process is influenced by soil conditions, four sandy soil configurations were analyzed.

The results showed that dense dominated soils generate a larger total amount of energy, of which a relatively large absolute fraction is present in the water column and can therefore potentially be mitigated. In addition, soil stratification introduces an impedance mismatch at the loose-dense interface, causing part of the energy to be reflected at this interface and redirected toward the seabed, where it has the opportunity to re-radiate back into the water column. Another part of the energy is reflected

back toward the loose-dense interface, initiating a new redirection cycle. These repeated reflections increase the potential for re-radiation of energy into the water column. For layered soils, thinner upper layers were found to promote more frequent interactions between seismic energy and the seabed, leading to increased leakage of energy back into the water column compared to thicker upper layers.

The main research question addressed in this study was:
To what extent do soil stratification and properties influence the noise mitigation performance of the NMS during offshore monopile installation?

This study concludes that, for equal hammer force and blow energy, soil stratification and soil properties have only a limited influence on unmitigated far field noise levels, with differences of up to 2.2 dB across the analyzed soil cases. Similarly, soil properties and layering have only a minor influence on the noise mitigation performance of the NMS representation, with a maximum deviation of 1.5 dB between the investigated soil configurations. However, soil properties and stratification have a clear influence on the noise mitigation potential, as defined by the Perfect System. The soil controls how much energy is generated near the pile and how this energy is distributed between the water column and the seabed. In addition, soil properties determine how effectively seismic energy propagates through the soil and re-radiates back into the water column at larger distances. It was found that dense dominated soils result in a higher mitigation potential, due to a larger absolute portion of energy generated in the water column which can potentially be mitigated by the NMS. In contrast, loose dominated soils lead to a higher modeled mitigation performance (η) of the NMS, as the SEL approach those of the Perfect System.

Overall, the results show that soil conditions influence both the noise mitigation potential and the performance of the NMS. However, due to the uncertainties in the numerical representation of the NMS, it is not possible to make a reliable ranking of the investigated soil conditions in terms of favourable or unfavourable application of the NMS. Instead, the findings provide guidance on identifying soil conditions where near field noise mitigation is likely to be more effective. At the same time, it should be noted that more advanced and more accurate representative models of the NMS are required before firm conclusions can be drawn regarding the mitigation performance.

8.1. Recommendations

Based on the findings of this study, the following recommendations are made for future application:

- The current numerical approach can be applied to assess relative trends and to determine the noise mitigation potential between different soil conditions. However, for accurate prediction of the NMS mitigation performance, more advanced modeling approaches, including non-linear effects, are recommended.
- When evaluating noise mitigation concepts, soil properties and stratification should be considered as part of the assessment, as they influence the noise mitigation potential and are therefore also assumed to influence performance of the NMS.
- Additional field measurements under a wider range of soil conditions are recommended to further validate the numerical model and to support the development of a more accurate numerical representation of the NMS.

References

Agelet de Saracibar, Carlos (2000). *Nonlinear Continuum Mechanics*. Chap. Chapter 1: Tensor Algebra. URL: https://link.springer.com/book/10.1007/978-3-031-15207-8.

Baldi, G. et al. (1989). "Modulus of sands from CPT's and DMT's". In: *Conf. Soil Mech. & Fdn. Engr., Rio de Janeiro* Vol 1, pp. 165–170.

Bellmann, Michael A et al. (2020). "Underwater noise during percussive pile driving: Influencing factors on pile-driving noise and technical possibilities to comply with noise mitigation values". In: *ERa Report: Experience report on piling-driving noise with and without technical noise mitigation measures*.

Blackledge, Jonathan M. (2005). "Chapter 5 - Green Functions". In: *Digital Image Processing*. Ed. by Jonathan M. Blackledge. Woodhead Publishing Series in Electronic and Optical Materials. Woodhead Publishing, pp. 113–152. ISBN: 978-1-898563-49-5. DOI: https://doi.org/10.1533/9780857099464.1.113. URL: https://www.sciencedirect.com/science/article/pii/B9781898563495500057.

Bonet, Javier and Richard D. Wood (1997). *Nonlinear Continuum Mechanics for inite Element Analysis*. The press syndicate of the University of Cambridge. URL: https://cdn.preterhuman.net/texts/science_and_technology/physics/Mechanics/Nonlinear%20Continuum%20Mechanics%20For%20Finite%20Element%20Analysis%20-%20Bonet,%20Wood.pdf.

Brandt, Karel (2022). *The Mitigation of Underwater Noise by a Big Bubble Curtain - A Study into the Optimization of a Big Bubble Curtain Configuration and a Contribution to Noise Mitigation Modelling*. Delft University of Technology.

BSH (Oct. 2011a). *Messvorschrift für Unterwasserschallmessungen: Aktuelle Vorgehensweise mit Anmerkungen*.

— (Oct. 2011b). *Offshore wind farms: Measuring instruction for underwater sound monitoring*.

Byrne, T. et al. (2018). "Performance of CPT-based methods to assess monopile driveability in North Sea sands". In: *Ocean Engineering* 166, pp. 76–91. ISSN: 0029-8018. DOI: https://doi.org/10.1016/j.oceaneng.2018.08.010. URL: https://www.sciencedirect.com/science/article/pii/S0029801818314926.

Castro, Raúl R. et al. (1999). "P- and S-wave attenuation in the region of Marche, Italy". In: *Tectonophysics* 302.1, pp. 123–132. ISSN: 0040-1951. DOI: https://doi.org/10.1016/S0040-1951(98)00277-7. URL: https://www.sciencedirect.com/science/article/pii/S0040195198002777.

Chandler-Wilde, Simon and Steve Langdon (2007). "Boundary element methods for acoustics". In: *Lecture notes, University of Reading, Department of Mathematics*.

Dahl, Peter H, Christ AF de Jong, and Arthur N Popper (2015). "The underwater sound field from impact pile driving and its potential effects on marine life". In: *Acoustics Today* 11.2, pp. 18–25.

Dahl, Peter H and Per G Reinhall (2013). "Beam forming of the underwater sound field from impact pile driving". In: *The Journal of the Acoustical Society of America* 134.1, EL1–EL6.

de Jong, Katrien (2025). *The Mitigation of Underwater Cumulative Noise for Impact Piling by Operational Strategies*. Delft University of Technology.

Defingou, Maria et al. (Dec. 2019). *PHAROS4MPAS - Safeguarding marine protected areas in the growing Mediterranean blue economy. Capitalization report for the offshore wind energy sector.*

Dekeling, R et al. (2013). "Monitoring guidance for underwater noise in European seas-Executive Summary". In: *2nd Report of the Technical Subgroup on Underwater Noise (TSH Noise)*, p. 14.

Dinh, Van Nguyen and Eamon McKeogh (2018). "Offshore wind energy: technology opportunities and challenges". In: *Vietnam Symposium on Advances in Offshore Engineering*. Springer, pp. 3–22.

European Committee for Standardization (2005). "EN 1993-1-1: Eurocode 3: Design of Steel Structures - Part 1-1: General Rules and Rules for Buildings". In: URL: https://eurocodes.jrc.ec.europa.eu.

Flores-Mendez, Esteban et al. (2012). "Rayleigh′ s, Stoneley′ s, and Scholte′ s Interface Waves in Elastic Models Using a Boundary Element Method". In: *Journal of applied mathematics* 2012.1, p. 313207.

Flynn, Kevin N and Bryan A McCabe (2016). “Energy transfer ratio for hydraulic pile driving hammers”. In.

Freiberger, Marianne (2021). *Complex square roots*. URL: https://plus.maths.org/content/maths-minute-choosing-square-roots#:~:text=The%20complex%20square%20root%20is%20a%20multi%2Dvalued,sheet%20and%20once%20around%20the%20bottom%20sheet..

Glasbergen, Govert Jan (2020). *Underwater Noise - An Analysis to the Relevant Criteria for Positioning a Bubble Curtain*. Delft University of Technology.

Gottsche, Klaus Marco, Peter Moller Juhl, and Ulrich Steinhagen (2013). “Numerical prediction of underwater noise reduction during offshore pile driving by a Small Bubble Curtain”. In: *INTER-NOISE and NOISE-CON Congress and Conference Proceedings*. Vol. 247. 7. Institute of Noise Control Engineering, pp. 1259–1268.

grow (n.d.). *Bubbles JIP*. URL: https://grow-offshorewind.nl/project/bubbles-jip.

Hall, Marshall V (2015). “An analytical model for the underwater sound pressure waveforms radiated when an offshore pile is driven”. In: *The Journal of the Acoustical Society of America* 138.2, pp. 795–806.

Hamilton, Edwin L (1980). “Geoacoustic modeling of the sea floor”. In: *The Journal of the Acoustical Society of America* 68.5, pp. 1313–1340.

Heerema Marine Contractors (2023). “Primary structural design report Template”. Company internal report.

— (2024a). *Construction of offshore wind farm ‘EnBW He Dreiht’: EnBW and Heerema showcase major noise reduction with innovative noise mitigation system — heerema.com*. https://www.heerema.com/news/heerema-showcases-major-noise-reduction-with-double-walled-t-nms-10000.

— (2024b). *Drone photography during the deployment of the NMS*.

— (n.d.). *Noise Mitigation for Offshore Pile Driving*. Company internal wikipage.

Hegazy, Y.A. and Paul Mayne (Jan. 1995). “Statistical correlations between Vs and CPT data for different soil types”. In: *Proc. Cone Penetration Testing (CPT’95)* 2, pp. 173–178.

IHC IQIP (2020a). *Noise mitigation: in search of the best solution*. URL: https://issuu.com/marcogeels/docs/osi_13-1_totaal_lr/s/10338199.

— (2020b). *Pulse – a smarter way to mitigate noise*. URL: https://iqip.com/pulse/.

IllInois, University of (2016). *Introduction to Galerkin Methods*. URL: https://fischerp.cs.illinois.edu/tam470/refs/galerkin2.pdf.

IQIP (2023). *IQIP’s latest and largest innovation in noise mitigation well on its way*. URL: https://iqip.com/iqips-latest-and-largest-innovation-in-noise-mitigation-well-on-its-way/.

— (2024). *Embarking on a mission: NMS-T-10000 stands ready for its voyage to the He Dreiht offshore wind farm*. URL: https://iqip.com/embarking-on-a-mission-nms-t-10000-stands-ready-for-its-voyage-to-the-he-dreiht-offshore-wind-farm/.

ISO (2017a). *ISO 17025: Testing and calibration laboratories*.

— (2017b). *ISO 18406: Underwater acoustics — Measurement of radiated underwater sound from percussive pile driving*.

itap GmbH (Dec. 2024). *Messung der Unterwasserschallimmissionen im Offshore Windpark He Dreiht*.

Jensen, Finn B et al. (2011). *Computational ocean acoustics*. Vol. 2011. Springer.

Kaldellis, J.K. and M. Kapsali (2013). “Shifting towards offshore wind energy—Recent activity and future development”. In: *Energy Policy* 53, pp. 136–148. ISSN: 0301-4215. DOI: https://doi.org/10.1016/j.enpol.2012.10.032. URL: https://www.sciencedirect.com/science/article/pii/S0301421512008907.

Kasteel, Elisabeth (2018). *Underwater Piling Noise - Predicting Sound Levels in Water with the Underwater Acoustic Simulator*. Delft University of Technology.

Kim, Incheol et al. (2025). “Characterizing Effects of Changes in Soil Phase on Elastic Wave Velocities for Sand with Different Moisture Contents”. In: *Journal of Geotechnical and Geoenvironmental Engineering* 151.6, p. 04025038.

Kriščiūnas, Andrius et al. (2016). “Minimization of numerical dispersion errors in 2D finite element models of short acoustic wave propagation”. In: *International Conference on Information and Software Technologies*. Springer, pp. 745–752.

Ku, Taeseo et al. (2017). “Stress dependency of shear-wave velocity measurements in soils”. In: *Journal of Geotechnical and geoenvironmental Engineering* 143.2, p. 04016092.

Kuhn, Christian et al. (2014). “Dynamic measurements of pile deflections as a source of underwater sound emissions during impact driving of offshore pile foundations”. In: *INTER-NOISE and NOISE-CON Congress and Conference Proceedings*. Vol. 249. 1. Institute of Noise Control Engineering, pp. 5643–5652.

Lengkeek, HJ, J De Greef, and Stan Joosten (2018). “CPT based unit weight estimation extended to soft organic soils and peat”. In: *Cone Penetration Testing 2018*. CRC Press, pp. 389–394.

Li, Yi et al. (2020). “Comparative study of onshore and offshore wind characteristics and wind energy potentials: A case study for southeast coastal region of China”. In: *Sustainable Energy Technologies and Assessments* 39, p. 100711. ISSN: 2213-1388. DOI: https://doi.org/10.1016/j.seta.2020.100711. URL: https://www.sciencedirect.com/science/article/pii/S2213138820301363.

Lippert, Stephan et al. (2016). “COMPILE—A generic benchmark case for predictions of marine pile-driving noise”. In: *IEEE Journal of Oceanic Engineering* 41.4, pp. 1061–1071.

Lippert, Tristan and Otto von Estorff (2014). “On a hybrid model for the prediction of pile driving noise from offshore wind farms”. In: *Acta Acustica United with Acustica* 100.2, pp. 244–253.

MacGillivray, Alexander O (2014). “Finite difference computational modeling of marine impact pile driving”. In: *J. Acoust. Soc. Am* 136, p. 2206.

Mayer, Andreas P and Alexander S Kovalev (2003). “Nonlinear waves guided at a liquid-solid interface”. In: *PROCEEDINGS-ESTONIAN ACADEMY OF SCIENCES PHYSICS MATHEMATICS*. Vol. 52. 1. Estonian Academy Publishers; 1999, pp. 43–62.

Mayne, Paul W (2001). “Stress-strain-strength-flow parameters from enhanced in-situ tests”. In: *Proc. Int. Conf. on In Situ Measurement of Soil Properties and Case Histories, Bali*, pp. 27–47.

Meegan, G Douglas et al. (1999). “Nonlinear stoneley and scholte waves”. In: *The Journal of the Acoustical Society of America* 106.4, pp. 1712–1723.

Oklahoma State University (n.d.). *Lecture 21: Green’s Identities*. URL: https://math.okstate.edu/people/binegar/5233-S96/5233-l21.pdf.

Onen, Onursal and Yusuf Can Uz (2015). “Investigation of Scholte and Stoneley Waves in Multi-layered Systems”. In: *Physics Procedia* 70. Proceedings of the 2015 ICU International Congress on Ultrasonics, Metz, France, pp. 217–221. ISSN: 1875-3892. DOI: https://doi.org/10.1016/j.phpro.2015.08.138. URL: https://www.sciencedirect.com/science/article/pii/S1875389215008792.

Pan, Haojie et al. (Dec. 2019). “Quantification of gas hydrate saturation and morphology based on a generalized effective medium model”. In: *Marine and Petroleum Geology* 113, p. 104166. DOI: 10.1016/j.marpetgeo.2019.104166.

Papadakis, Nikolaos M. and Georgios E. Stavroulakis (2018). “Effect of Mesh Size for Modeling Impulse Responses of Acoustic Spaces via Finite Element Method in the Time Domain”. In.

Peng, Yaxi, Apostolos Tsouvalas, and A Metrikine (2020). “A coupled modelling approach for the fast computation of underwater noise radiation from offshore pile driving”. In.

Peng, Yaxi, Apostolos Tsouvalas, Tasos Stampoultzoglou, et al. (2021). “Study of the sound escape with the use of an air bubble curtain in offshore pile driving”. In: *Journal of Marine Science and Engineering* 9.2, p. 232.

Piessens, Robert, Alexander D Poularikas, et al. (2000). “The hankel transform”. In: *The transforms and applications handbook* 2.9.

Reinhall, Per G and Peter H Dahl (2011). “Underwater Mach wave radiation from impact pile driving: Theory and observation”. In: *The Journal of the Acoustical Society of America* 130.3, pp. 1209–1216.

Rosales, RR (1999). *Branch points and branch cuts (18.04, MIT)*.

Sánchez, Sergio et al. (2019). “Foundations in offshore wind farms: Evolution, characteristics and range of use. Analysis of main dimensional parameters in monopile foundations”. In: *Journal of Marine Science and Engineering* 7.12, p. 441.

Sarma, GS, K Mallick, and VR Gadhinglajkar (1998). “Nonreflecting boundary condition in finite-element formulation for an elastic wave equation”. In: *Geophysics* 63.3, pp. 1006–1016.

Schecklman, Scott et al. (2015). “A computational method to predict and study underwater noise due to pile driving”. In: *The Journal of the Acoustical Society of America* 138.1, pp. 258–266.

Schmiechen, Philipp (1997). “Travelling wave speed coincidence”. PhD thesis. Imperial College London (University of London) UK.

Soares-Ramos, Emanuel P.P. et al. (2020). “Current status and future trends of offshore wind power in Europe”. In: *Energy* 202, p. 117787. ISSN: 0360-5442. DOI: https://doi.org/10.1016/

j . energy . 2020 . 117787. URL: https : / / www . sciencedirect . com / science / article / pii / S036054422030894X.

Soham, Banerjee and Kumar Abhishek (2016). “Determination of seismic wave attenuation: A Review”. In: *A* 2.1, p. 1.

Southall, Brandon L et al. (2019). “Marine mammal noise exposure criteria: updated scientific recommendations for residual hearing effects”. In: *Aquatic Mammals* 45.2, pp. 125–232.

The Cooper Union (2011). *ECE114 Digital Signal Processing - Lecture Notes: Complex Analysis*. URL: https://engfac.cooper.edu/pages/fred/uploads/complex0.pdf.

Thompson, Paul M et al. (2020). “Balancing risks of injury and disturbance to marine mammals when pile driving at offshore windfarms”. In: *Ecological Solutions and Evidence* 1.2, e12034.

Tsouvalas, Apostolos (2015). “Underwater noise generated by offshore pile driving”. In: *Energies*. DOI: https : / / doi . org / 10 . 4233 / uuid : 55776f60 - bbf4 - 443c - acb6 - be1005559a98. URL: https : //repository.tudelft.nl/record/uuid:55776f60-bbf4-443c-acb6-be1005559a98.

— (2020). “Underwater noise emission due to offshore pile installation: A review”. In: *Energies* 13.12, p. 3037.

— (2025). *Lecture 3.2: Seismo-acoustic wave propagation in the offshore environment (Part I)*. University Lecture.

Tsouvalas, Apostolos and AV Metrikine (2013a). “A semi-analytical model for the prediction of underwater noise from offshore pile driving”. In: *Journal of Sound and Vibration* 332.13, pp. 3232–3257.

— (2013b). “A three-dimensional semi-analytical model for the prediction of underwater noise generated by offshore pile driving”. In: *Fluid-Structure-Sound Interactions and Control: Proceedings of the 2nd Symposium on Fluid-Structure-Sound Interactions and Control*. Springer, pp. 259–264.

Tsouvalas, Apostolos, Yaxi Peng, and Andrei Metrikine (2019). “Underwater noise generated by offshore pile driving: A pile-soil-water vibroacoustic model based on a mode matching method”. In: *Proceedings of the 5th Underwater Acoustics Conference and exhibition*.

Wu, Xiaoni et al. (2019). “Foundations of offshore wind turbines: A review”. In: *Renewable and Sustainable Energy Reviews* 104, pp. 379–393.

Zampolli, Mario et al. (2013). “Validation of finite element computations for the quantitative prediction of underwater noise from impact pile driving”. In: *The Journal of the Acoustical Society of America* 133.1, pp. 72–81.

A

Illustrations of Main Components T-NMS 10000

This appendix provides an overview of the main components of the NMS used during the installation of the wind farm MPs to reduce underwater noise, as mentioned in Section 2.3.

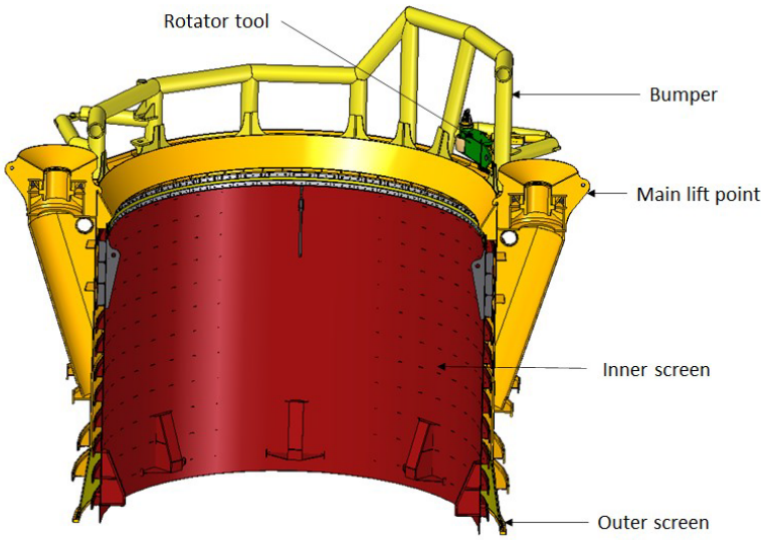

Figure A.1: Illustration of the top section. Its main components are indicated in the illustration.

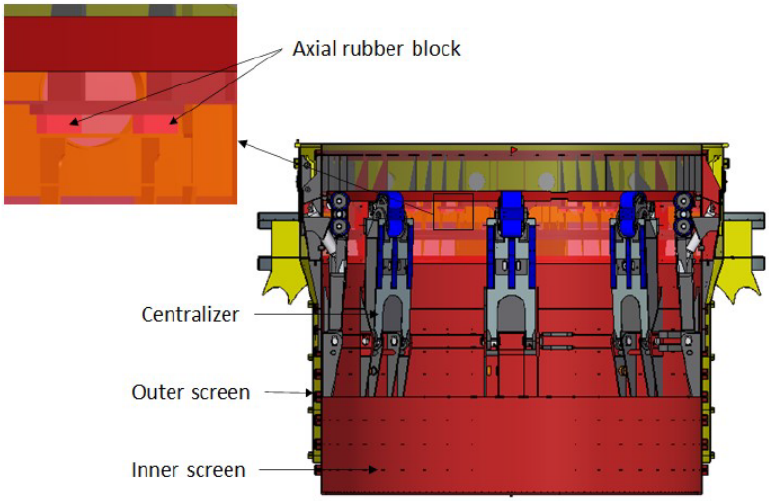

Figure A.2: Illustration of the upper middle section. Its main components are indicated in the illustration. PART 1

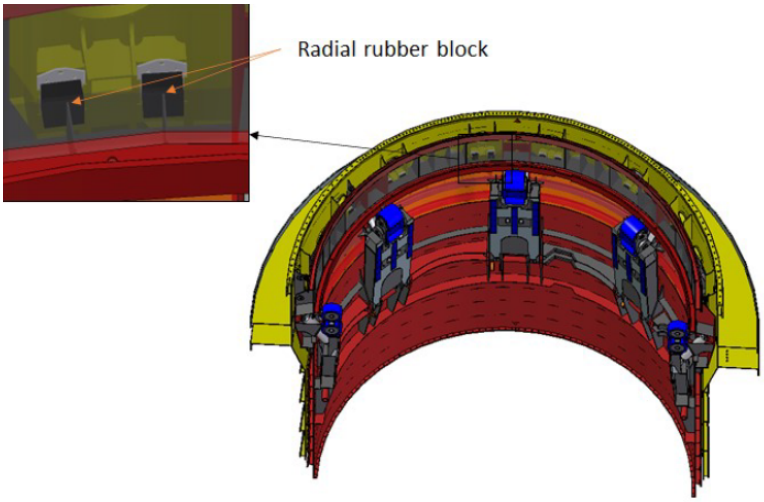

Figure A.3: Illustration of the upper middle section. Its main components are indicated in the illustration. PART 2

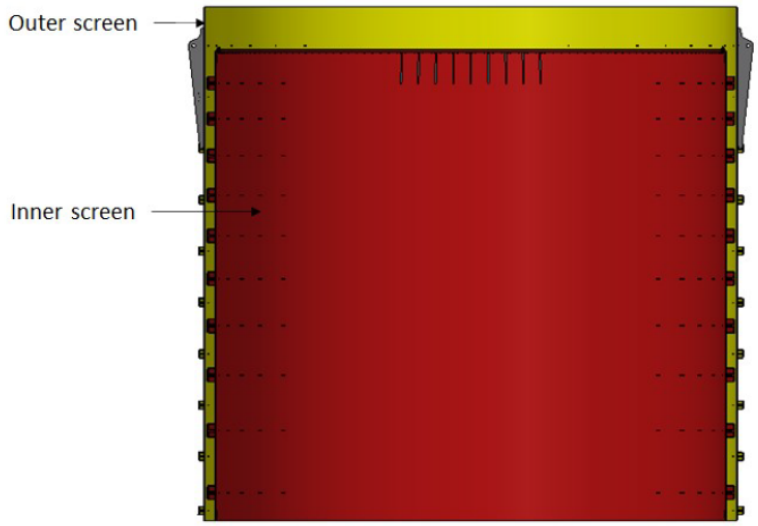

Figure A.4: Illustration of the lower middle section. Its main components are indicated in the illustration.

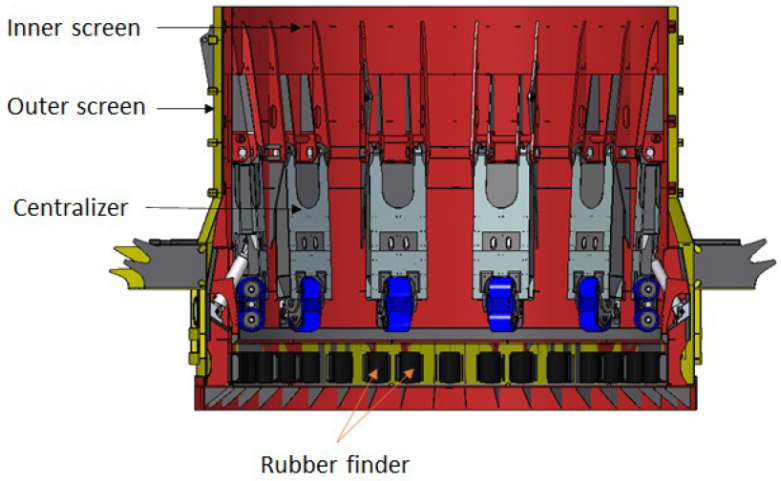

Figure A.5: Illustration of the bottom section. Its main components are indicated in the illustration. PART 1

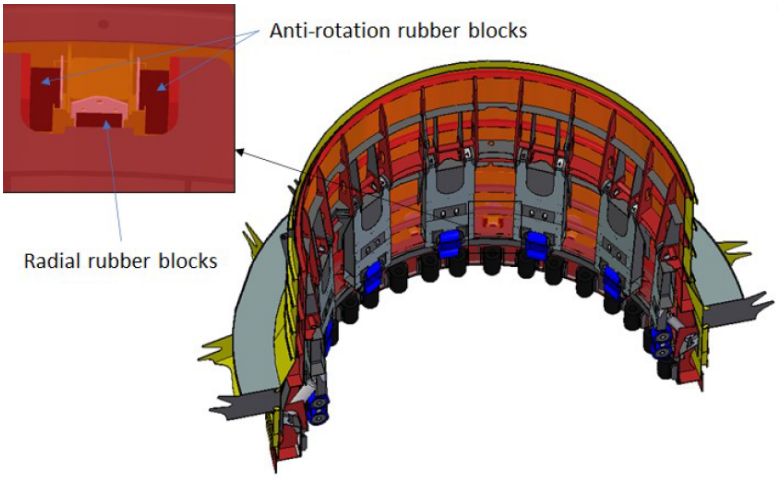

Figure A.6: Illustration of the bottom section. Its main components are indicated in the illustration. PART 2

B

Regulatory Framework for Underwater Noise During Offshore Pile Driving

The noise intensity that is released from the blow of the hammer can easily exceed SPL of 200 dB at 750 m from the pile without noise mitigation system (Bellmann et al., 2020). Such levels pose a significant risk of harm to the marine environment.

In 2002, the European Committee formalized a marine strategy that subsequently led to the Marine Strategy Framework Directive (MSFD). This directive requires European Member States to develop comprehensive strategies for their marine waters (Dekeling et al., 2013). Member States retain the autonomy to develop and adopt their own specific national legislation within the MSFD's overarching boundaries, which has resulted in varying regulatory noise limits across the European Union.

Beyond the MSFD, several regional conventions have been made for the protection of the marine environment (Heerema Marine Contractors, n.d.).

- OSPAR Convention: A coalition of 15 nations working to regulate and protect the North-East Atlantic.
- BIAS: An initiative established in 2012 that mirrors OSPAR's goals specifically for the Baltic Sea region.

These collaborative efforts have prompted several countries to establish specific noise limits for noise generated during pile driving. Germany has been a pioneer in this field, establishing the first requirements and currently serving as the benchmark for underwater noise regulations.

This study focuses specifically on the wind farm project located in the German North Sea. Given the project's location, the German underwater noise regulatory standards governed during the installation of the MPs.

B.1. German Underwater Noise Regulations

The German Umweltbundesamt (UBA, Federal Environmental Agency) and Bundesamt für Seeschiffahrt und Hydrografie (BSH, Federal Maritime and Hydrographic Agency) have defined the following general thresholds for allowable broadband sound levels, at a distance of 750 m from the source (i.e. pile driving location) (Bellmann et al., 2020).:

- $SEL_{5\%}$: max. 160 dB
- $L_{p,pk}$: max. 190 dB

The $SEL_{5\%}$ means that the noise limit must be met by 95% of all individual sound pulses (i.e. hammer blows). In other words, while the majority of the noise must stay below the threshold, a small margin of 5% of the blows is permitted to exceed it. The $SEL_{5\%}$ threshold corresponds to the 95th percentile of the underwater noise distribution.

In addition to the noise level limits, regulations also prescribe a maximum pile-driving duration of 180 minutes per MP. This timeframe includes acoustic deterrence (20-50 minutes depending on the device and BSH requirements), a soft-start phase (typically 10-15 minutes), and the subsequent continuous

pile-driving, with pauses for inclination checks until the final penetration depth is achieved. Furthermore, the BSH imposes project-specific restrictions on the maximum blow energy depending on hammer type and site conditions, as an additional measure to ensure compliance with the required noise mitigation values (Bellmann et al., 2020).

C

Overview of Measurement Dataset

Table C.1 and Table C.2 present an overview of all data related to noise measurements collected during the installation of the MPs for the wind farm.

Path	Type	Shape	dtype	Remarks
calibration_level	Dataset	()	float32	The calibration level of the hydrophone.
comments	Dataset	(0,)	float64	Placeholder for any notes or remarks about the dataset.
coordinates_measurement_position	Dataset	(2,)	float64	Geographic coordinates of the hydrophone position in [Latitude, Longitude] format.
dataset_type	Dataset	()	object	Describes the type of dataset.
dataset_version	Dataset	()	object	Version of the dataset format.
evaluation_type_leq	Dataset	()	object	Calculated over blocks time.
evaluation_type_lpeak	Dataset	()	object	Evaluated per individual pile-driving pulse.
evaluation_type_sel	Dataset	()	object	Evaluated per pile-driving pulse.
frequency_bands_per_octave	Dataset	()	float32	Number of frequency bands per octave.
frequency_count	Dataset	()	int32	Total number of frequency bands in the dataset.
frequency_index	Dataset	(32,)	float64	Array of center frequencies for each band (in Hz).
hydrophone_serial_number	Dataset	()	object	Unique identifier for the hydrophone used in the measurement.
hydrophone_type	Dataset	()	object	Hydrophone model type: Reson TC-4033
leq_averaging_time	Dataset	()	float32	Averaging time (in seconds) used to compute L_{eq}.
leq_count	Dataset	()	int32	Number of L_{eq} values recorded.
leq_datetime_index	Dataset	(8002,)	float64	Timestamps for each L_{eq} measurement.
leq_spectral_stats	Group	–	–	Table C.2 provides an overview of the contents of this group.

(Continued on next page)

(Continued from previous page)

Path	Type	Shape	dtype	Remarks
leq_spectro_temporal_values	Dataset	(Y, 32)	float64	Matrix of L_{eq} values for each time block (rows) and frequency band (columns).
leq_temporal_stats	Group	–	–	Table C.2 provides an overview of the contents of this group.
leq_temporal_values	Dataset	(Y,)	float64	L_{eq} values aggregated across all frequency bands for each time block.
lpeak_count	Dataset	()	int32	Number of L_{peak} measurements recorded.
lpeak_datetime_index	Dataset	(X,)	float64	Timestamps for each L_{peak} measurement.
lpeak_temporal_stats	Group	–	–	Table C.2 provides an overview of the contents of this group.
lpeak_temporal_values	Dataset	(X,)	float64	Array ofL_{peak} values for each recorded pulse.
measurement_height	Dataset	()	float32	Height of the hydrophone above the seabed in meters.
measurement_id	Dataset	()	object	Unique identifier for this measurement session.
measurement_purpose	Dataset	()	object	Purpose of the measurement campaign.
measurement_system_id	Dataset	()	object	Identifier for the measurement system used.
name_foundation	Dataset	()	object	Name of the pile.
name_measurement_position	Dataset	()	object	Identifier for the measurement position.
name_pile	Dataset	()	object	Name of the pile being installed.
name_windfarm	Dataset	()	object	Name of the wind farm.
rawdata_uuid	Dataset	()	object	Unique identifier for the raw dataset file.
sel_count	Dataset	()	int32	Number of SEL measurements recorded.
sel_datetime_index	Dataset	(X,)	float64	Timestamps for each SEL measurement.
sel_spectral_stats	Group	–	–	Table C.2 provides an overview of the contents of this group.
sel_spectro_temporal_values	Dataset	(X, 32)	float64	Matrix of SEL values for each pulse (rows) and frequency band (columns).
sel_temporal_stats	Group	–	–	Table C.2 provides an overview of the contents of this group.
sel_temporal_values	Dataset	(X,)	float64	SEL values aggregated across all frequency bands for each pulse.

(Continued on next page)

(Continued from previous page)

Path	Type	Shape	dtype	Remarks
sound_mitigation_bool	Dataset	()	bool	Indicates whether sound mitigation was applied during measurement.
sound_mitigation_name	Dataset	()	object	Name of the mitigation method.
system_calibration_procedure	Dataset	()	object	Calibration procedure used for the measurement system.

Table C.1: Structure of the dataset obtained for all 64 MPs. Here, X is the number of hammer impacts required to reach final penetration depth, and Y is the number of recorded timestamps. Both values vary per MP installation.

Path	Type	Shape	dtype	Remarks
leq_spectral_stats				
leq_spectral_stats/L01	Dataset	(32,)	float64	The 1st percentile of L_{eq} values for each frequency band
leq_spectral_stats/L05	Dataset	(32,)	float64	The 5th percentile of L_{eq} values for each frequency band
leq_spectral_stats/L50	Dataset	(32,)	float64	The 50th percentile of L_{eq} values for each frequency band
leq_spectral_stats/L90	Dataset	(32,)	float64	The 90th percentile of L_{eq} values for each frequency band
leq_spectral_stats/LMax	Dataset	(32,)	float64	The maximum L_{eq} value observed for each frequency band
leq_spectral_stats/LMin	Dataset	(32,)	float64	The minimum L_{eq} value observed for each frequency band
leq_temporal_stats				
leq_temporal_stats/L01	Dataset	()	float64	The 1st percentile of broadband L_{eq} values over the entire measurement period
leq_temporal_stats/L05	Dataset	()	float64	The 5th percentile of broadband L_{eq} values over the entire measurement period
leq_temporal_stats/L50	Dataset	()	float64	The 50th percentile of broadband L_{eq} values over the entire measurement period
leq_temporal_stats/L90	Dataset	()	float64	The 90th percentile of broadband L_{eq} values over the entire measurement period
leq_temporal_stats/LMax	Dataset	()	float64	The maximum broadband L_{eq} value observed over the entire measurement period
leq_temporal_stats/LMin	Dataset	()	float64	The minimum broadbandL_{eq} value observed over the entire measurement period

(Continued on next page)

(Continued from previous page)

Path	Type	Shape	dtype	Remarks
lpeak_temporal_stats				
lpeak_temporal_stats/L01	Dataset	()	float64	The 1st percentile of broadband L_{peak} values over the entire measurement period
lpeak_temporal_stats/L05	Dataset	()	float64	The 5th percentile of broadband L_{peak} values over the entire measurement period
lpeak_temporal_stats/L50	Dataset	()	float64	The 50th percentile of broadband L_{peak} values over the entire measurement period
lpeak_temporal_stats/L90	Dataset	()	float64	The 90th percentile of broadband L_{peak} values over the entire measurement period
lpeak_temporal_stats/LMax	Dataset	()	float64	The maximum broadband L_{peak} value observed over the entire measurement period
lpeak_temporal_stats/LMin	Dataset	()	float64	The minimum broadband L_{peak} value observed over the entire measurement period
sel_spectral_stats				
sel_spectral_stats/L01	Dataset	(32,)	float64	The 1st percentile of SEL values for each frequency band
sel_spectral_stats/L05	Dataset	(32,)	float64	The 5th percentile of SEL values for each frequency band
sel_spectral_stats/L50	Dataset	(32,)	float64	The 50th percentile of SEL values for each frequency band
sel_spectral_stats/L90	Dataset	(32,)	float64	The 90th percentile of SEL values for each frequency band
sel_spectral_stats/LMax	Dataset	(32,)	float64	The maximum SEL value observed for each frequency band
sel_spectral_stats/LMin	Dataset	(32,)	float64	The minimum SEL value observed for each frequency band
sel_temporal_stats				
sel_temporal_stats/L01	Dataset	()	float64	The 1st percentile of broadband SEL values over the entire measurement period
sel_temporal_stats/L05	Dataset	()	float64	The 5th percentile of broadband SEL values over the entire measurement period
sel_temporal_stats/L50	Dataset	()	float64	The 50th percentile of broadband SEL values over the entire measurement period

(Continued on next page)

(Continued from previous page)

Path	Type	Shape	dtype	Remarks
sel_temporal_stats/L90	Dataset	()	float64	The 90th percentile of broadband SEL values over the entire measurement period
sel_temporal_stats/LMax	Dataset	()	float64	The maximum broadband SEL value observed over the entire measurement period
sel_temporal_stats/LMin	Dataset	()	float64	The minimum broadband SEL value observed over the entire measurement period

Table C.2: Structure of the spectral and temporal statistics groups contained in the dataset.

D

Model Validation Approach

Chapter 4 describes the modeling methodology and the specific setup used in this study. Therefore, the focus of this section is solely on the validation approach, rather than on the modeling scenarios or the model development. The different model cases referred to here are explained in detail in Section 4.1.

To evaluate the noise mitigation effectiveness of the NMS at the wind farm, the numerical representation of the NMS must be validated. As there is currently no existing literature or previous modeling results available for the wind farm project or the NMS, a multi-stage validation approach is used. This involves developing and validating two sub-models sequentially. Each stage must be verified before proceeding to the next. This step-by-step procedure is outlined in Section 4.1.

As outlined in Section 3.5.1, a single blow SEL measurement has an associated standard uncertainty of approximately $\pm 1\,dB$, originating from factors such as hydrophone sensitivity variations and electronic chain variability. This value is treated as the standard deviation of an individual measurement. When averaging SEL values over many blows, the uncertainty of the mean decreases according to the statistical relation

$$\sigma_{mean} = \frac{\sigma_{single}}{\sqrt{N}}$$

which applies to independent measurements (ISO/IEC Guide 98-3, 2008).

For example, considering 50 blows recorded by four hydrophones around the MP at 750 m gives $N = 4 \cdot 50 = 200$ independent SEL values. The corresponding uncertainty of the mean is

$$\sigma_{mean} = \frac{1}{\sqrt{200}} \approx 0.071\,dB$$

which is negligible for model validation purposes.

Although the instrumental uncertainty becomes very small when many blows are averaged, additional physical variances must still be considered. These include, for example, variations in hammer energy (see Section 3.4) and environmental conditions.

In acoustic literature, it is standard practice to validate noise prediction models using broadband SEL and L_{peak} levels (Peng et al., 2021). In this study, each individual model is considered valid if its results deviate by no more than 3 dB from empirical measurements. The following subsections present the measured broadband SEL and L_{peak} values used for validation.

Model 1: Pile E - 24.75 m embedment depth

In this model, the pile embedment depth is 24.75 m. To determine the noise levels for validation, a depth range from 24.50 m to 25.0 m is analyzed. This interval corresponds to hammer blows 2378 through 2441, totaling 63 blows using only PULSE with a liquid height of 300 mm. This sequence spans a duration of 114 s, providing 23 measured L_{eq} values and 63 individual SEL and L_{peak} measurements.

Because the decibel scale is logarithmic, the values cannot be averaged in decibel unit. Instead, each decibel level must first be converted into its corresponding linear energy value using Eq. D.1, where L represents the dB value. These energy values are then averaged, and the resulting mean is converted back into a decibel level using Eq. D.2. From this it follows that for Pile E with embedment depth of 24.75 m, the SEL is calculated as X dB and L_{peak} as Y dB. This is the validation data for Model 1.

$$E = 10^{\frac{L}{10}} \tag{D.1}$$

$$\bar{L} = 10 \log_{10} \left(\frac{1}{n} \sum_{i=1}^{n} E_i\right) \tag{D.2}$$

Model 2: Pile E - 20.50 m embedment depth

In this model, the pile embedment depth is 20.50 m. To determine the noise levels for validation, a depth range from 20.25 m to 20.75 m is analyzed. This interval corresponds to hammer blows 1663 through 1758, totaling 95 blows using only PULSE with a liquid height of 700 mm. This sequence spans a duration of 153 s, providing 30 measured L_{eq} values and 85 individual SEL and L_{peak} measurements. The average of the different hydrophone locations is taken using Eqs. D.1 and D.2. From this it follows that for Pile E with embedment depth of 20.50 m, the SEL is calculated as X dB and L_{peak} as Y dB. This is the validation data for Model 2.

E

Underwater Noise Prediction Models

Underwater acoustics in deep water depths has been extensively studied because of the interest in developing and optimizing sonar technologies for defense applications (Tsouvalas, 2020). In contrast, predicting sound propagation in shallow water regions is more challenging. In such environments, acoustic waves undergo repeated reflections, refractions, and scattering at both the sea surface and seabed. When assessing noise generated by pile driving it gets more complex: the problem involves three coupled domains, the pile, the seawater, and the seabed, whose interaction governs the generation and propagation of underwater sound (Tsouvalas, 2020)

This section provides an overview of the modeling approaches that have been developed to predict underwater noise from impact piling. Following the classification introduced by Tsouvalas (2020), the models are grouped into three categories: first-generation models, second-generation models, and the state-of-the-art approaches. The first two categories are discussed as well as a global description of the model adopted in this study, respectively, in Sections E.1, E.2, and E.3.

E.1. First-Generation Models

Reinhall and Dahl (2011) developed the first numerical model specifically aimed at predicting underwater noise generated by impact pile driving (Tsouvalas, 2020). Their approach couples a FEM model of the pile with a surrounding axisymmetric water-soil domain to characterize the acoustic field close to the pile. To model how the sound propagates at larger distances, the parabolic equation is applied (Reinhall and Dahl, 2011). Their results showed that each hammer strike initiates a compressive stress wave that travels down the pile at a speed exceeding the sound speed in water. This rapid axial wave motion induces a radial expansion of the pile wall, which in turn generates outward radiating pressure waves. Because the pile wave travels faster relative to the surrounding fluid, these pressure waves form the Mach cones at a fixed angle within the water column and seabed.

Following the approach introduced by Reinhall and Dahl (2011), several researchers adopted a similar two-step modeling strategy in which a FEM is used to compute the near-field sound generation, and a separate propagation model is applied to predict the acoustic field at larger distances (Tsouvalas, 2020). Alternative formulations also exist; for example MacGillivray (2014) employed a finite-difference scheme for the near-field, assuming that bending effects of the pile wall can be neglected.

Depending on the required level of detail, various methods have been used for the far-field propagation, including normal mode models, wavenumber integration techniques, energy flux methods, and parabolic-equation formulations Tsouvalas (2020). Some models also combine finite elements for the structural response with boundary element formulations for the surrounding soil, although these typically focus on the vibration field close to the pile.

Alongside these numerical approaches, several semi-analytical models have been proposed. Hall (2015) developed an analytical formulation for a thin cylindrical shell in a fluid, whereas Tsouvalas and AV Metrikine (2013a) introduced semi-analytical model that represents the pile using shell theory, the water as an acoustic fluid, and the soil through distributed springs and dashpot. Their method employs modal expansions and a mode-matching procedure to solve the coupled pile-soil-water problem. The key advantage of semi-analytical approaches is their high computational efficiency, making them suitable when large number of simulations are required, though they cannot capture the same level of detail as FEM models (Tsouvalas, 2020).

E.2. Second-Generation Models

The models discussed in Subsection E.1 marked an important step toward understanding underwater noise generation from impact piling. However, they share a key limitation: the seabed is represented either as an acoustic fluid or through simplified spring-dashpot elements. While such assumptions may be acceptable in many ocean acoustics, they fall short for pile-driving problems for two main reasons: First, a substantial part of the released energy during piling is transmitted into the soil because the pile is partially embedded. Therefore, a realistic representation of the seabed is necessary to accurately predict the energy flux in the surrounding acousto-elastic region. Second, determining the true source amplitude, i.e. the dynamic response of the pile, requires a coupled soil-fluid-pile description. Without capturing this coupling, the source mechanism cannot be identified properly (Tsouvalas, 2020).

To address these shortcomings, Tsouvalas et al. (2014) and Tsouvalas and AV Metrikine (2013b) were among the first to incorporate an elastic seabed into pile-driving acoustics models. Their simulations illustrate the resulting wave-radiation pattern for a typical offshore installation scenario. Besides Mach-cone-type pressure waves in the water column, the response within the soil is dominated by vertically polarised shear waves, generated because the compressional wave in the pile travels down the pile at a velocity far exceeding the shear-wave speed in the seabed. Additional compressional waves also propagate through the soil. Furthermore, interface waves, Scholte waves, emerge along the seabed-water boundary and travel much more slowly than the compressional waves (Tsouvalas, 2020).

E.3. Modeling Framework Used in This Study

This study adopts a modeling strategy inspired by the SILENCE framework developed by Tsouvalas, Peng, and Andrei Metrikine (2019). In its original formulation, SILENCE is a semi-analytical model that separates the problem into two components: a near field (sound generation) module, which resolves the coupled pile-soil-water interaction in the vicinity of the pile, and a far field (sound propagation) module, which predicts the propagation at larger distances. These two modules are linked through a boundary integral representation at a cylindrical interface. The model employs high-order shell theory for the MP, represents the seabed as a three-dimensional elastic continuum, and solves the full coupled system in the frequency domain. Subsequent improvements by Peng et al. (2021) enhanced computational efficiency and accuracy through a direct boundary integral formulation and a more detailed representation of the ring source in the soil.

The modeling approach used in this study builds on the SILENCE framework but introduces a modification. Instead of employing the semi-analytical mode-matching procedure for the near-field, the near-field region is modeled using a FEM formulation implemented in COMSOL Multiphysics. The resulting field data on the coupling boundary are extracted and supplied to the SILENCE far-field module, where the boundary integral method is used to propagate the sound to larger distances.

F

Sound Generation Module - Finite Element Method

This appendix describes the SGM, which is implemented using FEM and constructed in the software COMSOL Multiphysics. The appendix provides an overview of the FEM formulation, beginning with the governing equations in Section F.1. This is followed by the definition of interface and boundary conditions in Section F.2, the weak form formulation in Section F.3, domain discretization in Section F.4, and the definition of shape functions in Section F.5. Subsequently, the elemental weak form formulation is presented in Section F.6, and finally, the assembly of the global system matrix is described in Section F.7.

The system is modeled in a cylindrical coordinate system (r, θ, z) using a 2D axisymmetric formulation. This assumption implies that the loading and the geometry are symmetric about the central vertical axis, reducing the problem to the radial (r) and axial (z) coordinates. The domain is divided into four primary regions:

- **The pile:** A linear elastic thin shell of length L, top radius r_1 and bottom radius r_2, and thickness h.
- **Water column:** An inviscid compressible fluid domain ranging from z_0 to z_2.
- **Soil Layer 1:** A linear elastic medium extending from z_2 to z_3.
- **Soil Layer 2:** A linear elastic medium extending from z_3 to z_{bot}.

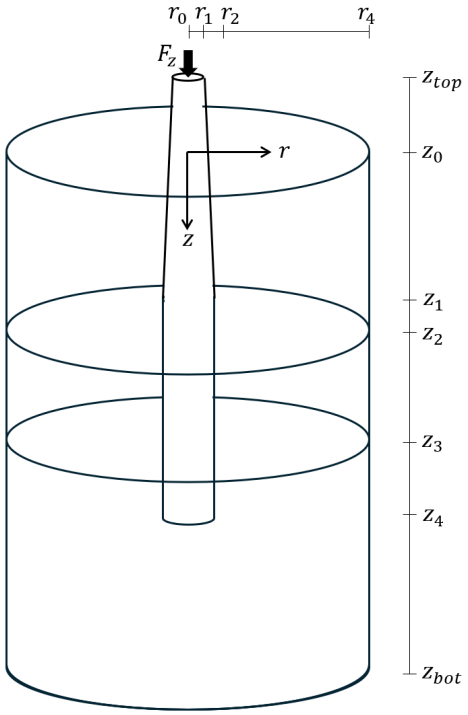

Figure F.1: Schematic representation of the SGM geometry. The computational domain consists of three layers: the water column ($z_0 \leq z \leq z_2$) and two underlying soil layers ($z_2 \leq z \leq z_3$ and $z_3 \leq z \leq z_{bot}$). The MP is defined by its length L, top radius r_1, and bottom radius r_2, is positioned centrally within the domain. The excitation is modeled as unit force F_z, applied to the pile head. At z_2, the linearly increasing radius of the MP stops and from that point goes straight down. The location z_4 represents the location of the pile tip.

F.1. Governing Equations: Strong Form

The following subsections introduce the governing equations for the coupled vibroacoustic system. While the literature Peng et al. (2021) and Tsouvalas et al. (2014) often utilizes Helmholtz decomposition to transform the equations of motion into uncoupled potential wave equations, this study utilizes the primary physical degrees of freedom. This approach aligns with the numerical implementation in COMSOL Multiphysics, where the primary degrees of freedom, acoustic pressure (p) in the fluid and displacements (u_r, u_z) in the solid, are solved directly using FEM.

Structural Dynamics of the Pile

The frequenc domain form of the governing equation for the pile was already introduced in Section 4.2. For convenience, it is repeated here:

$$-\omega^2 \rho_p h \tilde{\mathbf{u}} - \nabla \cdot \tilde{\boldsymbol{\sigma}}_p = \tilde{\mathbf{f}}_{ext} \tag{F.1}$$

Fluid Domain

The equation of motion of the water domain satisfies the Helmholtz equation mention in Section 4.2. For convenience, it is repeated here:

$$\nabla^2 \tilde{p}_f + k^2 \tilde{p}_f = 0 \tag{F.2}$$

Soil Domain

The equation of motion in the frequency domain of the soil is presented in Section 4.2. For convenience, it is repeated here:

$$\mu_j \nabla^2 \tilde{\mathbf{u}}_j + (\lambda_j + \mu_j) \nabla(\nabla \cdot \tilde{\mathbf{u}}_j) + \rho_j \omega^2 \tilde{\mathbf{u}}_j = \mathbf{0} \tag{F.3}$$

F.2. Interface & Boundary Conditions

To couple the various domains of the model, interface conditions are imposed at the boundaries between adjacent domains. The following interface conditions are implemented in both the time and

frequency domains.

- **Sea Surface ($z = z_0$):**
  The sea surface is modeled as a pressure-release boundary:

$$p_f(r, z_0, t) = 0; \qquad \tilde{p}_f(r, z_0, \omega) = 0 \tag{F.4}$$

- **Seabed ($z = z_1$):**
  At the fluid-soil interface, the model enforces vertical displacement continuity and vertical stress equilibrium. Since water is modeled as a perfect (inviscid) fluid, it cannot support tangential stress, meaning the shear stress at the seabed must vanish:
  - Vertical Displacement Continuity:

$$u_{z,f}(r, z_1, t) = w_{s_1}(r, z_1, t); \qquad \tilde{u}_{z,f}(r, z_1, \omega) = \tilde{w}_{s_1}(r, z_1, \omega) \tag{F.5}$$

  - Vertical Stress Balance:

$$\sigma_{zz,s1}(r, z_1, t) + p_f(r, z_1, t) = 0; \qquad \tilde{\sigma}_{zz,s_1}(r, z_1, \omega) + \tilde{p}_f(r, z_1, \omega) = 0 \tag{F.6}$$

  - Vanishing Shear Stress:

$$\sigma_{zr,s_1}(r, z_1, t) = 0; \qquad \tilde{\sigma}_{zr,s_1}(r, z_1, \omega) = 0 \tag{F.7}$$

- **Soil-Soil Interface ($z = z_2$):** At the boundary between the two soil layers, both stress equilibrium and displacement continuity are required to ensure the layers act as a single continuum:
  - Displacement Continuity:

$$u_{s_1}(r, z_2, t) = u_{s_2}(r, z_2, t); \qquad \tilde{u}_{s_1}(r, z_2, \omega) = \tilde{u}_{s_2}(r, z_2, \omega) \tag{F.8}$$

$$w_{s_1}(r, z_2, t) = w_{s_2}(r, z_2, t); \quad \tilde{w}_{s_1}(r, z_2, \omega) = \tilde{w}_{s_2}(r, z_2, \omega) \tag{F.9}$$

  - Stress Equilibrium:

$$\sigma_{zr,s_1}(r, z_2, t) = \sigma_{zr,s_2}(r, z_2, t); \quad \tilde{\sigma}_{zr,s_1}(r, z_2, \omega) = \tilde{\sigma}_{zr,s_2}(r, z_2, \omega) \tag{F.10}$$

$$\sigma_{zz,s_1}(r, z_2, t) = \sigma_{zz,s_2}(r, z_2, t); \quad \tilde{\sigma}_{zz,s_1}(r, z_2, \omega) = \tilde{\sigma}_{zz,s_2}(r, z_2, \omega) \tag{F.11}$$

- **Pile-Fluid Interface ($r = R$):**
  For the segment of the pile in contact with the water ($z_0 \leq z \leq z_1$), the radial displacement of the shell must match the radial displacement of the fluid:

$$u_r(z, t) = u_f(R, z, t); \qquad \tilde{u}_r(z, \omega) = \tilde{u}_f(R, z, \omega); \qquad z_0 \leq z \leq z_1 \tag{F.12}$$

- **Pile-Soil Interface ($r = R$):**
  For the segment of the pile embedded in the soil ($z_1 \leq z \leq L$), a perfectly bonded contact is assumed. This requires both the radial and vertical displacements of the pile to match those of the surrounding soil layers $j = 1, 2$:
  - Radial Displacement Continuity:

$$u_r(z, t) = u_j(R, z, t); \qquad \tilde{u}_r(z, \omega) = \tilde{u}_j(R, z, \omega); \qquad z_1 \leq z \leq L, \quad j = 1, 2 \tag{F.13}$$

  - Vertical Displacement Continuity:

$$u_z(z, t) = w_j(R, z, t); \qquad \tilde{u}_z(z, \omega) = \tilde{w}_j(R, z, \omega) \qquad z_1 \leq z \leq L, \quad j = 1, 2 \tag{F.14}$$

In the numerical model, the fluid and soil domains must be truncated to a finite size. To prevent artificial reflections from the external boundaries, which would lead to incorrect interference patterns, radiation conditions are applied to simulate an infinite medium.

- **Axisymmetric Boundary Condition:**
  The left boundary at $r = 0$ corresponds to the axis of symmetry. For a 2D axisymmetric model, the physical requirement that the solution remains symmetric about the axis is enforced by:

$$\left.\frac{\partial \tilde{p}}{\partial r}\right|_{r=0} = 0, \qquad \tilde{u}_r(r=0) = 0,$$

  meaning:
  - no radial displacement is allowed at the axis in the soil,
  - the acoustic field has zero radial gradient at the axis.

  This ensures that the model satisfies the geometric symmetry of the pile driving problem.
- **Cylindrical Wave Radiation (Fluid Domain):**
  For the outer radial boundary of the water column ($r \to \infty$), a Cylindrical Wave Radiation condition is applied. COMSOL uses a complex expression, for convience its simplified form is presented here. Its simplified form in the frequency domain, is expressed as:

$$-\mathbf{n} \cdot \left(-\frac{1}{\rho_f}\nabla \tilde{p}\right) + \left(\frac{ik + \frac{1}{2r}}{\rho_f}\right)\tilde{p} = 0 \tag{F.15}$$

  where $k = \omega/c_f$ is the wavenumber. The term $1/(2r)$ accounts for the geometric spreading of the cylindrical wave as it travels away from the axis of symmetry, ensuring that the pressure amplitude decays at a rate of $1/\sqrt{r}$.
- **Non-Reflecting Boundary (Solid Domain):**
  For the external boundaries of the soil layers, a Non-reflecting Boundary condition is utilized. Its simplified form is expressed as:

$$\tilde{\boldsymbol{\sigma}} \cdot \mathbf{n} = -i\omega\left(\rho_s c_P(\tilde{\mathbf{u}} \cdot \mathbf{n})\mathbf{n} + \rho_s c_S(\tilde{\mathbf{u}} \cdot \mathbf{t})\mathbf{t}\right) \tag{F.16}$$

  where:
  - $c_p = \sqrt{(\lambda_s + 2\mu_s)/\rho_s}$ is the longitudinal wave velocity.
  - $c_s = \sqrt{\mu_s/\rho_s}$ is the shear wave velocity.
  - $\mathbf{n}$ and $\mathbf{t}$ are the unit normal and tangential vectors to the boundary, respectively.

  By matching the acoustic impedance of the soil, this condition effectively absorbs the elastic energy radiating from the pile-soil interaction.

F.3. Governing Equations: Weak Form

To go from the strong form to the weak form, the Method of Weighted Residuals (specifically the Galerkin method) is used (IIIInois, 2016). This involves three main steps:

1. Multiplying the strong form of the governing equation by a test function (denoted as $\hat{p}$ or $\hat{u}$).
2. Integrating the equation over the entire domain.
3. Applying integration by parts (Green's Theorem) to reduce the derivative order and produces a place to include the the boundary conditions.

The process of going from the strong form to the weak form is explained below for first the shell, then the fluid domain, and lastly the solid domain.

Shell

1. Multiply by Test Function and Integrate
   The strong form (Eq. F.1) is multiplied by a test function $\hat{\boldsymbol{u}}$ and integrated over the shell domain Ω_s. This results in:

$$\int_{\Omega_s} \hat{\mathbf{u}} \cdot (-\omega^2 \rho_p \tilde{\mathbf{u}})\, d\Omega - \int_{\Omega_s} \hat{\mathbf{u}} \cdot (\nabla \cdot \tilde{\boldsymbol{\sigma}}_p)\, d\Omega = \int_{\Omega_s} \hat{\mathbf{u}} \cdot \tilde{\mathbf{f}}_{ext}\, d\Omega \tag{F.17}$$

2. Application of the Product Rule Identity:
   To reduce the derivative order of the stress term and facilitate boundary coupling, the divergence term $\hat{\mathbf{u}} \cdot (\nabla \cdot \tilde{\boldsymbol{\sigma}}_p)$ is expanded. The transformation of this term is performed using the product rule for the divergence of a second-order tensor $\boldsymbol{\sigma}$ and a vector (Agelet de Saracibar, 2000):

$$\nabla \cdot (\tilde{\boldsymbol{\sigma}}_p \cdot \hat{\mathbf{u}}) = \hat{\mathbf{u}} \cdot (\nabla \cdot \tilde{\boldsymbol{\sigma}}_p) + \tilde{\boldsymbol{\sigma}}_p : \nabla \hat{\mathbf{u}} \tag{F.18}$$

   Rearranging gives:

$$\hat{\mathbf{u}} \cdot (\nabla \cdot \tilde{\boldsymbol{\sigma}}_p) = \nabla \cdot (\tilde{\boldsymbol{\sigma}}_p \cdot \hat{\mathbf{u}}) - \tilde{\boldsymbol{\sigma}}_p : \nabla \hat{\mathbf{u}} \tag{F.19}$$

   Here, $\nabla \hat{\mathbf{u}}$ is the displacement gradient tensor, which contains both strain and rotation (Bonet and Wood, 1997).

$$\nabla \hat{\mathbf{u}} = \underbrace{\frac{1}{2}\left[\nabla \hat{\mathbf{u}} + (\nabla \hat{\mathbf{u}})^T\right]}_{\delta\tilde{\boldsymbol{\epsilon}} \text{ (Strain)}} + \underbrace{\frac{1}{2}\left[\nabla \hat{\mathbf{u}} - (\nabla \hat{\mathbf{u}})^T\right]}_{\boldsymbol{\Omega} \text{ (Rotation)}}$$

   When performing the double-dot product with the stress tensor $\tilde{\boldsymbol{\sigma}}_p$:

$$\tilde{\boldsymbol{\sigma}}_p : \nabla \hat{\mathbf{u}} = \tilde{\boldsymbol{\sigma}}_p : \delta\tilde{\boldsymbol{\epsilon}} + \tilde{\boldsymbol{\sigma}}_p : \boldsymbol{\Omega}$$

   The Cauchy stress tensor $\tilde{\boldsymbol{\sigma}}_p$ is symmetric ($\sigma_{ij} = \sigma_{ji}$) because of the balance of angular momentum. The rotation tensor $\boldsymbol{\Omega}$ is skew-symmetric ($\Omega_{ij} = -\Omega_{ji}$) (Bonet and Wood, 1997). The double-dot product of a symmetric tensor and a skew-symmetric tensor is always zero:

$$\tilde{\boldsymbol{\sigma}}_p : \boldsymbol{\Omega} = 0$$

   Therefore, the only part that remains is the strain energy term: $\tilde{\boldsymbol{\sigma}}_p : \delta\tilde{\boldsymbol{\epsilon}}$.

3. Integration by Parts (Principle of Virtual Work)
   Substituting the above into the volume integral expands the stress term:

$$\int_{\Omega_s} \hat{\mathbf{u}} \cdot (\nabla \cdot \tilde{\boldsymbol{\sigma}}_p)\, d\Omega = \int_{\Omega_s} \nabla \cdot (\tilde{\boldsymbol{\sigma}}_p \cdot \hat{\mathbf{u}})\, d\Omega - \int_{\Omega_s} \tilde{\boldsymbol{\sigma}}_p : \nabla \hat{\mathbf{u}}\, d\Omega \tag{F.20}$$

   The volume integral of the divergence of the stress-displacement product is converted into a surface integral using the Divergence Theorem (also known as Gauss's Theorem) (Bonet and Wood, 1997). This theorem relates the flux of a tensor field within the volume Ω_s to its values on the enclosing boundary surface $\partial\Omega_s$:

$$\int_{\Omega_s} \nabla \cdot (\tilde{\boldsymbol{\sigma}}_p \cdot \hat{\mathbf{u}})\, d\Omega = \int_{\partial\Omega_s} \hat{\mathbf{u}} \cdot (\tilde{\boldsymbol{\sigma}}_p \cdot \mathbf{n})\, d\Gamma \tag{F.21}$$

   In this expression, $\mathbf{n}$ is the outward-pointing unit normal vector to the boundary surface $d\Gamma$. The term $(\tilde{\boldsymbol{\sigma}}_p \cdot \mathbf{n})$ is defined as the surface traction vector, representing the external forces per unit area acting on the pile. By applying this theorem, the internal stress state of the pile is coupled to the pressures from the surrounding fluid and soil domains. This step allows for the natural imposition of boundary conditions within the integral formulation.

4. Final Weak Form for the Shell in Frequency Domain
   Combining all terms, the weak form reads:

$$-\omega^2 \int_{\Omega_s} \rho_p \tilde{\mathbf{u}} \cdot \hat{\mathbf{u}}\, d\Omega + \int_{\Omega_s} \tilde{\boldsymbol{\sigma}}_p : \nabla \hat{\mathbf{u}}\, d\Omega = \int_{\Omega_s} \hat{\mathbf{u}} \cdot \tilde{\mathbf{f}}_{ext}\, d\Omega + \int_{\partial\Omega_s} \hat{\mathbf{u}} \cdot (\tilde{\boldsymbol{\sigma}}_p \cdot \mathbf{n})\, d\Gamma \tag{F.22}$$

This weak formulation is the basis for the finite element discretizations, where $\hat{\mathbf{u}}$ and $\tilde{\mathbf{u}}$ are replaced by the element shape functions (see Section F.5). COMSOL performs these weak form transformations automatically in the Structural Mechanics interface.

Fluid Domain

1. Multiply by Test Function and Integrate
   The strong form Helmholtz equation (Eq. F.2) is multiplied by a test function $\hat{p}$ and integrated over the fluid volume V. This results in:

$$\int_{V_f} \hat{p} \left(\nabla^2 \tilde{p} + k^2 \tilde{p}\right) dV = 0 \tag{F.23}$$

2. Integration by Parts (Green's First Identity)
   To reduce the second-order spatial derivatives to first-order, the divergence theorem is applied to the Laplacian term. This mathematical operation shifts one derivative from the pressure field $\tilde{p}$ onto the test function $\hat{p}$ (Oklahoma State University, n.d.):

$$\int_{V_f} \hat{p} \nabla^2 \tilde{p} \, dV = \int_{\partial V} \hat{p} (\nabla \tilde{p} \cdot \boldsymbol{n}) \, dS - \int_{V_f} (\nabla \hat{p} \cdot \nabla \tilde{p}) \, dV \tag{F.24}$$

3. Final Weak Form for Pressure Acoustics:
   By substituting the identity into the integral statement and rearranging the terms, the final weak form solved by the COMSOL Multiphysics is obtained:

$$\int_{V_f} \left(\nabla \hat{p} \cdot \nabla \tilde{p} - k^2 \hat{p} \tilde{p}\right) dV = \int_{\partial V} \hat{p} (\nabla \tilde{p} \cdot \mathbf{n}) \, dS \tag{F.25}$$

Solid Domain

The derivation for the elastic soil domain follows a vector-based approach. The primary goal is to transform the differential equations of motion into an energy-based integral form.

1. Multiply by Test Function and Integrate
   The process begins by multiplying the frequency-domain Navier-Cauchy equation (Eq. F.3) by a vector test function, $\delta\tilde{\mathbf{u}}$, which represents a virtual displacement field. The equation is then integrated over the entire soil volume V_s:

$$\int_{V_s} \delta\tilde{\mathbf{u}} \cdot \left(\nabla \cdot \tilde{\boldsymbol{\sigma}}_j + \rho_j \omega^2 \tilde{\mathbf{u}}_j\right) dV = 0 \tag{F.26}$$

   This integral statement requires that the total virtual work done by the internal stress gradient and inertial forces vanishes for any arbitrary virtual displacement.

2. Application of the Product Rule Identity:
   To facilitate the coupling of boundaries and reduce the derivative order of the stress term, the divergence of the stress tensor $\delta\tilde{\mathbf{u}} \cdot (\nabla \cdot \tilde{\boldsymbol{\sigma}}_j)$ is expanded, the following product rule from vector calculus is utilized (Bonet and Wood, 1997):

$$\nabla \cdot (\tilde{\boldsymbol{\sigma}}_j \cdot \delta\tilde{\mathbf{u}}) = \delta\tilde{\mathbf{u}} \cdot (\nabla \cdot \tilde{\boldsymbol{\sigma}}_j) + \tilde{\boldsymbol{\sigma}}_j : \nabla(\delta\tilde{\mathbf{u}}) \tag{F.27}$$

   Rearranging this identity allows the strong-form stress term to be isolated:

$$\delta\tilde{\mathbf{u}} \cdot (\nabla \cdot \tilde{\boldsymbol{\sigma}}_j) = \nabla \cdot (\tilde{\boldsymbol{\sigma}}_j \cdot \delta\tilde{\mathbf{u}}) - \tilde{\boldsymbol{\sigma}}_j : \nabla(\delta\tilde{\mathbf{u}}) = \nabla \cdot (\tilde{\boldsymbol{\sigma}}_j \cdot \delta\tilde{\mathbf{u}}) - \tilde{\boldsymbol{\sigma}}_j : \delta\tilde{\boldsymbol{\epsilon}} \tag{F.28}$$

   In this expression, $\nabla(\delta\tilde{\boldsymbol{u}})$ is the displacement gradient tensor, which contains both strain and rotation, while $\delta\tilde{\boldsymbol{\epsilon}}$ is the strain tensor, which is only the symmetric part: $\delta\tilde{\boldsymbol{\epsilon}} = \frac{1}{2}[\nabla(\delta\tilde{\mathbf{u}}) + \nabla(\delta\tilde{\mathbf{u}})^T]$. Because the Cauchy stress tensor $\tilde{\boldsymbol{\sigma}}_j$ is symmetric, when performing the double-dot product with the gradient, the rotation part cancels out to zero (Bonet and Wood, 1997). Which means:

$$\tilde{\boldsymbol{\sigma}} : \nabla(\delta\tilde{\boldsymbol{u}}_j) = \tilde{\boldsymbol{\sigma}} : \delta\tilde{\boldsymbol{\epsilon}}$$

3. Integration by Parts (Principle of Virtual Work)
   By substituting Eq. F.28 into its volume integral, the stress term is expanded into two separate parts:

$$\int_{V_s} \delta\tilde{\mathbf{u}} \cdot (\nabla \cdot \tilde{\boldsymbol{\sigma}}_j) \, dV = \int_{V_s} \nabla \cdot (\tilde{\boldsymbol{\sigma}}_j \cdot \delta\tilde{\mathbf{u}}) \, dV - \int_{V_s} \tilde{\boldsymbol{\sigma}}_j : \delta\tilde{\boldsymbol{\epsilon}} \, dV \tag{F.29}$$

The Divergence Theorem is then applied to the first integral on the right-hand side to convert the volume integral of a divergence into a surface integral over the boundary ∂V_s:

$$\int_{V_s} \nabla \cdot (\tilde{\boldsymbol{\sigma}}_j \cdot \delta\tilde{\mathbf{u}})\, dV = \int_{\partial V_s} \delta\tilde{\mathbf{u}} \cdot (\tilde{\boldsymbol{\sigma}}_j \cdot \mathbf{n})\, dS \tag{F.30}$$

4. Final Weak Form for Solid Mechanics:
Combining Eqs. F.26, Eq. F.29 and Eq. F.30 results in the final weak form solved by COMSOL:

$$\underbrace{\int_{V_s} \tilde{\boldsymbol{\sigma}} s : \delta\tilde{\boldsymbol{\epsilon}}\, dV}_{\text{Internal Virtual Work}} - \underbrace{\int_{V_s} \rho_s \omega^2 \tilde{\mathbf{u}} s \cdot \delta\tilde{\mathbf{u}}\, dV}_{\text{Virtual Inertial Work}} = \underbrace{\int_{\partial V_s} \tilde{\mathbf{t}} \cdot \delta\tilde{\mathbf{u}}\, dS}_{\text{External Virtual Work}} \tag{F.31}$$

This energy-based formulation ensures that the internal strain energy and inertial work are balanced by the work performed by external tractions at the pile-soil and soil-water interfaces.

F.4. Domain Discretization and Meshing Strategy

While the weak form provides the governing energy balance, the displacement field $\tilde{\mathbf{u}}$ and pressure field $\tilde{p}$ are still continuous functions. To solve these numerically, the domains are divided into elements, and the unknown fields are approximated using shape functions, denoted as N_i. These are explained in Section F.5.

The accuracy of FEM for wave propagation is linked to the resolution of the mesh relative to the wavelength of the wave field. This is further explained in Appendix I.

F.5. Definition of Shape Functions

To convert the continuous weak form into a discrete algebraic system suitable for numerical solution, the computational domains are partitioned into a finite number of elements. Within each element, the unknown field variables are approximated using shape functions that provide a local interpolation of the solution

The continuous variables, e.g. the acoustic pressure $\tilde{p}$ in the fluid and the displacement vector $\tilde{\mathbf{u}}$ in the solid, are calculated only at discrete nodal points of the mesh. The field within an element is interpolated as a weighted sum of these nodal values:

- Trial Functions (The Solution): For an element with n nodes, the displacement and pressure fields are approximated as:

$$\tilde{\mathbf{u}}(r,z) \approx \sum_{j=1}^{n} N_j(r,z)\tilde{\mathbf{u}}_j = \mathbf{N}\mathbf{u}_e \tag{F.32}$$

$$\tilde{p}(r,z) \approx \sum_{j=1}^{n} N_j(r,z)\tilde{p}_j = \mathbf{N}\mathbf{p}_e \tag{F.33}$$

where $\mathbf{N}$ is the row vector of shape functions $[N_1, N_2, \ldots, N_n]$ and $\tilde{\mathbf{u}}_j, \tilde{p}_j$ are the nodal degrees of freedom.

- Test Functions: the test functions ($\delta\tilde{\mathbf{u}}$ and $\hat{p}$) are chosen from the same space as the trial functions. Meaning that the weak form is "tested'' against each shape function individually. This produces one algebraic equation per nodal degree of freedom.

$$\delta\tilde{\mathbf{u}} = N_i, \quad \hat{p} = N_i \quad (i = 1, \ldots, n) \tag{F.34}$$

Testing the weak form with each shape function produces one algebraic equation per node. Solving the resulting global system yields the nodal values for displacement and pressure. The shape functions then use these nodal values to reconstruct the approximate fields inside each element.

The shape functions are constructed such that they equal 1 at their own node and 0 at all other nodes. This ensures that the interpolation reproduces the exact nodal values and smoothly transitions between them across the element.

F.6. Elemental Weak Form and Matrix Formulation

After introducing the shape functions and their role in approximating the displacement and pressure fields, the next step is to substitute these interpolated fields into the weak forms of the governing equations. This procedure converts the continuous variational problem into a system of algebraic equations defined at the element level.

The finite element interpolations for displacement and pressure are given by $\tilde{\mathbf{u}}(r,z) \approx \mathbf{N}(r,z)\mathbf{u}_e$ and $\tilde{p}(r,z) \approx \mathbf{N}(r,z)\mathbf{p}_e$, as shown in Eqs. F.32-F.33. Their spatial derivatives follow directly from the analytical derivatives of the shape functions. For example,

$$\frac{\partial \tilde{\mathbf{u}}}{\partial r} = \sum_{j=1}^{n} \frac{\partial N_j}{\partial r}\, \tilde{\mathbf{u}}_j, \qquad \frac{\partial \tilde{\mathbf{u}}}{\partial z} = \sum_{j=1}^{n} \frac{\partial N_j}{\partial z}\, \tilde{\mathbf{u}}_j,$$

where the derivatives of the shape functions are known explicitly for each element type.

Substituting the trial and test functions into the weak forms of the governing equations yields a set of element level integrals. These integrals contain combinations of shape functions, their spatial derivatives, and the material parameters of each domain. Evaluating these integrals over the element domain produces the elemental matrices. For the coupled soil–pile–fluid problem, the following element matrices arise:

- The soil stiffness matrix $\boldsymbol{K}_e^s$ which captures the elastic response of the soil. It arises from the strain–stress relationship in the solid domain and contains contributions from the Lamé parameters and the gradients of the shape functions.
- The soil mass matrix $\boldsymbol{M}_e^s$, representing the inertial properties of the soil. It contains integrals of the shape functions multiplied by the soil density and contributes to the dynamic part of the frequency domain equation of the soil.
- The pile stiffness matrix $\boldsymbol{K}_e^p$, which describes the elastic deformation of the MP. Similar to the soil stiffness matrix, it is obtained from the elastic constitutive law of the pile material and depends on the pile's Young's modulus and Poisson ratio.
- The pile mass matrix $\boldsymbol{M}_e^p$ accounts for the inertia of the pile. It is obtained by integrating the shape functions weighted by the pile material density.
- The acoustic stiffness matrix $\boldsymbol{K}_e^w$ arises from the spatial part of the Helmholtz equation. It contains derivatives of the acoustic shape functions and incorporates the compressibility of the fluid.
- The acoustic mass matrix $\boldsymbol{M}_e^w$ corresponds to the temporal component of the Helmholtz equation. It contains the shape functions weighted by the fluid density and governs the inertia of the acoustic field.
- The coupling matrices $\boldsymbol{C}_e^{p-s}$, $\boldsymbol{C}_e^{p-w}$ and $\boldsymbol{C}_e^{w-s}$, which enforce continuity between the domains, such as displacements and traction continuity at the pile-soil interface,. They link the degrees of freedom of adjacent domains within the same elements.

Once these matrices are computed, the element level equilibrium can be expressed in a compact system of algebraic equations relating the element matrices to the element degrees of freedom. At this stage, each element is treated independently. The global finite element system emerges only after assembling all element matrices according to the global node numbering, as discussed in the next section.

F.7. Assembly of Global Matrix

Once the element-level matrices have been obtained for all domains, the next step in FEM is the assembly of these contributions into a single global system of equations. During assembly, each element matrix is mapped onto the global matrix using the global node numbering. Since elements share nodes, the contributions from all neighboring elements accumulate at those shared degrees of freedom, ensuring continuity of the finite element solution across element boundaries.

For this study, the global vector of unknowns is composed of the nodal soil displacement $\boldsymbol{u}^s$, the nodal pile displacement $\boldsymbol{u}^p$ and the nodal acoustic pressure $\boldsymbol{p}^w$. The assembled system then takes the

following form:

$$\begin{bmatrix} \boldsymbol{K}^s - \omega^2 \boldsymbol{M}^s & \boldsymbol{C}^{s-p} & \boldsymbol{C}^{s-w} \\ \boldsymbol{C}^{p-s} & \boldsymbol{K}^p - \omega^2 \boldsymbol{M}^p & \boldsymbol{C}^{p-w} \\ \boldsymbol{C}^{w-s} & \boldsymbol{C}^{w-p} & \boldsymbol{K}^w - \omega^2 \boldsymbol{M}^w \end{bmatrix} \begin{bmatrix} \boldsymbol{u}^s \\ \boldsymbol{u}^p \\ \boldsymbol{p}^w \end{bmatrix} = \begin{bmatrix} \mathbf{0} \\ \boldsymbol{f_{hammer}} \\ \mathbf{0} \end{bmatrix} \tag{F.35}$$

Here:

- $\boldsymbol{K}^s$ and $\boldsymbol{K}^p$ are the global elastic stiffness matrices of the soil and pile domains
- $\boldsymbol{K}^w$ is the global acoustic stiffness matrix of the water domain
- $\boldsymbol{M}^s$, $\boldsymbol{M}^p$, and $\boldsymbol{M}^w$ are the corresponding mass matrices
- The coupling matrices $\boldsymbol{C}^{s-p}$, $\boldsymbol{C}^{p-w}$, and $\boldsymbol{C}^{s-w}$ enforce the interface conditions.
- The vector f_{hammer} applies the external excitation to the pile head

These coupling terms arise only on the boundaries where two domains physically meet and ensure consistent transfer of energy between the soil, the pile, and the water. After assembly, the global system is solved for the nodal degrees of freedom using the linear solver MUMPS.

In summary, the finite element formulation provides a framework for solving the coupled soil-pile-fluid domain in the near field. Starting from the strong forms of the governing equations, the fields were rewritten into their weak formulations, discretized using shape functions, and assembled into a global system that captures the dynamic interaction between the MP, the surrounding soil, and the water column. This system is solved by COMSOL Multiphysics using the direct solver MUMPS.

G

Sound Propagation Module - SILENCE

In the SPM, the propagation domain is considered axisymmetric and vertically stratified, meaning that all material properties vary only with depth z and are independent of radial direction r. Linear acoustics governs wave propagation in the water column, while linear elasticity describes wave propagation in the seabed. Together, the water-soil system forms an infinite acousto-elastic half-space, in which radiation conditions ensure that waves propagate outward without generating reflections.

These assumptions are consistent with those used in the SGM. Consequently, the governing equations for the fluid and the soil domains, as well as the boundary and interface conditions, are identical to those specified for the SGM (see Appendix F). The only exceptions are Eqs. 4.3, F.12, F.13, and F.14, which correspond to the pile dynamics and the pile-fluid/soil interface conditions. Since the pile is not present in the SPM, these equations are omitted in the SPM. The near-field solution on a cylindrical surface $r = r_4$ enclosing the SGM must be known. The quantities prescribed on this boundary, pressure and particle velocity in the water column, and displacement and stresses in the seabed, constitute the input to the SPM. These near field data are extracted from the SGM in the frequency domain. For each frequency, the SGM provides complex-valued pressure, velocity, displacement, and stresses along the cylindrical boundary, discretized at a specified vertical resolution.

Within the SPM, the far-field acoustic pressure at any receiver position is computed using SILENCE, which is based on Peng et al. (2021). This appendix presents an overview of the SILENCE workflow. Section G.1 explains how the modal wavenumbers are obtained through a root-finding procedure. Section G.2 describes the construction of the Green's functions of the layered water-soil environment. Finally, Section G.3 shows how the extracted near-field boundary data are combined with the Green's functions, via the Boundary Integral Method, to compute the acoustic wave field in the far field.

G.1. Root-Finding of Modal Wavenumbers

After obtaining the near-field solution from the FEM model, the first step in the SPM is to determine the propagation characteristics of the acousto-elastic system. This step is independent of the near-field data extracted from the SGM. The propagation characteristics depend on the environmental properties: the water depth, the layering of the seabed, the densities of the layers, the compressional and shear wave speeds, and the associated damping parameters.

These propagation characteristics are derived from the modal structure of the water–soil waveguide (Tsouvalas et al., 2014). Each mode represents a distinct way in which waves can travel horizontally away from the pile. Each mode is described by a complex horizontal wavenumber $k_m(\omega)$, where the real part controls the radial phase speed and the imaginary part controls attenuation with distance.

To obtain the modal wavenumbers, the SILENCE model solves the acousto-elastic dispersion relation using a root finding algorithm. This dispersion relation identifies all admissible wave types at a given frequency, such as propagating, leaky, evanescent, and interface modes.

To provide insight into how these modal wavenumbers are constructed, the key steps of the analytical derivation presented by Tsouvalas et al. (2014) are followed and summarized below.

In the analytical formulation, the acoustic field in the water and the elastic field in the soil, given in Eqs. 4.7 and 4.9, are rewritten in terms of cylindrical wave potentials. Equations 5 and 10 from Tsouvalas et al. (2014) define the velocity potential in the fluid and the compressional and shear displacement potentials in the soil, respectively. These expressions can then be rewritten to the expres-

sions given in Eqs. 6 and 13 of Tsouvalas et al. (2014). It can be seen that the frequency-domain solutions consist of outgoing cylindrical waves (represented by Hankel functions) multiplied by depth dependent exponential functions.

Physically, these representations mean that each component of the wave field spreads outward radially as a cylindrical wave, while its variation with depth is governed by the medium properties and the specific wave type (compressional, shear, or interface wave). Analytical solutions contain a set of unknown coefficients $A_1, \ldots, A_6$, which weight the contributions of the different potentials.

In the next step, these field expressions are substituted into the boundary and interface conditions. This procedure yields a system of six linear equations, one equation for each of the six unknown coefficients $A1, \ldots, A_6$, corresponding to Eqs. 25-30 in Tsouvalas et al. (2014). It should be noted that the boundary conditions in Eqs. 18 and 19 in Tsouvalas et al. (2014), differ from those used in this study, and that an additional set of interface conditions is required because this study contains two soil layers instead of one. The boundary and interface conditions used in this study are presented in Appendix Section F.2.

The field expressions still contain three different horizontal wavenumbers: one associated with the fluid potential and two associated with the soil potentials (compressional and shear). This would imply that the water, the soil compressional field, and the soil shear field could each oscillate horizontally with different wavelengths. However, the boundary and interface conditions prevent this. At both the water-soil interface and the soil-soil interfaces, the conditions enforce continuity. For the interface quantities to remain continuous at all points along the interfaces, all components of the mode should share the same horizontal wavenumber. This condition is stated as Eq. 31 in Tsouvalas et al. (2014):

$$k_{\phi,f} = k_{\phi,s} = k_{\psi,s} = k_r$$

Here $k_{\phi,f}$ is the fluid wavenumber, $k_{\phi,s}$ the soil compressional wavenumber, and $k_{\psi,s}$ the soil shear wavenumber. All must equal the common modal horizontal wavenumber k_r.

A mode represents a single coherent wave pattern spanning the full depth of the waveguide. To remain physically compatible across all interfaces, the water column, sediment layers, and interface waves must “move together” horizontally. Thus, every mode is uniquely characterized by one horizontal wavenumber k_r. The vertical structure (mode shape) may vary strongly between layers, but the radial behavior must be consistent.

Once the common horizontal wavenumber k_r is introduced, the six boundary and interface equations can be written into a matrix system:

$$D(k_r, \omega)\, a = 0$$

which corresponds to Eq. 32 in Tsouvalas et al. (2014). Here, $D(k_r, \omega)$ is a 6×6 matrix that depends on the material properties, the excitation frequency ω, and the chosen horizontal wavenumber k_r. The vector $a = [A_1, \ldots, A_6]^T$ contains the unknown complex amplitudes that define the vertical shape of the mode.

This system is homogeneous, meaning that no external forcing is applied: it describes wave fields that can exist in the environment on their own, purely due to the intrinsic physics of the coupled water-soil system. The trivial solution $a = 0$ always satisfies the system, but it corresponds to no wave field and is therefore physically meaningless. A non-trivial solution $a \neq 0$ is only possible if the matrix $D(k_r, \omega)$ is singular, which mathematically requires:

$$det(D(k_r, \omega)) = 0$$

This condition, Eq. 33 in Tsouvalas et al. (2014), defines the dispersion relation of the layered acousto-elastic waveguide. Its roots $k_m(\omega)$ are the modal horizontal wavenumbers. Each root corresponds to a physically admissible mode.

Solving $det(D(k_r, \omega)) = 0$ for a given frequency ω yields a discrete set of complex values $k_1(\omega), k_2(\omega), ...$ Each value defines a complete, self-consistent wave field in which the acoustic pressure, the soil compressional motion, and the soil shear motion all satisfy the interface conditions simultaneously. The real part of $k_m(\omega)$ determines the radial phase speed, while the imaginary part controls attenuation with range. Modes with small imaginary parts (such as Scholte waves) can propagate over large distances, whereas evanescent modes decay rapidly.

Together, these complex-valued modal wavenumbers describe the full set of propagation mechanisms supported by the layered water-soil waveguide at the given frequency. Each root corresponds to one physically meaningful mode of the system.

G.2. Green's Functions

Once the modal wavenumbers $k_m(\omega)$ of the acousto-elastic environment are known (Section G.1), the next step in the SPM is to determine how the layered water-soil system responds to elementary sources (e.g. the extracted data from FEM in which each data extraction point represents an elementary source). This response is described by the Green's functions of the layered water-soil system. Green's functions describe how an unit source located at some point in the domain (either in the water or in the soil) radiates pressure, velocity, and stress to any receiver point. In this context, Green's functions are used to propagate the extracted FEM data at $r = r_4$ into the far field. Note, this step again does not depend on the FEM near-field results, it depends only on the environmental layering, its material properties, and the modal structure of the waveguide.

The approach followed here is consistent with the formulation of Peng et al. (2021), who derive Green's functions for a fluid layer overlaying a multilayered elastic half-space using Hankel transforms and complex wavenumber integration. In this formulation, the contributions of all admissible modes are superimposed to obtain the pressure, displacement, and stress fields at any receiver point. Each modal contribution is governed by its horizontal wavenumber $k_m(\omega)$ and the corresponding vertical mode shapes in the water and sediment layers.

G.2.1. Representation of Green's Functions

A Green's function represents the response of a linear system to a unit source placed at a specific location. In the context of this study, this means that:

- a unit pressure source is applied at a point within the water column produces a characteristic pressure, particle velocity, and displacement throughout the domain
- a unit radial or vertical force applied within the seabed generates compressional and shear disturbances that propagate into both the soil and the water domain.

As described by Blackledge (2005), the Green function is the solution of a linear inhomogeneous partial differential equation (PDE), such as the Helmholtz equation in acoustics or the elastodynamic equation in solids. Because the PDEs are linear, the response to any arbitrary distributed source can be obtained by superposition of the responses to individual point sources (Huygens' principle) (Blackledge, 2005). Once the Green's function for the environment is known, it can therefore be reused to compute the field generated by any excitation without re-solving the full PDE.

Within the SPM framework, the near-field FEM solution supplies the pressure, particle velocity, displacements, and stresses along the cylindrical extraction boundary at $r = r_4$. The Green's functions of the layered water-soil system then determine how each of these boundary source contributions radiates into the far field. For the stratified environment considered in this study, the Green's function automatically incorporates all physically relevant propagation mechanisms: cylindrical spreading, reflections at the free surface, transmission and mode conversion in the sediments, excitation of compressional and shear body waves, and interface-guided waves such as Scholte waves.

G.2.2. Determination of Green's Functions

The underwater environment is axisymmetric, so wave propagation depends only on radial distance r, depth z, and frequency ω. In cylindrical coordinates, the radial waves are described by cylindrical waves, rather than plane waves. Accordingly, the Hankel transform plays the same role in cylindrical geometries as the Fourier transform does in Cartesian coordinates. Whereas a Fourier transform decomposes a function into plane waves e^{ikx} with wavenumber k, the Hankel transform decomposes a function into circular waves $J_0(k_r r)$, each associated with radial wavenumber k_r (Piessens, Poularikas, et al., 2000). In other words, any axisymmetric radial wave field can be represented as a superposition of infinitely many concentric cylindrical wave components, each contributing a ripple like pattern with its own radial wavelength.

Following Peng et al. (2021), the zeroth-order Hankel transform pair (their Eq. 15) is used:

$$\hat{f}(k_r) = \int_0^\infty f(r) J_0(k_r r) r \, dr \qquad \text{and} \qquad f(r) = \int_0^\infty \hat{f}(k_r) J_0(k_r r) k_r \, \mathrm{d}k_r$$

The advantage of the Hankel transform is that it separates the radial and vertical dependencies of the governing wave equations. Before the transform, the acoustic pressure $p(r, z)$ satisfies a coupled PDE in (r, z). After the transform, each radial wavenumber k_r produces an independent one-dimensional vertical Ordinary Differential Equations (ODE) in z (Peng et al., 2021). Thus, the original three-dimensional problem is reformulated as a family of uncoupled vertical problems, one for each value of k_r. This decomposition simplifies the construction of the Green's functions for the layered water-soil system used in the SPM.

After applying the Hankel transform, the governing wave equations in the fluid and soil (Eqs. 17-19 in Peng et al. (2021)) reduce to a set of ODEs in depth z.

- In the fluid, the transformed equation becomes a forced ODE for the acoustic velocity potential, where the forcing term accounts for the location of the source in the water column.
- In the soil, the transformed equations become homogeneous ODEs for the compressional and shear displacement potentials.

Each of these ODEs involves a vertical wavenumber, defined as:

$$k_{z,f} = \sqrt{k_f^2 - k_r^2}, \qquad k_{z,p} = \sqrt{k_p^2 - k_r^2}, \qquad k_{z,s} = \sqrt{k_s^2 - k_r^2}$$

where k_f, k_p, and k_s denote the acoustic, compressional, and shear wavenumbers of the respective media. As explained by Peng et al. (2021), these vertical wavenumbers arise naturally once the Hankel transform has separated the radial and vertical dependencies of the governing equations (see their Eqs. 17-22).

The form of each vertical wavenumber determines how the corresponding wave behaves with depth for a given wavenumber k_r:

- If k_z is real, the wave field oscillates in depth. This corresponds to vertically propagating acoustic waves in the water or body waves in the soil.
- If k_z is imaginary, the wave field decays exponentially with depth. This produces vertically evanescent behavior, typically associated with evanescent or interface components.

So in short, the Hankel transform rewrites the radial dependence in terms of circular waves. After the transform, each radial wavenumber k_r produces a separate vertical equation. The square-root expression for k_z tells whether the wave oscillates with depth (propagating) or decays (evanescent). This is why different k_r values correspond to different physical behaviors like water-borne waves, leaky waves, and interface waves. For example, a Scholte interface wave propagates horizontally along the seabed, but its amplitude decays upward into the water and decays downward into the soil. This is specified in the specific k_r value which produces exponential decay in z in the ODE.

For each radial wavenumber k_r, the vertical ODE solutions obtained from the Hankel transformed wave equations must satisfy all boundary and interface conditions in the layered water-soil system (Eqs. 8-11 in Peng et al. (2021)). Substituting the vertical ODE solutions into these boundary and interface conditions produces a linear algebraic system for the unknown coefficients A_i, which weight the upward- and downward- going wave components in the fluid and sediment layers (see Appendix A in Peng et al. (2021)). Solving this algebraic system for each k_r yields the complete set of wave amplitudes, and therefore determines the Hankel-domain Green's function:

$$\hat{U}(k_r, z, \omega)$$

The quantity $\hat{U}(k_r)$ represents how strongly the system responds to a unit source for a given radial wavenumber. It describes how efficiently each circular wave component (each k_r) contributes to the total wave field.

To obtain the Green's function in real space ($r,\ z$), the inverse Hankel transform must be performed:

$$U(r,z,\omega) = \frac{1}{2}\int_0^\infty \hat{U}(k_r,z,\omega)H_0^{(2)}(k_r r)k_r\,\mathrm{d}k_r$$

Here, $H_0^{(2)}$ is the Hankel function of the second kind, representing outward-radiating cylindrical waves. This integral reconstructs the full acoustic field by superimposing all the cylindrical wave components weighted by $\hat{U}(k_r)$. However, this integral cannot be evaluated simply along the real k_r-axis, since the integrand contains poles, branch points, and branch cuts (Peng et al., 2021). These complex-valued features arise naturally when the wave equation is transformed into the Hankel domain. The three types of singularities are explained below.

- **Poles: Radial Resonances (Discrete Modes)**
  The Hankel-domain Green's function $\hat{U}(k_r)$ contains a denominator that is proportional to the dispersion determinant of the system:

  $$\hat{U}(k_r) \propto \frac{1}{det(D(k_r,\omega))}$$

  This is the same determinant introduced in Section G.1, where it was used to identify the modal horizontal wavenumbers $k_m(\omega)$ through the dispersion relation. Whenever

  $$det(D(k_r,\omega)) = 0$$

  the denominator vanishes and $\hat{U}(k_r)$ develops a singularity. These singular points are known as poles (The Cooper Union, 2011).

  A pole corresponds to a horizontal wavenumber at which the system can support a self-sustaining wave field, which is a normal mode of the layered water-soil waveguide. This includes Scholte waves, trapped modes, water borne modes, and other propagation mechanisms identified in Section G.1. In a plot of $\hat{U}(k_r)$, these poles appear as sharp peaks where the system's response is really strong (The Cooper Union, 2011).

  Thus, a pole is mathematically a singularity of the Green's function and physically a natural resonance of the waveguide. Each pole corresponds to a specific mode.

- **Branch Points: Wave Behavior Changes**
  Branch points arise at the values of k_r for which the vertical wavenumbers become zero:

  $$k_{z,p} = 0 \Rightarrow k_r = k_p, \qquad k_{z,s} = 0 \Rightarrow k_r = k_s$$

  These are the locations where the arguments of the square-root expressions

  $$k_{z,p} = \sqrt{k_p^2 - k_r^2} \qquad \text{and} \qquad k_{z,s} = \sqrt{k_s^2 - k_r^2}$$

  change sign (Rosales, 1999; Freiberger, 2021). At these points, the vertical wavenumbers transition from real to imaginary (or vice versa), and the associated field components undergo an abrupt change in physical character. Branch points therefore mark boundaries between different propagation regimes. For example, when $k_r < k_p$, the compressional vertical wavenumber $k_{z,p}$ is real, and compressional waves in the soil oscillate with depth, i.e. they propagate vertically. While, when $k_r > k_p$, the same wavenumber becomes imaginary and the vertical dependence becomes evanescent, meaning the wave field decays exponentially with depth. An analogous transition occurs for shear waves at $k_r = k_s$.

  These transition points are of importance in the system since it describes where a wave field can propagate vertically (body-wave regime) versus where it becomes trapped or decays (evanescent regime). Branch points separate behaviors such as water-borne propagating components versus evanescent water waves, as well as propagating soil P- and S-waves versus trapped or leaky soil waves.

  Thus branch points are the mathematical points of the transitions between these physically distinct wave phenomena and play a role in shaping the structure of the Green's function in the Hankel domain.

- **Branch Cuts: Single-Valued Physical Solution**
  The vertical wavenumbers in the soil ($k_{z,p} = \sqrt{k_p^2 - k_r^2}$ and $k_{z,s} = \sqrt{k_s^2 - k_r^2}$), contain square-root terms. A square root is a multi-valued function in the complex plane: for any nonzero complex number z: $\sqrt{z} = \pm w$, meaning that the function can take two different values depending on how the complex plane is traversed (Freiberger, 2021). As a result, if one moves around a singularity in the complex k_r-plane, the value of the square root can switch between its two branches.

  To prevent this and to ensure a single valued and physically consistent solution, one must specifiy which branch of the square root is used. This is enforced by introducing branch cuts, this are curves in the complex k_r-plane across which the square root is not allowed to cross.

  A branch cut is therefore not a physical phenomenon but a mathematical tool that ensures the solution of the Green's function is single valued.

  The contributions that arise from integration along the branch cuts correspond to the continuous spectrum of the system. Unlike poles, which represent discrete normal modes with distinct horizontal wavenumbers, branch-cut contributions represent the continuous set of radiating states available in an elastic medium.

Together, these features ensure that the Green's function captures all physical wave components. Because of the poles and branch cuts in the complex k_r-plane, the inverse Hankel transform must be evaluated using contour integration, as formulated in Eq. 34 of Peng et al. (2021). The resulting representation is:

$$U = \pi \sum_m Res[\hat{U}(k_m)] H_0^{(2)}(k_m r) k_m + \frac{1}{2} \int_{\text{branch cuts}} \hat{U}(k_r) H_0^{(2)}(k_r r) k_r \, \mathrm{d}k_r$$

Thus, the Green's function of the layered water-soil system is composed of different types of wave contributions. Together, these contributions form the physical wave field in the layered water-soil system. The Green's function thereby characterizes things as:

- How pressure at $(r_s,\, z_s)$ produces pressure, velocity, displacement, and stress at $(r,\, z)$
- How shear waves in the soil contribute to water pressure
- How interface waves transport energy horizontally
- How much energy leaks into deeper sediment layers
- How waves interact with the water surface

In essence, the Green's function provides the complete response of the coupled water–soil system to a unit source.

G.3. Boundary Element Method

Once the Green's functions of the system are known (Section G.2), the final step in the SPM is to propagate the near-field wave field, obtained from the SGM at the cylindrical boundary $r = r_4$, into the far-field. This is achieved using the Boundary Integral Method (BIM). The BIM offers a way of computing the response in the entire water-soil domain without meshing the far-field region, since the governing equations are solved analytically through the Green's functions of the medium (Peng et al., 2021).

Inside the FEM domain, the wave field is influenced by complexities such as the geometry of the pile, the hammer–pile interaction, soil–pile coupling, and the generation of Mach cones and Scholte waves. Beyond $r = r_4$, however, the environment simplifies to a horizontally stratified water column overlying a layered elastic halfspace. In this region, wave propagation is governed by linear PDEs whose solutions are described by the previously derived Green's functions.

The conceptual idea of the BIM is that the cylindrical boundary surrounding the pile can be regarded as being covered by an equivalent distribution of acoustic sources. Each infinitesimal boundary element radiates sound into the environment according to the local boundary data extracted from the SGM: pressure and particle velocity in the water column, and displacements and stresses in the sediment. The Green's functions then determine how a unit source at each boundary element propagates through

the system. The total acoustic field at a receiver is the superposition of these individual contributions (Peng et al., 2021).

For any receiver point $\mathbf{x} = (r, z)$ outside the SGM, the acoustic pressure in the fluid satisfies Green's third identity (Peng et al., 2021):

$$p(\mathbf{x}, \omega) = \int_{\Gamma} \left[G(\mathbf{x}, \mathbf{x}', \omega) \, \frac{\partial p}{\partial n'}(\mathbf{x}', \omega) - \frac{\partial G}{\partial n'}(\mathbf{x}, \mathbf{x}', \omega) \, p(\mathbf{x}', \omega) \right] \mathrm{d}\Gamma'$$

where Γ is the cylindrical boundary at $r = r_0$. Here,

- $p(\mathbf{x}', \omega)$ is the pressure on the boundary supplied by the SGM
- $\frac{\partial p}{\partial n'}$ is the normal pressure gradient
- $G(\mathbf{x}, \mathbf{x}', \omega)$ is the Green's function of the layered water-soil system
- $\frac{\partial G}{\partial n'}$ is its normal derivative with respect to the boundary surface

This integral expression states that both normal velocity and pressure loading on the boundary act as sources that radiate through the environment. It encapsulates all mechanisms of acoustic radiation from the near field into the far field and is valid for any point outside the SGM.

To evaluate the Boundary Integral Equation numerically, the cylindrical boundary is discretized into a finite number of surface elements. On each element, the SGM provides the required boundary values, and the relevant Green's functions are evaluated. The total acoustic field at a receiver location is then obtained by summing the contributions from all elements. This discretized implementation is known as the Boundary Element Method (BEM). Because only the boundary needs to be discretized, rather than the full three-dimensional propagation domain, the method is computationally efficient (Chandler-Wilde and Langdon, 2007).

H

Numerical Representation of NMS Case Study

The NMS has been designed by IQIP, which also holds the intellectual property rights. Although IQIP consulted with HMC during the design phase, this collaboration primarily concerned operational aspects, such as deployment procedures and lifting point design, rather than structural or acoustic design details. As a result, modeling the NMS in FEM presents several challenges, and it must be acknowledged that a complete validation of the NMS is not possible since different design parameters are assumed.

The primary objective of this case study is to determine a model representation of the NMS within a 2D axisymmetric FEM model. Because the physical NMS includes non-axisymmetric components, i.e., its supporting frame, a 2D model of its geometry is not feasible. Consequently, the focus of this calibration procedure is to achieve functional compliance of the system's acoustic behavior rather than to model the geometry in detail. The goal is to identify a configuration that is based on the physical aspects of the NMS and that accurately replicates the observed noise mitigation performance, i.e., targeting the field measured SEL of X dB at 750 m.

To achieve this, five distinct configurations were analyzed in both the time and frequency domains. This chapter provides an overview of these cases, summarizes the primary findings, and defines the final model used to represent the NMS in this study.

H.1. Methodology & Definitions

A simplified illustration of the five configurations is presented in Figure H.1. The models are defined as follows:

- **Case 1 - Unmitigated Case:** This configuration serves as the reference case. No mitigation system is present, therefore, the results reflect the baseline noise propagation belonging to the environmental system.
- **Case 2 - Air Layer:** This model features an air layer positioned in the near-field of the NMS. As detailed in Section 2.3, the NMS utilizes an air gap between the inner and outer shell. Given that this air layer is contributing to a large impedance mismatch, it is assumed to be one of the main noise mitigation aspects of the NMS. It is isolated here to determine its individual contribution to mitigation.
- **Case 3 - Air Layer & Outer Shell:** This configuration introduces a steel outer shell immediately following the air layer. This model is critical for evaluating whether the shell acts as a secondary radiator when excited by seismic waves (soil displacement). In the physical system, the shell is stabilized by a support frame. In this model, these connections are represented as pinned (zero-displacement) boundary conditions. The shell is coupled to the seabed using continuity interface conditions and is assumed to share the material properties and wall thickness of the MP.
- **Case 4 - Bubble & Air Layer:** This configuration builds upon Case 2 by adding a 0.5 m thick bubble layer immediately preceding the air gap. This mimics the bubble injection system used within the NMS cavity to attenuate energy before it reaches the air layer. For this study, the bubble layer is modeled using material properties that assume a large void-fraction mixture.

- **Case 5 - Air Layer with Sound Hard Boundary (SHB):** This configuration is similar to Case 3, but the structural outer shell is replaced by a ”Sound Hard Boundary” condition in COMSOL. This assumes the air layer is supported by an infinitely rigid boundary. Unlike Case 3, this rigid boundary cannot vibrate or act as a secondary noise source.

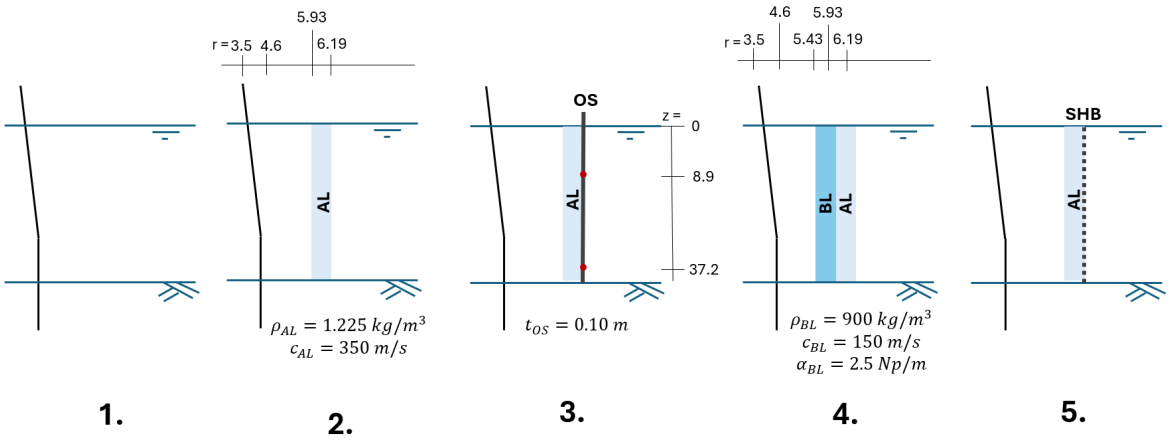

Figure H.1: Schematic representation of the five model configurations analyzed in this case study: (1) Unmitigated, (2) Air layer, (3) Air layer & Outer Shell, (4) Bubble & Air Layer, and (5) Air Layer with SHB.

To ensure comparison between the five configurations, the same material properties for the MP, fluid, and seabed domain are utilized, as well as the same excitation force. The excitation force assumed in this case study is a Gaussian exponential pulse, as illustrated in Figure H.2 and defined by Eq. H.1.

$$F(f) = \exp\left(-\frac{(f - f_0)^2}{2\sigma^2}\right) \cdot \exp(-i2\pi f t_0) \tag{H.1}$$

where:

- f_0 is the dominant frequency, defined as $f_0 = \frac{106}{2\pi} \approx 16.87$,Hz. This value corresponds to the dominant frequency described in Eq. 3.1.
- σ is the frequency deviation, assumed to be 30 Hz to provide sufficient spectral bandwidth.
- t_0 is the time delay of the impulse, assumed to be 0.05 s, to ensure that the signal is fully contained within the time window.

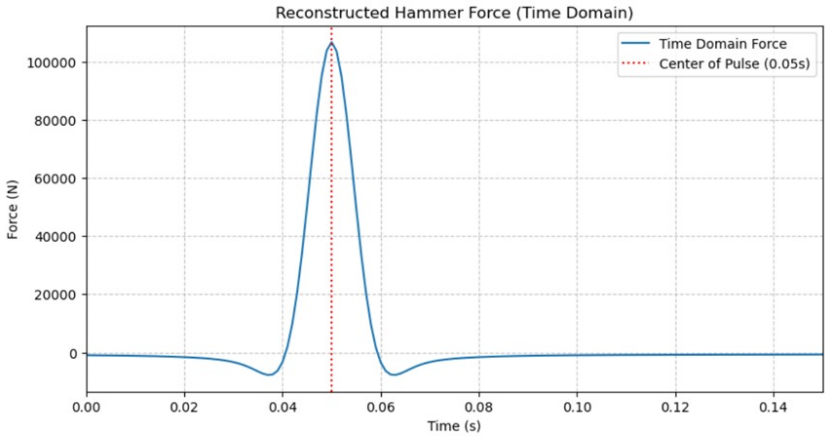

Figure H.2: Hammer force used for the time domain analysis. The force is described in Eq. H.1.

The analysis is conducted as follows:

1. **Qualitative Time Domain Analysis:**
   Using 2D axisymmetric animations, the propagation of energy through the system is visually inspected. In the fluid domain, the total acoustic pressure (Pa) is plotted, while in the soil domain, the radial displacement (m) is visualized.
2. **Quantitative Energy Flux Analysis:**
   Intensity values are integrated on specific boundaries to determine power flux (W). This quantification allows for an assessment of how energy propagates through the system. Two boundary integrations are performed to map the energy and are described below. These integration bounds are also illustrated in Figure H.3. The plus ($+$) and minus ($-$) signs in the power flux notation indicate whether the energy vector is aligned with the positive or negative direction of the coordinate axis.

   - **Seabed Interface- Mitigation Zone (P_{FS+}):** Represents the vertical power that travels from the fluid into the seabed within the cavity (between the pile and the air layer).
   - **Seabed Interface-Far Field (P_{SF-}):** Represents the vertical power leaking back into the water column from the seabed behind the air layer.

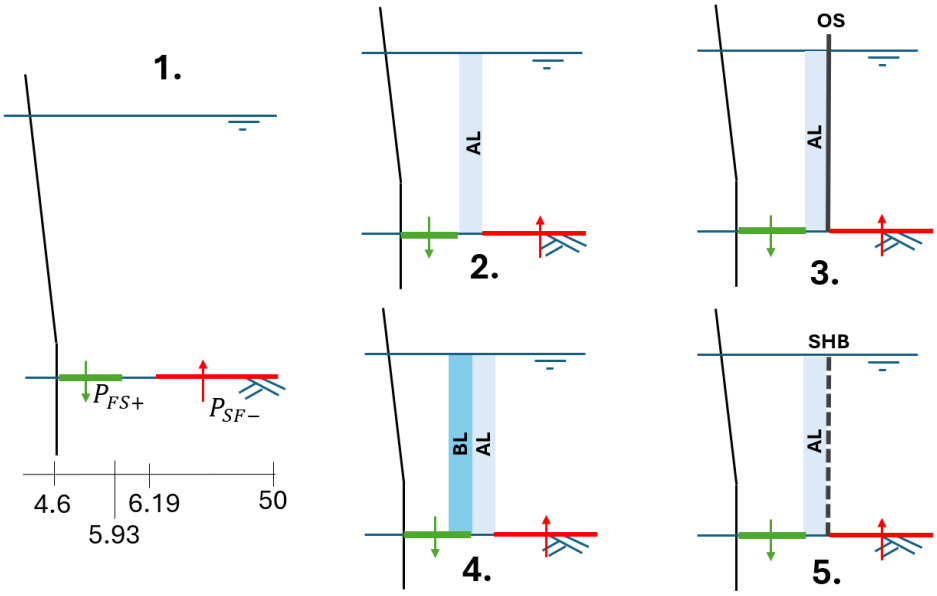

Figure H.3: Illustration of the definition of the used interfaces to calculate the powers P_{FS+}, and P_{SF-}.

Furthermore, the intensity magnitude is plotted over the depth at two locations: $r = 5.0\,m$ (within the cavity) and $r = 6.5\,m$ (immediately behind the air layer). These depth profiles allow for a comparison of the vertical energy distribution and the effectiveness of the barriers.

The definitions and units for the power and intensities described above are summarized in Table H.1. The expressions are based on the built-in frequency domain expressions defined by COMSOL.

Symbol	Definition	Unit	Remark
P_{FS}	$\max(\mathrm{Re}(I_z), 0)$	W	Downward power flux in the cavity into the seabed
P_{SF}	$\min(\mathrm{Re}(I_z), 0)$	W	Upward power flux behind barrier into the water.
$\lvert\vec{I}_F\rvert$	$\sqrt{I_r^2 + I_z^2}$	W/m^2	Intensity magnitude profile in the fluid domain.
$\lvert\vec{I}_S\rvert$	$\sqrt{I_r^2 + I_z^2}$	W/m^2	Intensity magnitude profile in the solid domain.

Table H.1: Definitions and units for the power and intensity metrics used in the quantitative analysis.

Energy flux, represented by intensity (W/m^2) and power (W), is used to analyze the defined NMS cases performance. These metrics are required because pressure (in the fluid) and stress (in the soil) cannot be compared directly due to their different units. COMSOL calculates power by integrating the intensity over $360°$ revolution ($\cdot 2\pi r$). Consequently, while intensity represents a localized value at a specific point in the cross-section, the power values reflect the total 3D energy transmission across the entire boundary.

H.2. Case Analysis

In this section, the defined numerical representations of the NMS are studied.

H.2.1. Case 1: Unmitigated

Case 1 represents the reference scenario where the MP is driven into the seabed without mitigation. A SEL of 192.4 dB is calculated at $r = 50\,m$, 2 m above the seabed.

Visual Observations (Time-Domain)

The time-domain animations, show that the primary noise source is the Mach wave radiation from the longitudinal stress waves in the MP. This Mach wave is clearly visible in the water, propagating at the Mach angle. At the seabed, energy is both transmitted into the soil and reflected back into the water. Significant soil displacement occurs near the pile-soil interface, indicating seismic energy generation. This energy propagates further as body waves (P and S waves) and interface waves.

Energy Flux Data

Table H.2 summarizes the power across the defined boundaries.

Parameter	Symbol	Value
Vertical Pumping into Soil	P_{FS+}	$0.183 \times 10^5\,W$
Vertical Leakage into Fluid	P_{SF-}	$0.775 \times 10^5\,W$

Table H.2: Quantitative power flux results for Case 1 (Unmitigated).

The intensity magnitude profiles ($|\vec{I}|$) in Figure H.4 show how energy is distributed with depth. A dominant peak of approximately $4.5 \times 10^4\,W/m^2$ occurs at the mudline ($z = 40\,m$).

The detailed view in Figure H.4b shows the waterborne field. The intensity fluctuates between 1000 and 2000 W/m^2. These oscillations, visible in both the fluid and soil domains, are a byproduct of the magnitude calculation: $|\vec{I}| = \sqrt{I_r^2 + I_z^2}$. Because acoustic intensity is the product of harmonic pressure and particle velocity, the individual components (I_r, I_z) alternate between positive and negative values in space. Squaring these components to find the magnitude removes the directional sign. The resulting ”wiggly” behavior is a mathematical artifact of visualizing a vector field as a scalar magnitude.

A reduction in peak intensity is visible between $r = 5.0\,m$ and $r = 6.5\,m$. At $r = 5.0\,m$, only $0.4\,m$ from the pile wall, the field is dominated by direct mechanical coupling and evanescent (non-propagating) waves. These components decay rapidly with distance. These components decay rapidly with distance. At $r = 6.5\,m$, these near□field evanescent waves have significantly reduced in magnitude due to their exponential decay with distance. In addition, cylindrical geometrical spreading further contributes to the lower magnitude observed at $r = 6.5\,m$.

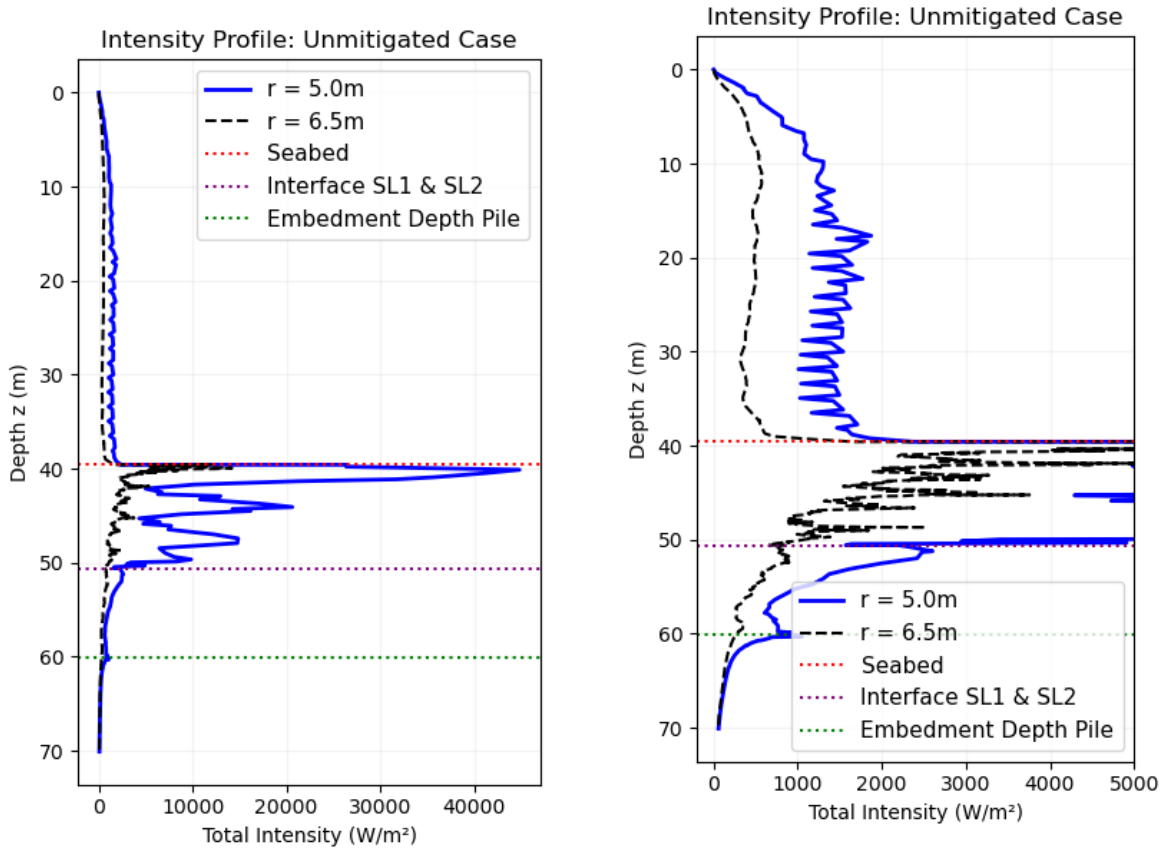

(a) Full-scale intensity magnitude profile.

(b) Detailed profile (0–5000 W/m^2) highlighting waterborne propagation.

Figure H.4: Intensity magnitude $|\vec{I}|$ as a function of depth for Case 1 (Unmitigated) at $r = 5.0\,m$ and $r = 6.5\,m$. The profiles illustrate the dominance of the Scholte wave at the mudline ($z = 40\,m$) relative to the Mach wave field in the water column.

Key Findings

The unmitigated case demonstrates that the fluid-soil interface is the zone of highest energy density. The vertical "leakage" (P_{SF-}) is significantly larger than the P_{FS+}, primarily because P_{SF-} is integrated over a much larger distance ($r = 6.19\,m$ to $50\,m$). However, this still indicates that that the seabed acts as a medium that 'leaks' energy back into the water column. These findings align with the secondary noise path theory explained in Chapter 2.2.

H.2.2. Case 2: Air Layer

In Case 2, an air layer is introduced in the near-field of the pile. This configuration isolates the effect of the large impedance mismatch between the water ($Z = \rho c \approx 1.54 \times 10^6\,kg/m^2 s$) and the air ($z = \rho c \approx 429\,kg/m^2 s$). Theoretically, this interface should act as a pressure release boundary, reflecting the majority of the incident waterborne energy. A SEL of 186.3 dB is calculated at $r = 50\,m$, 2 m above seabed. This means that the air layer has reduced SEL with 6.1 dB at 50 m from the piling location.

Visual Observations (Time-Domain)

In the time domain animation, the air layer acts as an acoustic barrier, reflecting the Mach wave. A standing wave pattern emerges within the cavity between the MP and the air barrier due to the superposition of incident and reflected waves. However, at the base of the air layer, it looks like energy 'leaks' to the other side of the air layer. This observation is driven by two mechanisms. First, as illustrated in Figure H.5, the edge of the air layer creates a sharp corner, causing incident waves to diffract around the base. Simultaneously, energy that has bypassed the air layer through the seabed re-radiates into the water column. Because the speed of sound in the seabed is higher than in the water column, the energy radiates into the water column at an angle (similar to the Mach cone generation).

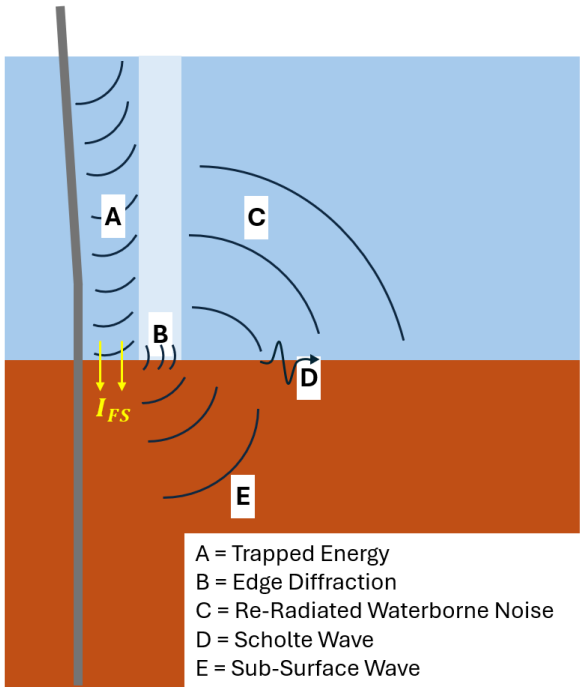

Figure H.5: Schematic of the diffraction wave physics in Case 2 (Air Layer). (A) Waterborne energy is reflected, forming a high-energy standing wave field and entering the seabed as P_{FS+}. (B) Diffraction occurs at the air layer-mudline interface. (C) Re-radiation into the fluid domain from the air layer edge acting as a secondary point source. (D) Energy couples into an interface Scholte wave. (E) Energy is refracted further into the soil as P- and S-waves."

Additionally, the time-domain animations show that the air barrier acts as a frequency dependent filter. While higher frequency components are reflected, the low frequency energy passes through the NMS. This is because the width of the air layer (0.26 m) is too thin to reflect the wavelength of these low frequencies. This means that for the low frequencies, the air layer is 'acoustically transparent'. Instead of providing an impedance mismatch that reflects the energy, the low-frequency pressure wave excites the air layer, causing the layer to vibrate and re-radiate the energy into the water column on the other side.

Energy Flux Data

The transition from unmitigated case to the air layer configuration resulted in a redistribution of energy, as summarized in Table H.3.

Parameter	Symbol	Value	Comparison to Case 1
Vertical Pumping into Soil	P_{FS+}	$0.948 \times 10^5\, W$	418% increase
Vertical Leakage into Fluid	P_{SF-}	$0.388 \times 10^5\, W$	49.9% reduction

Table H.3: Quantitative power flux results for Case 2 (Air Layer).

The intensity magnitude profile for Case 2 (Figure H.6a) demonstrates that the air layer is efficient as waterborne energy barrier. At $r = 6.5\,m$ (immediately behind the air layer) the intensity in the water column drops to near-zero. In contrast, the profile at $r = 5.0\,m$ (within the cavity) the intensity exhibit magnitudes reaching up to 5000 W/m^2 in the water column, nearly triple the intensity observed in the unmitigated case.

This intensity redistribution indicates that the incident Mach waves are reflected by the air barrier, resulting in a standing wave field. Part of this trapped energy is redirected towards the mudline, leading to a significant 418% increase in vertical power flux (P_{FS+}) into the seabed compared to Case 1. While

the peak intensity magnitude at the seabed is lower than in the unmitigated case, energy is distributed deeper into the soil.

While the time-domain animations show that low-frequency waves propagate through the air layer, the intensity magnitude profiles indicate that this does not result in significant intensity located just behind the air layer. Figure H.6b shows that at $r = 6.5\,m$, the intensity in the water column remains near-zero. Consequently, the vibration of the air layer itself is not a major noise path, the energy observed in the far-field must therefore originate from the seismic bypass through the seabed rather than direct transmission through the air layer.

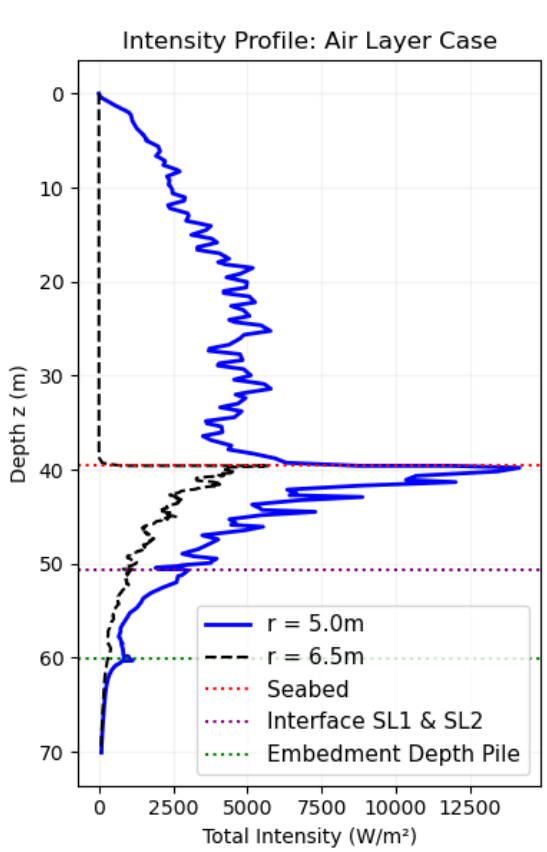

(a) Full-scale intensity magnitude profile.

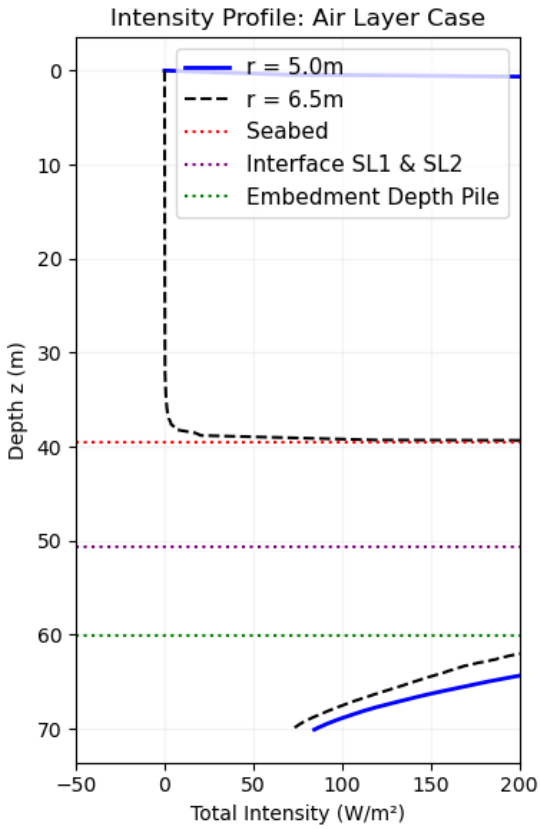

(b) Detailed profile (-50–200 W/m^2) highlighting the intensity magnitude at $r = 5.0\,m$.

Figure H.6: Intensity magnitude $|\vec{I}|$ for Case 2 (Air Layer). The standing wave within the cavity ($r = 5.0$,m) and the effectively shielded zone ($r = 6.5$,m) illustrate the redirection of waterborne energy into the seabed.

Key Findings

The air layer functions as a reflective boundary. The reflecting energy interacts with the MP which changes the vibrations of the MP. The energy trapped within the cavity is redirected downward, significantly increasing the pressure loading on the seabed. This means that the air layer converts a part of the waterborne energy into a seismic propagation path.

This redirected energy contributes to the seismic bypass, where waves propagate through the soil and re-radiate into the fluid domain beyond the barrier. Despite the high reflectivity of the air barrier, the SEL at 50 m decreased by only 6.1 dB, confirming that energy re-emerges in the water column through the soil. Notably, while the downward flux (P_{FS+}) increased significantly, the vertical leakage (P_{SF-}) within the modeled 50 m radius actually decreased compared to Case 1. A reason for this could be that the energy is being captured by Scholte waves. These waves are localized at the mudline and radiates the energy over much larger distance than the 50 m modeled.

H.2.3. Case 3: Air Layer & Outer Shell

This configuration adds a steel outer shell ($r = 6.19\,m$) immediately behind the air layer. The shell is connected with continuity conditions to the seabed. The goal is to determine if the additional air-steel impedance mismatch improves mitigation or if the shell acts as a secondary radiator when excited by soil vibrations. A SEL of 187.3 dB is calculated at at $r = 50\,m$, 2 m above seabed. This means that adding the shell has increased SEL with 1.0 dB at 50 m from the piling location compared to case 2.

Visual Observations (Time-Domain)

The time-domain animation shows a complex interaction. While the air layer and the shell block the Mach wave, the shell itself undergoes vibrations. This vibration of the outer shell is driven by the energy in the seabed. Consequently, the shell acts as a secondary source, radiating a new wave field into the far field.

Also the time domain plot of the radial distance of the outer shell is studied. In this animation it can be seen that indeed the shell is excited by the displacement of the soil. The radial displacement of the shell is in the order of $10^{-5}\,mm$.

Energy Flux Data

Table H.4 summarized the integrated power across the defined boundaries for Case 3.

Parameter	Symbol	Value	Comparison to Case 1
Vertical Pumping into Soil	P_{FS+}	$0.945 \times 10^5\,W$	416% increase
Vertical Leakage into Fluid	P_{SF-}	$0.647 \times 10^5\,W$	16.5% reduction

Table H.4: Quantitative power flux results for Case 3 (air layer and outer shell).

When comparing the power values in Table H.4 (Case 3) and Table H.3 (Case 2), the vertical leakage back into the water column (P_{SF-}) increases significantly from $0.388 \times 10^5\,W$ to $0.647 \times 10^5\,W$, a 67% increase. This indicates that, although the energy pumped from the water column into the seabed within the cavity remains approximately constant, a larger portion of energy is re-radiated back into the water column.

This increase may be attributed to the presence of the outer shell, as well as changes in the vibration pattern of the MP caused by wave reflections at the air layer. The introduction of the outer shell alters the wave reflection characteristics, which in turn affects the pile's vibrational response compared to Case 2 and therefore more energy or different frequency content energy may be radiated by the MP. Additionally, the outer shell is connected to the seabed, its vibrations, particularly near resonance frequencies, can inject additional energy into the seabed. This energy then propagates radially into the far field, potentially enhancing the magnitude of the Scholte waves and consequently increasing the vertical power re-radiates into the water column.

The intensity magnitude profiles confirm this radiation of the shell. When comparing the zoomed-in profiles at $r = 6.5\,m$, Case 2 (air layer only) shows near-zero intensity in the water column. In Case 3, the intensity at $r = 6.5\,m$ is no longer zero, averaging roughly $25\,W/m^2$ across the depth. This confirms that energy is radiated by the vibrating shell into the water column.

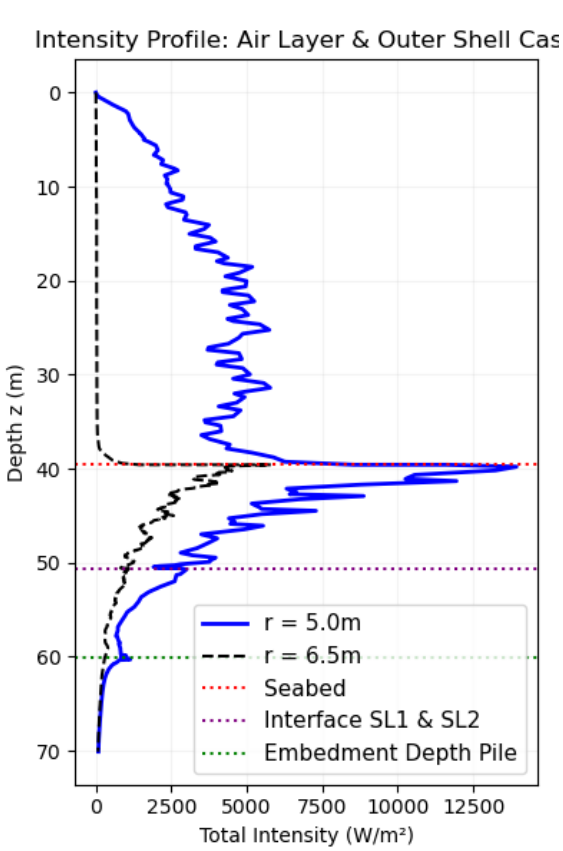

(a) Full-scale intensity magnitude profile.

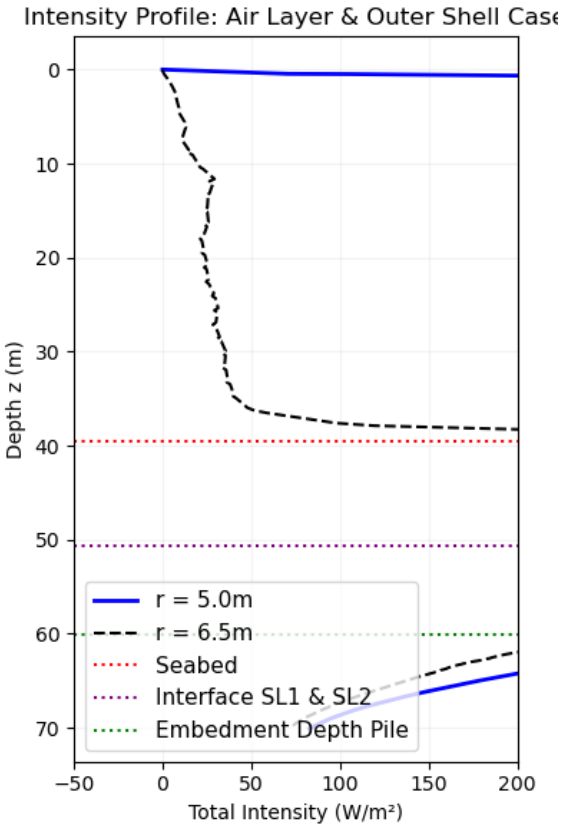

(b) Detailed profile (-50–200 W/m^2) highlighting the intensity magnitude at $r = 5.0\,m$.

Figure H.7: Intensity magnitude $|\vec{I}|$ as a function of depth for Case 3 (air layer and outer shell) at $r = 5.0\,m$ and $r = 6.5\,m$. The profiles illustrate

Key Findings

The addition of the steel outer shell introduces a coupling. While the air layer is an effective barrier for waterborne waves, the shell acts as a bridge for seismic energy at the mudline. Because the shell is connected to the seabed through continuity conditions, it is excited by soil vibrations and therefore radiates energy into the water column. This is confirmed with the intensity over depth plot just behind the outer shell where approximately 25 W/m^2 intensity is present in the water column, while in Case 2 near-zero intensity values were observed.

Another evidence of this effect is the 67% increase in vertical leakage (P_{SF-}) compared to Case 2. This suggests that the connection between the shell and the seabed facilitates that energy from the outer shell, particularly near resonance frequencies, may enter the soil. Adding the outer shell leads to a 1.0 dB increase of SEL at $r = 50\,m$ compared to Case 2, proving that adding a structural component can also lead to increased noise levels since the structural component acts as a second source.

H.2.4. Case 4: Bubble & Air Layer

Case 4 utilizes a multi-layered NMS approach consisting of a 0.5 m bubble layer followed by an air layer. The objective of this case is to evaluate whether the addition of a dissipative medium can mitigate the incident and reflective waves. Potentially, this can reduce the injected energy into the soil in the cavity and also the energy that leaks back from the soil into the water column behind the air layer.

A SEL of 186.0 dB is calculated at at $r = 50\,m$, 2 m above seabed. This means that adding the bubble layer reduces SEL with 0.3 dB at 50 m from the piling location compared to case 2.

Visual Observations (Time-Domain)

In the time domain animation, similar behavior as in Case 2 is observed. The air layer acts as an acoustic barrier, reflecting the Mach wave. A standing wave pattern emerges within the cavity between the MP and the air barrier due to the superposition of incident and reflected waves. However, in this case, a dissipative bubble layer is present in the cavity, making the space where standing waves can occur smaller. Additionally, similar as for Case 2, a localized 'leakage' of energy is observed at the base of the barrier. This wave field behind the barrier originates from edge diffraction and re-radiation of seismic energy into the water column.

Additionally, the time-domain animations show that the air barrier acts as a frequency dependent filter, like case 2. However, in the time domain animations it looks like there is less energy directly behind the air layer. This suggests that these low frequencies, that in Case 2 were transmitted through the air layer, are partially dissipated by the air layer.

Energy Flux Data

Table H.5 summarizes the integrated power across the defined boundaries for Case 4.

Parameter	Symbol	Value	Comparison to Case 1
Vertical Pumping into Soil	P_{FS+}	$0.125 \times 10^5\, W$	31.7% reduction
Vertical Leakage into Fluid	P_{SF-}	$0.273 \times 10^5\, W$	64.8% reduction

Table H.5: Quantitative power flux results for Case 4 (bubble and air layer).

The quantitative results in Table H.5 show that P_{FS+} is lower than the unmitigated Case 1 ($0.125 \times 10^5\, W$ versus $0.183 \times 10^5\, W$). This confirms that the bubble layer successfully dissipates the incident wave and its reflections, significantly reducing the energy injected into the seabed within the cavity.

Almost all energy is blocked in the water column by the bubble and air layer (see Figures H.6a and H.8b), implying that energy can only enter the water column via the seabed. Although P_{SF-} is relatively low compared to Case 2, the SEL at 50 m differs by only 0.3 dB compared to that case. This small SEL difference can be caused by the logarithmic scale of the metric dB.

However, it is important to note that the vertical power flux does not capture the full energy propagation. For instance, when energy is transferred into Scholte wave propagation, it can be re-emitted into the water column over large distances. In that case, the energy propagates primarily as radial intensity rather than vertical intensity. Consequently, the vertical power flux represents only a portion of the total propagation pathway and does not provide a complete picture of the acoustic energy distribution.

The intensity magnitude plots provide a more suitable metric for assessing the mitigation performance. The intensity magnitude profiles (Figure H.8) demonstrate the mitigation improvement achieved. Within the cavity ($r = 5.0\, m$), the peak intensity in the water column has dropped to approximately 1500 W/m^2, compared to 5000 W/m^2 observed in Case 2.

Earlier, it was observed that Case 3 exhibits a smaller P_{SF-} than Case 2, which would suggest that less energy is present at the fluid-soil interface in Case 3. The intensity magnitude plots reveal the same behavior. At the fluid–soil interface, the intensity magnitude decreases from approximately 13,500 W/m^2 in Case 2 to about 10,000 W/m^2 in Case 3.

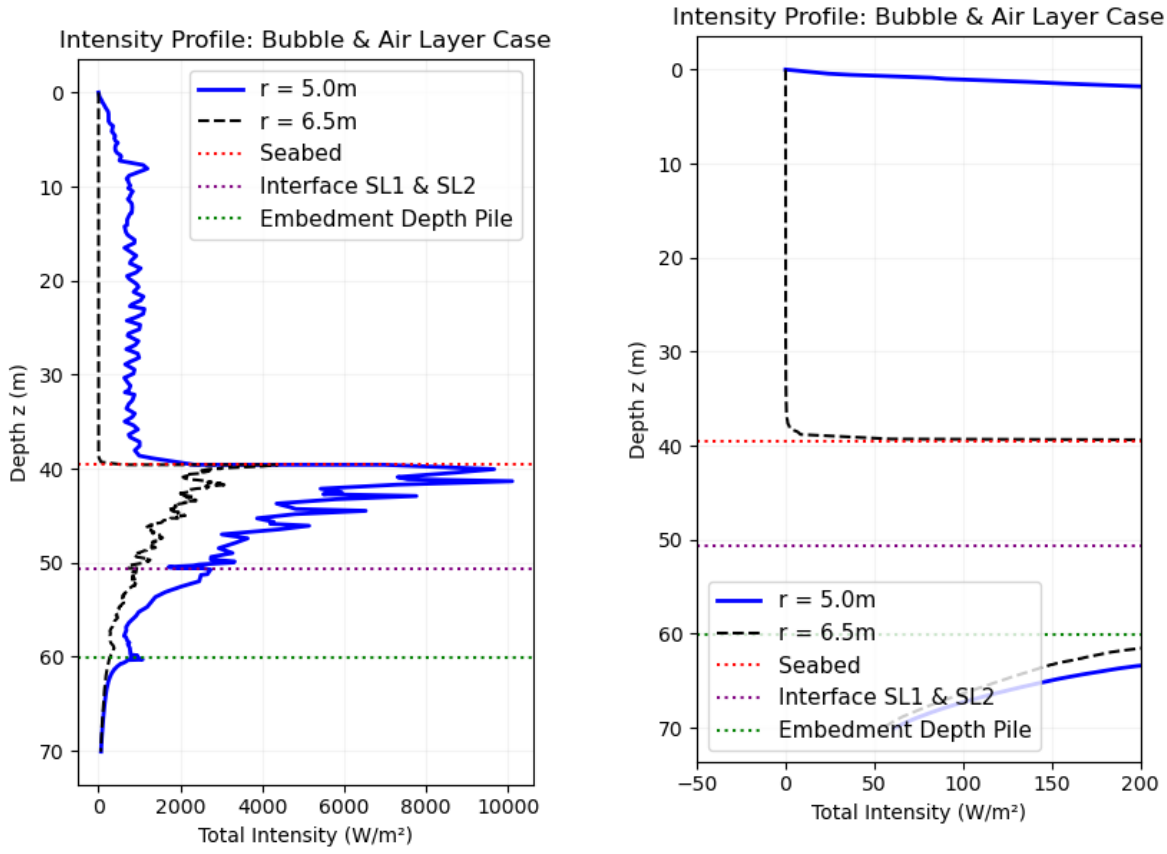

(a) Full-scale intensity magnitude profile.

(b) Detailed profile (-50–200 W/m^2) highlighting the intensity magnitude at $r = 5.0\,m$.

Figure H.8: Intensity magnitude $|\vec{I}|$ as a function of depth for Case 4 (bubble and air layer) at $r = 5.0\,m$ and $r = 6.5\,m$.

Key Findings

By introducing a dissipative medium into the cavity, the system prevents high-pressure standing waves that is present in Case 2 and Case 3. This results in less energy traveling from the fluid inside the cavity into the seabed. The term P_{FS+} reduces by nearly 87% compared to Case 2.

Furthermore, the vertical leakage (P_{SF-}) reached its lowest value in this configuration. This suggests that when less energy is present in the soil domain, also less energy is transmitted to the fluid domain in the near-field. The total SEL reduction (6.4 dB) is only slightly better than the air layer case (6.1 dB). This marginal extra reduction is due to the logarithmic scale of the dB unit.

H.2.5. Case 5: Air Layer & Sound Hard Boundary

Lastly, Case 5 investigates the impact of an air layer constrained by a rigid boundary. In this configuration, the outer radial boundary of the air layer is modeled using the Sound Hard Boundary condition in COMSOL. This setup prevents the air layer from being displaced by the incident waves, particularly at lower frequencies where the wavelengths are significantly larger than the layer thickness. Case 2 demonstrated that low frequencies propagate through the air layer. By imposing this rigid boundary, the support ensures that long-wavelength pressure waves are also reflected back toward the MP. A SEL of 188.6 dB is calculated at $r = 50\,m$, 2 m above seabed. This means that including a rigid boundary has increased the SEL with 2.3 dB compared to Case 2 where only an air layer was present. Compared to the unmitigated case, this case has reduced the SEL by 3.8 dB.

Visual Observations (Time-Domain)

Visual analysis of the time-domain animations confirms that the rigid boundary in Case 5 prevents acoustic energy from propagating through the air layer. While in Case 2, it could be observed that energy propagate through the air layer. Furthermore, the pressure field within the near-field cavity

(between the MP and the NMS) deviates from the patterns seen in Case 2. This is governed by including the rigid boundary condition, whereas Case 2 acts as a pressure-release surface. This total reflection of the incident waves leads to the development of different standing wave patterns and a different superposition of pressure phases within the cavity compared to Case 2, where there was no total reflection.

Besides that, no major changes are observed compared to Case 2. For example, edge diffraction at the base of the air layer and the re-radiation of energy into the water column via the seismic waves are visible.

Energy Flux Data

The power fluxes calculated for the defined boundaries are presented in Table H.6.

Parameter	Symbol	Value	Comparison to Case 1
Vertical Pumping into Soil	P_{FS+}	$0.950 \times 10^5\, W$	419% increase
Vertical Leakage into Fluid	P_{SF-}	$-0.695 \times 10^5\, W$	10.3% reduction

Table H.6: Quantitative power flux results for Case 5 (air layer and rigid boundary).

Based on the calculated power fluxes, it can be concluded that the same mechanisms observed in previous cases are present. Inside the cavity, the pressures are large, this results in that energy is ”pumped” into the seabed. The value for vertical pumping (P_{FS+}) remains relatively consistent with those found in Case 2 and 3. However, a discrepancy arises in the vertical leakage term (P_{SF-}), which nearly doubles when the rigid boundary is introduced. This increase in re-radiated energy from the soil accounts for the 2.3 dB SEL at 50 m increase compared to Case 2.

Figure H.9a presents the intensity magnitude profiles over depth at two radial positions for Case 5. While the overall profiles appear similar to those of Case 2 (see Figure H.6a), a difference is visible in the zoomed-in plot at $r = 6.5\, m$. In this rigid-boundary configuration, the intensity profile near the seabed increases exponentially as it approaches the mudline, whereas in Case 2, this value remains near-zero. This suggests that the rigid constraint on the air layer eliminates any energy dissipation through displacement, leading to an increase in intensity around the seabed. The intensity profiles exhibit an exponential decay with distance from the seabed into the water column, which is consistent with the characteristic behavior of Scholte waves. This observation provides an explanation for why the vertical leakage (P_{SF-}) nearly doubles in Case 5 compared to Case 2.

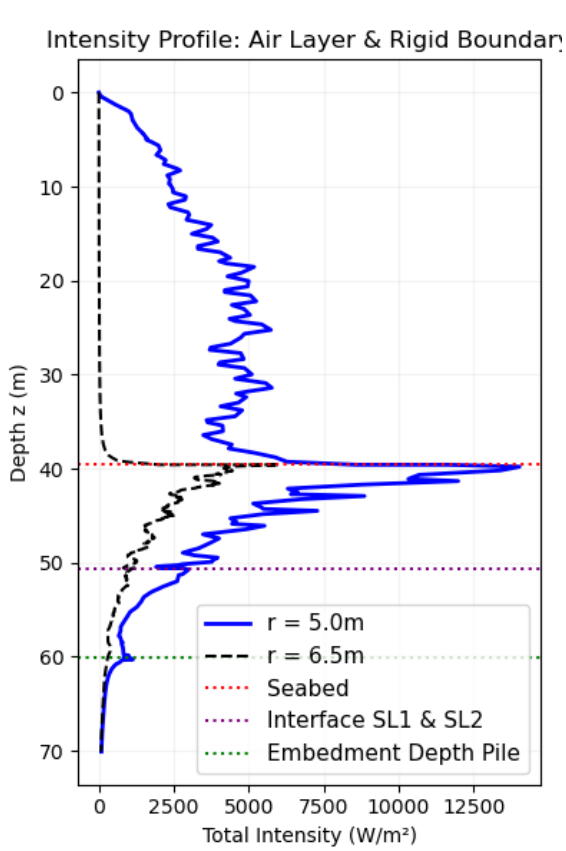

(a) Full-scale intensity magnitude profile.

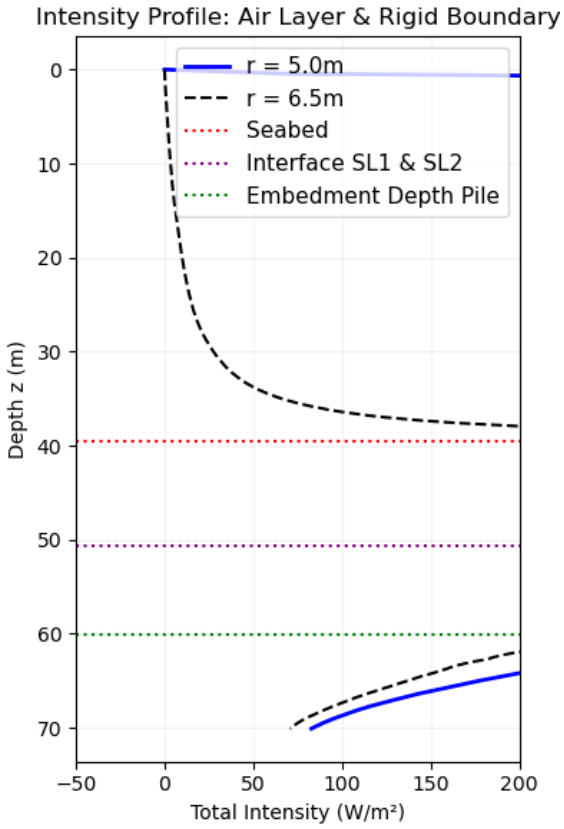

(b) Detailed profile (-50–200 W/m^2) highlighting the intensity magnitude at $r = 5.0\,m$.

Figure H.9: Intensity magnitude $|\vec{I}|$ as a function of depth for Case 5 (air layer and rigid boundary) at $r = 5.0\,m$ and $r = 6.5\,m$.

Key Findings

The main behavior observed in Case 2 and Case 3 is largely consistent with that of Case 5. The air layer reflects a significant portion of the acoustic energy, causing it to remain trapped within the cavity and subsequently be transferred into the soil. The soil then re□radiates part of this energy back into the water column behind the barrier.

In addition, the intensity-over-depth profiles behind the barrier exhibit behavior that differs from Case 2. An exponentially decaying intensity profile is observed in the water column near the seabed, which corresponds to the characteristic behavior of a Scholte wave. This implies that introducing a rigid boundary behind the air layer hinders energy dissipation by the low frequency excitation of the air layer. As a result, this energy is instead converted into an amplified Scholte wave component, which leads to an increase in the calculated SEL.

H.3. Conclusion

This case study of various simplified NMS configurations demonstrates that while the model captures some noise reduction, a direct match with the measured data remains difficult to achieve using these simplified representations. This discrepancy is attributed to the high degree of uncertainty regarding the physical parameters of the NMS, as well as the limitations of the 2D axisymmetric framework, which cannot fully account for the non-axisymmetric components of the NMS frame.

To reduce these uncertainties, the subsequent stages of this research focus on Case 2, in which the air layer is adopted as the representative model for the NMS. This approach is justified because the air layer functions as the primary mitigation mechanism within the NMS. From a theoretical perspective, this impedance boundary reflects the vast majority of the incident acoustic energy back toward the MP,

thereby limiting the amount of energy propagating into the far field.

In contrast, the parameters governing the bubble layer are uncertain and were an assumption in Case 4. Moreover, this case study revealed that several aspects of the outer shell of the NMS are still not fully understood and cannot yet be explained. Consequently, further investigation into the behavior and functional role of the outer shell is required before it can be incorporated into NMS modeling.

H.3.1. Neglecting Back-Scattering from Air Layer

The current model is governed by linear acoustic equations, which assume only small perturbations. In practice, this assumption may be violated in the immediate vicinity of the MP, where large displacements and high acoustic pressure amplitudes occur, potentially giving rise to nonlinear acoustic effects

In this alternative approach, the reflections from the air layer are intentionally omitted since the linear model cannot accurately capture the real behavior inside the cavity. Instead, the incident waves are scaled by a transfer function derived from the impedance mismatch between water and air. Consequently, the pressure and velocity magnitudes are reduced as they pass through the boundary, and this attenuated field is then propagated into the far-field. In this simplified modeling framework, the enlarged secondary noise path, where trapped energy is pumped into the soil inside the cavity and subsequently re-radiated into the water column behind the barrier, is not represented.

In 1D wave propagation, the pressure transmission coefficient at an interface between two media is defined by Jensen et al. (2011) as shown in Eq. H.2:

$$T = \frac{2Z_2}{Z_2 + Z_1} \tag{H.2}$$

The transmission through the air layer is determined by scaling the incident wave field first by the transmission coefficient from water to air (T_{wa}), and subsequently by the coefficient from air to water (T_{aw}).

The pressure and particle velocity components extracted from the unmitigated COMSOL model at $r = 6.19\,m$ (location of the NMS) are scaled as follows:

$$p_{silence}(z,f) = p_{comsol}(z,f) \cdot \frac{2Z_a}{Z_a + Z_w} \cdot \frac{2Z_w}{Z_w + Z_a} = p_{comsol}(z,f) \cdot 0.001115$$

$$v_{r,silence}(z,f) = v_{r,comsol}(z,f) \cdot 0.001115$$

$$v_{z,silence}(z,f) = v_{z,comsol}(z,f) \cdot 0.001115$$

Applying this approach yields a broadband SEL of 159.5 dB at 750 m from the pile and 2 m above the seabed. Figure H.10 illustrates the one third octave band spectra for the air layer model (Case 2), the newly proposed model neglecting back-scattering, and the measured data.

It is observed that neglecting back-scattering results in an improved alignment of the low-frequency content with the measured data. In contrast, the air layer model tends to overestimate these lower frequencies, as they propagate through the relatively thin air layer compared to the low-frequency wavelengths.

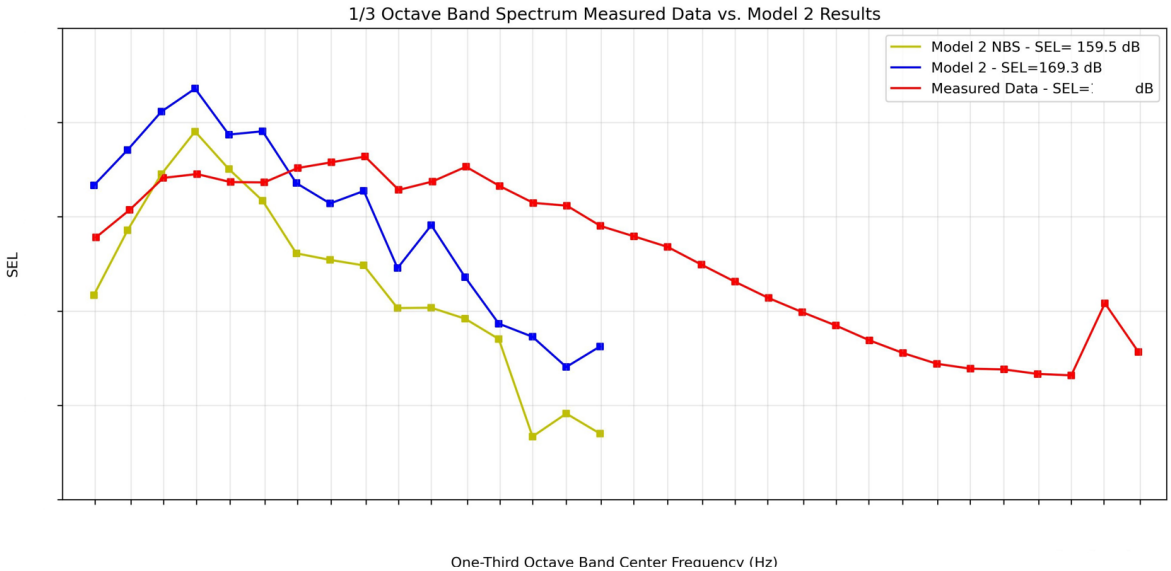

Figure H.10: One third octave band spectrum which compares Model 2 results using the air layer as NMS (Case 2) and the new proposed model where back scattering is neglected (NBS).

This indicates that simplifying the NMS as a 1D wave propagation problem by applying a transmission coefficient, significantly decreases the simulated noise levels, dropping even below the empirical measured data.

For the subsequent phases of this study, the focus will remain on the air layer as the modeled NMS. However, it must be noted that neglecting back-scattering provides a ”lower bound” for noise levels of the NMS, as it assumes only the impedance mismatch. In contrast, the air layer model accounts for back-scattering and resonances inside the cavity, albeit within a linear modeling framework that cannot account for the non-linear effects present in an environment.

H.3.2. Influence of Soil

A finding of this case study is that the high reflectivity of the air layer creates an acoustic cavity between the MP and the NMS. Because the energy is blocked from traveling horizontally through the water column, a significant proportion of the energy is forced downward and injected into the seabed.

Consequently, the performance of the NMS is no longer only dependent on the air layer itself, but is significantly dependent on the properties of the soil. By isolating the air layer as the main mitigation variable, the next phase of this study investigates how different soil compositions influence the leakage of energy back into the far field water column.

I

Model Input Parameters

In this section, all input variables used for the SGM and SPM are presented for the different models described in Section 4.1. The SGM input parameters are provided in Section I.1, while the corresponding SPM input parameters are summarized in Section I.2.

I.1. Sound Generation Module: Input Variables

In this section, all input variables used in the SGM are presented. The section is structured into several subsections. First, the frequency and force input parameters are introduced. Next, the material properties of the MP steel, the water, and the soil layers are described. Finally, the parameters related to the extraction of wave field data from the SGM are discussed.

I.1.1. Frequency & Force Parameters

The hammer force used in this study is described in Section 3.4. In the SGM model, this force is applied as a vertical load on the top of the pile. Figure 3.8 in Section 3.4 illustrates the frequency components of the hammering force. This figure shows that beyond 600 Hz, the amplitude becomes significantly smaller compared to lower frequencies. Therefore, the frequency range for which the numerical model is solved is up to 600 Hz. This ensures that all the important parts of the force are included while reducing the calculation time.

In this study, the modeling is done for a position of 750 m and 1500 m from the MP. The analysis duration must therefore be sufficient for sound waves to propagate across 1500 m. Given that the speed of sound in water is approximately 1500 m/s (Peng, Tsouvalas, and Metrikine, 2020), the minimum required duration for the analysis is:

$$T_{min} = \frac{1500\,m}{1500\,m/s} = 1.0\,s$$

To account for potential variations and dispersion of the wave field, a conservative duration of 2 s is selected for the time duration of the model T. Using $T = 2\,s$ all other frequency and time parameters for the modeling can be identified and are presented in Table I.1.

In the SGM, an unit force is applied as input rather than the actual hammer force measured during pile driving. This approach is based on the assumption that the system behaves linearly with respect to the excitation force, meaning that the resulting sound pressure scales proportionally with the applied force. By using a unit force, the model computes a normalized acoustic response, e.g. transfer function. This normalization offers the advantage that the model only needs to be solved once for the unit force, avoiding repeated simulations for different force magnitudes (see Section 4.2.4).

Parameter	Value	Unit	Remark
T	2.0	s	Total analysis duration.
df	0.5	Hz	Frequency resolution, calculated as $df = \frac{1}{T}$.
f_0	0.5	Hz	Start frequency of the analysis, chosen equal to df.
$f_{\max}$	600	Hz	Maximum frequency used in the propagation model.
N_f	1200	–	Number of frequency points, computed as $\left(\frac{f_{\max}-f_0}{df}\right)+1$.
N_t	2400	–	Number of time samples, calculated as $N_t = 2N_f$.
Δt	0.000833	s	Time-step size, computed as $\Delta t = \frac{T}{N_t}$.
F_z	1	MN	External force applied at the pile head

Table I.1: Time and frequency domain input parameters used in the SGM simulations for Model 1 and 2.

I.1.2. Material Properties

The model setup and its required parameters are shown in Figure 4.2. In this subsection, the material properties of the different domains are presented. First, the material parameters of the pile and the water are described, followed by the properties of the soil layers.

Pile & Water Parameters

The MPs considered in this study are made of S355 steel. The corresponding material properties are listed in Table I.2. These values are based on the typical values provided in Eurocode 3 and the wave speeds obtained using Eqs. I.1 and I.2, which define the compressional and shear wave velocities of steel in accordance with Eurocode 3.

$$c_p = \sqrt{\frac{E(1-\nu)}{\rho(1+\nu)(1-2\nu)}} \tag{I.1}$$

$$c_s = \sqrt{\frac{E}{2\rho(1+\nu)}} \tag{I.2}$$

Parameter	Value	Unit	Remark
-	S355	$-$	Steel grade used for MP construction
ρ_{MP}	7850	kg/m^3	Density of MP material (European Committee for Standardization, 2005)
ν_{MP}	0.28	$--$	Poisson's ratio (Eurocode 3)
E_{MP}	210	GPa	Young's modulus (Eurocode 3)
$c_{p,MP}$	5848	m/s	Compressional wave speed of steel, calculated as Eq. I.1
$c_{s,MP}$	3233	m/s	Shear wave speed of steel, calculated as Eq. I.1

Table I.2: MP material properties used as input for the SGM for Model 1 and 2.

Table I.3 gives an overview of the input parameters related to the water layer.

The water column is modeled as a homogeneous fluid. The speed of sound in water is assumed constant. In reality, sound speed varies with factors such as salinity, temperature, and hydrostatic pressure; for the frequency range considered in this study (up to 600 Hz), the formation of dominant sound channels is unlikely (Jensen et al., 2011). Therefore, stratification effects such as temperature and salinity gradients are neglected, and seawater is assumed to have uniform properties throughout the depth (Jensen et al., 2011). Furthermore, due to the relatively shallow water depth, variations in hydrostatic pressure have a negligible influence on the speed of sound. Consequently, the sound speed is treated as constant across the entire water column. In addition, the bathymetry is assumed constant, which is a common simplification in underwater acoustic models for near-field wave propagation (approximately 1–2 km) (Tsouvalas, 2025). This assumption is further supported by the bathymetric data of the surrounding MPs at pile E, where no significant variations in water depth are observed. Consequently, treating the bathymetry as horizontally uniform is considered a valid approximation for this study.

Parameter	Value	Unit	Remark
ρ_{water}	1025	kg/m^3	Typical value
c_{water}	1500	m/s	Typical value

Table I.3: Input parameters for the SGM related to the air and water properties and the force for Model 1 and 2.

Soil Parameters

Table I.4 summarizes the defined soil layering for the two models, based on Section 3.3.

Model	Layer	Depth [m LAT]	Thickness [m]
Model 1 & 2	SL1	39.58–50.58	11.00
	SL2	50.58–70.08	19.50

Table I.4: Soil layering defined based on the CPT data for tModel 1 and 2. Depths are referenced to LAT.

For acoustic and elastodynamic modeling, the pressure wave speed (c_p), shear wave speed (c_s), and soil density (ρ) must be defined for each soil layer. These parameters serve as input for the SGM.

Because the literature provides a wide range of empirical relationships for estimating soil wave speeds and densities, a soil calibration study was performed to identify which parameter set best represents the soil behavior at the wind farm site. The selected literature with their resulted soil parameters are shown in Figure I.1 and are summarized below.

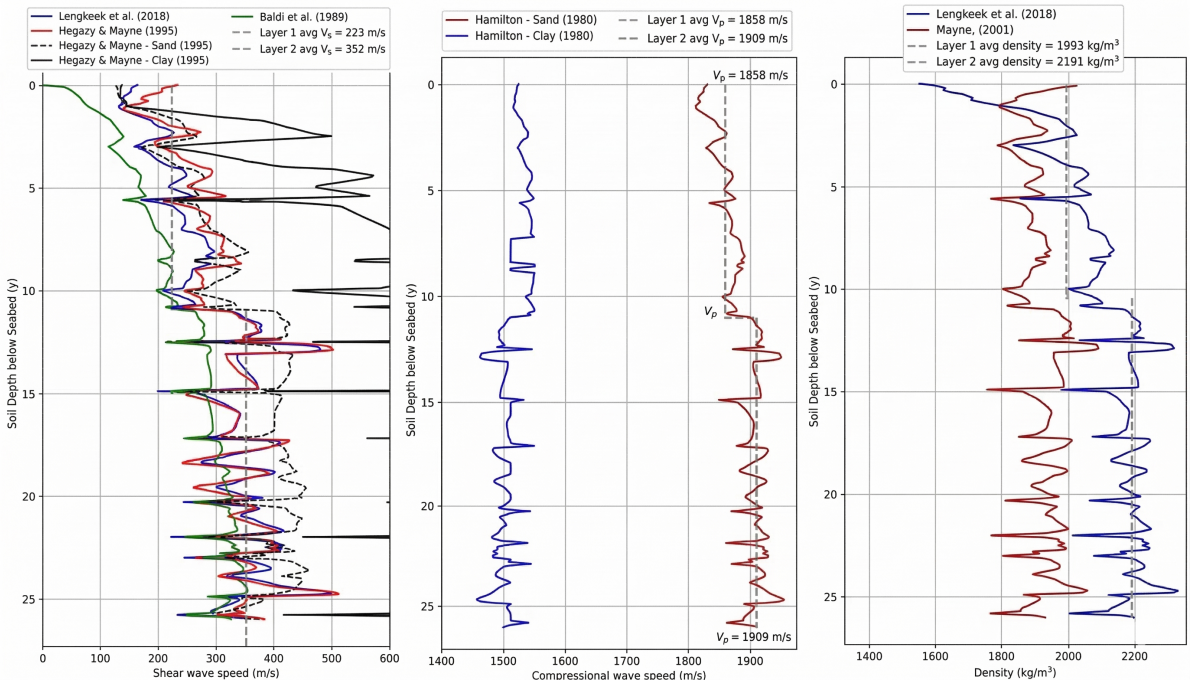

Figure I.1: Results from the soil calibration process using different literature sources. The dashed grey line represents the final selected parameter set. The left plot shows the shear wave speed estimates based on Lengkeek, De Greef, and Joosten (2018), Hegazy and P. Mayne (1995) and Baldi et al. (1989). The middle plot presents the compressional wave speed results derived from Hamilton (1980). The right plot shows the density values obtained from Hegazy and P. Mayne (1995) and P. W. Mayne (2001).

The left plot of Figure I.1 presents shear wave speed profiles from various literature sources. Since the wind farm site consists mainly of sand, the clay based relationship were discarded. Based on the sand curves, a shear wave speed of 223 m/s was selected for the upper soil layer and 352 m/s for the underlying layer.

For compressional wave speed, only the relationship from Hamilton (1980) was considered. This results in an assumed compressional wave speed of 1858 m/s for the upper layer and 1909 m/s for the lower layer.

Finally, soil density was assessed using two literature references. Following the empirical CPT based relationship in Lengkeek, De Greef, and Joosten (2018), the density was estimated as 1993 kg/m^3 for the upper layer and 2191 kg/m^3 for the lower layer.

Because empirical relationships carry uncertainty and the soil calibration study indicated that a stiffer soil improves agreement with measured behavior, an uncertainty factor of +15% was applied to all real parts of the wave speeds and the densities. The real part of the wave speeds and the densities are listed in Table I.5.

	Parameter	Unit	Assumed Value	Value (+15%)	Reference
SL1	$c_{s,\mathbb{R}}$	m/s	223	256.5	Hegazy and P. Mayne (1995)
	$c_{p,\mathbb{R}}$	m/s	1858	2137	Hamilton (1980)
	ρ	kg/m^3	1993	2292	Lengkeek, De Greef, and Joosten (2018)
SL2	$c_{s,\mathbb{R}}$	m/s	352	404.8	Hegazy and P. Mayne (1995)
	$c_{p,\mathbb{R}}$	m/s	1909	2195	Hamilton (1980)
	ρ	kg/m^3	2191	2520	Lengkeek, De Greef, and Joosten (2018)

Table I.5: Real parts of the wave speed and the densities used after applying a +15% uncertainty factor for Model 1 and 2.

To account for energy dissipation in soils, wave speeds are modeled as complex quantities: the real part represents phase velocity, and the imaginary part accounts for attenuation. Attenuation is expressed in decibels per wavelength (dB/λ) and depends on frequency and empirical constants k_s and k_p (Hamilton, 1980).

Based on Figures I.2 and I.3, together with the soil parameter calibration results, the following values are selected: for the upper soil layer, $k_s = 10.29$ and $k_p = 0.433$, for the underlying layer, $k_s = 6.64$ and $k_p = 0.392$.

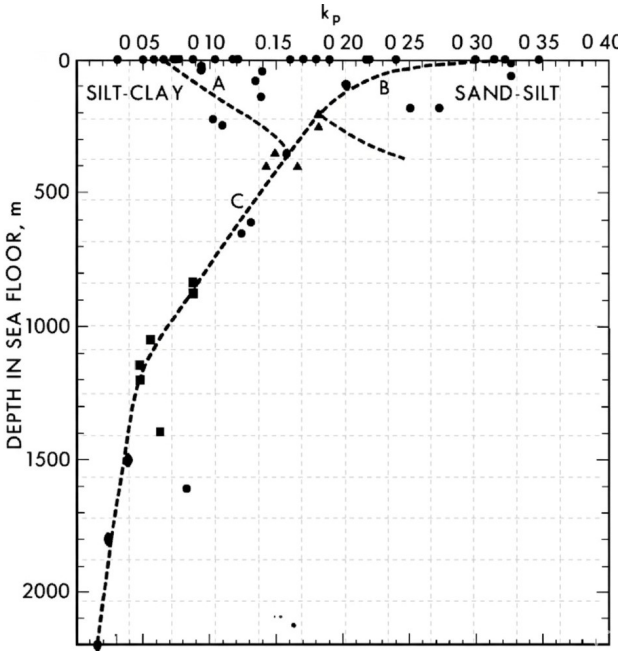

Figure I.2: k_p values from Hamilton (1980)

Material	k_s in $\alpha_s = k_s f$
Diluvial sand	13,2
Diluvial sand and clay	4,8
Alluvial silt	13,4
Mud (silt-clay)	17,3
Water-saturated clay	15,2
Tertiary mudstone	10,1
Pierre shale	3,4
Solenhofen limestone	0,02 to 0,05
Chalk	0,1
Basalt	0,07

Figure I.3: k_s values from Hamilton (1980)

The governing equations for complex wave speed and attenuation are given in Eqs. I.3–I.6. The real part of the shear wave speed and pressure wave speed are presented in table I.5. In the equations below, $\eta = (40\pi \log_{10}(e))^{-1}$:

$$\alpha_s = k_s \frac{c_s}{1000} \tag{I.3}$$

$$c_s = \frac{c_{s,\mathbb{R}}}{1 - \eta^2 \alpha_s^2} + i \frac{c_{s,\mathbb{R}} \eta \alpha_s}{1 - \eta^2 \alpha_s^2} \tag{I.4}$$

$$\alpha_p = k_p \frac{c_{p,\mathbb{R}}}{1000} \tag{I.5}$$

$$c_p = \frac{c_{p,\mathbb{R}}}{1 - \eta^2 \alpha_p^2} + i \frac{c_{p,\mathbb{R}} \eta \alpha_p}{1 - \eta^2 \alpha_p^2} \tag{I.6}$$

Table I.6 presents the soil parameters used for the SGM.

Parameter	Unit	SL1	SL2
$c_{s,\mathbb{R}}$	m/s	256.5	404.8
k_s	–	10.29	6.64
α_s	dB/λ	2.64	2.69
c_s	m/s	255.9 + 12.4i	404.8 + 19.9i
$c_{p,\mathbb{R}}$	m/s	2137	2195
k_p	–	0.433	0.392
α_p	dB/λ	0.93	0.86
c_p	m/s	2136 + 36.2i	2195 + 34.6i
ρ	kg/m^3	2292	2520

Table I.6: Calculated wave properties for Model 1 and 2. SL1 and SL2 represent the upper and lower soil layers, respectively. The comple wave speed and the densities are used as input for the SGM.

I.1.3. Meshing Strategy

An important aspect of FEM is the appropriate construction of the mesh. Acoustic fields satisfy the wave equation and therefore exhibit oscillatory behavior in both space and time. These oscillations are characterized by the wavelength λ, which depends on the sound speed c and the frequency f through $\lambda = c/f$. To accurately reproduce wave propagation, the mesh must be sufficiently fine to resolve these spatial variations. In practice, this requires the element size to be smaller than the shortest wavelength present in the model, corresponding to the highest frequency considered (Papadakis and Stavroulakis, 2018).

Although a minimum of two elements per wavelength is theoretically enough to represent a sinusoid, such a coarse discretization does not capture correct mode shapes and leads to numerical dispersion. Therefore, a more conservative resolution, typically three to five elements per wavelength, is recommended for vibroacoustic analyses (Schmiechen, 1997).

The accuracy of FEM solutions for coupled vibro-acoustic problems is thus strongly linked to the ratio between element size and wavelength. In this study, the air, water, soil and pile domains are discretized in COMSOL Multiphysics.

To ensure that all relevant frequencies are resolved the maximum element size h_{max} is defined based on the shortest wavelength λ_{min} in each medium for the highest analyzed frequency $f_{max} = 600\,Hz$. The applied mesh criterion is:

$$h_{max} = \frac{\lambda_{min}}{N} = \frac{c_{medium}}{f_{max} \cdot N} \tag{I.7}$$

where:

- c_{medium} is the speed of sound in the corresponding domain
- f_{max} is the maximum frequency of interest ($600\,Hz$).
- N is the number of elements per wavelength.

Table I.7 summarizes the meshing parameters. For the soil domain, the smallest shear wave speed c_s (soil layer 1) is used to define the mesh resolution across the entire seabed. This ensures that even the shortest wavelengths occurring in the soil are adequately resolved.

Domain	c [m/s]	Maximum Frequency	N	h_{max} [m]	Discretizations Logic
Fluid	1500	600	5	0.5	Primary acoustic medium; high resolution for pressure wave accuracy.
SL1	256.5	600	4	0.107	Smallest wave speed used to resolve the shortest wavelengths; $N = 4$ balances accuracy and computational time.
SL2	404.8	600	4	0.167	Smallest wave speed used to resolve the shortest wavelengths; $N = 4$ balances accuracy and computational time.
Air	350	600	5	0.117	High resolution to capture near field behavior

Table I.7: Summary of domain-specific meshing parameters and wave resolution logic. The air domain is only applied in Model 2. The fluid, SL1, and SL2 domains are applied in Model 1 and Model 2.

I.1.4. Extraction of Coupling Data

After running the COMSOL Multiphysics model, the wave field data are extracted on a specified boundary surface, which serves as input for the SPM. Table I.8 lists the extracted variables, together with the extraction radius and the vertical sampling applied along the boundary. To avoid numerical inaccuracies at the domain interfaces, the extraction starts 0.001 m downwards from the domain boundary.

Each output file generated by COMSOL contains the data for all $N_{z_s,pro}$ vertical sampling points, and for each depth the full set of N_f frequency components is provided. All extracted quantities are complex-valued, representing both amplitude and phase information required for the subsequent propagation in the SPM.

Quantity	Unit	$r_{s,pro}$	$\Delta z_{s,pro}$	z–range	$N_{z_s,pro}$
Pressure (p)	Pa	55	0.5	$[z_0 + \Delta z_{s,pro},\ z_2 - \Delta z_{s,pro}]$	77
Particle velocity, v_r	m/s	55	0.5	$[z_0 + \Delta z_{s,pro},\ z_2 - \Delta z_{s,pro}]$	77
Particle velocity, v_z	m/s	55	0.5	$[z_0 + \Delta z_{s,pro},\ z_2 - \Delta z_{s,pro}]$	77
Stress σ_{rr}	Pa	55	0.5	$[z_2 + \Delta z_{s,pro},\ z_{bot} - \Delta z_{s,pro}]$	43
Stress σ_{rz}	Pa	55	0.5	$[z_2 + \Delta z_{s,pro},\ z_{bot} - \Delta z_{s,pro}]$	43
Stress σ_{zz}	Pa	55	0.5	$[z_2 + \Delta z_{s,pro},\ z_{bot} - \Delta z_{s,pro}]$	43
Stress $\sigma_{\theta\theta}$	Pa	55	0.5	$[z_2 + \Delta z_{s,pro},\ z_{bot} - \Delta z_{s,pro}]$	43
Displacement u_r	m	55	0.5	$[z_2 + \Delta z_{s,pro},\ z_{bot} - \Delta z_{s,pro}]$	43
Displacement u_z	m	55	0.5	$[z_2 + \Delta z_{s,pro},\ z_{bot} - \Delta z_{s,pro}]$	43

Table I.8: Overview of the wave field quantities extracted at the SGM boundary and transferred to the SPM. For each variable, the extraction radius $r_{s,pro}$, vertical sampling interval $\Delta z_{s,pro}$, vertical extraction range, and number of sampling points $N_{z_s,pro}$ are listed. Within the soil domain, the available sampling points in the range $[z_2 + \Delta z_{s,pro},\ z_{bot} - \Delta z_{s,pro}]$ are reduced by selecting a subset of the first 48 values to limit computational cost.

I.2. Sound Propagation Module: Input Variables

Since a coupled modeling approach is employed, many input parameters in the SGM and SPM are aligned to ensure consistency between both models. However, the SPM requires additional input variables, and some parameters are defined slightly differently. This section presents the frequency and time parameters, the material properties, and the source and receiver input variables used in the SPM.

I.2.1. Frequency & Time Parameters

The SPM must employ the same frequency and time parameters as the SGM to ensure that the frequency-domain solutions are fully aligned. The only additional parameter required by the SPM is the index of the first frequency to be included in the simulation, which in this study corresponds to the first element of the frequency vector.

All remaining frequency- and time-domain parameters match those used in the SGM. For completeness, the input parameters of the SPM are summarized in Table I.9.

Parameter	Value	Unit	Remark
$freq_{1st}$	1	–	Index of the first frequency used in the SPM simulation.
T	2.0	s	Total analysis duration.
df	0.5	Hz	Frequency resolution, calculated as $df = \frac{1}{T}$.
$f_{\max}$	600	Hz	Maximum frequency used in the propagation model.
f_0	0.5	Hz	Start frequency of the analysis, chosen equal to df.
$freq$	range(f_0, $f_0 + df \cdot (N_f - 1)$, N_f)	Hz	Frequency array used in the SPM analysis.
n_f	1200	–	Number of frequency points, computed as $\left(\frac{f_{\max} - f_0}{df}\right) + 1$.
N_f	1200	–	Total number of frequencies evaluated; for full-spectrum analysis, $N_f = n_f$.
N_t	2400	–	Number of time samples, calculated as $N_t = 2N_f$.
Δt	0.000833	s	Time-step size, calculated as $\Delta t = \frac{T}{N_t}$.

Table I.9: Frequency- and time-domain input parameters used in the SPM simulations.

Force

In the SPM domain, no external force is applied because the impact force acts on the MP, which lies outside the SPM domain. After running the SILENCE model, the computed pressure at the hydrophone location must therefore be scaled by the actual forcing, as described in Section 4.2.4. Here, $F(\omega)$ denotes the force in the frequency domain.

The force in the time domain is known and is presented in Section 3.4. This force-time diagram corresponds to a nominal hammer blow energy of 5500 kJ. In practice, however, the actual energy transmitted into the pile during installation is lower. Although, in principle, the force-time signal could be scaled using the ratio between the measured blow energy and 5500 kJ, this approach was not applied in the present study. The relationship between blow energy and the resulting force-time response is not strictly linear due to energy losses and non-linear interactions within the hammer-pile-soil system. Applying scaling based on energy could therefore introduce additional uncertainty.

Instead, the nominal 5500 kJ force-time diagram is used directly and transformed into the frequency domain using a Fourier transform to obtain $F(\omega)$. This frequency domain force is subsequently multiplied with the unit load pressure response obtained from SILENCE to compute the final pressure field.

The measured blow energy is nevertheless reported for each model in Table I.10 to provide context for the modeled scenarios. These values are obtained from blow log measurements provided by HMC and averaged over a penetration interval of 0.5 m to reduce the influence of outliers.

Parameter	Unit	Model 1	Model 2
Force average range	m	[24.50–25.00]	[20.25–20.75]
PULSE liquid height	–	Smoothed exponential	700 mm
E_{actual}	kJ	4871	5168
E_{max}	kJ	5500	5500
Ratio	—	0.886	0.940

Table I.10: Scaling factors used to adjust the nominal 5500 kJ force-time diagram to the actual force applied during piling. The value of E_{actual} is based on the measured blow energy provided by HMC. To minimise the influence of outliers, blow energy is averaged over a 0.5 m penetration interval. The penetration depth interval over which this averaging is performed is listed as "average range".

I.2.2. Material Properties

The model setup and its required parameters are shown in Figure 4.5. In this subsection, the material properties of the different domains are presented. First, the material parameters of the water are described, followed by the input variables of the soil layers of the SPM.

Water Parameters

In the SPM, no MP is modeled because the pile is not part of the far-field domain. Consequently, no pile related parameters are required as input. The water column, however, is included in the SPM. To ensure consistency between the SGM and SPM, the same water properties are used in both modules. The relevant water parameters can be found in Table I.3.

Soil Parameters

For the SPM, additional soil parameters are required compared to the SGM. Specifically, the density, compressional- and shear-wave attenuation coefficients, Young's modulus, and Poisson's ratio must be provided as input. Some of these quantities are already known from the SGM, while the remaining parameters are computed using Eqs. I.8–I.11. Table I.11 summarizes all soil input parameters and their values for each model for the SPM.

$$\lambda = \rho \left(c_{p,\mathbb{R}}^2 - 2c_{s,\mathbb{R}}^2 \right) \tag{I.8}$$

$$\mu = \rho c_{s,\mathbb{R}}^2 \tag{I.9}$$

$$E = \frac{\mu(3\lambda + 2\mu)}{\lambda + \mu} \tag{I.10}$$

$$\nu = \frac{\lambda}{2(\lambda + \mu)} \tag{I.11}$$

Parameter	Unit	SL1	SL2	Description
λ	GPa	6.53	6.68	First Lamé parameter, computed using Eq. I.8. The parameters $c_{s,\mathbb{R}}$, and ρ, $c_{p,\mathbb{R}}$ are taken from Table I.6.
μ	MPa	131	273	Second Lamé parameter (shear modulus), computed using Eq. I.9. The parameter ρ is taken from Table I.6.
ρ	kg/m^3	1931	1967	Soil density. Values given in Table I.6.
α_p	dB/λ	0.446	0.498	Compressional wave attenuation coefficient. Values given in Table I.6.
α_s	dB/λ	3.49	4.92	Shear wave attenuation coefficient. Values given in Table I.6.
E	MPa	390	809	Young's modulus calculated using Eq. I.10
ν	–	0.490	0.48	Poisson's ratio, computed using Eq. I.11.

Table I.11: Soil parameters for the SPM for Model 1 and 2. Numerical values of ρ, c_p, c_s, α_p, and α_s for each layer and model are provided in Table I.6.

I.2.3. Source & Receiver Parameters

In the SPM, the wave field data extracted from the SGM are interpreted as sources that radiate sound into the layered water–seabed environment. The source parameters defined in the SPM must therefore be consistent with the extraction settings used in the SGM, such as the extraction radius and the vertical sampling resolution.

In addition to the source definition, receiver locations must be specified. These receivers represent the positions at which underwater noise levels are evaluated. In this study, two receiver points are of interest: the measurement locations at 750m and 1500m from the MP, both positioned 2m above the seabed. These correspond directly to the hydrophone positions used during the wind farm installation measurements.

Table I.12 summarizes the source and receiver parameters used in the SPM for all modeled scenarios.

Parameter	Unit	Value	Description
$r_{s,pro}$	m	30	Extraction radius: location of equivalent sources (consistent with SGM).
$\Delta z_{s,pro}$	m	0.5	Vertical spacing between source points on the extraction boundary.
$N_{z_{s,pro}}$	–	180	Number of source points along the vertical extraction line (79 in water + 101 in soil).
$r_{0,pro}$	m	750	First receiver radius in the r-grid.
Δr_{pro}	m	750	Radial spacing between receivers; chosen such that receivers occur at 750m and 1500m.
$N_{r_{r,pro}}$	–	2	Number of receivers in the r-grid (at 750m and 1500m).
$z_{0,pro}$	m	$T_{WD} - 2$	Receiver depth: 2m above the seabed.
Δz_{pro}	m	arbitrary	Vertical receiver spacing (irrelevant here because $N_{z_{r,pro}} = 1$).
$N_{z_{r,pro}}$	–	1	Number of receivers in the vertical grid (only one depth considered).

Table I.12: Source and receiver parameters used in the SPM. Source definitions correspond directly to the SGM extraction settings, ensuring consistent coupling between the two modules. Receiver positions represent the hydrophone locations used during the wind farm measurements.

J

Description of Sensitivity Analysis Model 1 & 2

To validate Model 1 and Model 2, a sensitivity analysis is performed to ensure that none of the modeling assumptions introduced to reduce computational time compromise the accuracy of the results. The sensitivity analysis examines four parameters: the mesh size, the frequency range, the truncation domain of the SGM, and the extraction radius used to obtain the wave field within the SGM. The mesh size is evaluated in Subsection J.1, the truncation frequency range in Subsection J.2, and the truncation domain of the SGM in Subsection J.3. Finally, Subsection J.4 assesses the sensitivity to the extraction radius.

J.1. Sensitivity to Mesh Size

Accurate spatial discretizations is fundamental for a FEM model. The mesh determines how well the numerical solution captures the wavelengths present in the system. If the mesh is too coarse relative to the smallest wavelengths of interest, numerical dispersion and artificial attenuation occur (Kriščiūnas et al., 2016). This leads to an under prediction of sound levels, especially at higher frequencies. Conversely, a sufficiency fine mesh ensures that the wave field is represented in a correct way.

In this study, mesh sensitivity is relevant to check since the impact force contains broadband components, meaning that the model must resolve wavelengths spanning over a broad frequency range. Higher frequencies have shorter wavelengths and are most sensitive to insufficient mesh density. If these frequencies are not properly captured, the model will lose energy, leading to incorrect SEL and L_{peak} values.

By verifying that mesh refinements does not alter the predicted noise levels, the analysis confirms that the mesh chosen for the OM balances accuracy and computational efficiency. If significant differences appear, further refinement is required to avoid under resolving higher frequency components.

The mesh size in the Original Model (OM) is determined based on the maximum modeled frequency, the wave speed in each domain, and the required numerical accuracy. A more detailed explanation of the meshing strategy is provided in Subsection I.1.3.

In the Sensitivity Analysis Model (SAM), the model is re-run with a uniformly refined mesh, using a mesh size that is 20% smaller in each domain. An overview of the mesh parameters used in both the OM and SAM is presented in Table J.1.

Domain	**OM:** $\mathbf{h_{max}}$ **[m]**	**SAM:** $\mathbf{h_{max}}$ **[m]**
Fluid	0.500	0.400
SL1	0.142	0.114
SL2	0.225	0.180
Air	0.117	0.094

Table J.1: Overview of the Original Model (OM) mesh size and the Sensitivity Analysis Model (SAM) mesh size. The SAM are calculated as 0.8 times the mesh size used in the OM.

The results are presented in Table J.2. The comparison shows that the SAM and OM outputs do not differ much. This indicates that further mesh refinement does not lead to higher noise levels. Therefore, the mesh used in the OM is sufficiently fine to allow all relevant frequencies to propagate through the model. If this had not been the case, the SAM would have exhibited higher noise levels, because the finer mesh would have allowed high-frequency components (which cannot be accurately resolved in the OM) to propagate correctly.

Model	Noise Metric	OM Result [dB]	SAM Result [dB]
1	SEL at 750 m	177.9	177.9
	L_{peak} at 750 m	197.6	197.6
2	SEL at 750 m	169.2	169.3
	L_{peak} at 750 m	180.6	180.6

Table J.2: Comparison of the mesh Sensitivity Analysis Model (SAM) with the Original Model (OM) for both Model 1 and Model 2. The results show no significant differences between the OM and SAM, confirming that the mesh size used in the OM is sufficient for accurate model results.

J.2. Sensitivity to Frequency Range

In frequency domain modeling, the choice of maximum modeled frequency determines which parts of the wave field can be represented in the numerical solution. Each frequency component corresponds to a specific wavelength, and together they reconstruct the full time domain signal. Truncating the frequency range removes the shorter wavelengths associated with the high frequency content. Although this reduces computational cost, it risks omitting relevant portions of the spectrum.

Assessing the sensitivity to the selected frequency range is therefore essential for several reasons:

- As mentioned in Subsection J.1, impact piling excites a broadband spectrum. While the force spectrum often decays at higher frequencies, even small high frequency contributions play an important role in shaping the waveform, particularly its peak amplitude (Jensen et al., 2011). If the upper frequency limit is chosen too low, the model may not accurately reconstruct the impulsive nature of the signal, leading to an underestimation of mainly L_{peak}.
- The sharpness of the initial pressure arrival is controlled by high frequency content (Jensen et al., 2011). Truncating frequencies removes the narrow peaks responsible for the steep front wave. This is particularly important because the noise metric L_{peak} depends on instantaneous pressure which is sensitive to these high frequency components. Conversely, lower frequencies dominate the total acoustic energy, which explains why SEL is typically less sensitive to frequency truncation. Evaluating a higher frequency limit ensures that the chosen truncation preserves the correct wave field.

By verifying that extending frequency range does not alter the resulting noise levels, the analysis confirms that the truncated upper frequency limit is sufficient for accurately capturing the noise propagation. If substantial differences are observed, a higher maximum frequency is required to avoid underpredicting peak pressures.

The maximum frequency solved by the model is based on the frequency spectrum of the hammer force, presented in Section 3.4, where the force amplitude is significantly smaller for frequencies above 600 Hz compared to lower frequencies. Therefore, limiting the model to 600 Hz was considered an efficient and reasonable assumption.

To assess whether the truncated frequency range influences the results, the OM is re-run using an extended frequency range. Specifically, the model is solved for frequencies between 0.5 and 800 Hz with a resolution of 0.5 Hz. The corresponding time and frequency domain input parameters for both the OM and the SAM are given in Table J.3.

Parameter	OM Value	SAM Value	Unit	Remark
T	2.0	2.0	s	Total analysis duration.
df	0.5	0.5	Hz	Frequency resolution, calculated as $df = \frac{1}{T}$.
f_0	0.5	0.5	Hz	Start frequency of the analysis, chosen equal to df.
$f_{\max}$	600	800	Hz	Maximum frequency used in the propagation model.
N_f	1200	1600	–	Number of frequency points, computed as $\left(\frac{f_{\max}-f_0}{df}\right)+1$.
N_t	2400	3200	–	Number of time samples, calculated as $N_t = 2N_f$.
Δt	0.000833	0.000625	s	Time-step size, computed as $\Delta t = \frac{T}{N_t}$.

Table J.3: Time and frequency domain input parameters used in the Original Model (OM) and Sensitivity Analysis Model (SAM). The SAM extends the maximum modeled frequency to assess whether the truncated frequency range in the OM influences the results.

The results of the frequency range sensitivity analysis are presented in Table J.4. The comparison shows that the SAM and OM outputs do not differ significantly in SEL and L_{peak}. This indicates that extending the maximum modeled frequency to 800 Hz does not lead to higher noise levels. Therefore, the truncated frequency range used in the OM is sufficient to accurately capture all relevant frequency components in the input force and their propagation through the model.

In any time domain pressure signal, the high frequency components generate sharp, narrow peaks of the wave field, whereas the low frequency components produce the broader, smoother variations (Jensen et al., 2011). When the model truncates the maximum frequency, these sharp high frequency components are removed. Because L_{peak} depends on the maximum instantaneous pressure (see Eq. 2.10), its value is strongly influenced by the presence of these high frequency contributions. Commonly, L_{peak} corresponds to the sharp initial arrival of the wave field. If the high frequency terms are omitted, the reconstructed time signal becomes smoother, the spike is rounded, and the maximum amplitude decreases, resulting in a lower L_{peak}.

Conversely, SEL depends on the total acoustic energy, i.e., the time integral of $p^2(t)$ (see Eq. 2.9). The bulk of this energy is still present in the truncated frequency range. The contribution of the high frequency tail to the overall energy is relatively small, meaning that truncating high frequencies has only a minor effect on SEL.

Model	Noise Metric	OM Result [dB]	SAM Result [dB]
1	SEL at 750 m	177.9	177.8
	L_{peak} at 750 m	197.6	197.7
2	SEL at 750 m	169.2	169.2
	L_{peak} at 750 m	180.6	180.6

Table J.4: Comparison of the frequency range Sensitivity Analysis Model (SAM) with the Original Model (OM) for both Model 1 and Model 2. The results show no significant differences between the OM and SAM, confirming that the truncated frequency range used in the OM is sufficient for accurate model results.

J.3. Sensitivity to Truncation Domain SGM

In FEM models, the computational domain must be truncated at a finite distance from the source. Because waves cannot propagate infinitely in a numerical model, a truncation boundary approximates

the unbounded environment. Although these boundaries are designed to minimize reflections, they always introduce some degree of numerical approximation. If the truncation surface is positioned too close to the region of interest, reflections or numerical leakage may contaminate the computed wave field (Sarma, Mallick, and Gadhinglajkar, 1998).

For this reason, it is essential to verify that the chosen truncation radius is sufficiently large for both models.

In both models, a truncation boundary at 55 m and an extraction radius at 50 m are used. The purpose of this analysis is to verify that the boundary is positioned sufficiently far from the extraction location so that reflections or numerical artifacts caused by the truncated domain do not contaminate the extracted wave field.

To evaluate whether the truncation domain used in the OM is sufficiently large, the SAM increases the truncation boundary to 70 m. This ensures that no artificial numerical effects influence the data extracted at the 50 m radius.

The results of this truncation domain sensitivity analysis are presented in Table J.5. The comparison shows that the SAM and OM outputs do not differ significantly in terms of noise levels. This indicates that moving the truncation boundary farther away from the extraction location does not significantly affect the model results. Therefore, the domain size used in the OM is adequate and does not introduce significant artificial deviations in the extracted noise levels.

If this had not been the case, the SAM would have exhibited different noise levels, as reflections or numerical artifacts originating from the outer boundary could have altered the extracted wave field. Such contamination would then propagate into the far field predictions at 750 m from the pile, resulting in noticeable discrepancies between the OM and SAM outputs.

Model	Noise Metric	OM Result [dB]	SAM Result [dB]
1	SEL at 750 m	177.9	177.8
	L_{peak} at 750 m	197.6	197.6
2	SEL at 750 m	169.2	169.5
	L_{peak} at 750 m	180.6	180.7

Table J.5: Comparison of the truncation domain Sensitivity Analysis Model (SAM) with the Original Model (OM) for both Model 1 and 2. The results show no significant differences between the OM and SAM, confirming that the truncation radius of the SGM domain used in the OM is sufficient for accurate model results.

J.4. Sensitivity to Extraction Radius

In a coupled SGM-SPM modeling approach, the extraction radius defines the interface between the detailed near-field solution obtained from FEM model and the far-field propagation computed using SILENCE. This radius must be chosen such that all near-field mechanisms have fully developed before the wave field is transferred to the SPM. If the extraction radius is chosen too close to the pile, the wave field may still be influenced by near-field mechanisms. In that case, the SPM would receive a distorted or incomplete wave field, which would propagate errors into the far-field predictions.

If increasing the extraction radius does not alter the resulting noise metrics, then the initially chosen radius is appropriate and produces a correct input for the SPM. To evaluate whether the extraction radius used in the OM is sufficiently far from the pile so that all relevant wave field components have fully developed, the SAM increases the extraction radius to 60 m. Consequently, the truncation radius is extended to 70 m to ensure that no numerical artifacts occur at the boundary, as validated in Subsection J.3.

The results of this extraction radius sensitivity analysis are presented in Table J.6. The comparison shows that the SAM and OM outputs do not differ significantly in terms of noise levels. This demonstrates that increasing the extraction radius does not significantly influence the model results. Therefore,

the extraction radius used in the OM is adequate and ensures that all relevant wave field components have developed before the data are passed to the SPM for far field propagation.

If this had not been the case, the SAM would have shown different noise levels, as not all wave field mechanisms would have been captured at the smaller extraction radius. The data that contains missing components would then propagate into the far field predictions at 750 m, resulting in noticeable discrepancies between the OM and SAM outputs.

Model	Noise Metric	OM Result [dB]	SAM Result [dB]
1	SEL at 750 m	177.9	177.8
	L_{peak} at 750 m	197.6	197.7
2	SEL at 750 m	169.2	170.3
	L_{peak} at 750 m	180.6	181.6

Table J.6: Comparison of the data extraction radius Sensitivity Analysis Model (SAM) with the Original Model (OM) and the measured data. The results show no significant differences between the OM and SAM, confirming that the extraction radius used in the OM is sufficient for accurate model results.

K

Soil Case Analysis

In this appendix, a soil case study is conducted to investigate the effectiveness of the NMS deployed in different soil configurations defined in Section 6.1. The chapter begins with an overview of the obtained SEL for the various soil case models, considering the Unmitigated, NMS, and Perfect System configurations (Section K.1). This is followed by a more detailed analysis of the Unmitigated results in Section K.2. Finally, Section K.3 presents a comparison of the NMS and Perfect System results for each individual soil case. The conclusions of this soil case study are summarized in Section 6.2.

K.1. Overview of the Results

Table K.1 summarizes the calculated SEL for the Unmitigated, Perfect System, and NMS configurations across the different soil cases defined in Section 6.1. In addition, peak sound pressure levels ($L_{p,peak}$) are presented for each soil case and scenario. Although the analysis in this case study focuses primarily on SEL, peak values are included for completeness. For reference, the soil cases are illustrated again in Figure K.1.

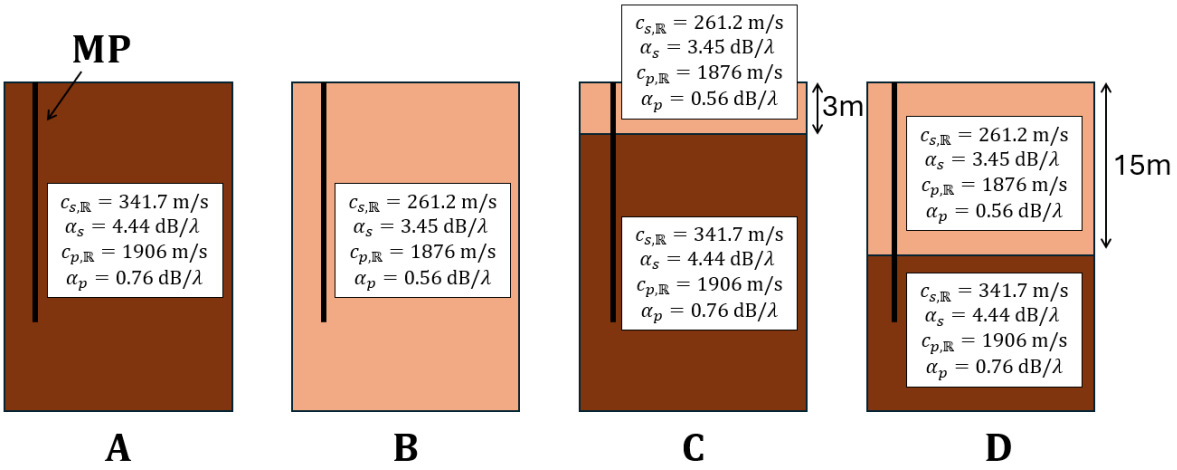

Figure K.1: Illustration of the soil cases considered in this study, as described in Section 6.1. Soil Case A represents uniform dense sand, while Soil Case B represents uniform loose sand. Soil Cases C and D correspond to layered soil configurations consisting of a loose upper layer overlying dense sand. Soil Case C features a thin upper layer, whereas Soil Case D has a thicker upper layer.

Soil Case	System Configuration	SEL at 750m [dB]	$L_{p,peak}$ at 750m [dB]
A	Unmitigated	176.2	198.7
	Perfect System	155.7	169.8
	NMS	166.1	180.3
B	Unmitigated	177.5	197.9
	Perfect System	163.3	177.6
	NMS	165.3	190.2
C	Unmitigated	178.5	198.0
	Perfect System	158.8	173.4
	NMS	166.8	182.3
D	Unmitigated	177.6	198.0
	Perfect System	162.8	177.6
	NMS	166.0	182.9

Table K.1: Summary of calculated SEL and Peak Sound Pressure Levels ($L_{p,peak}$) at 750 m for the evaluated soil stratifications and mitigation scenarios. While the present case study focuses on SEL, peak sound pressure levels are included for completeness.

From Table K.1, it can be observed that the SEL values for the Unmitigated cases vary by only 2.3 dB, indicating relatively minor sensitivity to soil properties in the absence of mitigation. This is consistent with findings reported by Bellmann et al. (2020), who observed that, for Baltic Sea projects with comparable blow energies, noise levels typically vary by approximately 2 dB.

When including the NMS, the cases only differ 1.5 dB which also indicates minor sensitivity. In contrast, the Perfect System exhibits substantially larger variations. Specifically, the SEL differs by 7.6 dB between Soil Case A and Soil Case B for the Perfect System configuration.

To examine these results in greater detail, Sections K.2 and K.3 provide an analysis of the Unmitigated case and of the NMS and Perfect System cases for each soil configuration, respectively.

K.2. Unmitigated Cases

Before assessing the noise mitigation performance of the NMS, it is essential to first understand the influence of soil properties and stratification on underwater noise generation and propagation for the unmitigated cases. The unmitigated cases serve as a baseline against which the mitigation effects of the NMS can be interpreted. In this section, the unmitigated results for the defined soil cases are analyzed. First, in Subsection K.2.1, the main observations are presented based on the calculated SEL and one third octave band spectra at 750 m and the energy distribution in across the soil and water column at 50 m. Subsequently, in Subsection K.2.2, these observations are explained. Finally, a conclusion is formulated summarizing the key insights obtained from the unmitigated cases (Subsection K.2.3).

K.2.1. Observations

From Table K.1, it can be seen that the calculated SEL at 750 m and 2 m above the seabed show relatively small differences between the soil cases. All cases fall within a range of 2.3 dB. When comparing the SEL results at 750 m, the following observations can be made:

- The lowest SEL is obtained for Soil Case A (uniform dense sand)
- A higher SEL is found for Soil Case B (uniform loose sand)
- The highest SEL is obtained for Soil Case C (thin layer over dense sand)

- Soil Case D (thick loose layer over dense sand) shows a slightly lower SEL than Soil Case C, but remains higher than both uniform soil cases

This ordering suggests that not only the stiffness of the soil, but also the presence and thickness of soil layering, influences the far-field sound levels.

Figure K.2 presents the one third octave band spectra at 750 m and provides further insight into the frequency dependent behavior. The following observations are made:

- At low frequencies (below approximately 31.5 Hz), all soil cases exhibit very similar spectral levels, with a pronounced peak around 25 Hz.
- For frequencies above 40 Hz, the spectral behavior diverges significantly between Soil Case A and Soil Cases B, C, and D.
- Soil Case A exhibits a decrease in spectral levels with increasing frequency
- Cases B, C, and D maintain higher spectral levels, up to approximately 8–15 dB above Soil Case A in the mid- to high frequency range.

The similarity in the one third octave band spectra observed for Soil Cases B, C, and D indicates that the acoustic response in the water column is primarily governed by the properties of the upper soil layer.

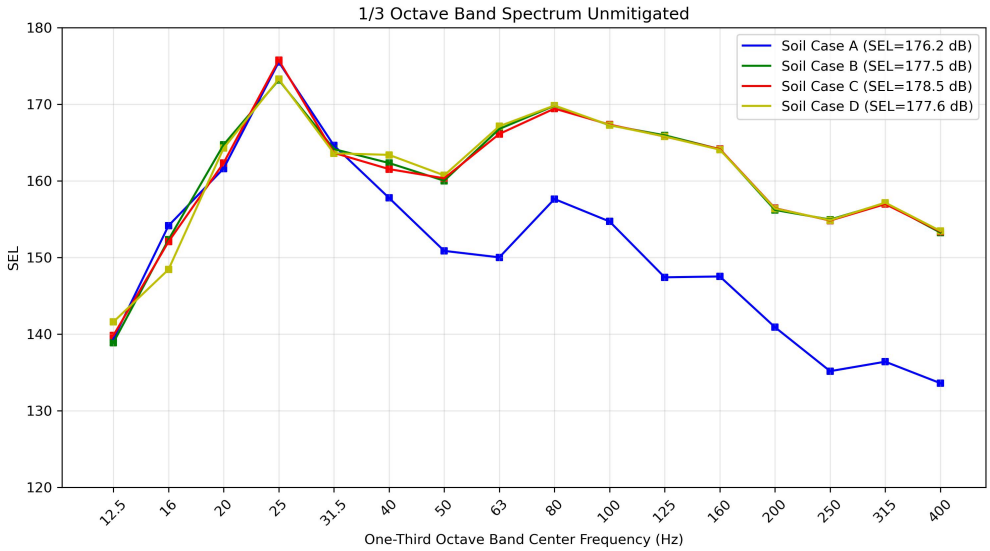

Figure K.2: One third octave band spectrum for all the unmitigated investigated soil cases at $r = 750\,m$ and 2 m above the seabed: Soil Case A (uniform dense sand), B (uniform loose sand), C (thin loose upper layer with underlying dense sand), and D (thick loose upper layer with underlying dense sand).

In addition, the distribution of near field energy at a radial distance of 50 m illustrates how the generated energy from the pile is divided between the soil and the water column, as well as the total amount of energy generated. This distribution is shown in Figure K.3. The following observations can be made:

- Soil Case A shows the highest total energy level at 50 m, with the majority (approximately 60%) of the energy propagating within the soil.
- Soil Case B retains an even larger fraction of energy in the soil (approximately 64%), while the total energy generation is smaller compared to Soil Case A.
- The layered soil configurations contain less total energy at 50 m, but exhibit a relatively higher fraction of energy present in the water column.
- In absolute terms, the amount of energy present in the water column at 50 m decreases in the order: Soil Case A, C, B, and D.

- In relative terms, the fraction of the total energy present in the water column is highest for Soil Cases C and D, followed by Soil Case A, and lowest for Soil Case B.

This indicates that higher far field noise levels are not directly associated with higher total energy generation, but rather with a more efficient transfer of energy from the soil into the water column and the efficiency with which this energy propagates to the far field.

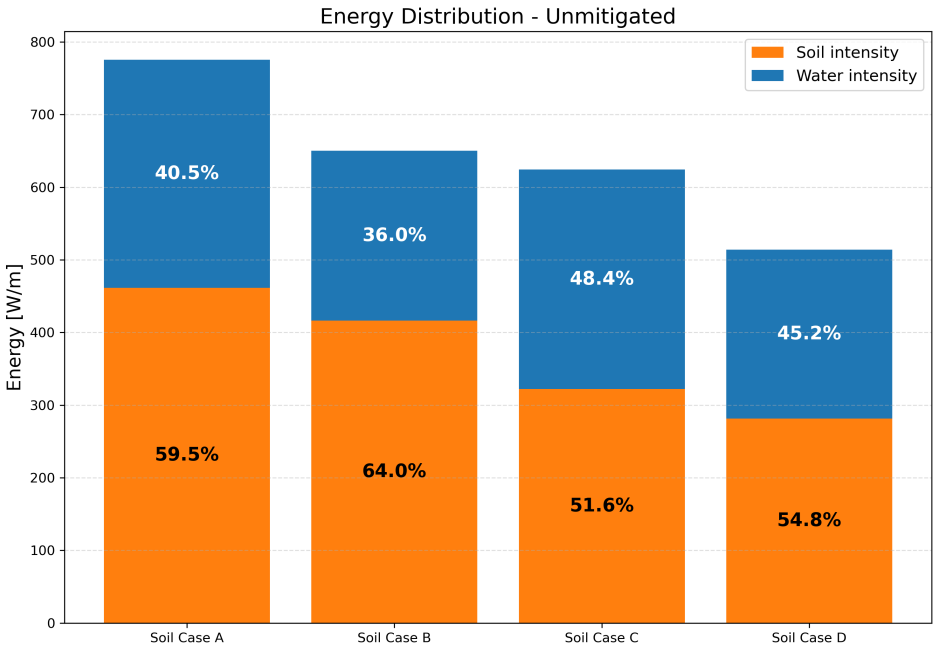

Figure K.3: Stacked bar plot showing the distribution of acoustic energy between the soil and the water column at $r = 50\,m$ from the pile for all unmitigated soil cases: Soil Case A (uniform dense sand), B (uniform loose sand), C (thin loose upper layer with underlying dense sand), and D (thick loose upper layer with underlying dense sand).

K.2.2. Explanation of Observations

This subsection provides an explanation of the observations identified for each soil case. The uniform soil cases are discussed individually, while in the subsection for the layered soil configurations a distinction is made between Soil Case C and Soil Case D.

Soil Case A -- Uniform Dense Sand

In the uniform dense sand configuration, the soil is characterized by high stiffness and a relatively high mechanical impedance, which describes how strongly a medium resists motion when it is dynamically excited. Compared to loose sand, dense sand has a higher mechanical impedance that is closer to that of the steel pile, resulting in a smaller mechanical impedance mismatch at the pile–soil interface and stronger coupling between the pile and the surrounding soil. In addition, dense sand exhibits relatively high frequency dependent attenuation, expressed in terms of decibel loss per wavelength (dB/λ).

The high impedance leads to strong coupling between the pile and the soil, resulting in efficient transfer of pile vibration energy into soil borne waves. However, dense sand also exhibits relatively strong attenuation, particularly at mid and high frequencies. Since the attenuation is defined per wavelength, the combination of high attenuation coefficients and high wave speeds leads to relatively large energy losses over propagation distance. Consequently, much of the mid- and high frequency energy is dissipated within the soil before it contributes to waterborne sound, explaining the spectral decay beyond approximately 40 Hz and the low SEL observed at 750 m.

Additionally, no impedance mismatch within the soil profile is present, downward radiating energy escapes into the soil half-space. Once this energy propagates away from the seabed, it will not interact with the water-soil interface again and therefore will not radiate back into the water column.

Soil Case B -- Uniform Loose Sand

In the uniform loose sand configuration, the lower stiffness and mechanical impedance reduce the efficiency with which pile motion is converted into wave energy when compared to Soil Case A. This is reflected by the lower total near field energy levels observed at 50 m.

Due to the lower attenuation of loose sand compared to dense sand, mid- and high frequency components experience less damping during propagation, resulting in higher spectral levels than those observed for dense sand. This explains the increase in SEL at 750 m compared to Soil Case A. Nevertheless, in the absence of impedance mismatch within the soil profile, downward radiating energy escapes into the soil half-space. Once this energy propagates away from the seabed, it will not interact with the water-soil interface again and therefore will not radiate back into the water column. As a result, although Soil Case B produces higher far-field SEL than Soil Case A, the efficiency of energy transfer to the water column remains limited due to the loss of energy into the deeper soil.

Soil Case C and D -- Layered Soils

For the layered soil configurations, a loose upper layer overlies a dense sand layer, introducing an impedance mismatch at the loose-dense interface. When downward propagating soil borne energy (Mach wave) encounters this interface, it is partially transmitted into the dense soil and partially reflected upward.

As a result, energy is no longer lost into the deeper soil (which was the case in Soil case A and B), but is repeatedly redirected between the seabed and the loose-dense interface. This does not imply that the energy is fully trapped, as a fraction is still transmitted into the dense underlying layer and into the water column at each interaction. However, the repeated redirection significantly increases the number of interactions between soil energy and the seabed and therefore the energy that is re-radiated back into the water column.

The thickness of the loose upper layer governs how frequently these redirection events occur and is illustrated in Figure K.4:

- In Soil Case C, the thin loose layer results in a short horizontal distance between encounters with the seabed. This leads to a larger number of redirection cycles and seabed interactions over the propagation distance toward 750 m compared to Soil Case D.
- In Soil Case D, the thicker loose layer increases the horizontal distance between seabed encounters, resulting in fewer redirection cycles and fewer opportunities for interaction with the seabed.

Each seabed interaction provides an opportunity for only a small fraction of energy to leak into the water column due to the relatively large impedance mismatch between soil and water. Although individual leakage events are weak and energy losses into the underlying dense soil are dominant since the impedance mismatch between loose and dense sand is relatively smaller, the significantly higher number of seabed interactions in Soil Case C leads to a larger cumulative transfer of energy into the water column compared to Soil Case D.

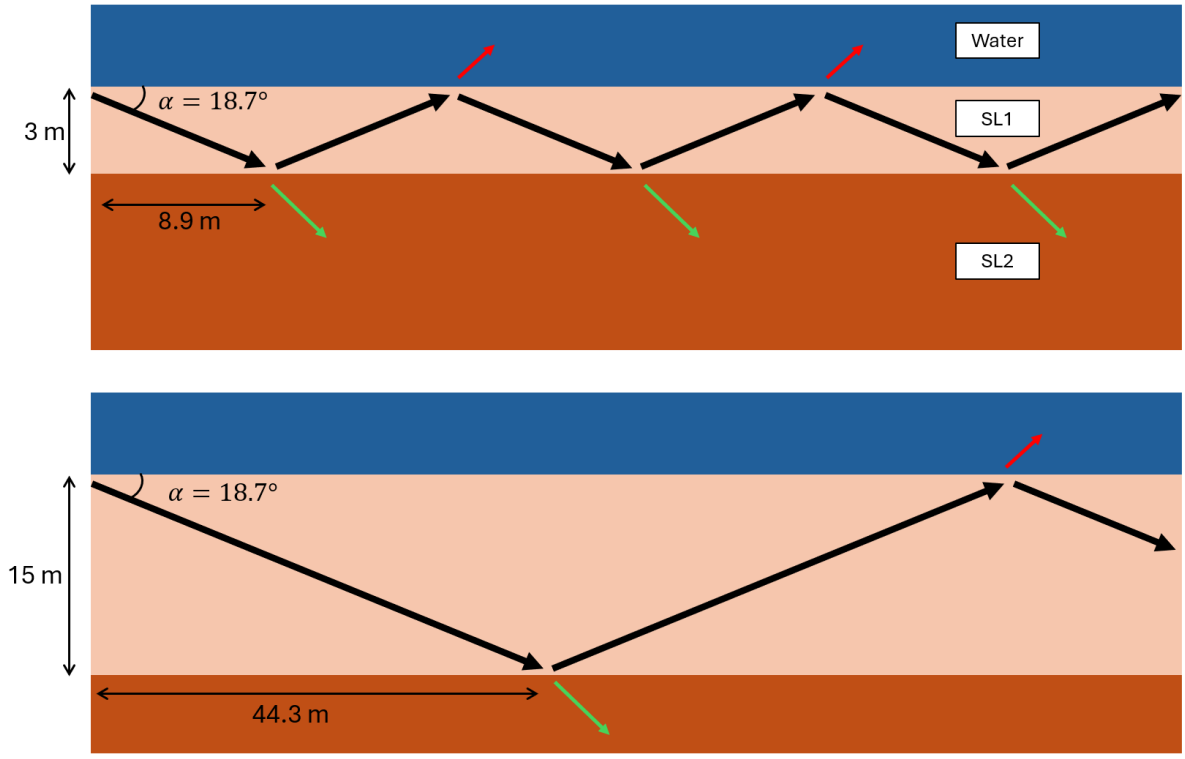

Figure K.4: Illustration of the noise propagation paths within the top soil layer for Soil Case C and Soil Case D. In Soil Case C, the noise path encounters 42 interaction points at the seabed where energy can re-radiate into the water column, whereas in Soil Case D only 8 such interaction points occur over a propagation distance of 750 m. These values are derived from the Mach angle, calculated as $\alpha = \sin^{-1}(\frac{c_{p,loose}}{c_{p,MP}}) = \sin^{-1}(\frac{1876}{5848}) = 18.7°$, and the thickness of the loose top soil layer. Green arrows indicate energy transmission into the deeper soil, while red arrows represent locations where the noise path can re-radiate back into the water column.

In addition, as dense soils convert pile motion into radiated energy more efficiently than loose soils, the larger contribution of dense soil behavior in Soil Case C also helps explain the higher near field energy levels observed at 50 m compared to Soil Case D. Although a thicker loose layer has more generated pile energy within the soil, the far field underwater noise level is governed by the amount of cumulative energy leaking into the water column. This cumulative energy leaking into the water column is assumed to be larger in Soil Case C compared to D based on the higher SEL at 750 m.

K.2.3. Conclusion Unmitigated Cases

The analysis of the unmitigated cases leads to the following conclusions:

- Underwater noise levels at 750 m are governed not only by the total energy generated by the pile and its partitioning between the water column and the soil, but also by the efficiency with which this energy propagates to the far field and couples from the seabed into the water column.
- Uniform dense sand generates relatively high energy due to strong pile-soil coupling, but the larger assigned frequency dependent attenuation suppresses mid- and high frequency components over propagation distance.
- Uniform loose sand reduces attenuation of mid- to high frequency sound levels compared to dense sand.
- In uniform soils, energy gets 'lost' in the deeper soil which result in smaller amount of energy re-radiating back into the water column compared to layered soils.
- The similarity of the one third octave band spectra for Soil Cases B, C, and D indicates that the acoustic response in the water column is primarily governed by the properties of the upper soil layer, whereas deeper stratification mainly influences the magnitude of the generated energy.

- Layered soil profiles alter the radiation mechanism by repeatedly redirecting soil energy toward the seabed, enabling energy leakage into the water column.
- A thin loose upper layer results in a higher amount of energy transfer to the water column than a thick loose layer, leading to larger cumulative energy transfer to the water column and the highest far-field SEL values.

K.3. Mitigation Cases: NMS and Perfect System

Having established the influence of soil properties and stratification on underwater noise generation and propagation in the unmitigated configuration, the effects of the NMS and the Perfect System are investigated in this section.

The NMS is modeled as an air layer, representing a simplified approximation of the NMS and capturing its dominant mitigation mechanism, namely the large impedance mismatch between water and air (see Appendix H). In addition, a Perfect System is considered, which is represented by an absorbing boundary condition at the location of the NMS. This configuration serves as an idealized upper bound for noise mitigation and provides insight into the maximum achievable noise reduction that could be obtained.

In this section, the performance of the NMS and the Perfect System is first compared across the different soil cases. After this general comparison, the results are discussed for each soil case individually. For each soil case, observations are first presented based on the broadband SEL at 750 m, the one third octave band spectra at 750 m, and the intensity distribution over depth at 50 m. These observations are then used to analyze and interpret the observed mitigation behavior. Finally, conclusions are drawn for each soil case.

K.3.1. General Observations Across the Soil Cases

Figures K.7 and K.8 present the one third octave band spectra for all soil cases obtained using the Perfect System and the NMS, respectively. In addition, Figure K.9 shows the distribution of intensity at $r = 50\,m$ for both the Unmitigated and NMS cases. Furthermore, Figures K.5 and K.6 presents the one third octave band spectrum of ΔSEL for Unmitigated minus NMS case, and for Unmitigated minus Perfect System case, respectively. These figures are included to facilitate a direct comparison between the different soil configurations.

From Figure K.5, it can be seen that the NMS performs less effectively at lower frequencies and generally better at higher frequencies. Below about 50 Hz, the mitigation is relatively low (mostly below 10 dB). A clear dip in ΔSEL is visible at 125 Hz for all soil cases (around 13 dB). A second dip is observed at 250 Hz, which is a multiple of 125 Hz. This suggests that these frequencies are related to the geometry of the modeled scenario. At these frequencies, the wavelength likely matches characteristic dimensions of the system (such as the cavity width or air layer thickness), which can lead to resonance or standing wave effects. As a result, the air layer could be excited more due to the larger pressures, allowing more energy to pass through the NMS instead of being reflected, and therefore reducing the mitigation effectiveness. Because this behavior is observed for all soil cases, it is likely caused by the NMS itself and not by the soil properties. This supports the idea that these dips are driven by the geometry of the system rather than energy transmission into the soil.

After these dips, the mitigation increases again towards higher frequencies, reaching values above 20 dB. A notable difference between soil cases is seen at 200 Hz, where Soil Case A shows a strong peak (around 30 dB), much higher than the other cases. Since this only occurs for Soil Case A, it is likely related to the soil properties. Only in this soil case, a dense sand layer is in contact with the water column. This could influence the frequency content that re-radiates back into the water column, however a clear explanation for this is not found yet and more research should be done to explain this behavior.

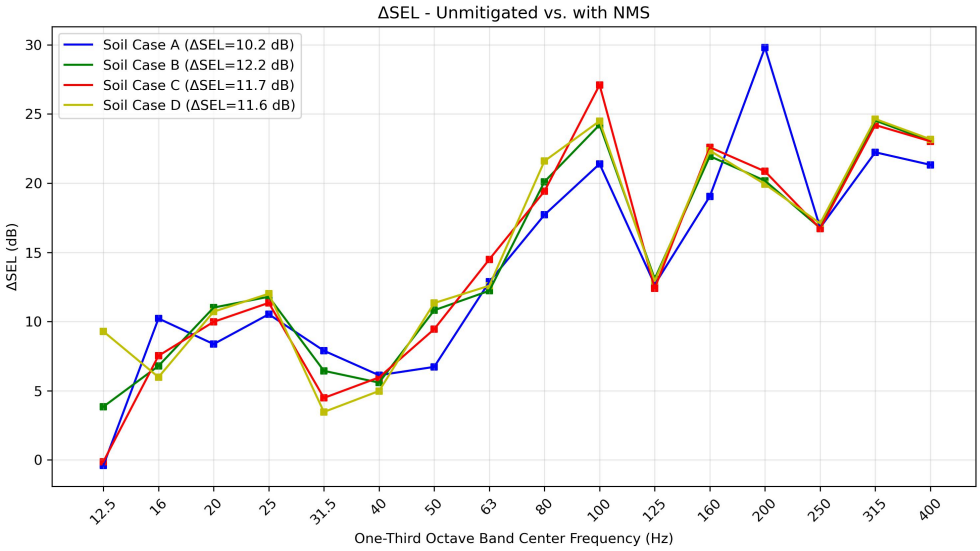

Figure K.5: One third octave band spectrum of ΔSEL (unmitigated minus NMS) for Soil Case A (uniform dense sand), B (uniform loose sand), C (thin loose upper layer with underlying dense sand), and D (thick loose upper layer with underlying dense sand).

From Figure K.6, the ΔSEL represents the difference between the unmitigated case (water + soil paths) and the perfect system case (soil path only). Therefore, this figure shows the contribution of the waterborne propagation path. A high ΔSEL indicates that a large part of the energy travels through the water column, while a low ΔSEL indicates that propagation through the soil dominates.

At low frequencies, a minimum is observed at 31.5 Hz for all soil cases (around 7–14 dB). The low ΔSEL at this frequency indicates that only a limited part of the energy propagates through the water column, meaning that most energy is generated into the soil. This suggests efficient coupling of energy into the seabed at this frequency.

For increasing frequencies, the ΔSEL generally increases, reaching values between 20 and 45 dB. This indicates that the waterborne contribution becomes more dominant at higher frequencies.

Despite this overall increase, a clear dip is again observed around 200 Hz for all soil cases. At this frequency, the ΔSEL decreases (to around 22–28 dB), indicating a temporary reduction in the waterborne contribution. It could be that in this frequency band the pile is more effectively coupled to the soil and therefore generates more energy in the soil rather than in the water column.

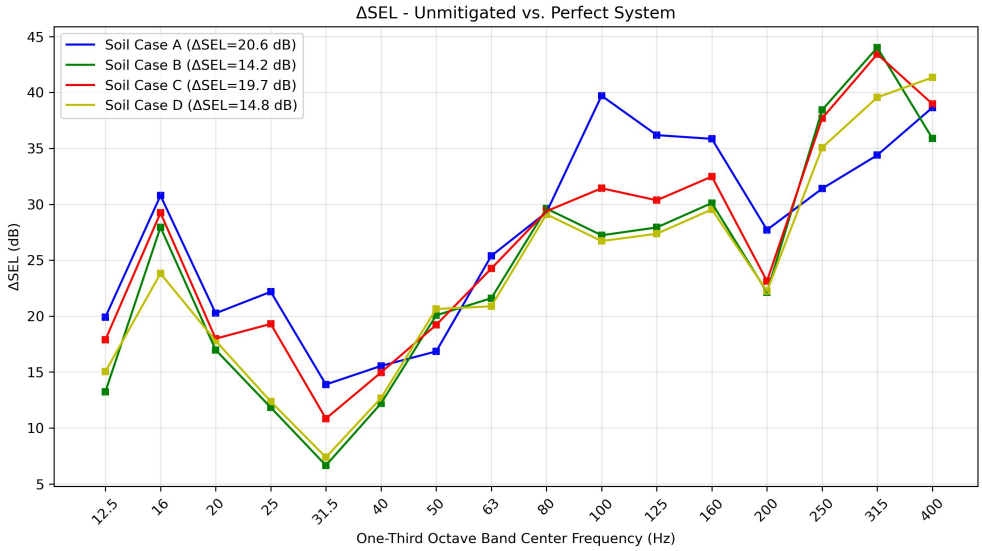

Figure K.6: One-third octave band spectrum of ΔSEL (unmitigated minus Perfect System) for Soil Case A (uniform dense sand), B (uniform loose sand), C (thin loose upper layer with underlying dense sand), and D (thick loose upper layer with underlying dense sand).

The overview figures (K.7, K.8, and K.9) are presented here to highlight the differences between the soil cases but are not explained individually.

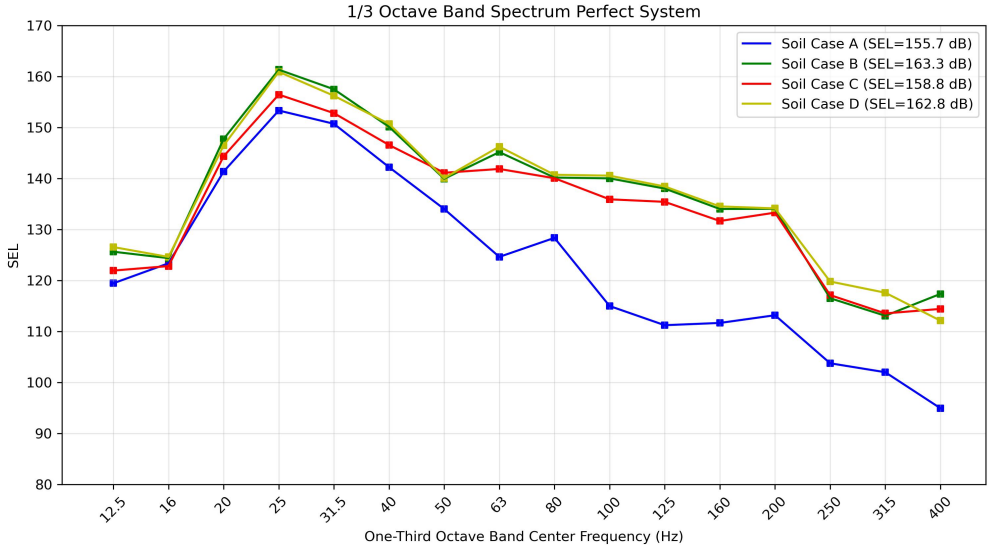

Figure K.7: One third octave band SEL spectrum for Soil Case A (uniform dense sand), B (uniform loose sand), C (thin loose upper layer with underlying dense sand), and D (thick loose upper layer with underlying dense sand) for the Perfect System scenario.

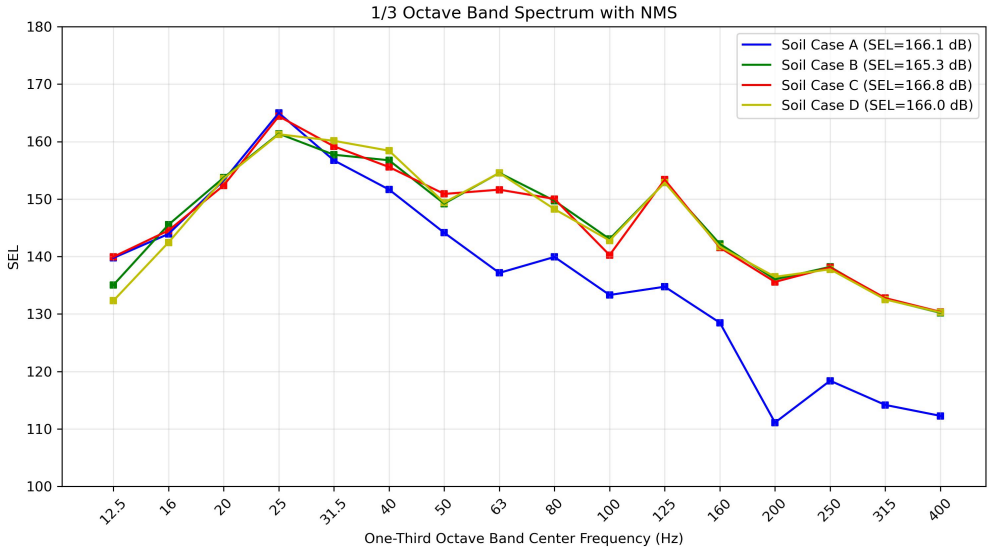

Figure K.8: One third octave band SEL spectrum for Soil Case A (uniform dense sand), B (uniform loose sand), C (thin loose upper layer with underlying dense sand), and D (thick loose upper layer with underlying dense sand) for the NMS scenario.

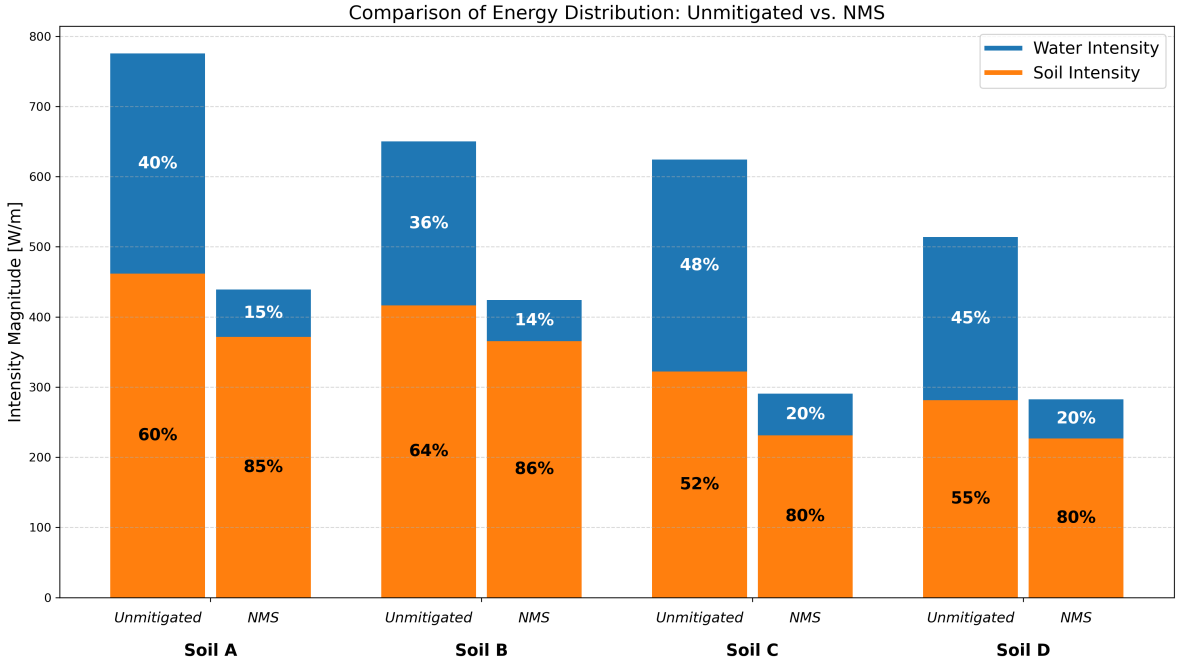

Figure K.9: Intensity distribution across the water column and the soil at $r = 50\,m$ for Soil Case A (uniform dense sand), B (uniform loose sand), C (thin loose upper layer with underlying dense sand), and D (thick loose upper layer with underlying dense sand) for the Unmitigated and NMS scenarios.

K.3.2. Soil Case A -- Uniform Dense Sand

In this subsection, the performance of the NMS and the Perfect System is analyzed for Soil Case A, consisting of a uniform dense sand profile.

Observations

The calculated SEL at distance of 750 m for this soil case is presented in Table K.1. The Perfect System achieves a noise reduction of 20.5 dB at 750 m, while the NMS achieves a reduction of 10.1

dB. This indicates that Soil Case A provides a relatively high mitigation potential, of which the simplified numerical representation of the NMS achieves approximately half.

Based on the one third octave band spectra for Soil Case A (see Figure K.10), the following observations can be made when comparing the Unmitigated, the NMS, and the Perfect System case:

- For the lower frequencies, the SEL difference between Unmitigated and Perfect System is smaller compared to the higher frequencies.
- At low frequencies (below approximately 50 Hz), the noise reduction achieved by the NMS is limited. In this range, the NMS spectrum remains close to the Unmitigated spectrum, indicating that low frequency energy is only weakly mitigated.
- In the mid- to high frequency range, the separation between the Unmitigated and NMS spectra increases, demonstrating that the NMS becomes more effective at reducing sound levels in these frequency bands.
- The 200 Hz band, the SEL predicted for the NMS case is lower than that of the Perfect System, indicating a locally stronger mitigation effect than the Perfect System.

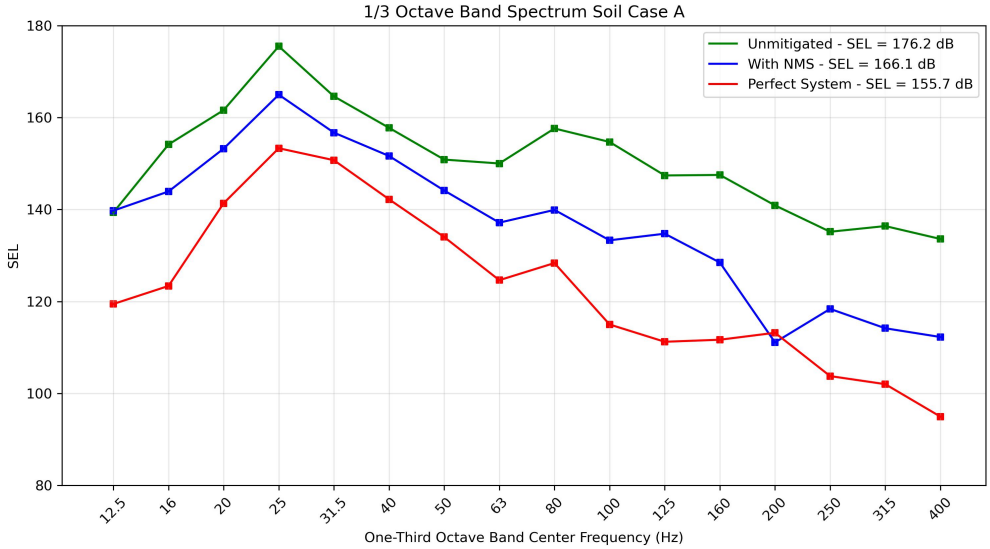

Figure K.10: One third octave band SEL spectrum for Soil Case A (uniform dense sand), comparing the Unmitigated, the NMS, and Perfect System scenario.

Based on the intensity over depth profile at $r = 50\,m$ for Soil Case A, the following observations can be made:

- The application of the NMS leads to a clear reduction in intensity throughout the water column compared to the Unmitigated case, indicating that the NMS effectively blocks a significant portion of the waterborne acoustic energy. The reduction is water column intensity is approximately 78.5%.
- The highest intensity levels are observed near the seabed, suggesting strong exchange of energy between the water column and the soil.
- A localized relative increase in soil intensity is observed for the NMS case compared to the Unmitigated case near the seabed. However, the soil intensity near the seabed is smaller for the NMS case compared to the Unmitigated case.
- In the deeper soil layers, the difference between the Unmitigated and NMS intensity profiles becomes negligible, demonstrating that the impact of the NMS is confined to depths up to approximately the pile embedment depth.

- The overall soil energy at a distance of 50 m is lower for the NMS case than for the Unmitigated case, 462 W/m versus 372 W/m, this is a reduction of approximately 19.5%.

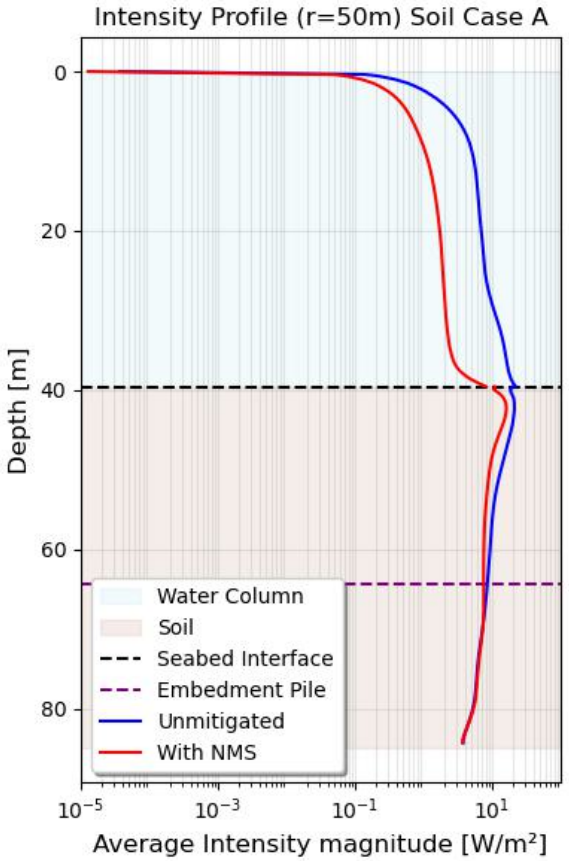

Figure K.11: Intensity as function of depth at $r = 50\,m$ for Soil Case A (uniform dense sand), comparing unmitigated conditions and the application of the NMS.

Analysis of Observations

The relatively large mitigation potential observed for Soil Case A can be explained by the unmitigated energy distribution presented in Figure K.3. In the Unmitigated case, this soil case exhibited the highest absolute amount of energy present in the water column. Consequently, there is a large amount of energy available in the water column for mitigation which result in the high mitigation potential. For the Perfect System, which removes all the energy in the water column at the NMS location, this results in a large achievable noise reduction of 20.5 dB at 750 m. The simplified NMS representation achieves approximately half of this reduction, indicating that a fraction of the waterborne energy can be mitigated through the impedance contrast introduced by the air layer, however, this also suggests that energy propagates through the air layer or that energy is redirected into the soil and re-radiate back into the water column behind the NMS.

The one third octave band spectra show a frequency dependent mitigation behavior. At low frequencies (below approximately 50 Hz), the mitigation achieved by the NMS is limited. The associated wavelengths are large compared to the thickness of the air layer, reducing its effectiveness and allowing low frequency energy to propagate past the NMS. At mid- and high frequencies, wavelengths decrease and the large impedance mismatch between water and air leads to increased reflection, resulting in stronger mitigation. The locally stronger mitigation observed around the 200 Hz band, where the NMS predicts lower levels than the Perfect System, is assumed to be a numerical artifact and should not be interpreted as an physical realizable improvement of the NMS. However, further research is required to confirm this.

At mid- to high frequencies, the mitigation effectiveness of the NMS improves, as reflected by the increasing separation between the Unmitigated and NMS spectra. Showing that namely the mid to higher frequencies are present in the water column in the near field while the lower frequencies propagate namely through the soil as seen by the small difference in low frequencies for the Unmitigated and Perfect System case compared to the mid- to high frequencies.

The one third octave band spectra also show that the differences in SEL between the Unmitigated and Perfect System scenarios are small at low frequencies compared to those at higher frequencies. This indicates that lower frequency energy propagates relatively more through the soil than higher frequency energy. Otherwise, the Perfect System would have resulted in a greater reduction of low frequency energy in the water column.

The intensity over depth profiles at $r = 50\,m$ confirm that the NMS significantly reduces intensity throughout the water column compared to the Unmitigated case. In both configurations, the largest intensities are observed near the seabed, indicating strong fluid-soil energy exchange.

For the NMS case, a localized relative increase in soil intensity near the seabed is observed for the NMS case. However the soil intensity is lower compared to the Unmitigated case. As identified in Appendix H, the reflected energy is redirected back toward the pile, becomes confined within the cavity formed by the pile and air layer, and is subsequently injected into the soil as seismic waves. Despite this redistribution, the integrated soil intensity over depth shows that the total energy at $r = 50\,m$ is lower for the NMS case than for the Unmitigated case (461 W/m versus 372 W/m respectively). This indicates that the energy reflected by the air layer results in smaller pile vibration, which results in lower energy generation. Additionally, part of the reflected energy is redirected into the soil, where it is dissipated through soil attenuation, which is relatively strong for dense sand and therefore does not significantly amplify the soil intensity near the seabed.

Conclusions

Based on the observations and analysis for Soil Case A, the following conclusions can be drawn:

- Soil Case A provides favorable conditions for noise mitigation in terms of overall mitigation potential. The Perfect System achieves a reduction of 20.5 dB, confirming that strong mitigation is theoretically possible for a uniform dense sand profile.
- The simplified NMS representation captures the primary mitigation mechanism based on impedance mismatch and achieves approximately half of the theoretical mitigation potential.
- Low frequency energy remains dominant and is only weakly mitigated, which limits the achievable reduction in broadband SEL by the NMS for this soil configuration.
- Although the NMS significantly reduces waterborne energy (about 78.5%), a portion of the reflected energy is redistributed into the soil which result in a relative increase of soil intensity near the seabed. This energy propagates near the seabed toward the far field, potentially re-radiating back into the water column.
- While in the NMS case energy is injected into the soil from the cavity, the resulting soil intensity remains lower than in the Unmitigated case (soil intensity reduces by 19.5%). This suggests that the energy reflected by the air layer reduces pile vibrations and, consequently, the total generated energy.
- The energy injected from the cavity into the soil is predominantly high frequency content and is therefore strongly attenuated due to the relatively larger attenuation coefficients at higher frequencies. As a result, this redirected energy, in combination with the reduced pile vibrations, prevents a significant amplification of intensity near the seabed.

K.3.3. Soil Case B -- Uniform Loose Sand

In this subsection, the performance of the NMS and the Perfect System is analyzed for Soil Case B, consisting of a uniform loose sand profile.

Observations

The calculated SEL at a distance of 750 m for Soil Case B is presented in Table K.1. Compared to the Unmitigated case, the Perfect System achieves a noise reduction of 14.2 dB, while the NMS achieves

a reduction of 12.2 dB. This indicates that, for Soil Case B, the overall mitigation potential is 6.3 dB lower than for Soil Case A. In addition, the simplified NMS representation provides 2.1 dB more noise reduction for Soil Case B compared to Soil Case A.

Based on the one third octave band spectra for Soil Case B (Figure K.12), the following observations can be made when comparing the Unmitigated, NMS, and Perfect System cases:

- At lower frequencies, the SEL difference between the Unmitigated and Perfect System cases is smaller than at higher frequencies.
- At low frequencies (below approximately 16 Hz), the NMS spectrum closely follows the Unmitigated spectrum.
- For frequency bands above approximately 16 Hz, the NMS spectrum follows the Perfect System spectrum more closely.

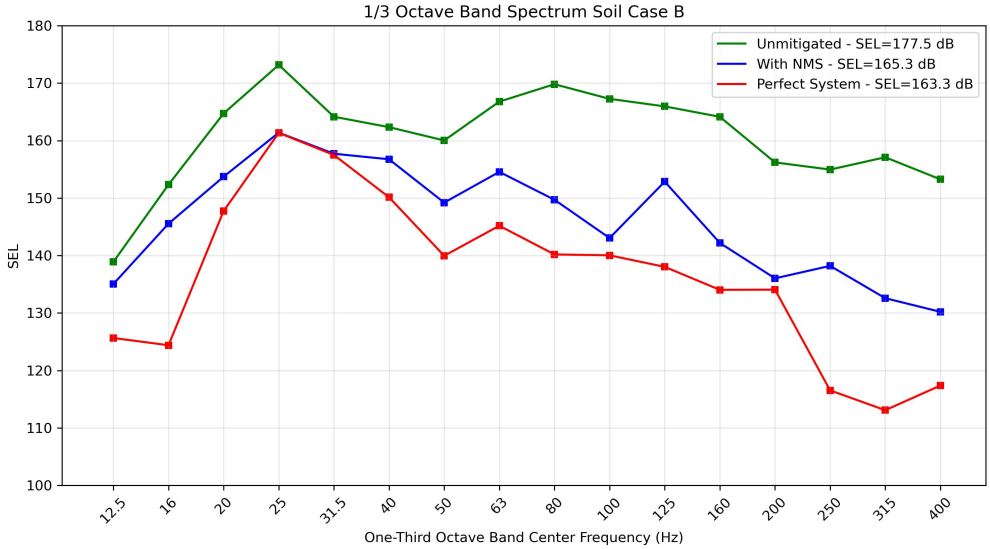

Figure K.12: One third octave band SEL spectrum for Soil Case B (uniform loose sand), comparing the Unmitigated, the NMS, and Perfect System scenario.

The intensity over depth profiles at a radial distance of 50 m for Soil Case B (Figure K.13) shows the following characteristics:

- The application of the NMS leads to a reduction in acoustic intensity within the water column compared to the Unmitigated case. The reduction in water column intensity is approximately 74.9%.
- The soil intensity does not change significantly when the NMS is applied. However, the intensity magnitude in the upper part of the soil is relatively higher for the NMS case than for the Unmitigated case.
- In the deeper soil layers, the difference between the Unmitigated and NMS intensity profiles becomes negligible, indicating that the influence of the NMS is confined to depths approximately up to the pile embedment.
- The total integrated intensity at $r = 50\,m$ is lower for the NMS case than for the Unmitigated case, indicating a decrease in the total generated energy for Soil Case B when the NMS is applied.

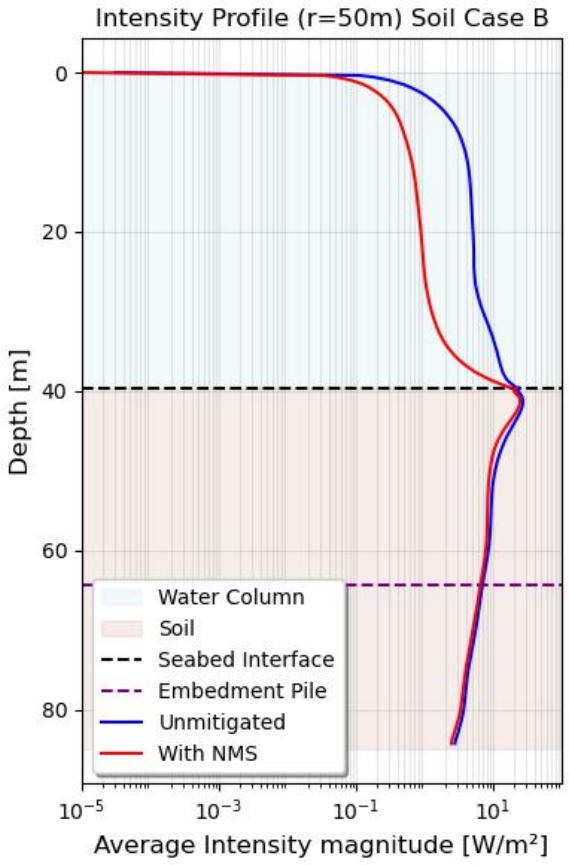

Figure K.13: Intensity as function of depth at $r = 50\,m$ for Soil Case B (uniform loose sand), comparing unmitigated conditions and the application of the NMS.

Analysis of Observations

In the Unmitigated case, a relatively larger fraction of the generated energy propagates within the soil for uniform loose sand compared to Soil Case A, while a smaller fraction is present in the water column. As a result, less waterborne energy is available for mitigation at the location of the NMS, which limits the maximum achievable noise reduction by the Perfect System. This is reflected by the lower noise reduction achieved by the Perfect System for Soil Case B (14.2 dB) compared to Soil Case A (20.9 dB). When the NMS is applied, a noise reduction of 12.2 dB is achieved at 750 m, indicating that the simplified NMS representation performs relatively close to the Perfect System compared to Soil Case A.

In uniform loose sand, the lower mechanical impedance compared to dense sand implies that energy reflected by the air layer can more easily propagate from the water domain into the soil within the cavity. In addition, loose sand is characterized by lower attenuation than dense sand, meaning that this redirected energy is dissipated less rapidly within the soil. Despite the lower attenuation, the NMS performance for Soil Case B remains closer to the Perfect System than for Soil Case A. This suggests that the energy injected from the cavity is less effective at re-radiating back into the water column compared to dense sand. A possible explanation could be that, in loose sand, a larger part of the injected energy is directed downward into the soil rather than for example horizontally or as interface wave. In contrast, the stiffer dense sand may promote a more horizontal redistribution of energy, increasing the likelihood of re-radiation into the water column in the far field.

From the one third octave band spectra it was observed that at low frequencies, mitigation remains limited, as expected due to the large acoustic wavelengths relative to the thickness of the air layer. For frequencies above approximately 16 Hz, the mitigation effectiveness of the NMS increases, as shown by the growing separation between the Unmitigated and NMS spectra.

The intensity over depth profiles show that the NMS reduces the intensity in the water column, resulting in a different energy redistribution compared to the Unmitigated case. The depth integrated soil intensity at $r = 50\,m$ is lower for the NMS case than for the Unmitigated case, indicating a reduction in the total generated energy. This indicates that the energy reflected by the air layer results in smaller pile vibration, which results in lower energy generation. Additionally, part of the reflected energy is redirected into the soil, where it is dissipated through soil attenuation, which therefore does not significantly amplify the soil intensity near the seabed.

At the same time, the soil intensity for the NMS case is relatively more concentrated in the upper part of the soil compared to the Unmitigated case. This suggests that energy is injected into the soil from the cavity. Since the intensity plots do not provide information on the direction of energy transport, it is not possible to directly assess whether this energy is predominantly directed upward or downward. However, since the NMS performs relatively closely to the Perfect System, this suggests that for Soil Case B, a smaller portion of the seismic energy re-radiates back into the water column at far field distances.

Conclusions

Based on the observations and analysis for Soil Case B, the following conclusions can be drawn:

- Soil Case B exhibits a significantly lower overall mitigation potential compared to Soil Case A. The Perfect System achieves a reduction of 14.2 dB at 750 m, reflecting the reduced amount of waterborne energy available for mitigation in uniform loose sand. In Soil Case B, the energy present in the water column amounts to only 74.5% of that observed in Soil Case A.
- The simplified NMS representation provides broadband noise reduction of 12.2 dB. This indicates that, for uniform loose sand, the NMS performs relatively closely to the Perfect System.
- The one third octave band spectra show that mitigation is limited at low frequencies, where wavelengths are large relative to the air layer thickness, while mitigation becomes more effective at mid to high frequencies.
- Intensity over depth profiles indicate a strong reduction of intensity in the water column when the NMS is applied, while changes in the soil are limited. However, a relatively near surface soil intensity increase is observed, while in the deeper soil the difference in soil intensity compared to the Unmitigated case is small.
- The NMS performance remains close to that of the Perfect System. This suggests that, for this soil case, energy redirected into the soil is less effective in re-radiating back into the water column at far field distances.
- The integrated intensity magnitude at $r = 50\,m$ decreases when applying the NMS compared to the Unmitigated case. This indicates that the energy reflected by the air layer results in smaller pile vibration, which results in lower energy generation.

K.3.4. Soil Case C -- Thin Loose Upper Layer over Dense Sand

In this subsection, the performance of the NMS and the Perfect System is analyzed for Soil Case C, consisting of a thin loose sand upper soil and underlying dense sand.

Observations

The calculated SEL at a distance of 750 m for Soil Case C is presented in Table K.1. Compared to the Unmitigated case, the Perfect System achieves a noise reduction of 19.7 dB, while the NMS achieves a reduction of 11.7 dB. This indicates that Soil Case C exhibits a relatively high mitigation potential, comparable to that of Soil Case A and higher than that of Soil Case B. The simplified NMS representation achieves more than half of the mitigation obtained by the Perfect System.

Based on the one third octave band spectra for Soil Case C (Figure K.14), the following observations can be made when comparing the Unmitigated, NMS, and Perfect System cases:

- For the lower frequencies, the SEL difference between Unmitigated and Perfect System is smaller compared to the higher frequencies.

- At low frequencies (below approximately 40 Hz), the separation between the Unmitigated and NMS spectra is limited, indicating a modest mitigation in this frequency range.
- In the mid- to high frequency range, the NMS achieves a clear reduction relative to the Unmitigated case.

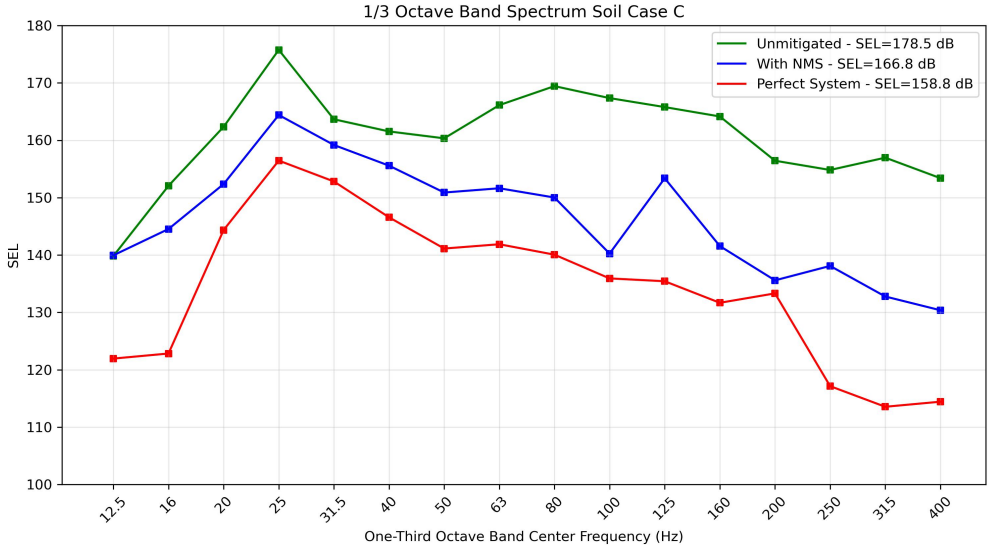

Figure K.14: One third octave band SEL spectrum for Soil Case C (thin loose sand top layer with underlying dense sand), comparing the Unmitigated, the NMS, and Perfect System scenario.

Based on the intensity over depth profile at a radial distance of $r = 50\,m$ for Soil Case C (Figure K.15), the following observations can be made:

- The application of the NMS leads to a clear reduction in intensity throughout the water column compared to the Unmitigated case. The water column intensity reduction is approximately 80.3%.
- The highest intensity levels are observed near the seabed, suggesting strong exchange of energy between the water column and the soil.
- A localized relative increase in soil intensity is observed near the seabed for the NMS case compared to the Unmitigated case.
- In the deeper soil, the difference between the Unmitigated and NMS intensity profiles becomes smaller, demonstrating that the impact of the NMS is confined to the upper soil.
- At the loose-dense interface no change in intensity is observed, indicating that no strong interface wave is present.
- The overall soil energy at $r = 50\,m$ is lower for the NMS case than for the Unmitigated case (soil intensity reduction of about 28.2%).

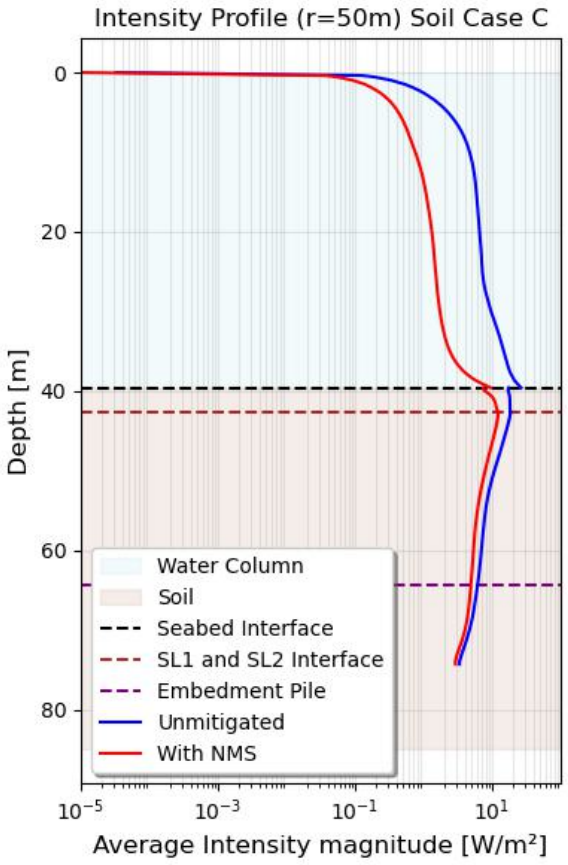

Figure K.15: Intensity as function of depth at $r = 50\,m$ for Soil Case C (thin loose sand top layer with underlying dense sand), comparing unmitigated conditions and the application of the NMS.

Analysis of Observations

In the Unmitigated case, Soil Case C exhibits relatively high far field noise levels. As discussed previously, this behavior is caused by the thin loose upper layer, which repeatedly redirects seismic energy toward the seabed and thereby enhances the coupling between the soil and the water column. Figure K.3 shows that a relatively large fraction of the total energy is present in the water column. Consequently, the Perfect System is able to remove a large amount of waterborne energy, resulting in a high mitigation potential of 19.7 dB. This value is lower than that of Soil Case A, as the absolute intensity present in the water column is smaller for Soil Case C (approximately 302 versus 314 W/m, respectively), and a portion of the seismic energy bypasses the NMS and subsequently re-radiates into the water column behind the NMS.

For the NMS case, part of the energy reflects on the air layer and propagates back toward the pile. Due to large energy build up in the cavity, this reflected energy is injected into the soil and propagates within the loose upper layer as seismic energy. Due to the relatively thin thickness of this layer, the energy is frequently redirected between the seabed and the loose-dense interface, which results in continued interaction with the water column. As a result, a portion of the energy leaks back into the water column, which explains why the NMS achieves a lower noise reduction of 11.7 dB compared to the Perfect System. Soil Case A, however, performs worse in this respect, likely because the dense sand generates a larger absolute amount of soil borne energy (462 versus 322 W/m, respectively. See Figure K.3). Consequently, the secondary noise path through the dense sand is more pronounced, leading to a greater contribution of re-radiated energy to the water column.

The one third octave band spectra show that the mitigation behavior is frequency dependent. At low frequencies, mitigation is limited because the wavelengths are large compared to the thickness of the air layer, reducing the effectiveness of the impedance mismatch. At mid- and high frequencies,

wavelengths decrease and the air-water impedance mismatch becomes more effective, resulting in a clear reduction of the NMS spectrum relative to the Unmitigated case.

At mid- to high frequencies, the mitigation effectiveness of the NMS improves, as reflected by the increasing separation between the Unmitigated and NMS spectra. Showing that namely the mid to higher frequencies are present in the water column in the near field while the lower frequencies propagate namely through the soil as seen by the small difference in low frequencies for the Unmitigated and Perfect System case compared to the mid- to high frequencies.

From the intensity over depth plot it was observed that similar to Soil Case A and B, the NMS leads to a significant reduction of intensity throughout the water column, confirming that waterborne energy is effectively mitigated. Elevated intensity levels near the seabed are observed for both the Unmitigated and NMS cases, indicating strong fluid-solid energy exchange. Additionally, for the NMS case, a localized relative increase in soil intensity is observed near the seabed compared to the unmitigated case. This indicates that part of the energy reflected by the NMS is redirected back toward the pile and subsequently injected into the soil. Due to the impedance mismatch between the loose and dense soil, some energy reflects and stays trapped in the upper soil layer. As a result, the increase in soil intensity remains confined to the upper part of the soil domain, and no large amplification is observed at greater depths.

Finally, the total integrated intensity at $r = 50\,m$ is lower for the NMS case than for the Unmitigated case. This indicates that the energy reflected by the NMS does lead to reduced pile vibrations for this soil configuration, resulting in a net reduction of generated energy. Additionally, the energy redirected from the water column into the soil undergoes attenuation, leading to a lower amount of energy remaining at $r = 50\,m$.

Conclusions

Based on the observations and analysis for Soil Case C, the following conclusions can be drawn:

- Soil Case C exhibits a relatively large overall mitigation potential. The Perfect System achieves a reduction of 19.7 dB at 750 m, indicating that a significant amount of energy is generated in the water column.
- The simplified NMS representation performs moderate for this soil configuration, achieving a reduction of 11.7 dB, corresponding to a bit more than half of the theoretical mitigation potential. In the water column, the NMS reduces the energy with 80.3% at 50 m.
- Noise mitigation remains frequency dependent. At low frequencies, mitigation is limited due to the large wavelengths relative to the air layer thickness, whereas at mid- and high frequencies the impedance mismatch between air and water results in better noise reduction compared to lower frequencies.
- The thin loose upper soil layer enhances interaction between seismic energy and the seabed, increasing the amount of energy that bypasses the NMS and re-radiates into the water column which reduces the noise mitigation performance of the NMS.
- Energy reflected by the NMS is partially redirected into the soil. This redistribution of energy remains localized near the seabed and within the upper soil layer due to the impedance mismatch with the dense underlying sand.
- While in the NMS case energy is injected into the soil from the cavity, the resulting soil intensity remains lower than in the Unmitigated case (soil intensity reduces by 28.2%). This suggests that the energy reflected by the air layer reduces pile vibrations and, consequently, the total generated energy.

K.3.5. Soil Case D -- Thick Loose Upper Layer over Dense Sand

In this subsection, the performance of the NMS and the Perfect System is analyzed for Soil Case D, consisting of a thick loose sand upper soil and underlying dense sand.

Observations

The calculated broadband SEL at a distance of 750 m for Soil Case D is summarized in Table K.1. For this soil configuration, the Perfect System achieves a noise reduction of approximately 14.8 dB relative

to the Unmitigated case (177.7 dB to 162.8 dB). The NMS results in a smaller reduction of 11.6 dB, yielding a broadband SEL of 166.0 dB. This indicates that, although mitigation is achieved, the overall mitigation potential for Soil Case D is lower than for Soil Case A and C and comparable to Soil Case B.

Based on the one third octave band SEL spectrum for Soil Case D (Figure K.16), the following observations can be made when comparing the Unmitigated, NMS, and Perfect System cases:

- For the lower frequencies, the SEL difference between Unmitigated and Perfect System is smaller compared to the higher frequencies.
- In these spectra, the frequency dependent performance of the NMS is less clearly visible than for the other soil cases. Notably, in the 25 Hz band, the NMS performs comparably to the Perfect System.
- In the mid- to high frequency range, the separation between the Unmitigated and NMS spectra increases, while the NMS spectrum remains relatively close to that of the Perfect System. This indicates an improved mitigation effectiveness of the NMS at these frequencies.

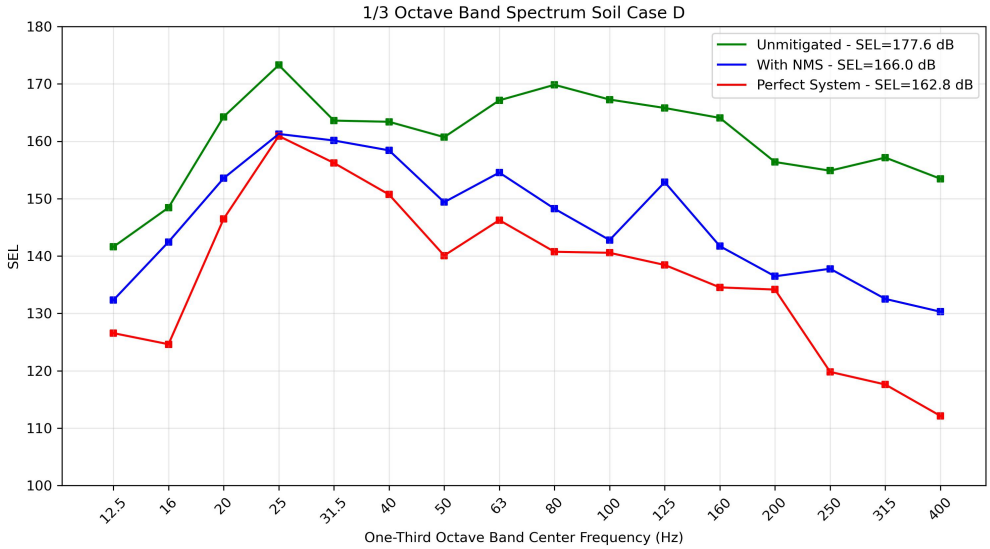

Figure K.16: One third octave band SEL spectrum for Soil Case C (thick loose sand top layer with underlying dense sand), comparing the Unmitigated, the NMS, and Perfect System scenario.

Based on the intensity over depth profile at a radial distance of $r = 50\,m$ for Soil Case C (Figure K.17), the following observations can be made:

- The application of the NMS leads to a clear reduction in intensity throughout the water column compared to the Unmitigated case. The reduction in water column intensity is approximately 75.8%.
- The highest intensity levels occur near the seabed, suggesting a strong exchange of energy between the water column and the soil.
- While the intensity in the water column decreases significantly, the soil intensity shows a less pronounced change and follows a similar depth dependent trend and order of magnitude. The depth integrated soil intensity is reduces by approximately 19.4%.
- At the interface between the loose upper layer and the underlying dense sand an increase in intensity is observed, indicating an interface wave and an exchange of energy between the loose and dense media.

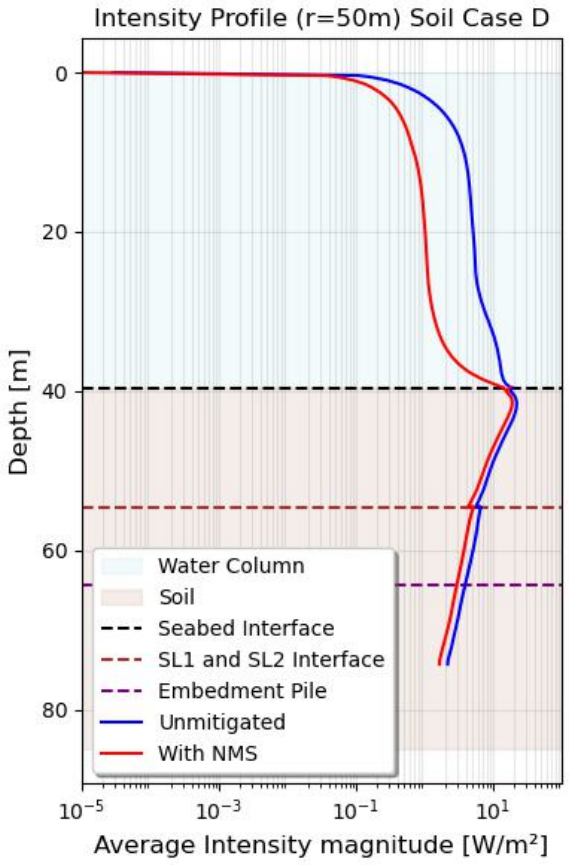

Figure K.17: Intensity as function of depth at $r = 50\,m$ for Soil Case D (thick loose sand top layer with underlying dense sand), comparing unmitigated conditions and the application of the NMS.

Analysis of Observations

In the Unmitigated case, the presence of a loose upper layer enhances coupling between the soil and the water column, as seismic energy is repeatedly redirected toward the seabed. As a result, a relatively large fraction of the energy is present in the water column in the far field, which explains the higher SEL observed for this soil case compared to the uniform soil cases. The Perfect System achieves a broadband noise reduction of 14.8 dB, indicating that in a relatively smaller amount of energy is generated in the water column for this soil case. This is consistent with the fact that the soil profile is dominated by loose sand, as observed in Soil Case B, loose sand reduces the total generated energy and, consequently, the achievable noise mitigation potential. This is because the pile is less clamped in the soil which result is less efficient coupling between the pile and the soil. The NMS representation achieves a reduction of 11.6 dB, suggesting that for Soil Case D the performance of the NMS is relatively close to that of the Perfect System compared to the other soil cases. This could partly be explained by less re-directions of the seismic energy back into the water column due to the thicker top layer compared to Soil Case C.

The one third octave band spectra reveals a less pronounced frequency dependent mitigation behavior compared to the other cases. This results in that lower frequencies are more mitigated which reduces the SEL. In particular, the comparable performance of the NMS and the perfect system around 25 Hz band suggests that energy in this band is propagating namely through the soil and re-radiates back into the water column behind the NMS instead of exciting the NMS.

At mid- to high frequencies, the mitigation effectiveness of the NMS improves, as reflected by the increasing separation between the Unmitigated and NMS spectra. Showing that namely the mid to higher frequencies are present in the water column in the near field while the lower frequencies propagate namely through the soil as seen by the small difference in low frequencies for the Unmitigated

and Perfect System case compared to the mid- to high frequencies.

The intensity over depth profiles at $r = 50\,m$ shows that the NMS significantly reduces intensity throughout the water column, confirming that a large portion of the waterborne energy is mitigated (approximately 78.5%). In both configurations, peak intensities occur near the seabed which indicates strong energy exchange between the water column and the soil. A localized increase in soil intensity near the seabed is observed for the NMS case, suggesting that energy reflected by the air layer is redirected back toward the pile and injected into the soil. Additionally, an increase in intensity at the interface between the loose upper layer and the dense sand indicates the presence of interface waves and enhanced energy exchange between the two soil layers. Despite these local effects, the depth-integrated soil intensity decreases with approximately 19.4%.

The intensity discontinuity observed at the interface between the loose upper layer and the underlying dense sand in Soil Case D is not clearly visible in Soil Case C. This difference is thought to be related to the thickness of the top layer. In Soil Case C, the loose upper layer is relatively thin. The vertical separation between the seabed and this interface is only 3 m, causing the seabed interactions to overlap spatially with the loose-dense interface interactions. As a result, the energy does not have the opportunity to propagate freely within the loose layer before reaching the interface. Instead, energy is continuously exchanged between the water column, the loose upper layer, and the dense layer over a small depth range. This leads to a more gradual transition, and no clear discontinuity in the intensity profile is observed. In contrast, for Soil Case D, the loose upper layer is sufficiently thick to allow energy to propagate within the loose sand over a larger vertical distance before interacting with the dense layer. This enables a more developed energy field within the loose layer. When this energy reaches the loose-dense interface, the energy transport changes more suddenly at the loose-dense interface, leading to a clear and localized discontinuity in the intensity profile at that depth.

Finally, the total integrated intensity at $r = 50\,m$ is lower for the NMS case than for the Unmitigated case. This indicates that, for Soil Case D, the reflected energy leads to a reduction of pile vibrations and therefore a net decrease in generated energy in the soil. Additionally, part of the energy redirected into the soil is attenuated, resulting in a net reduction of energy available to contribute to far field noise levels.

Conclusions

Based on the observations and analysis for Soil Case D, the following conclusions can be drawn:

- Soil Case D exhibits a moderate overall mitigation potential. The Perfect System achieves a broadband noise reduction of approximately 14.8 dB at 750 m, which is lower than for Soil Cases A and C and comparable to Soil Case B. This reflects the dominance of loose sand in the soil profile, which limits the total amount of energy generated and available for mitigation in the water column.
- The simplified NMS representation achieves a reduction of 11.6 dB, performing relatively close to the Perfect System compared to the other soil cases.
- The thick loose upper layer reduces the frequency of energy redirection toward the seabed compared to Soil Case C. This results in a better noise mitigation effectiveness of the NMS compared to Soil Case C.
- The frequency dependent behavior of the NMS is less pronounced than for the other soil cases. In particular, the comparable performance of the NMS and the Perfect System around the 25 Hz band suggests that low frequency energy is primarily transmitted through the soil and re-radiated into the water column behind the NMS, rather than propagating through the NMS since then this content would be mitigated by the Perfect System.
- At mid- to high frequencies, the mitigation potential and effectiveness of the NMS improves, as these frequency components are predominantly present in the water column and can therefore more effectively blocked by the air layer impedance mismatch.
- The intensity over depth profiles show that the NMS significantly reduces intensity throughout the water column (approximately 75.8%), confirming strong mitigation of waterborne energy. In contrast, the reduction in depth integrated soil intensity is more limited (approximately 19.4%).

This indicates that the application of the NMS does lead to reduced pile vibrations. but instead results in reduced pile vibrations and increased dissipation of energy within the soil.

- A clear intensity discontinuity is observed at the interface between the loose upper layer and the underlying dense sand. This indicates that, due to the thickness of the loose layer, energy is able to propagate within the loose sand and form a coherent wave field before interacting with the dense layer, leading to an abrupt change in energy transport properties at the interface and a jump in intensity.